

Institut für Physikalische und Theoretische Chemie

**Quantitative photoactivated localization microscopy
reveals the oligomeric state of the tumor necrosis factor
receptor 1**

DISSERTATION

Zur Erlangung des Doktorgrades

der Naturwissenschaften

vorgelegt beim Fachbereich Biochemie, Chemie und Pharmazie

der Johann Wolfgang Goethe-Universität

in Frankfurt am Main

von

Christos Karathanasis

aus Frankfurt am Main

Frankfurt 2019

(D30)

Vom Fachbereich Biochemie, Chemie und Pharmazie der Johann Wolfgang Goethe-Universität
als Dissertation angenommen.

Dekan: Prof. Dr. Clemens Glaubitz

Gutachter: Prof. Dr. Mike Heilemann
Prof. Dr. Gerhard Hummer

Datum der Disputation:

ZUSAMMENFASSUNG

Die Plasmamembran eukaryotischer Zellen dient als Barriere zwischen dem Inneren einer Zelle und ihrer Umgebung. Eine wichtige Aufgabe von Proteinen, die sich in der Plasmamembran befinden, besteht in der Erkennung der Umgebung, der Übermittlung dieser Informationen über die Plasmamembran in das Innere einer Zelle und der Einleitung einer zellulären Antwort. Membranrezeptoren binden Liganden, was zu ihrer Aktivierung und der Rekrutierung von intrazellulären Proteinen führt. Funktionelle Signalkomplexe werden gebildet und leiten einen Informationstransfer durch die Zellmembran ein, so dass die Expression bestimmter Gene stimuliert oder unterdrückt wird. Eine Störung der Signalinitiierung und -übertragung tritt bei vielen Krankheiten auf, so dass Membranproteine ein wichtiges Ziel in der Medikamentenentwicklung sind.

In dieser Arbeit wird die Fragestellung bearbeitet, wie der Tumornekrosefaktor-Rezeptor 1 (TNFR1) in funktionelle Komplexe in der Plasmamembran einer intakten Zelle organisiert ist. TNFR1 besitzt vier Cystein-reiche Domänen (CRDs) in seiner extrazellulären Region. Die erste und von der Plasmamembran am weitesten entfernte CRD ist die *pre-ligand assembly domain* (PLAD). Kristallstrukturen zeigten, dass sich in einem TNFR1-Dimer zwei PLAD in unmittelbarer Nähe befinden. *Crosslinking*-Experimente berichteten über mehrere oligomere Zustände von TNFR1; die Ergebnisse unterschieden sich nach Art und Konzentration des *Crosslinkers*. In der nativen Umgebung einer intakten Zelle wurde der oligomere Zustand von TNFR1 bisher nicht bestimmt. Der kanonische Ligand für TNFR1 ist der Tumornekrosefaktor alpha (TNF α), ein Homotrimer, welches in löslicher oder membrangebundener Form vorliegt. Nach der Bindung von TNF α an TNFR1 bilden sich Rezeptoroligomere. Diese Proteinkomplexe rekrutieren intrazellulär Proteine und bilden einen funktionellen Membrankomplex, der intrazelluläre Signalkaskaden aktiviert. Die kanonische Signalweiterleitung erfolgt durch den *nuclear factor kappa-light-chain-enhancer of activated B-cells* (NF- κ B), welcher Zellteilung oder Entzündung induziert. TNFR1 kann auch andere Signalwege wie beispielsweise Apoptose durch einen zytosolischen Komplex und die Procaspase-8, oder Nekroptose durch das Nekrosom und die *mixed lineage kinase domain-like* (MLKL)-Domäne einleiten. Die Dysregulation von TNFR1 ist bei einer Vielzahl von Krankheiten zu finden. Erhöhte TNFR1-Expressionsraten treten bei *acquired immune deficiency syndrome* (AIDS), multipler Sklerose und verschiedenen Krebsarten auf.

In einem zweiten Projekt wurde in Zusammenarbeit mit Prof. Dr. Michael Lanzer (Heidelberg, Deutschland) der Expressionsgrad des Proteins VAR2CSA in membranassoziierten *knobs* bestimmt, welche in Erythrozyten vorkommen, die mit dem Parasiten *Plasmodium falciparum* infiziert wurden. VAR2CSA gehört zur Proteinfamilie des *Plasmodium falciparum erythrocyte membrane protein 1* (pfEMP1). Nach einer Infektion wird VAR2CSA zur Wirtszellmembran transportiert und in *knobs* eingelagert. Patienten, die Sichelzellanämie-Erythrozyten (HbAS) aufweisen, sind im Gegensatz zu

Patienten mit gesunden Erythrozyten (HbAA) immun gegen Malaria. Während die beiden Erythrozytentypen eine unterschiedliche Morphologie der *knobs* aufweisen, blieb ihre Zusammensetzung in Bezug auf VAR2CSA bisher ungeklärt.

Das Verständnis der Proteinfunktion erfordert eine Beschreibung der molekularen Organisation funktioneller Einheiten in der zellulären Umgebung. Hierfür ist die Fluoreszenzmikroskopie eine geeignete Methode, da sie eine gezielte Markierung von Zielproteinen ermöglicht. Die hohe Sensitivität ermöglicht die Visualisierung einzelner Proteine. Eine Einschränkung in der konventionellen Fluoreszenzmikroskopie ist die Auflösungsgrenze. Strukturelle Elemente, die kleiner als etwa die halbe Anregungswellenlänge sind (für die meisten Anwendungen 200 bis 300 nm) können nicht aufgelöst werden. Die Entwicklung der hochauflösenden Fluoreszenzmikroskopie ermöglichte es, diese Auflösungsgrenze zu umgehen und eine räumliche Auflösung von wenigen Nanometern zu erreichen, was die Visualisierung und Charakterisierung einzelner Proteinkomplexe ermöglichte. Eine Art der hochauflösenden Fluoreszenzmikroskopie ist die *single-molecule localization microscopy* (SMLM), die auf der Detektion einzelner Fluorophore, einer genauen Bestimmung ihrer Position (Lokalisation) und der Erzeugung eines rekonstruierten Bildes unterhalb der optischen Auflösungsgrenze basiert. Da die meisten Proben in der Fluoreszenzmikroskopie eine zu hohe räumliche Dichte an Fluorophoren aufweisen, um den Nachweis von einzelnen Fluorophoren zu ermöglichen, werden Verfahren zur Kontrolle der Emission von Fluorophoren eingesetzt. Eine Möglichkeit ist der Einsatz von Fluorophoren, die optisch zwischen einem nicht-fluoreszierenden und einem fluoreszierenden Zustand geschaltet werden können, z.B. photoschaltbare fluoreszierende Proteine in *photoactivated localization microscopy* (PALM) oder organische Farbstoffe in *(direct) stochastic optical reconstruction microscopy* ((d)STORM). SMLM erreicht eine räumliche Auflösung von 20 nm, was in den meisten Fällen ausreicht, um einzelne Proteinkomplexe in einer Zelle aufzulösen. Diese räumliche Auflösung ist jedoch nicht ausreichend, um Untereinheiten innerhalb eines Proteinkomplexes zu visualisieren. Zu diesem Zweck wurde SMLM erweitert und die verfügbare kinetische Information genutzt, die bei der Detektion einzelner Fluorophore ausgelesen wird. Viele Fluorophore weisen metastabile Dunkelzustände auf, die eine Lebensdauer von bis zu Sekunden aufweisen. Diese Übergänge erscheinen als "Blinken" der Fluoreszenzemission. In Kombination mit kinetischen Modellen kann aus der Anzahl an Blink-Ereignissen die Anzahl der Fluorophore ermittelt werden. Angewendet auf hochaufgelöste Proteinkomplexe kann die Auflösungsgrenze von hochauflösender Mikroskopie umgangen werden, und die Anzahl der Protein-Untereinheiten in einem hochaufgelösten Proteincluster ermittelt werden. Hierzu wird beispielsweise das photoschaltbare fluoreszierende Protein mEos2 an ein Zielprotein fusioniert (*quantitative PALM* (qPALM)).

Um den oligomeren Zustand von TNFR1 zu bestimmen, wurde eine stabile TNFR1/2^{-/-} Maus-Embryo-Fibroblasten- (MEF)-Zelllinie mit TNFR1-mEos2 rekonstituiert (Dr. Sjoerd van Wijk und Prof. Dr. Ivan Dikic, Frankfurt, Deutschland) und mittels quantitativem PALM analysiert. In dieser Zelllinie wurde

die Funktionalität von TNFR1 durch die Zellantwort nach Stimulation mit TNF α durch die Translokation von NF- κ B in den Zellkern gezeigt. Darüber hinaus wurde die Induktion von nicht-kanonischen, durch TNFR1 induzierte Signalkaskaden, wie Apoptose und Nekroptose, nachgewiesen.

Quantitative PALM-Daten von TNFR1 in MEF-Zellen wurden unter Anwendung des *Bayesian information criterion* (BIC) und einer *Log-Likelihood*-Analyse analysiert. Für nicht stimulierte Zellen ergab diese Analyse, dass TNFR1 als Monomer (66 ± 4 %) und Dimer (34 ± 4 %) auftritt. Dies steht im Einklang mit früheren Kristallisations-, Western Blot- und FRET-Studien, welche zeigten das TNFR1 als Monomer und Dimer vorliegt und unterstützt ein Niedrig-Affinitäts-Modell der PLAD-PLAD-Wechselwirkung, welches zu einem Gleichgewicht von monomerem und dimerem TNFR1 führt. Um zu untersuchen, wie sich dieses Gleichgewicht bei Stimulation mit TNF α ändert, wurde SNAP-Flag-TNC-TNF α (Prof. Dr. Harald Wajant, Würzburg, Deutschland) mit Alexa Fluor 647 markiert (TNF α -SNAP-A647). Zweifarben-Mikroskopie und eine Kolokalisationsanalyse erlaubte die Trennung von TNFR1-Clustern mit und ohne gebundenen Liganden. Für die Kolokalisierung von TNFR1-mEos2 mit TNF α -SNAP-A647 ergaben die BIC- und Log-Likelihood-Analysen ein Modell mit drei Zuständen, die als 13 ± 2 % Monomere, 64 ± 2 % Trimere und 23 ± 3 % Nonamere identifiziert wurden. Der Anteil an Trimeren stimmt mit den kristallographischen Daten eines ligandengebundenen TNFR1 überein. In dieser Arbeit wurde erstmals TNFR1 in Form eines Trimers auf der Plasmamembran einer intakten Zelle nachgewiesen. Darüber hinaus zeigte die quantitative Analyse die Existenz größerer Oligomere, welche wahrscheinlich Nonamere darstellen. Frühere Studien diskutierten die Existenz von Hexameren und Nonameren von TNFR1 durch PLAD-PLAD-Interaktionen von zwei oder drei TNFR1₃-TNF α ₃ Clustern. Die Ergebnisse aus dieser Arbeit unterstützen das Modell von TNFR1 Nonameren, geben aber keine Hinweise auf das Vorhandensein von Hexameren. Eine mögliche Erklärung ist, dass eine einzige PLAD-PLAD-Interaktion zwischen zwei TNFR1₃-TNF α ₃-Einheiten (Hexamer) zu schwach und damit transient ist, während drei PLAD-PLAD-Interaktionen in einer TNFR1₃-TNF α ₃-Einheit (Nonamer) stabiler sind.

Die Funktion der PLAD in der TNFR1-Dimerisierung wurde daraufhin durch das Einbringen einer Punktmutation (K32A) untersucht, welche die PLAD-PLAD-Interaktion inhibiert. Quantitative PALM-Experimente ergaben 100 % monomeres TNFR1. Darüber hinaus konnte keine Ligandenbindung beobachtet werden. Dieses Ergebnis unterstützt das Modell, dass die PLAD-Interaktion für die Bildung von TNFR1-Dimeren in intakten Zellen erforderlich ist, und dass diese Interaktion für die Ligandenbindung notwendig ist. Die Erzeugung der Mutation N66F in die Ligandenbindedomäne (CRD2) von TNFR1 zeigte eine Verteilung von 54 ± 3 % Monomeren und 46 ± 3 % Dimeren, mit nur geringer Veränderung bei der Behandlung mit TNF α zu 56 ± 3 % Monomeren und 44 ± 3 % Dimeren. Diese Ergebnisse bestätigen frühere Studien und zeigten, dass TNFR1-N66F kein TNF α bindet.

Basierend auf den Ergebnissen der Mikroskopie und ergänzt durch biochemische Daten wurde ein quantitatives Modell entwickelt. In unstimulierten Zellen liegt TNFR1 als Monomer und Dimer in einem

Gleichgewicht vor. Nach der Aktivierung durch TNF α organisiert sich der Großteil von TNFR1 zu einem Trimer. Darüber hinaus liegt ein kleiner Teil von TNFR1 als Monomer vor, und ein weiterer Teil in Oligomeren höherer Ordnung. Die Oligomere höherer Ordnung wurden mit statistischen Kriterien und einer *Log-Likelihood*-Analyse analysiert. Das wahrscheinlichste Ergebnis, das aus dieser Analyse gewonnen wurde, ist die Anordnung zu Nonameren. Diese Nonamere sind möglicherweise durch drei individuelle PLAD-PLAD-Interaktionen stabilisiert.

Mithilfe der rekonstituierten Zelllinie, quantitativen PALM-Experimenten und dem erhaltenen Modell zur TNFR1-Aktivierung kann der Einfluss von Manipulationen von Zellen auf die TNFR1-Organisation untersucht werden. Die Wirkung von drei Substanzen wurde untersucht, von denen bekannt ist, dass sie die TNFR1-Signalwege beeinflussen. Zuerst wurden die Zellen mit dem Medikament Zafirlukast behandelt, das die PLAD-Interaktionen von TNFR1 hemmen soll. Quantitative PALM-Experimente von mit Zafirlukast behandelten Zellen ergab eine Verteilung von 90 ± 3 % Monomeren und 10 ± 3 % Dimeren, die sich bei einer zusätzlichen Behandlung mit TNF α nicht wesentlich veränderte. Diese Ergebnisse bestätigen, dass TNFR1-Dimere für die Signalaktivierung erforderlich sind. In früheren Studien zeigten Western Blot-Experimente, dass die NF- κ B-Signalkaskade in mit Zafirlukast behandelten Zellen nicht aktiviert wird. Anschließend wurden die Zellen mit BV6 und TNF α beziehungsweise mit BV6, zVAD-fmk und TNF α behandelt, um Apoptose beziehungsweise Nekroptose zu induzieren. Der oligomere Zustand von TNFR1 änderte sich im Vergleich zu Zellen, wo der NF- κ B Signalweg aktiviert war, nicht signifikant. Dieses Ergebnis bestätigte die Erwartung, dass BV6 und zVAD-fmk intrazellulär in der Signalkaskade wirken, und deutet darauf hin, dass keine direkte Modulation der Stöchiometrie von TNFR1 an der Plasmamembran auftritt.

In Zusammenarbeit mit der Arbeitsgruppe von Prof. Dr. Michael Lanzer (Heidelberg, Deutschland) wurde quantitatives PALM angewendet, um die Anzahl der VAR2CSA-Proteine in einzelnen Membran-exponierten *knobs* in HbAA- und HbAS-Erythrozyten zu bestimmen. Zu diesem Zweck wurden gesunde Erythrozyten (HbAA) und Erythrozyten von Patienten mit Sichelzellanämie (HbAS) mit einer Mutante des Parasiten *Plasmodium falciparum* infiziert. Hierdurch wurde VAR2CSA-mEos2 exprimiert, zur Plasmamembran transportiert und in *knobs* verankert. PALM-Aufnahmen zeigten einzelne Cluster von VAR2CSA auf der Plasmamembran der Erythrozyten. Unter Verwendung eines *density-based spatial clustering of application with noise* (DBSCAN) Algorithmus wurden VAR2CSA Cluster identifiziert und ihre Anzahl pro μm^2 auf $2,9 \pm 1,2$ (HbAA) und $1,6 \pm 0,7$ (HbAS) bestimmt. Der Durchmesser der VAR2CSA-Cluster wurde aus der DBSCAN-Analyse extrahiert und ergab 54 ± 27 nm für HbAA- und 64 ± 31 nm für HbAS- Erythrozyten. Diese Werte sind kleiner als die elektronenmikroskopisch bestimmten Durchmesser von 80-90 nm und 200 nm für HbAA- und HbAS-Erythrozyten. Aufgrund der kreisförmigen Form der Cluster und unter Berücksichtigung der räumlichen Auflösung der PALM-Experimente (Lokalisierungsgenauigkeit von 13 bis 15 nm) ist es wahrscheinlich, dass VAR2CSA zentral im *knob* verankert ist. Die Anzahl der VAR2CSA pro *knob* wurde aus der Anzahl der

Blinkereignisse des fluoreszierenden Proteins mEos2, und mittels Kalibrierung an einzelnen fluoreszierenden Proteinen, quantifiziert. In HbAA und HbAS Erythrozyten wurden $3,3 \pm 1,7$ und $4,3 \pm 2,5$ VAR2CSA pro *knob* bestimmt. Obwohl HbAS-Erythrozyten mehr VAR2CSA pro *knob* besitzen, ist die Anzahl der *knobs* pro Fläche geringer. Das deutet darauf hin, dass eine Mindestanzahl von *knobs* vorhanden sein muss, um Zyto-Adhäsionseffekte zu induzieren.

Im Rahmen dieser Arbeit wurde das Konzept der quantitativen und hochauflösenden Einzelmolekül-Lokalisierungsmikroskopie auf organische Fluorophore erweitert. Der photoschaltbare Fluorophor Alexa Fluor 647 wurde an eine doppelsträngige DNA konjugiert, auf einer Glasoberfläche immobilisiert und mit *d*STORM gemessen. Trimere von Alexa Fluor 647 wurden mittels DNA Origami generiert und ebenfalls mit *d*STORM gemessen. Die Analyse ergab, dass die Blinkeigenschaften von Alexa Fluor 647 sensitiv von dessen Nanoumgebung abhängen. Sowohl Monomere als auch Trimere wurden zuverlässig identifiziert.

In dieser Arbeit wurde mittels quantitativer Einzelmolekül-Lokalisierungsmikroskopie die molekulare Organisation von Membranproteinen direkt in Zellen untersucht. Eine detaillierte molekulare Beschreibung, wie Proteine sich zu funktionellen Einheiten organisieren, entschlüsselt Mechanismen, welche zelluläre Interaktionen zugrunde liegen, und ebnet den Weg für die Entwicklung von Medikamenten für ihre gezielte Manipulation.

SUMMARY

The plasma membrane of eukaryotic cells serves as a barrier between the inside of a cell and its environment. An important task of proteins that reside in the plasma membrane is to sense the environment, to communicate this information across the membrane into the inner of a cell, and to initiate a response of the cell. Membrane receptors typically bind ligands, which leads to their activation and the recruitment of intracellular proteins. Functional multi-protein signaling hubs are formed, initiate an information transfer through the cell membrane and stimulate or repress the expression of specific genes as a response to the extracellular stimulus. Dysregulation of signaling initiation and transfer are found in multiple diseases, which make membrane proteins an important target in drug development.

The major project in this thesis addressed the question on how tumor necrosis factor receptor 1 (TNFR1), a cytokine receptor, organizes into functional complexes in the plasma membrane of an intact cell. TNFR1 contains four cysteine-rich domains (CRDs) on its extracellular domain. The first and most distal CRD is the pre-ligand assembly domain (PLAD). Crystal structures revealed that in dimers of TNFR1, two PLADs are in close vicinity. Crosslinking experiments reported several oligomeric states of TNFR1; these results showed to be sensitive to the type of crosslinker and its concentration. In the native environment of an intact and unperturbed cell, the oligomeric state of TNFR1 was so far not determined. The canonical ligand for TNFR1 is tumor necrosis factor alpha (TNF α), a trimeric protein that is found soluble and membrane-bound. After binding of TNF α , TNFR1 oligomerizes, recruits downstream proteins and forms a functional membrane complex that activates intracellular signaling cascades. Canonical signaling occurs through the nuclear factor kappa-light-chain-enhancer of activated B-cells (NF- κ B), which induces cell division or inflammation. TNFR1 may also initiate other pathways such as apoptosis through a cytosolic complex and the procaspase-8, or necroptosis through the necrosome and the mixed lineage kinase domain-like (MLKL) domain. Dysregulation of TNFR1 is found in a variety of diseases. Elevated levels of TNFR1 expression occur in acquired immune deficiency syndrome (AIDS), multiple sclerosis and various types of cancer.

In a second project, the expression level of the protein VAR2CSA was determined in membrane-associated knobs that occur in erythrocytes infected with the parasite *Plasmodium falciparum*. VAR2CSA belongs to the protein family of *Plasmodium falciparum* erythrocyte membrane protein 1 (pfEMP1). Following an infection, VAR2CSA is transported to the host cell membrane and is deposited into membrane knobs. Patients that exhibit sickle cell anemia erythrocytes (HbAS) show immunity against malaria in contrast to patients with healthy erythrocytes (HbAA). While the two types of erythrocytes exhibit different knob morphologies and numbers, their decoration with VAR2CSA remained elusive.

Understanding protein function requires a molecular-level description of their organization into functional units and directly in the cellular environment. Fluorescence microscopy is a suitable tool for this purpose, since it allows specific labeling of target proteins. The high sensitivity enables the visualization of single proteins. A limitation in conventional fluorescence microscopy is the diffraction barrier. Structural features that are smaller than about half the wavelength, i.e. 200 to 300 nm for most applications, cannot be resolved. The development of super-resolution fluorescence microscopy allowed bypassing this diffraction limit and achieving a spatial resolution down to tens of nanometers, which opened the door to visualize and characterize single protein complexes. One type of super-resolution microscopy is single-molecule localization microscopy (SMLM), which builds on the isolated detection of single fluorophores, a precise determination of their position (localization), and the generation of a reconstructed image with sub-diffraction resolution. Since most samples in fluorescence microscopy have a too high spatial density of fluorophores to enable the detection of single emitters, methods to control the emission of fluorophores are implemented. One option is to operate fluorophores that can be optically modulated between a non-fluorescent and a fluorescent state, e.g. photoswitchable fluorescent proteins in photoactivated localization microscopy (PALM) or organic fluorophores in (*direct*) stochastic optical reconstruction microscopy ((*d*)STORM). SMLM can achieve a spatial resolution of 20 nm or better, which in most cases is sufficient to visualize single protein complexes in a cell. However, this spatial resolution is not sufficient to visualize subunits within a protein complex. For this purpose, SMLM was extended by additionally exploiting the available kinetic information that is observed in the detection of single fluorophores. Multiple fluorophores undergo reversible transitions into metastable dark states that exhibit a lifetime of up to seconds, before they return to their fluorescent state. Multiple of such transitions appear as repetitive “blinks” of fluorescence emission. In combination with kinetic models, the analysis of photoswitching kinetics reports on the number of fluorophores. Applied to super-resolved protein complexes, this kinetic analysis allows bypassing the resolution limit of super-resolution SMLM and extracting the number of protein subunits. A common route for this method is the conjugation of the photoswitchable fluorescent protein mEos2 to a target protein (quantitative PALM (qPALM)).

In order to determine the oligomeric state of TNFR1, a stable TNFR1/2-/- double knock out mouse embryo fibroblast (MEF) cell line reconstituted with TNFR1-mEos2 was used in combination with quantitative PALM (kind gift by Dr. Sjoerd van Wijk and Prof. Dr. Ivan Dikic, Frankfurt, Germany). The cell line was fully functional and responded to stimulation with the ligand TNF α , monitored by translocation of NF- κ B into the nucleus. The induction of non-canonical pathways induced by TNFR1, such as apoptosis and necroptosis, was verified.

Quantitative PALM data of TNFR1 in MEF cells were recorded and analyzed by applying the Bayesian information criterion (BIC) and a log-likelihood analysis. For unstimulated cells, this analysis revealed TNFR1 to be organized into 66 ± 4 % monomers and 34 ± 4 % dimers. This is consistent with previous

SUMMARY

studies using crystallization, western blot and FRET experiments, reporting that TNF α -untreated TNFR1 is present as monomer and dimer. This supports a low-affinity binding model of two TNFR1 by their PLAD that are in equilibrium with monomeric TNFR1. In order to investigate how the oligomeric state of TNFR1 changes upon stimulation with TNF α , a SNAP-Flag-TNC-TNF α was labeled with Alexa Fluor 647 (TNF α -SNAP-A647) and used to stimulate the cells. Two-color imaging and colocalization analysis allowed separating TNFR1 clusters binding a ligand from ligand-free clusters. For TNFR1-mEos2 colocalizing with TNF α -SNAP-A647, the BIC and log likelihood analyses revealed that the model with the largest probability comprises three states that were identified as 13 ± 2 % monomers, 64 ± 2 % trimers and 23 ± 3 % nonamers. The dominant trimeric fraction is in agreement with crystallographic data of a ligand-bound TNFR1. Here, for the first time, trimeric TNFR1 was shown on the plasma membrane of an intact cell. In addition, the quantitative analysis indicated for the first time the existence of larger oligomers, with the most likely solution for nonamers. Previous studies proposed the existence of hexameric and nonameric arrangements of TNFR1 by PLAD-PLAD interactions of two or three clusters of TNFR1₃-TNF α ₃. The results obtained in this thesis support this model, with an indication for the presence of TNFR1 nonamers but so far no indication for the presence of hexamers. This suggests that three TNFR1₃-TNF α ₃ assemble to a stable nonameric structure. A possible explanation is that a single PLAD-PLAD interaction between two TNFR1₃-TNF α ₃ units (the hexamer) is too weak and thus transient, whereas three PLAD-PLAD interactions between three TNFR1₃-TNF α ₃ units (the nonamer) organized as a triangle are more stable.

To investigate the function of the PLAD in TNFR1 dimerization directly in cells, a point mutation was generated (K32A) that was reported to inhibit the PLAD-PLAD interaction. Quantitative PALM revealed the existence of 100 % TNFR1 monomers. Treatment of TNFR1-K32A with TNF α showed no ligand binding. This result supports the model that the PLAD interaction is required for the formation of TNFR1 dimers in intact cells, and that this interaction or presumably the equilibrium of monomeric and dimeric TNFR1 is required for ligand binding. Integration of the mutation N66F into the ligand binding domain (CRD2) of TNFR1 revealed the existence of 54 ± 3 % monomeric and 46 ± 3 % dimeric TNFR1, with only little change upon treatment with TNF α , to 56 ± 3 % monomeric and 44 ± 3 % dimeric TNFR1. These results are in agreement with previous studies, which showed that N66F mutated TNFR1 does not bind TNF α .

Based on the results of quantitative PALM experiments, and complemented by biochemical data, a quantitative model for TNFR1 was developed. Ligand-free TNFR1 is present as monomer and dimer in the plasma membrane of an intact cell. Following activation by its cognate ligand TNF α , the majority of TNFR1 organizes into trimers. In addition, a small fraction of TNFR1 remains monomeric, and another fraction organizes into higher-order oligomers. The higher-order oligomers were analyzed with statistical criteria and a log-likelihood analysis. The most probable result that was obtained from this analysis attributes the higher-order oligomers to nonamers. Given the presence of a weak-affinity

interaction conveyed by the PLAD domain, a possible explanation is that three trimers of TNFR1 are stabilized through three individual PLAD-PLAD interactions.

The reconstituted cell line together with quantitative PALM experiments and the above model on TNFR1 activation represents an ideal system to test how manipulations of cells affect TNFR1 organization and subsequent signaling. This experimental model was used to investigate the effect of three reagents that are known to interact with TNFR1 signaling. First, cells were treated with the drug zafirlukast, which was reported to inhibit PLAD interactions in TNFR1. Quantitative PALM for cells treated with zafirlukast revealed a distribution of 90 ± 3 % monomers and 10 ± 3 % dimers, which did not change much upon additional treatment with TNF α . These results are consistent with the assumption that the presence of dimers of TNFR1 are required for signaling activation. In previous studies, western blot experiments revealed that the NF- κ B signaling cascade is not activated in cells treated with zafirlukast. Next, drugs that initiate apoptosis or necroptosis were used, and cells were treated with BV6 and TNF α (induction of apoptosis) or BV6, zVAD-fmk and TNF α (induction of necroptosis). The oligomeric state of TNFR1 did not change significantly compared to untreated cells. This result confirmed the expectation that BV6 and zVAD-fmk act downstream, and proved that no direct modulation of the stoichiometry of TNFR1 occurs at the plasma membrane.

In collaboration with the group of Prof. Dr. Michael Lanzer (Heidelberg, Germany), quantitative PALM was applied to determine the number of VAR2CSA proteins in single membrane-exposed knobs in HbAA and HbAS erythrocytes. For this purpose, healthy erythrocytes (HbAA) and erythrocytes of patients with sickle cell anemia (HbAS) were infected with a mutant of the parasite *Plasmodium falciparum* that carried the fusion VAR2CSA-mEos2. In infected cells, VAR2CSA-mEos2 is transported to the plasma membrane and deposited in the membrane knobs. PALM images showed individual clusters of VAR2CSA on the plasma membrane of the erythrocytes. Using a density-based spatial clustering of application with noise (DBSCAN) algorithm, the nano-scale clusters were identified and their numbers per μm^2 determined to be 2.9 ± 1.2 (HbAA) and 1.6 ± 0.7 (HbAS). The diameter of VAR2CSA clusters was extracted from the DBSCAN analysis, yielding 54 ± 27 nm (HbAA) and 64 ± 31 nm (HbAS). These values are smaller than the knob diameters of 80-90 nm and 200 nm determined by electron microscopy for HbAA and HbAS erythrocytes. Due to the circular shape of the clusters, and considering the spatial resolution in the PALM experiment (localization precision of 13 to 15 nm), it is likely that VAR2CSA is anchored centrally in the knob. The number of VAR2CSA per knob was quantified from the number of blinking events of the fluorescent protein mEos2 using single fluorescent proteins on a glass surface as a reference sample. In HbAA, 3.3 ± 1.7 VAR2CSA were determined per knob, compared to 4.3 ± 2.5 in HbAS. Although HbAS erythrocytes possess more VAR2CSA per knob, the number of knobs per area is smaller. That suggests that a minimum number of knobs must be present to induce cytoadhesion effects.

SUMMARY

During this thesis, the concept of quantitative SMLM by analyzing photoswitching kinetics was extended towards organic fluorophores. The photoswitchable fluorophore Alexa Fluor 647 was conjugated to a double-stranded DNA, immobilized on a glass surface and measured with *d*STORM. In order to mimic a protein cluster, trimers of Alexa Fluor 647 were generated using DNA origami and measured with *d*STORM. The analysis revealed that the blinking properties of Alexa Fluor 647 are sensitive to the nano-environment. Monomers as well as trimers were reliably identified.

In summary, this thesis reports the use of quantitative single-molecule super-resolution microscopy to study the molecular organization of membrane proteins directly in cells. A detailed molecular description of how proteins organize into functional units unravels mechanisms that underlie cellular interactions and pave the way to design tools for directed manipulation.

CONTENTS

ZUSAMMENFASSUNG	i
SUMMARY	vi
CONTENTS	xi
1 INTRODUCTION	1
1.1 TNFR1 and TNF α	1
1.1.1 The signaling cascade of TNFR1	5
1.1.2 Programmed necrosis	7
1.1.3 Pharmaceutical impact	8
1.2 <i>Plasmodium falciparum</i> erythrocyte membrane protein 1	9
2 THEORETICAL BACKGROUND	11
2.1 Absorption and fluorescence	11
2.2 Light microscopy	12
2.3 Fluorescent proteins	15
2.4 Organic fluorophores	17
2.5 Labeling techniques	19
2.5.1 Genetic expression of fluorescent proteins	19
2.5.2 Tag-technologies	20
2.5.3 Immunofluorescence	20
2.6 Super-resolution microscopy	22
2.7 Resolution in single-molecule localization microscopy	24
2.8 Cluster analysis in SMLM	25
2.9 Quantitative super-resolution fluorescence microscopy	25
3 MATERIAL AND METHODS	28
3.1 Cell lines and plasmids	28
3.2 Labeling of TNF α	28
3.3 Glass coating and flexiperm constitution	29
3.4 Sample preparation for quantitative PALM of TNFR1	29
3.5 Cell fixation	29

CONTENTS

3.6	Western blot.....	30
3.7	NF- κ B activation.....	30
3.8	Immunofluorescence	30
3.9	Induction of cell death.....	30
3.10	Fluorescence-activated cell sorting	31
3.11	Luciferase assay.....	31
3.12	Determination of the number of TNFR1 per cell by light microscopy	32
3.13	Transfection.....	32
3.14	Quantification of pfEMP1	32
3.15	Establishment of molecular quantification with <i>d</i> STORM	33
3.16	Sample preparation for quantitative <i>d</i> STORM with Alexa Fluor 647.....	33
3.17	SMLM microscope.....	33
3.18	SMLM imaging	35
3.19	Quantitative SMLM data analysis.....	35
4	RESULTS AND DISCUSSION.....	37
4.1	Quantifying the oligomeric state of TNFR1 using PALM	37
4.1.1	Reconstitution of TNFR1 ^{2/-} + TNFR1-mEos2 mouse embryo fibroblast.....	37
4.1.2	Investigating the blinking properties of mEos2 in MEF cells	40
4.1.3	qPALM analysis of TNFR1 in TNF α -untreated cells	41
4.1.4	Analyzing TNF α -treated TNFR1 in cells with qPALM.....	42
4.1.5	qPALM of TNFR1 carrying mutations in the PLAD or ligand binding domain.....	43
4.1.6	The influence of zafirlukast on the stoichiometry of TNFR1.....	46
4.1.7	The influence of chemical-induced apoptosis on the stoichiometry of TNFR1	47
4.1.8	The influence of chemical-induced necroptosis on the stoichiometry of TNFR1	48
4.1.9	Discussing the oligomeric state of TNFR1.....	49
4.1.10	Comparison of the oligomeric state of TNFR1 of 4 °C and 37 °C incubated MEFs.....	54
4.1.11	TNFR1 cluster analysis by DBSCAN	56
4.2	Molecular quantification with Alexa Fluor 647	60
4.2.1	Photoswitching properties of Alexa Fluor 647.....	60

4.2.2	Quantitative <i>d</i> STORM imaging	61
4.2.3	Future directions for molecular quantification with organic fluorophores.....	63
4.3	Quantitative PALM analysis of pfEMP1 in erythrocytes.....	65
4.3.1	Super-resolution imaging of VAR2CSA in erythrocytes.....	65
4.3.2	A spatial model of VAR2CSA in HbAA and HbAS erythrocytes.....	68
5	CONCLUSION AND OUTLOOK.....	70
5.1	A quantitative model for TNFR1	70
5.2	A quantitative model of VAR2CSA.....	73
5.3	Quantification with organic fluorophores	74
6	REFERENCES.....	75
	APPENDIX	I
	SUPPLEMENTARY FIGURES	I
	SUPPLEMENTARY TABLES.....	VIII
	LIST OF ABBREVIATIONS	XXIX
	LIST OF FIGURES.....	XXXIV
	LIST OF TABLES	XXXVI
	LIST OF SUPPLEMENTARY FIGURES	XXXVII
	LIST OF SUPPLEMENTARY TABLES.....	XXXVIII
	Acknowledgments.....	XL
	Curriculum Vitae.....	XLII
	List of Publications	XLIII

INTRODUCTION

The cell is a fundamental unit of life (Hooke and Allestry, 1667). Eukaryotic cells possess a plasma membrane, which separates the inside of a cell from the outside (Tan et al., 2008). This prevents various molecules produced in the cell from escaping or unwanted molecules from entering the cell. Numerous proteins are anchored in the plasma membrane and connect a cell with its environment. Some of them function as transporter proteins, which transport molecules either into or out of the cell (Plattner and Hentschel, 2002). Other membrane proteins sense the cellular environment and activate specific signaling cascades (Karp, 2005). This may initiate the expression of specific proteins leading to cell proliferation, cell inflammation or cell death (Aggarwal, 2003). The central importance of membrane proteins is clearly demonstrated from a pharmaceutical point of view. Membrane proteins represent more than half of all possible targets for therapeutics (Overington et al., 2006; Yin and Flynn, 2016).

1.1 TNFR1 and TNF α

A membrane protein family of high medical relevance is the tumor necrosis factor receptor superfamily (TNFSF), comprising 29 receptors and 19 ligands (Aggarwal et al., 2012; Dostert et al., 2019). The tumor necrosis factor receptor superfamily (TNFRSF) is divided into three subgroups (Vanamee and Faustman, 2018). The first group includes receptors that contain within their intracellular region one or more tumor necrosis factor receptor associated factors (TRAF) interacting motifs (TIM). The activation of TIM leads to the recruitment of TRAF proteins, triggering numerous signaling responses, e.g. the activation of the nuclear factor kappa-light-chain-enhancer of activated B-cells (NF- κ B) (Dempsey et al., 2003; Vanamee and Faustman, 2018). The second group contains a death domain within its intracellular region, controlling cell proliferation, inflammation and pro-survival signaling through NF- κ B (Wajant and Scheurich, 2011) but also programmed cell death via caspase-dependent or -independent signaling cascades (Dempsey et al., 2003; Vanamee and Faustman, 2018). A third group comprises decoy receptors (Bridgham and Johnson, 2003; Vanamee and Faustman, 2018). These receptors do not possess an intracellular domain, causing no intracellular signaling (Dempsey et al., 2003; Vanamee and Faustman, 2018). However, the decoy receptors are able to cluster with other members of the TNFSF to inhibit their signaling (Boado et al., 2010). In addition, decoy receptors bind soluble ligands, preventing the ligand to activate other receptors (Chen et al., 2004). One of the fundamental characteristics of the TNFSF is the existence of one to four cysteine-rich domains (CRDs) in their extracellular domain (Aggarwal, 2003; Marsters et al., 1992). All of these cysteine-rich domains offer six cysteines resulting in three disulfide bridges (Bodmer et al., 2002). All known receptors and

INTRODUCTION

ligands of the TNFSF, the respective specification of the intracellular domain and the number of CRDs are listed in Table 1.

Table 1: Tumor necrosis factor superfamily. Listed are receptors, corresponding ligands, number of CRDs and the intracellular domain comprising TRAF domain (TD), death domain (DD) or decoy receptor (DR).

RECEPTOR	BINDING LIGAND	CRDS	INTRACELLULAR DOMAIN
TNFR1	TNF α , TNF β	4	DD
TNFR2	TNF α , TNF β	4	TD
RANK	RANKL	4	TD
LT β R	LT α , LT β , LIGHT	4	TD
FN14	TWEAK	0	TD
HVEM	TNF β , LIGHT	3	TD
CD27	CD27L	2	TD
CD30	CD30L	4	TD
CD40	CD40L	4	TD
4-1BB	4-1BBL	3	TD
OX40	OX40L	3	TD
GITR	GITRL	2	TD
BCMA	APRIL, BAFFL	1	TD
TACI	APRIL, BAFFL	2	TD
BAFFR	BAFFL	1	TD
XEDAR	EDA-A2	2	TD
TROY	LT α	2	TD
RELT	-	1	TD
CD95	CD95L	3	DD
DR3	VEGI	3	DD
DR4	TRAIL	2	DD
DR5	TRAIL	2	DD
DR6	-	4	DD
EDAR	EDA-A1	2	DD
NGFR	NGF	4	DD
DCR1	TRAIL	2	DR
DCR2	TRAIL	2	DR
DCR3	CD95L, VEGI	3	DR
OPG	TRAIL, RANKL	4	DR

The tumor necrosis factor receptor 1 (TNFR1) is one member of the TNFSF, possessing a molecular weight of 55 kDa and a height of 85 Å (Banner et al., 1993). The secondary structure of TNFR1 is formed out of eight β-sheets (Banner et al., 1993). Overall, the outer side of the receptor is hydrophilic and the inner side is hydrophobic (Banner et al., 1993). TNFR1 contains four cysteine-rich domains within its extracellular region (Banner et al., 1993; Fischer et al., 2015) (Figure 1A). The first CRD is the membrane most distal part known as the pre-ligand assembly domain (PLAD) (Cao et al., 2011; Chan, 2000). Due to the PLAD, different studies revealed that TNFR1 oligomerizes to a dimeric (Naismith et al., 1995) or trimeric (Chan, 2000) form, without the activation by its ligand TNFα. Since these results are different, the oligomeric state of TNFR1 in its native environment, the plasma membrane, remains unclear.

The affinity for the binding of two or three single TNFR1 through their PLAD is in the μM-mM range (Cao et al., 2011) and thus lower than the affinity of TNFα binding to TNFR1, which is in the nM range (Dietz et al., 2014; Grell et al., 1998). Advocating the dimeric model of TNFR1, it is reported that TNFR1 forms pH-dependent either a parallel (Figure 1B) or an antiparallel (Figure 1C) dimer (Naismith et al., 1995; Naismith et al., 1996; Vanamee and Faustman, 2018). Parallel dimers are formed at a pH of 7.5, in contrast to a lower pH of about 3.7 where antiparallel dimers are formed (Mukai et al., 2010; Naismith et al., 1995; Naismith et al., 1996). In the parallel conformation, the receptors are arranged head to tail where the ligand binding sites are open and the cytoplasmic regions are close to each other (Naismith et al., 1995). It is actually debated why there is the dimeric or trimeric form of parallel receptors present in the absence of ligand. There is the assumption that these dimeric or trimeric forms are necessary for efficient ligand binding (Vanamee and Faustman, 2018; Wajant, 2015). In the antiparallel arrangement, TNFα is not able to bind the receptor, as the binding site of TNFR1 is blocked. In addition, the cytoplasmic regions of the receptors are strongly separated by about 100 Å (Boschert et al., 2010; Naismith et al., 1995).

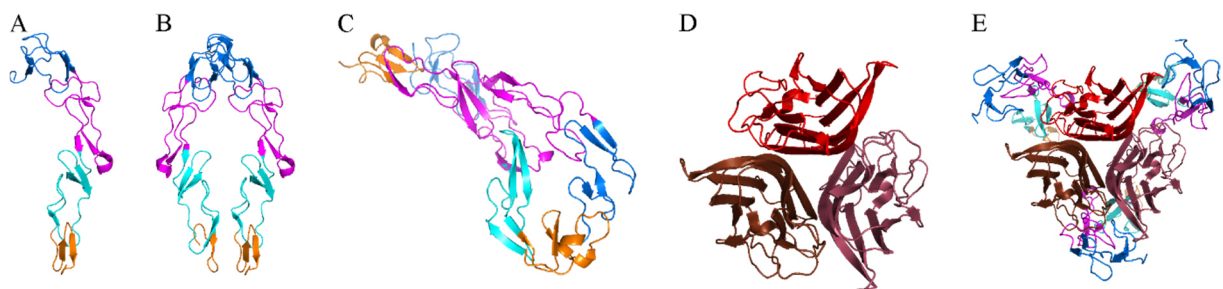


Figure 1: Crystal structures of TNFR1 and its ligand TNFα. Side view of TNFR1 as monomer (PDB 1ncf) (A), as parallel dimer (PDB 1ncf) (B), as antiparallel dimer (PDB 1ext) (C), the top view of trimeric TNFα (PDB 1TNF) (D) and a TNFR1-TNFα complex with a 3:3 stoichiometry (PDB 1ncf and 1TNF) (E). CRD1 is illustrated in blue, CRD2 in magenta, CRD3 in cyan and CRD4 in orange. Individual TNFα of the trimer scaffold are represented in red tones.

INTRODUCTION

The PLAD is clearly separated from the ligand-binding domain but essential for ligand binding (Chan, 2000). Actually, the PLAD offers high potential for the treatment of several diseases (Deng, 2007; Wang et al., 2011). A strategy to inhibit the PLAD is to use a drug called zafirlukast that specifically binds the PLAD thus preventing further TNFR1 signaling cascades (Lo et al., 2017) (Figure 2). Zafirlukast is an anti-inflammatory drug (Conway et al., 2003), which is already used against several diseases such as asthma (Adkins and Brogden, 1998) or dermatitis (Carucci et al., 1998). However, zafirlukast does not affect the ligand binding interaction (Lo et al., 2017). This is an innovative approach, since zafirlukast does not need to compete with TNF α for the binding site (Lo et al., 2017).

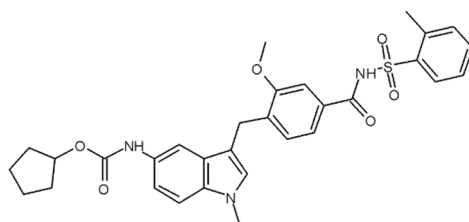


Figure 2: Chemical structure of zafirlukast.

The ligand TNF α , first identified in 1985 (Old, 1985), is a 17.3 kDa (soluble) or 26 kDa (membrane-bound) type 2 transmembrane protein (Ardley and Robinson, 2005; Kriegler et al., 1988; Tang et al., 1996), with the membrane-bound form showing a stronger affinity to TNFR1 (MacEwan, 2002; Winkel et al., 2012). As a β -protein, its secondary structure possesses two β -sheets (Banner et al., 1993). TNF α is released by macrophages after lipopolysaccharide (LPS) exposure (Agbanoma et al., 2012; Monick and Hunninghake, 2002; Parameswaran and Patial, 2010). As a pleiotropic cytokine (Tracey and Cerami, 1994), TNF α is responsible e.g. for cell growth and differentiation regulation (Boussiotis et al., 1994; Kaiser and Polk, 1997). TNF α assembles to homotrimers by non-covalent binding (Tang et al., 1996) (Figure 1D). The trimer forms a pyramid-like structure, where the bottom side is broader and more hydrophobic than the top, which is narrower and more hydrophilic (Banner et al., 1993). TNF α possess a diameter of 30 Å on the top, 50 Å on the bottom and a height of 60 Å (Banner et al., 1993). Trimeric TNF α contains three identical binding sites where single TNFR1 can bind. A receptor binds through its CRD2 and CRD3 into the groove of two TNF α of a TNF α trimer. Thus, one TNF α trimer binds up to three TNFR1 resulting in a trimeric TNF α -trimeric TNFR1 complex by non-covalent interactions (Banner et al., 1993) (Figure 1D). Since the transmembrane and intracellular regions of the receptor in the TNFR1₃-TNF α ₃ scaffold converge closely, it is suspected that TNFR1 is involved in a conformational change (Lewis et al., 2012; Lo et al., 2019).

After the activation of TNFR1 by its ligand TNF α , cell proliferation (Tarrats et al., 2011), cell inflammation (Rickard et al., 2014) or cell death (O'Donnell and Ting, 2011; Pasparakis and Vandeneabeele, 2015; Schmitz et al., 2000) is activated through signaling cascades. Since these signaling outputs are different, TNFR1 is defined as 'double-edged-sword' (Aggarwal, 2003) and offers large

potential as clinical target (Blüml et al., 2012; Croft et al., 2013; Martínez-Reza et al., 2017). Elevated levels of TNFR1 expression occur in several diseases (Cubillas et al., 2010; Puimège et al., 2014). The specific manipulation of the signaling cascade of TNFR1 represents a large potential since e.g. cancer cells could be programmed to degrade.

1.1.1 The signaling cascade of TNFR1

Activation of TNFR1 by TNF α leads to the activation of NF- κ B (Hayden and Ghosh, 2008; Wajant and Scheurich, 2011). After ligand binding and TNFR1 clustering, the silencer of death domain (SODD) is released from the death domain of the intracellular region of TNFR1 (Jiang et al., 1999; Takada et al., 2003). Next, the unrestricted death domain binds the death domain of the 34 kDa monomeric form of the TNF receptor-associated death domain (TRADD) (Ermolaeva et al., 2008). Furthermore, the receptor interacting protein 1 (RIP1) (Hsu et al., 1996), the trimeric form of the TNFR associated factor 2 (TRAF2) (Wajant and Scheurich, 2001) and the cellular inhibitors of apoptosis (cIAP) 1 and 2 (Bertrand et al., 2011; Mahoney et al., 2008) are recruited to TRADD to form complex I at the plasma membrane (Chen and Goeddel, 2002). The trimeric TRAF2 operates as adapter protein for cIAP1 and 2 (Wajant and Scheurich, 2001). cIAP1 and 2 itself are E3 ligases which ubiquitinate RIP1 and thus stabilize complex I (Bertrand et al., 2008). Overall, cIAP1 and 2 inhibit the non-canonical NF- κ B signaling cascade by the inhibition of the NF- κ B-inducing kinase (NIK) (Sun, 2011) and they also inhibit the apoptotic signaling cascade (Eckelman and Salvesen, 2006; Labbé et al., 2011).

After complex I is assembled, the I κ B kinase (IKK) (comprising IKK α , IKK β and IKK γ (also known as the NF- κ B essential modulator (NEMO))) is recruited (Hayden and Ghosh, 2008; Scheidereit, 2006). NEMO is necessary for IKK activation in the canonical signaling cascade (Sun, 2011; Tarantino et al., 2014) and contains with the ubiquitin-binding in A20-binding inhibitor of NF- κ B (ABIN) and NEMO (UBAN) also known as the NEMO Optineurin Abin (NOA), one ubiquitin-binding domain (UBD) (Lo et al., 2009; Rahighi et al., 2009; Tarantino et al., 2014). Through UBAN, NEMO ubiquitinates and activates the IKK complex (Chen, 2012; Ea et al., 2006; Israël, 2010). After IKK activation, the homo-oxidized ubiquitin ligase 1 (HOIL-1), HOIL-1 interacting protein (HOIP) and Sharpin, also known as the linear ubiquitin chain assembly complex (LUBAC), bind NEMO (Haas et al., 2009; Li et al., 2013; Wallach et al., 2011a, 2011b). Sharpin has only stabilizing properties, while both HOIL-1 and HOIP contain a ring and a zinc finger motif to bind several ubiquitin chains leading to further stabilization of complex I (Kumari et al., 2014; Tokunaga et al., 2008; Walczak, 2011) (Figure 3).

If ubiquitination of complex I is disturbed, RIP1 and TRADD dissociate from complex I and start to build up complex II (also known as the death inducing signaling complex (DISC)) with the Fas associated protein with a death domain (FADD) and the procaspase-8 in the cytosol (Micheau and Tschopp, 2003; Rath and Aggarwal, 1999). In complex II, FADD and procaspase-8 possess a death effector domain (DED) sequence, through which they interact with each other (Carrington et al., 2006).

INTRODUCTION

In this complex, the procaspase-8 is the initiator caspase that activates caspase-8, which activates apoptosis (Kominami et al., 2012; Thornberry, 1998) (Figure 3).

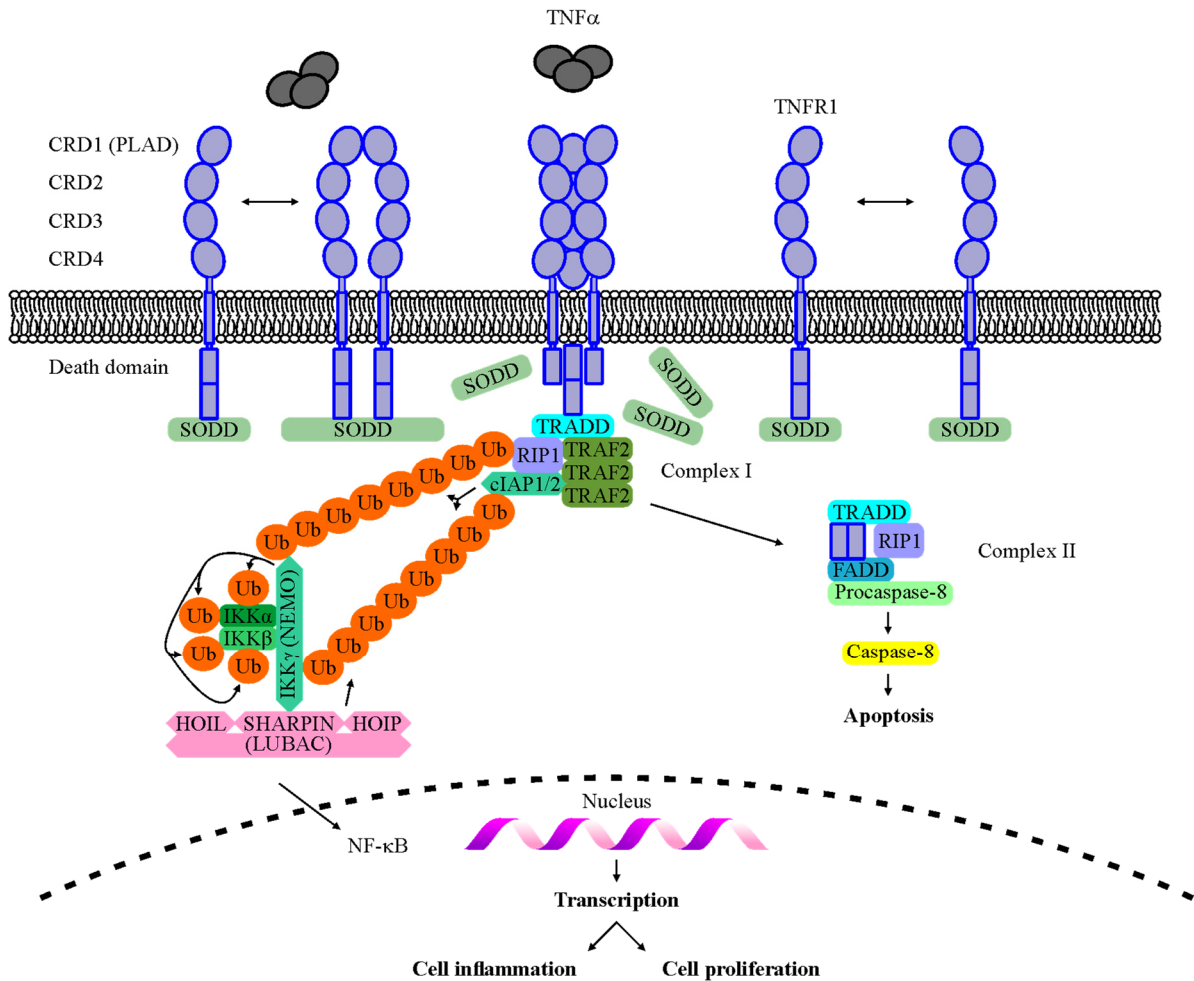


Figure 3: TNFR1 signaling cascade. *TNF α activates downstream signaling of TNFR1 by releasing SODD from the death domain leading to the recruitment of TRADD, TRAF2, RIP1 and cIAP1/2 to form complex I. Ubiquitination starts and the IKK complex is recruited. HOIL, HOIP and Sharpin is activated, mediating NF- κ B signaling which leads to cell inflammation and cell proliferation. If ubiquitination of complex I stops, TRADD and RIP1 bind with FADD and the procaspase-8 to complex II. Caspase-8 is activated and apoptosis starts.*

Although TNFR1 is a death receptor, activation of TNFR1 causes no activation of apoptosis. Actually, the common signaling cascade is the activation of the NF- κ B cascade, which inhibits the apoptotic signaling cascade (Luo et al., 2005; Tsuchiya et al., 2015). Apoptosis is only activated when proteins e.g. cIAPs, are inhibited (Rodrigues et al., 2013). If complex I is active, the cellular FADD-like IL-1 β -converting enzyme (FLICE)-inhibitory protein (cFLIP) is expressed as one of many proteins, which binds to procaspase-8 and inhibits the apoptotic signaling cascade (Micheau, 2003). Second mitochondrial derived activator of caspases (SMAC) mimetics (e.g. BV6 (Figure 4)) induce the apoptotic signaling cascade (Bai et al., 2014; Varfolomeev et al., 2007; Vince et al., 2007; Wu et al.,

2007), by the degradation of cIAP1 and 2 (El-Mesery et al., 2016; Fischer et al., 2017). This results first to an activation of the non-canonical NF- κ B signaling cascade (Berger et al., 2011; Tchoghandjian et al., 2013). After about two hours, the caspase activity increases and apoptosis starts (Schmidt et al., 2018).

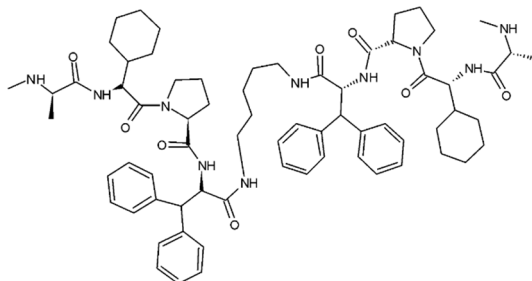


Figure 4: Chemical structure of the apoptosis inducing BV6.

1.1.2 Programmed necrosis

Apoptosis is a variant of programmed cell death and part of the homeostasis (Alberts et al., 2002; Elmore, 2007; Kerr et al., 1972; Kerr, 2002). The cell starts to bulge and to shrink and the DNA and the nucleus are degraded (He et al., 2009; Kerr et al., 1972; Nagata et al., 2003). Furthermore, numerous molecules are released preventing the production of damage-associated molecular patterns (DAMPs) (Li, 2012; Ravichandran, 2010; Segawa and Nagata, 2015). Thus, cell death of more cells is reduced since DAMPs induce a chain reaction of cell death of multiple cells (Vénéreau et al., 2015). Recently, a second form of programmed cell death, necroptosis, was discovered by inhibiting apoptosis via the pan caspase inhibitor zVAD-fmk (van Noorden, 2001) (Figure 5).

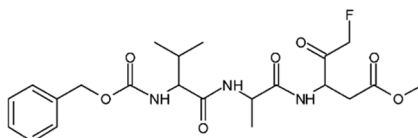


Figure 5: Chemical structure of apoptosis inhibitor zVAD-fmk.

In the TNFR1 signaling cascade, zVAD-fmk inhibits the procaspase-8, resulting in the dissociation of RIP1 from complex II. RIP1 binds with RIP3 through their RIP homotypic interaction motif (RHIM) (Li et al., 2012; Sun et al., 2002; Wu et al., 2014). This complex is also known as the necrosome where RIP1 phosphorylates and activates RIP3 (Cho et al., 2009; McQuade et al., 2013). Activated RIP3 phosphorylates the mixed lineage kinase domain like pseudokinase (MLKL) (Sun et al., 2012; Wang et al., 2014; Yang et al., 2016). Phosphorylated MLKL permeabilizes the plasma membrane causing cell death (Galluzzi et al., 2014) (Figure 6).

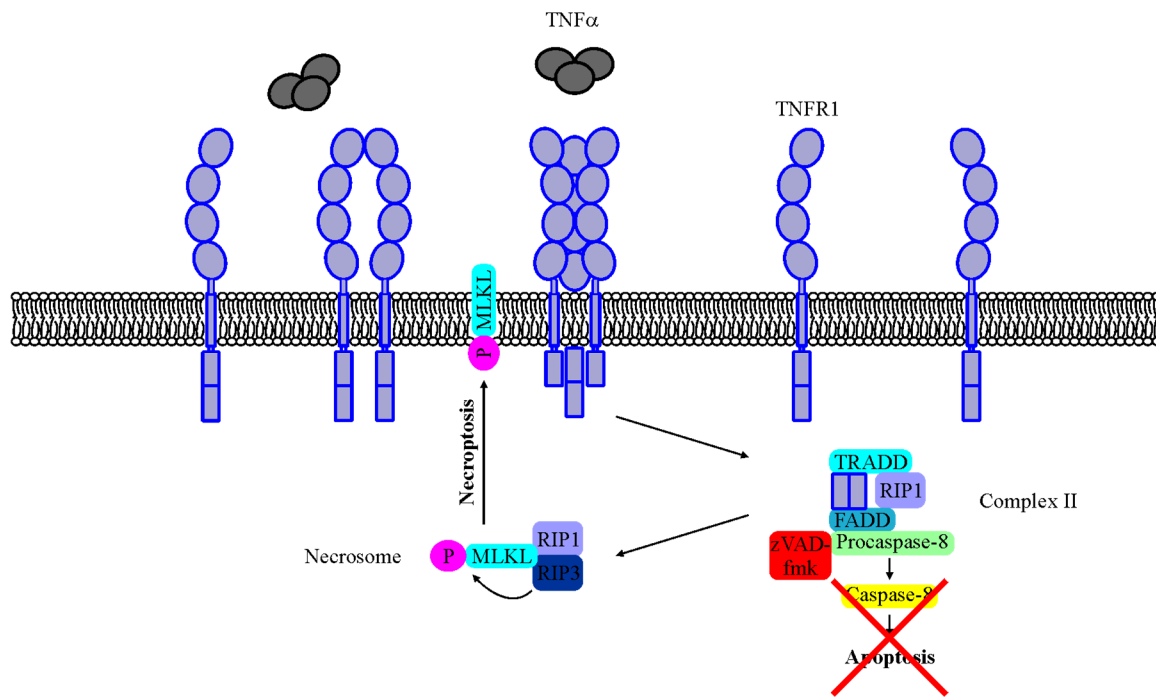


Figure 6: Necroptotic signaling cascade after TNFR1 activation. *If the procaspase-8 is inhibited by zVAD-fmk, RIP1 binds with RIP3 to the necrosome. MLKL binds and is phosphorylated by RIP3. Phosphorylated MLKL permeabilizes the plasma membrane.*

1.1.3 Pharmaceutical impact

The potential to induce cell death in tumor cells turns TNF α into a powerful target for cancer treatment (Cai et al., 2008; van Horssen et al., 2006), Crohns disease (Gibson, 2004; van Deventer, 2002), multiple sclerosis (Hare et al., 2014; Pegoretti et al., 2018; Titelbaum et al., 2005), diabetes (type II) (Akash et al., 2018; Mirza et al., 2012; Moller, 2000; Swaroop et al., 2012) and others (Aggarwal, 2003). Nevertheless, the therapeutic application is debated since TNF α also possesses toxic characteristics as it is involved in the pathogenesis of endotoxic shock (Kettelhut et al., 1987). More adverse effects of TNF α treatment are hypotony (Weinberg et al., 1988; Weinberg et al., 1992), thrombopenia (Brunasso and Massone, 2009; Chen et al., 2011; Pathare et al., 2006), leukopenia (Azevedo et al., 2012; Ulich et al., 1989), phlebitis (Saxena et al., 2010), fever (Mabika and Laburn, 1999; Stefferl et al., 1996; Sundgren-Andersson et al., 1998), headache (Rozen and Swidan, 2007; Schürks et al., 2011), liver damage (Bradham et al., 1998; Schwabe and Brenner, 2006; Simeonova et al., 2001) and others (Aggarwal, 2003). However, the ability to manipulate the signaling cascade of TNFR1 offers great potential for the treatment of these diseases (Fischer et al., 2015). For instance the necroptotic signaling cascade provides a huge potential to treat pancreatitis cancer as pancreatitis cancer cells can somehow develop resistance against the apoptotic signaling cascade (Hannes et al., 2016).

1.2 *Plasmodium falciparum* erythrocyte membrane protein 1

Another membrane protein family is the *Plasmodium falciparum* erythrocyte membrane protein 1 (pfEMP1), which is crucial in the pathophysiology of tropical malaria (Leech et al., 1984). Malaria infection occurs after a sting from a malaria infected mosquito, where the parasite *Plasmodium falciparum* infects the human liver, which then segregates parasite infected erythrocytes (Nocht and Mayer, 1936). pfEMP1 is expressed on the plasma membrane of infected erythrocytes (Leech et al., 1984), which interact with receptors from endothelial cells and with receptors from uninfected erythrocytes including the cluster of differentiation 54 (CD54) (Favre et al., 1999), the cluster of differentiation (CD36) (Barnwell et al., 1989) and the complement receptor 1 (CR1) (Rowe et al., 1997). pfEMP1 contains defined domains which induce cytoadhesion effects resulting in the segregation in the microvasculature (Smith, 2014). Thus, infected erythrocytes avoid to passage into the vascular system and a clearance by the spleen (Chotivanich et al., 2002). However, the cytoadhering erythrocytes interfere with the blood flow and cause impaired tissue perfusion. This leads to cerebral malaria and other life-threatening complications (White et al., 2014). pfEMP1 is expressed on the cell surface of erythrocytes in defined areas called knobs (Sharma, 1997). It is known that knobs from erythrocytes from patients with sickle cell anemia (HbAS) are larger than knobs from humans with normal healthy erythrocytes (HbAA) (Fairhurst et al., 2012) (Figure 7). Furthermore, it is known that patients with sickle cell anemia are immune against malaria (Allison, 1964; Willcox et al., 1983) and it is supposed that the knob size and the pfEMP1 arrangement are crucial for this immunity (Quadt et al., 2012). However, it is unknown how the knob size and potentially pfEMP1 organization in these knobs contribute to the immunity of sickle cell anemia patients. pfEMP1 numbers per knob range from about six to more than one hundred copies (Horrocks et al., 2005; Joergensen et al., 2010; Xu et al., 2013). Since these results are different, the oligomeric state of pfEMP1 in its native environment, the plasma membrane, remains unclear.



Figure 7: Electron microscopy images of HbAA and HbAS erythrocytes. *Electron microscopy (Em) images of HbAA (two left) and HbAS (two right) erythrocytes reveal more knobs in HbAA than in HbAS erythrocytes (scale bars, 1 μ m). Em-images were provided by Dr. Cecilia Sanchez (Heidelberg, Germany).*

One member of the pfEMP1 family is the VAR2CSA (Salanti et al., 2003). With 350 kDa, it is a large protein with multiple domains comprising six Duffy binding like (DBL) domains. Each of these domains

INTRODUCTION

possess three DBLX and DBL ϵ domains. Furthermore, VAR2CSA possess a cysteine-rich domain between DBL2X and DBL3X (Andersen et al., 2008; Salanti et al., 2003; Smith et al., 2000). The production of large scale amounts of VAR2CSA for experimental studies is challenging owing the large size and complex structure of the protein (Clausen et al., 2012). Thus, there exist only PDB structures of single domains but not of the entire protein. It is suggested that VAR2CSA interacts with chondroitin sulfate A (CSA) in placental malaria, which is covering the intervillous space of the placenta (Salanti et al., 2004). This interaction leads to a disturbance of sufficient supply of the fetus by the blood system during pregnancy. Thus, the investigation of vaccines to inhibit the interplay of VAR2CSA and CSA in the placenta is of great importance (Chêne et al., 2018; Fried and Duffy, 2015; Gbédandé et al., 2017).

THEORETICAL BACKGROUND

In the following, the basics of fluorescence, fluorescence microscopy and super-resolution microscopy are described. An introduction to fluorophores and labeling techniques is given.

2.1 Absorption and fluorescence

Absorption of light is the process in which a molecule is excited in a higher electronic or vibronic state and is described by the law of Lambert and Beer (Beer, 1852; Lambert, 1760) (Equation 1).

$$A = \varepsilon \cdot c \cdot d \quad (1)$$

A describes the absorption, ε the extinction coefficient, c the concentration and d the thickness of the measured substance.

Fluorescence describes the transition of the higher electronic state to the ground state in combination with the emission of light. These processes are schematically represented in a Jablonski diagram (Figure 8). The Jablonski diagram is a simplified representation of the relative positions of the energy levels of a molecule (Hof et al., 2005). From the electronic ground state S_0 with the electron in the highest occupied molecular orbital (HOMO), a molecule may absorb light and is transferred into an excited state (e.g. S_1 or S_2) (Lakowicz, 2006), with the electron transferred to the lowest unoccupied molecular orbital (LUMO). This process occurs fast ($<10^{-15}$ s), resulting in no reorientation of the nuclei (Lakowicz, 2006). The lifetime of an excited state is much longer (10^{-10} to 10^{-12} s), transferring the molecule into the lowest excited energy state due to internal conversion (IC) and vibrational relaxation (Engelborghs and Visser, 2014; Geddes and Lakowicz, 2009; Hof et al., 2005). Fluorescence occurs through the transition from the lowest vibrational state S_1 (Kasha's rule (Kasha, 1950)) to S_0 . As a result, fluorescence emission is shifted to longer wavelengths compared to absorption (Stokes shift) (Stokes, 1852). Spin-prohibited intersystem crossing (ISC) from S_1 to the triplet state T_1 can also occur (Lakowicz, 2002). The transition from the triplet state T_1 to the ground state S_0 is either radiation-free or via the emission of a photon (phosphorescence) (Shanker and Bane, 2008; Wolfbeis, 1993). Phosphorescence has a lifetime of a few milliseconds to hours (Konev, 1967).

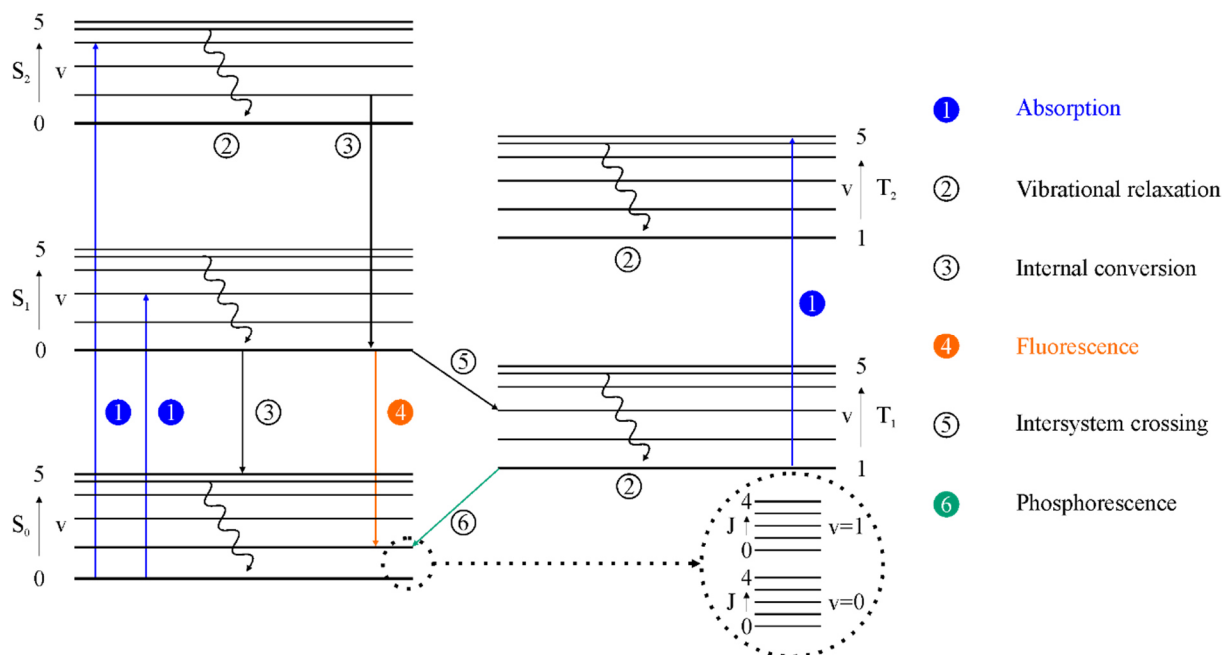


Figure 8: Jablonski diagram. The electronic ground state S_0 as well as the first and second electronic singlet states S_1 and S_2 and triplet states T_1 and T_2 are shown. Electronic levels are further subdivided into vibrational- (0, 1, 2, ..., n) and rotational levels ($J_0, J_1, J_2, \dots, J_n$). Absorption, vibrational relaxation, internal conversion, fluorescence, intersystem crossing, and phosphorescence are illustrated.

2.2 Light microscopy

The first version of a light microscope was invented in the 17th century when Zacharias Janssen achieved an image magnification with a factor of nine using a two-lens system (Hartley, 1993). The first lens is the objective, which magnifies and reverses the resulting image (intermediate image) (Lawlor, 2019). The second lens is called the ocular, which magnifies and reverses the resulting image again, followed by focusing the image on a detector (Figure 9) (Ferraro et al., 2011).

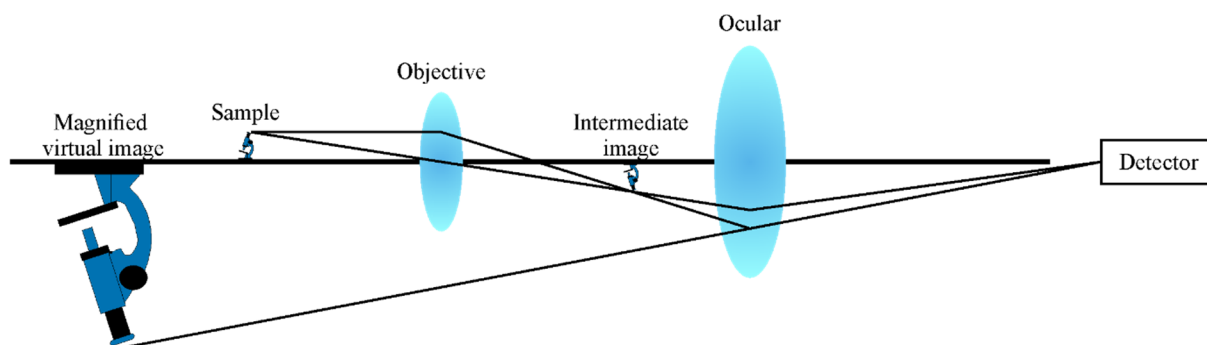


Figure 9: Scheme of a light microscope. A sample is magnified by an objective and focused on a detector by an ocular. An intermediate image between objective and ocular is created and an enlarged virtual image is generated in front of the objective.

Objectives possess a defined property to collect or transmit light in a certain angle, which is called the numerical aperture (NA). It is described as the product of the refractive index of the medium between the sample and the objective n and the sinus of the half opening angle α (Abbe, 1873) (Equation 2).

$$NA = n \cdot \sin(\alpha) \quad (2)$$

The spatial resolution of the image displayed on the camera is limited, which is defined by Abbe (Abbe, 1873). This limitation is given by the excitation wavelength λ divided by two times the NA (Abbe, 1873) (Equation 3).

$$d_{min} = \frac{\lambda}{2 \cdot NA} \quad (3)$$

Considering this criterion, the spatial resolution of light microscopy is limited by about the half of the excitation wavelength.

Fluorescence microscopy is a special application of light microscopy to visualize dynamics and structures in cells with high contrast (Lakowicz, 2006). The fluorescence signal for single emitters is detected on a camera as three-dimensional point spread function (PSF) (Lakowicz, 2006). The PSF was first described by Airy in 1835 (Airy, 1835). The PSF possesses a central intensity maximum (Airy disc) and several intensity minima (Airy pattern) (Figure 10A) (Webb, 1996). In 1896, Rayleigh described a resolution limit postulating that two emitters could only be separated when the minimum distance of the intensity maximum of the first PSF overlaps with the first intensity minima of the second PSF (Rayleigh, 1903, 2009). PSFs that are closer than this distance cannot be separated (Figure 10B) (Rayleigh, 1903, 2009).

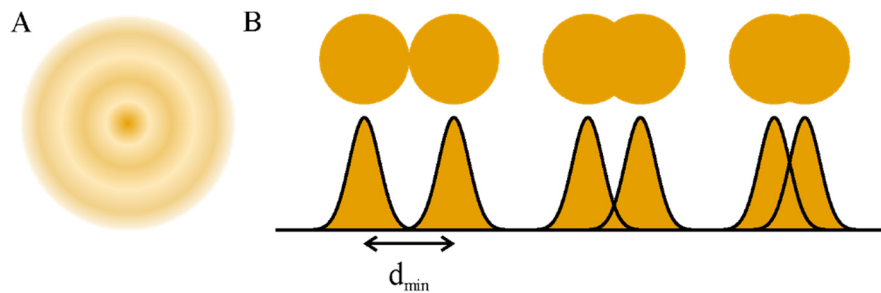


Figure 10: Airy disc and Rayleigh limit. (A) Airy pattern of a point spread function. The central Airy disc is represented together with two concentric rings. (B) Illustration of the diffraction-limit according to Rayleigh with the minimum distance d_{min} .

Rayleigh described this minimum distance in dependency of the NA and the wavelength λ (Equation 4) (Rayleigh, 1903, 2009), which results in a lateral resolution of 200-300 nm for common wavelengths and objectives.

$$d_{min} = \frac{0.61 \cdot \lambda}{NA} \quad (4)$$

THEORETICAL BACKGROUND

Possibilities to illuminate a sample in fluorescence microscopy are wide-field (wf), total internal reflection fluorescence (TIRF) (Axelrod et al., 1984) or highly inclined and laminated optical sheet microscopy (HILO) (Tokunaga et al., 2008) modes (Figure 11).

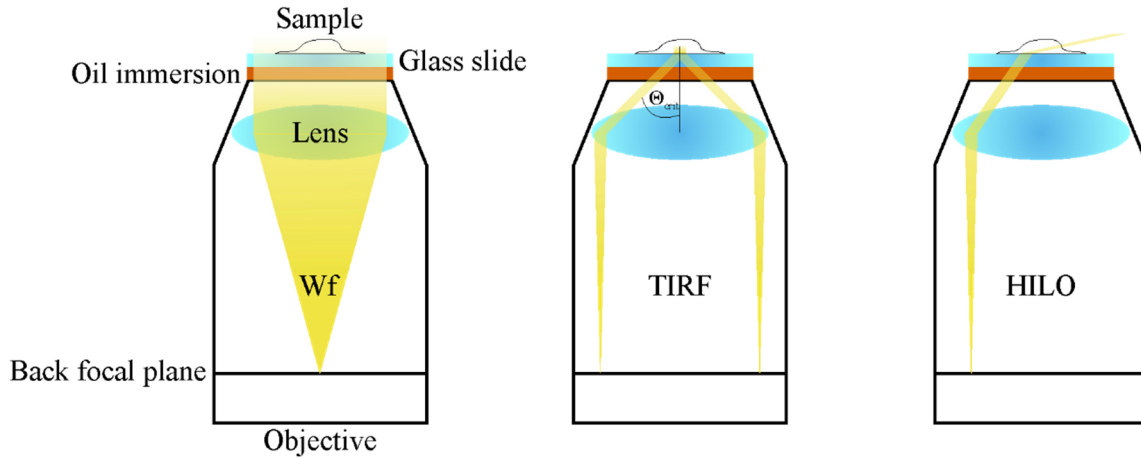


Figure 11: Wide-field, TIRF and HILO illumination schemes. *Conventional wide-field illumination excites homogeneously the whole sample. In TIRF mode, excitation light hits the glass slide with the angle Θ_{crit} . The laser light is totally reflected and only an exponentially decaying evanescent light field penetrates the sample. In HILO mode, the excitation light hits the glass slide with an angle below the critical angle, leading to a thin optical light sheet passing the sample.*

In these three cases, the excitation light is first expanded and then focused by a telescope to the back focal plane of the objective. In the wide-field mode the laser beam is fully directed towards the sample, leading to the illumination of the whole sample structure (Lakowicz, 2006). TIRF mode is used to illuminate just the surface of the sample, e.g. to visualize membrane protein structures or to observe internalization effects of cells (Axelrod et al., 1984). This is accomplished by directing the excitation laser beam through the objective, to be fully reflected by the glass-medium interphase on the sample as it strikes this phase in the critical angle Θ_{crit} . This angle Θ_{crit} is only dependent on the refractive indices n_1 (medium of the sample) and n_2 (medium of the glass slide) (Equation 5) (Axelrod et al., 1984; Lakowicz, 2006).

$$\Theta_{crit} = \arcsin\left(\frac{n_1}{n_2}\right) \quad (5)$$

Total reflection generates an evanescent field, illuminating just the region over the objective. The intensity of the evanescent field decays exponentially, so only fluorophores within 0-200 nm are excited (Axelrod et al., 1984; Fish, 2009). In HILO mode, the illumination angle on the objective glass-medium phase increases, resulting to a thin optical sheet leading through the sample. Thus, HILO enables imaging of deeper focal planes compared to TIRF mode, yet with less background than wide-field illumination (Tokunaga et al., 2008).

A second possibility to visualize a certain sample is by confocal laser-scanning microscopy (CLSM) (Pawley, 1995). CLSM was invented in 1957 from Marvin Minsky (Minsky, 1988). Compared to wide-field techniques, the laser beam is not focused on the back focal plane of the objective. At CLSM the laser beam is focused into the sample and screened stepwise by e.g. galvanometer-driven mirrors (Pawley, 1995). Using CLSM enables imaging in three dimensions without collecting out-of-plane signal. Thus, CLSM facilitates reconstructing images either in two dimensions (2D) or three dimensions (3D) with high contrast (Pawley, 1995).

2.3 Fluorescent proteins

In 1992, the complementary DNA (cDNA) of the green fluorescent protein (GFP) was isolated from the jellyfish *Aequorea Victoria* (Prasher et al., 1992). In 1994, GFP was used for the first time *in vivo* as a fluorescent tag (Heim et al., 1994), enabling the visualization of structures in cells. Afterwards, there was great interest in elucidating the biochemical, biophysical and structural properties of fluorescent proteins (Remington, 2011). A large number of studies in the development and application of new fluorescent proteins were performed. GFP-like fluorescent proteins such as YFP (Ormö et al., 1996), mMaple (McEvoy et al., 2012) and mCherry (Shaner et al., 2004) are just a few of the proteins that were developed in recent decades.

Further advances lead to fluorescent proteins that are photoactivatable (Lippincott-Schwartz and Patterson, 2009; Lippincott-Schwartz and Patterson, 2008; Lukyanov et al., 2005), photoconvertible (Baker et al., 2010) and photoswitchable (Zhou and Lin, 2013) (Figure 12). Photoactivatable fluorescent proteins (PAFPs) change their spectral characteristics after illumination with light of a certain wavelength and intensity (Lippincott-Schwartz and Patterson, 2008). Photoactivation is accomplished with the transition rate k_{act} from a dark to a fluorescent bright state after irradiation with e.g. ultraviolet (UV) light. Next, PAFPs switch irreversibly with the transition rate k_{bleach} from the activated fluorescent state to a dark photobleached state (Figure 12A). This enables PAFPs to visualize structures or dynamics in cells (Lippincott-Schwartz and Patterson, 2009). paGFP was the first photoactivatable protein that was developed (Patterson and Lippincott-Schwartz, 2002). A point mutation (Thr203His) transformed GFP to a non-fluorescent mutant with the chromophore (Ser-Tyr-Gly) (Patterson and Lippincott-Schwartz, 2002), whose protonated state is stabilized by Glu222 (Shcherbakova and Verkhusha, 2014; van Thor et al., 2002). Upon illumination with UV light, the chromophore switches to an anionic form by a proton transfer. Glu222 is decarboxylated, stabilizing the anionic form (Shcherbakova and Verkhusha, 2014). PAmCherry1 is another example for a photoactivatable fluorescent protein, which also photoswitches after irradiation with UV light from a green to red state (Subach et al., 2009).

Photoconvertible fluorescent proteins possess two fluorescent states, typically a green and a red fluorescent state (Baker et al., 2010). Usually the green fluorescent state occurs due to activation of the His-Tyr-Gly anionic chromophore (k_{on,λ_1}) (Shcherbakova and Verkhusha, 2014). After illumination with UV light, a spectral shift to the emission of red light occurs (k_{act}), indicating an enlargement of

THEORETICAL BACKGROUND

the π -electron system of the chromophore. The cleavage of a peptide bond by a β -elimination and proximate generation of a C = C bond in the chromophore is proposed (Mizuno et al., 2003; Nienhaus et al., 2005). Figure 12B illustrates the kinetic model of the photokinetics of photoconvertible fluorescent proteins. After illumination with UV light, photoconvertible proteins are photoconverted to the second fluorescent state (k_{on,λ_2}), from which they either reversibly switch to a non-fluorescent dark state ($k_{on,\lambda_2}, k_{off}$) or irreversibly to a photobleached state (k_{bleach}). This “blinking” occurs due to UV-induced cis-trans-isomerization of the tyrosine in the chromophore (Day and Davidson, 2009). EosFP is a photoconvertible protein and was due to its large photon output one of the best-performing green-to-red fluorescent proteins (Lelimosin et al., 2009; Wiedenmann et al., 2004). However, in its natural form EosFP forms homotetramers (Wiedenmann et al., 2004). Thus, photoconvertible proteins like the monomeric Eos fluorescent protein (mEosFP) (Mathur et al., 2010), tandem dimer (td)EosFP (Wiedenmann et al., 2004) and mEos2 (McKinney et al., 2009) were investigated. Since mEosFP denatures at 37 °C it is not useful for experiments in cells (Zhang et al., 2012). tdEosFP exhibits inaccurate localization of biological structures, which is assumed to be caused due to its large size (McKinney et al., 2009). These challenges were solved with the invention of mEos2. However, mEos2 also tends to aggregate in dense structures, since it forms dimers and tetramers (Hoi et al., 2010; McKinney et al., 2009) (Figure 12B). Due to the mutation of I102N, I157V, H158E and Y189A, the tendency of oligomerization of mEos2 vanished and the brightness increased. This variant of mEos2 is called mEos3.2, which offers large potential for fluorescence microscopy (Zhang et al., 2016).

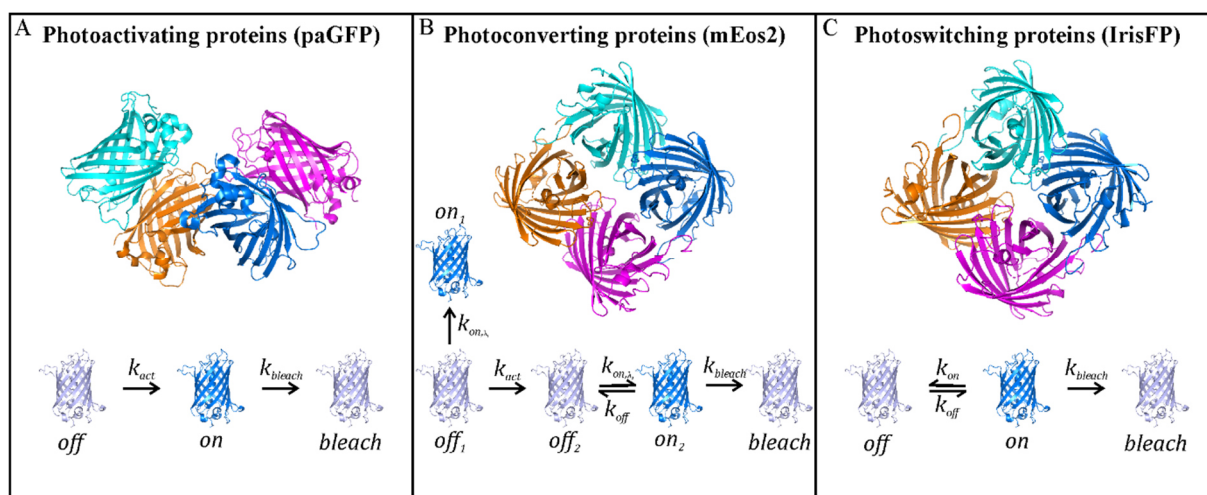


Figure 12: Kinetic schemes of fluorescent proteins. The crystal structures of (A) tetrameric paGFP (PDB 3gj2) as photoactivating-, (B) tetrameric mEos2 (PDB 3s05) as photoconverting- and (C) IrisFP (PDB 2vvh) as photoswitching protein are illustrated. The monomeric proteins are shown in cyan, orange, blue and magenta, respectively. The schemes show on, off and bleached states with k_{act} , k_{on} , k_{off} and k_{bleach} rates.

Compared to photoactivatable and photoconvertible fluorescent proteins, photoswitchable proteins switch reversibly between a dark and a bright state (k_{on} , k_{off}) before they irreversibly switch to a non-fluorescent photobleached state (k_{bleach}) (Zhou and Lin, 2013) (Figure 12C). An example of a photoswitchable protein is Dronpa (Ando et al., 2004). Its switching kinetic is generated by a cis-trans isomerization of the chromophore (Andresen et al., 2007). Further examples for photoswitchable proteins are reversibly switching enhanced green fluorescent protein 2 (rsEGFP2) (Grotjohann et al., 2012) and Iris fluorescent protein (IrisFP) (Adam et al., 2008) (Figure 12C).

2.4 Organic fluorophores

Organic fluorophores find large application in the field of fluorescent microscopy. In 1845, Sir John Herschel discovered quinine sulfate, the first fluorescent organic molecule, which emits blue light after UV irradiation (Herschel J. F. W., 1845). Moreover, the organic chemistry developed a whole set of organic fluorophores with improved stability, large brightness and across the spectra (Lavis, 2017).

Organic fluorophores have a typical size of about 1-2 nm, possess a larger brightness and are more photostable than fluorescent proteins (Waggoner, 2006; Zhang et al., 2002). The most prominent classes of organic dyes for fluorescence microscopy are rhodamines (Figure 13A), carbocyanines (Figure 13B), carbopyronines (Figure 13C) and oxazines (Figure 13D). Rhodamines absorb between 488 and 570 nm (Lopez Arbeloa et al., 1991; Sauer et al., 2011; Stennett et al., 2014). If the amino groups are alkylated, the quantum yield of rhodamines show sensitivity to viscosity and temperature. Rhodamines, which are fractional alkylated or where the amino groups are part of aliphatic fixed rings, reach a quantum yield of approximately one (Lopez Arbeloa et al., 1991; Sauer et al., 2011; Stennett et al., 2014). When rhodamines contain a non-esterified carboxyl group, a protonated cationic form (pH = 2) and a deprotonated zwitterion (pH = 8) exist in equilibrium. After excitation, both forms show fluorescence, but the zwitterionic form exhibits a larger quantum yield (Lopez Arbeloa et al., 1991; Sauer et al., 2011; Stennett et al., 2014). Examples for rhodamines are Alexa Fluor 488, Alexa Fluor 532, ATTO 565 and TAMRA.

Carbopyronines have a similar chemical structure as rhodamines, with the difference that instead of the oxygen atom a dimethyl-methin group is present. Carbopyronines, such as ATTO 647N, show a red-shifted fluorescence emission (Stennett et al., 2014). Oxazines (e.g. ATTO 655 and ATTO 700) show a similar red shift. The basic structure of an oxazine is again the same as for rhodamines and carbopyronines, with the difference that the central atom of the xanthene chromophore is a nitrogen. Since oxazines exhibit a larger electron affinity, they are more resistant to photobleaching (Stennett et al., 2014). Carbocyanines consist out of two amino groups, which are linked by a polymethine chain. Since this structure is unstable, two heterocyclic groups are added to the ends of the chains to stabilize the dye (Stennett et al., 2014). Cy3, Cy3B, Cy5, Alexa Fluor 647 and Cy7 are examples for carbocyanines. The organic fluorophores discussed in this chapter, are commonly used for fluorescence microscopy and represent a wide range of spectral properties, facilitating multi-color imaging.

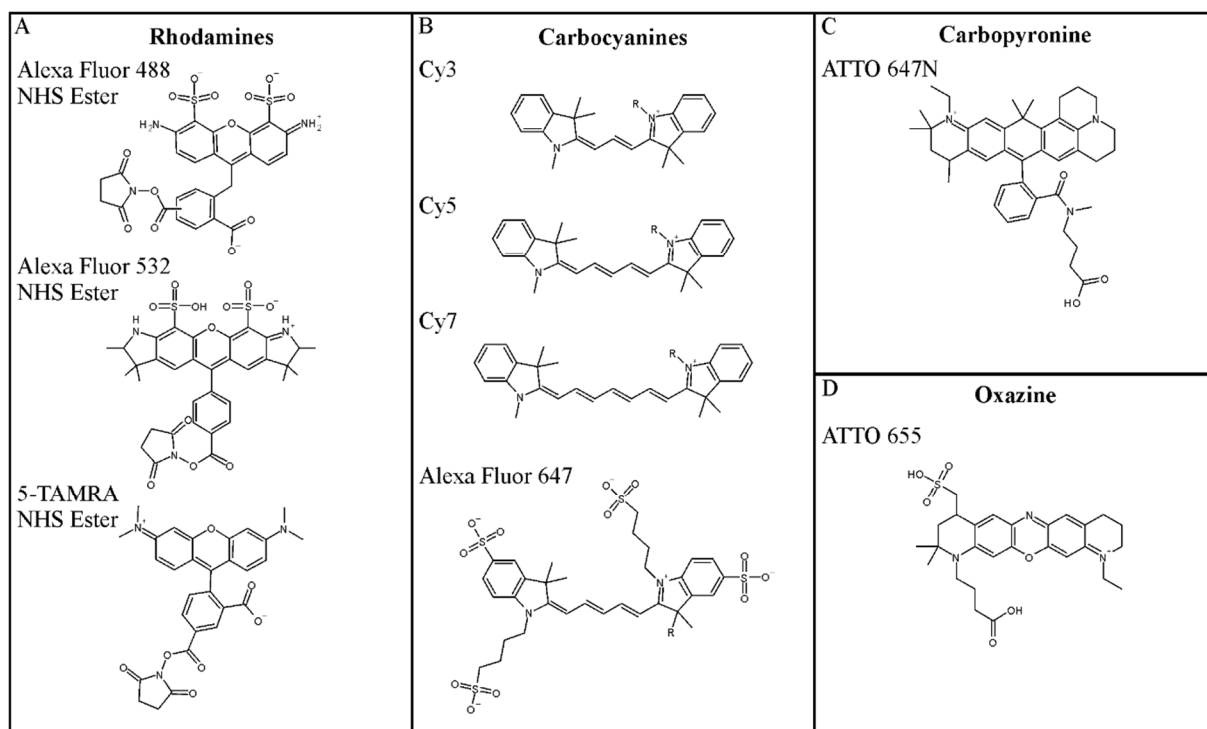


Figure 13: Chemical structures of selected organic fluorophores. (A) Rhodamine dyes Alexa Fluor 488, Alexa Fluor 532 and 5-TAMRA (B) the carbocyanines Cy3, Cy5, Cy7 and Alexa Fluor 647 (C) the carbopyronine ATTO 647N and (D) the oxazine ATTO 655.

Numerous organic fluorophores can be operated as photoswitches under defined chemical conditions (Figure 14). The carbocyanine Cy5 was the first organic fluorophore, where photoswitching was demonstrated (Heilemann et al., 2005). If Cy5 is in an aqueous environment in presence of a primary thiol, e.g. β -mercaptoethylamine (MEA) and is illuminated with red light, a transition from the triplet to a long-lived dark state occurs. This long-lived dark state resides between milliseconds to seconds and arises due to the disruption of the π -electron system by the thiol (Dempsey et al., 2009). The oxygen content affects organic fluorophores in aqueous buffer solutions. It is known that ground state triplet oxygen reacts with excited organic fluorophores in the triplet state, causing the formation of reactive singlet oxygen. It is assumed that singlet oxygen is a primary source for photobleaching of organic fluorophores. Oxygen degradation prevents these effects using an enzymatic oxygen scavenger system consisting of glucose oxidase and catalase (Uppoor and Niebergall, 1996; van de Linde and Sauer, 2014). However, glucose oxidase with catalase is incompatible for experiments in cells. Furthermore, its application causes the formation of hydrogen peroxide, which damages fluorophores. The protocatechuic acid/protocatechuate-3,4-dioxygenase system (PCA/PCD) avoids these problems for fixed cells and also improves the stability of the used organic fluorophore (Aitken et al., 2008). However, upon irradiation with UV light the anionic radical state $F^{\cdot-}$ and the leuco-form FH depopulate, allowing the adjustment of the emission of the organic fluorophores in *d*STORM experiments (van de Linde et al., 2011a).

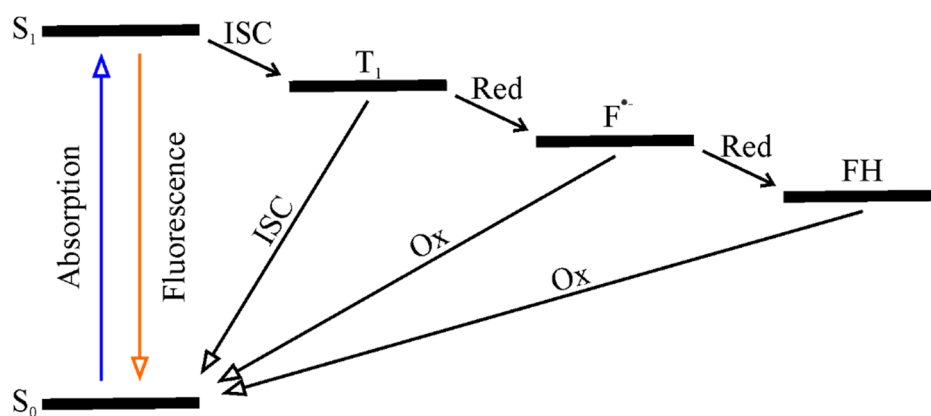


Figure 14: Photoswitching scheme of organic fluorophores. *An organic fluorophore is excited from the ground state S_0 to the first excited state S_1 . The fluorophore either switches back to the ground state S_0 by emitting fluorescence or switches to the T_1 state by intersystem crossing (ISC). From the T_1 state the fluorophore switches to S_0 by ISC, or to the radical form F^\bullet , or to the leuco-form FH by reduction (Red), from where the fluorophore switches back to the S_0 state due to the reaction with oxygen (Ox). Photoswitching scheme adapted from van de Linde et al., 2011b, © 2011, with permission from Nature Publishing group.*

The most prominent photoswitching organic fluorophore is Alexa Fluor 647, a variant of Cy5. Due to its superior photoswitching property and its excellent brightness, Alexa Fluor 647 is the most widely used organic fluorophore for single-molecule localization microscopy (chapter 2.6).

Another group of organic fluorophores are photoactivatable fluorophores, also known as caged dyes (Krafft et al., 1988; Mitchison, 1989; Peters and Trendelenburg, 1986; Taylor and Waggoner, 1986). Similar to photoactivatable fluorophores, these dyes can be transformed into a fluorescent state by light.

2.5 Labeling techniques

Fluorescence microscopy requires tools to link fluorophores to target molecules. For this purpose, strategies such as genetic attachment, immunofluorescence and tag technologies are available.

2.5.1 Genetic expression of fluorescent proteins

Fluorescent proteins are fused to a target protein by cloning the DNA sequence of the fluorescent protein to the gene of the protein (Cabral, 2016; Lodish and Matsudaira, 2000). The genetic information is introduced into the cell and the fusion protein consisting of fluorescent protein and target structure is expressed in a 1:1 stoichiometry. This process is known as transfection and is divided into stable and transient transfection (Kim and Eberwine, 2010). Stable transfection describes the stable insertion of DNA into a cell. In contrast, transient transfection describes the insertion of DNA into a cell, which is limited in time (Kim and Eberwine, 2010). Overall DNA is inserted into a cell by chemical, e.g. lipofection (Felgner et al., 1987), or physical transfection methods like electroporation (Potter, 2003). Lipofection uses endocytosis to assimilate unilamellar liposomes with DNA into the cell. These liposomes are composed of cationic or neutral lipids (Felgner et al., 1987). In electroporation, cells are

exposed to high voltage pulses, leading to permeabilization and incorporation of DNA. Since electroporation possesses the higher mortality rate, chemical transfection methods are more established (Potter and Heller, 2017). Overall, transfection efficiencies vary among different plasmids. It is affected by the size of the plasmid, the pH of the buffer and the concentration of DNA (Cabral, 2016). For optimal and efficient transfection, a protocol suitable for each cell line and a specific plasmid needs to be established. Apart from transfection, polymerase chain reaction (PCR) also enables the implementation of genetically fluorescent proteins in cells. The gene encoding for the protein is transferred as a plasmid with a helper plasmid and a Cas12a endonuclease into the desired cell, resulting in the incorporation into the target gene (Baudin et al., 1993; Janke et al., 2004). The clustered regularly interspaced short palindromic repeat (CRISPR)/Cas is another method for modifying and implementing genes in cells. The Cas9 endonuclease recognizes and binds a specific ribonucleic acid (RNA) sequence (CRISPR sequence, first described in 1987 (Ishino et al., 1987)) to cleave the DNA at this particular position allowing the desired DNA to be inserted (Deveau et al., 2010).

2.5.2 Tag-technologies

Small protein or peptide tags, e.g. the Halo-, Clip- or the SNAP-tag, are genetically fused to a target. The SNAP-tag is a mutant of the O⁶-alkylguanine-DNA alkyltransferase and currently one of the most adroit chemical tag-technologies applied in multiple scientific works. The SNAP-tag reacts fast and specific with benzylguanine (BG) derivatives (Figure 15) (Keppler et al., 2003). Thus, organic fluorophores carrying an O⁶-benzylguanine (O⁶-BG) group can be used to label the SNAP-tag. The SNAP-tag possesses a molecular mass of 20 kDa (Keppler et al., 2003) and is thus smaller than fluorescent proteins with about 26 kDa (GFP) (Morise et al., 1974).

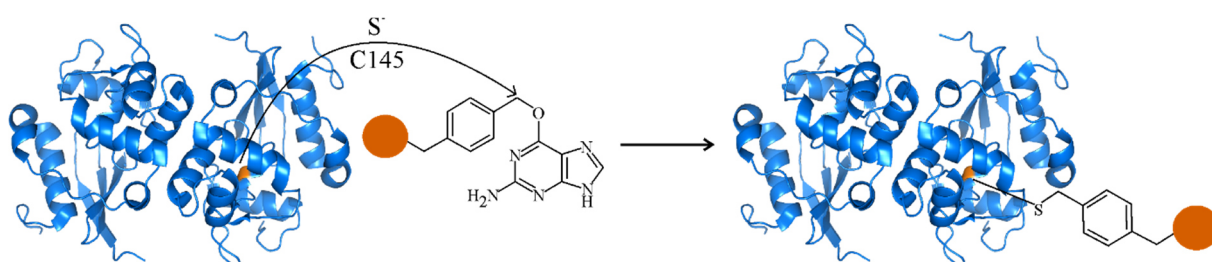


Figure 15: SNAP-tag reaction with O⁶-benzylguanine. *The negatively charged sulfur of the C145 of the SNAP-tag (PDB 3KZY) reacts with the O⁶-benzylguanine, creating a covalent bond between the SNAP-tag and its substrate.*

2.5.3 Immunofluorescence

A common technique for labelling proteins with organic fluorophores is immunofluorescence using fluorophore-labelled antibodies. In principle, there are two immunofluorescence strategies: direct and indirect immunofluorescence (Aoki et al., 2010) (Figure 16). Direct immunofluorescence is a one-step process in which an organic fluorophore is bound to a specific primary antibody that binds to a specific structure (Coons et al., 1941; Coons et al., 1942). Indirect immunofluorescence is a two-step process

(Lewis Carl et al., 1993) in which first a primary antibody binds to a desired target structure. Afterwards a second antibody binds with high affinity to the primary antibody, which itself is coupled to an organic fluorophore. Thus, a high degree of labeling is possible by using e.g. multiple labeled or polyclonal antibodies enabling a better signal-to-noise ratio for fluorescence microscopy (Wheatley and Wang, 1998). In contrast to transfection, where a fluorescent protein is directly coupled to a target structure, immunofluorescence leads to an increased distance between dye and target structure. This occurs due to the large size (12-14 nm) of a full immunoglobulin G (IgG) antibody (Edelman, 1971; Lee et al., 2006), leading to a distance to up to 30 nm between target structure and organic fluorophore. An option to reduce this distance is to use only a small part of an antibody, the fragment antigen binding (F(ab')₂) fragment (Lamoyi and Nisonoff, 1983; Nisonoff et al., 1960). This fragment is obtained by using pepsin or papain, which split the IgG antibody into a F(ab')₂ and Fc fragment (Coulter and Harris, 1983; Lamoyi and Nisonoff, 1983). The size of an antibody fragment is thus smaller with about 5-7 nm (Coulter and Harris, 1983; Edelman, 1971; Lamoyi and Nisonoff, 1983; Lee et al., 2006). Antibodies of camelids, termed nanobodies, further minimize the distance between organic fluorophore and target structure, since nanobodies exhibit a size of about 2-3 nm (Hamers-Casterman et al., 1993). Typically, the nanobody is targeted against GFP, with GFP fused to the desired structure (Rothbauer et al., 2008).

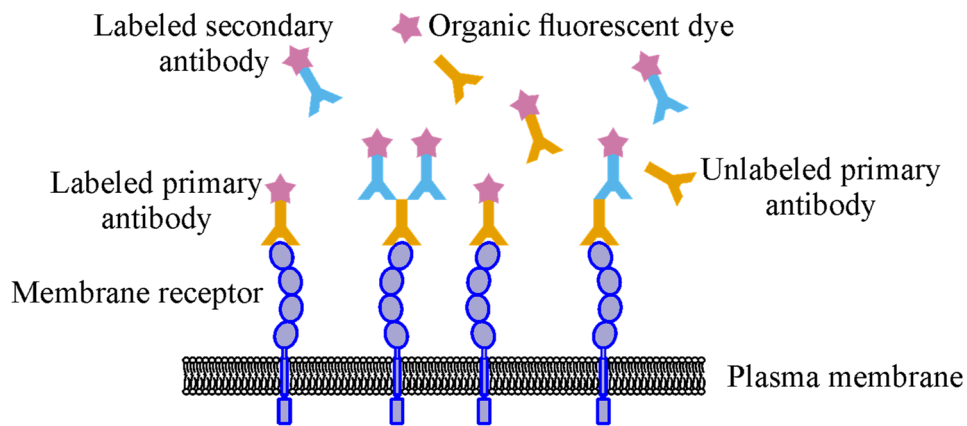


Figure 16: Direct and indirect immunofluorescence. For direct immunofluorescence, a primary antibody (orange) labeled with an organic fluorophore (pink) binds to a target structure (e.g. a membrane receptor, dark blue). In indirect immunofluorescence, a labeled secondary antibody (light blue) binds to a primary antibody, which is bound to the target structure.

2.6 Super-resolution microscopy

The limit in spatial resolution in fluorescence microscopy is about the half of the wavelength, i.e. about 200 nm in the imaging plane. As a result, some super-resolution methods were developed to circumvent these limits. One approach uses a deterministic detection of fluorophores, e.g. in stimulated-emission depletion (STED) (Hell and Wichmann, 1994) and structured illumination microscopy (SIM) (Gustafsson, 2000) (Figure 17A). STED microscopy uses a confocal setting with a second laser in a doughnut profile overlaid to the excitation laser, depleting fluorescence outside the center of the excitation laser. The size of the effective PSF depends on the power of the STED laser, accomplishing a lateral resolution of ~ 20 nm (Westphal and Hell, 2005) and an axial resolution of ~ 30 nm (Dyba and Hell, 2002).

In SIM, patterned illumination high spatial frequency features are translated to lower frequencies. Through different orientations of the structured illumination pattern, several images are recorded and reconstructed to a super-resolved image (Gustafsson, 2000). SIM accomplishes a resolution of about 100 nm in lateral and 300 nm in axial direction (Gustafsson, 2000). Owing the fast measurement performance and the low laser intensities, 3D-SIM is currently the method of choice for performing live cell measurements.

The second type of super-resolution microscopy methods is based on stochastic photoactivation of fluorophores (Figure 17B), called single-molecule localization microscopy (SMLM). This group includes (fluorescence) photoactivated localization microscopy ((f)PALM) (Betzig et al., 2006; Hess et al., 2006), (*direct*) stochastic optical reconstruction microscopy ((*d*)STORM) (Heilemann et al., 2008; Rust et al., 2006), ground-state depletion followed by individual molecule return (GSDIM) (Fölling et al., 2008) and point accumulation for imaging in nanoscale topography (PAINT) (Sharonov and Hochstrasser, 2006) (Figure 17C). During SMLM experiments, PSFs of fluorophores are temporally and spatially separated and individually detected on a camera (Figure 17B). Each detected PSF is approximated with a two-dimensional Gaussian function (Equation 6) (Small and Stahlheber, 2014; Wolter et al., 2010).

$$I(x, y) = \frac{A}{2\pi\sigma_x\sigma_y} \exp\left(-\frac{1}{2}\left(\frac{(x-x_0)^2}{\sigma_x^2} + \frac{(y-y_0)^2}{\sigma_y^2}\right)\right) + B \quad (6)$$

I describes the intensity of the Gaussian, x and y the corresponding coordinates, x_0 and y_0 the center coordinates, A the amplitude, σ_i the distribution width in x and y , respectively, and B the background noise. A super-resolution image is reconstructed from the coordinates of all PSFs.

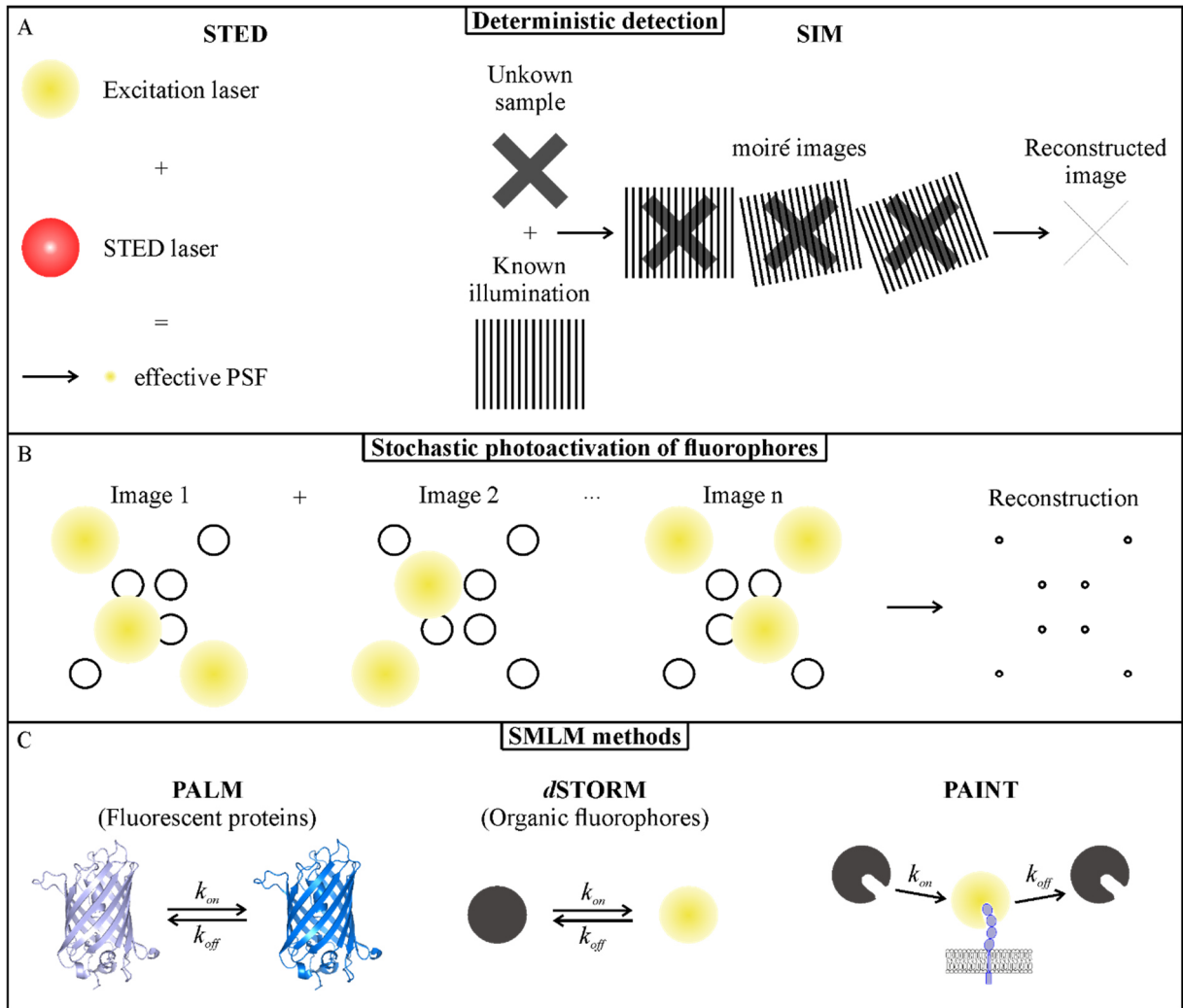


Figure 17: Deterministic and stochastic super-resolution microscopy techniques. (A) Simplified representations of STED and SIM methods are illustrated. (B) The basic strategy of single-molecule localization microscopy with (C) PALM, dSTORM and PAINt are shown.

2.7 Resolution in single-molecule localization microscopy

The localization precision (or localization uncertainty σ_{loc}) depends on the number of photons and was described by Mortensen *et al.* (Mortensen et al., 2010) (Equation 7 and 8).

$$\sigma_{loc} = \sqrt{\frac{\sigma_{PSF}^2}{N_{photon}} \cdot \left(\frac{16}{9} + \frac{8\pi\sigma_{PSF}^2 B^2}{N_{photon} a^2} \right)} \quad (7)$$

$$\sigma_{PSF}^2 = \sigma^2 + \frac{a^2}{12} \quad (8)$$

Here, σ_{PSF} describes the standard deviation of the PSF, N_{photon} the number of detected photons, a the pixel size and B the background signal.

Considering that the background signal is neglectable the uncertainty σ_{loc} was determined by Thompson *et al.* (Equation 9) (Thompson et al., 2002).

$$\sigma_{loc} = \frac{\sigma_{PSF}}{\sqrt{N_{photon}}} \quad (9)$$

The same fluorophore may be detected in consecutive camera frames, so that the localization precision can also be calculated by a nearest neighbor based analysis (NeNA) (Endesfelder et al., 2014). In theory, the true distance between two detected PSFs of the same fluorophore of two consecutive camera frames would be zero. In the experiment, there is a displacement dependent of σ_{loc} . The probability distribution $p(d)$ of this displacement is given (Equation 10) as:

$$p(d) = A_1 \left(\frac{d}{2\sigma_{loc}^2} \exp\left(\frac{-d^2}{4\sigma_{loc}^2}\right) \right) + A_2 \left(\frac{1}{\sqrt{2\pi\omega^2}} \exp\left(\frac{-(d-d_c)^2}{2\omega^2}\right) \right) + A_3 d \quad (10)$$

A_1 , A_2 and A_3 describe the amplitude of the particular terms, d represents the distance between the two PSFs of the consecutive frames and σ_{loc} gives the experimental localization precision. ω represents the standard deviation of the correction term with the center d_c (Churchman et al., 2006; Endesfelder et al., 2014).

In addition to the localization precision, the density of fluorophores determines the resolution. The Nyquist-Shannon sampling theorem specifies that two adjacent fluorophores have to have a distance of at least half of the resolution. Thus, fluorophores must be placed every 15 nm to resolve a structure with a resolution of 30 nm (Nyquist, 1928).

2.8 Cluster analysis in SMLM

Cluster analysis was first described by Robert Tryon in 1939 as the separation of data points in a dataset into subgroups, where the points of each subgroup belong more to each other than to other points of other subgroups (Tryon, 1939). Since then, several cluster algorithms were investigated. One cluster algorithm is the density-based spatial clustering of application with noise (DBSCAN) (Ester et al., 1996). DBSCAN identifies clusters and noise in a certain dataset (Figure 18). DBSCAN defines clusters as locally increased data points inside a certain distance. Data points, which do not show this increased density, are defined as noise. DBSCAN requires only two parameters for the analysis, a cluster radius ϵ_{min} and the minimum number of data points N_{pts} , which have to be within this radius. DBSCAN takes a data point and searches for other data points in the given radius. If the minimum number of data points is reached, the selected data point is defined as a core point. If the minimum number of data points is not found, the respective data point is either a noise or an edge point. An edge point is defined as a data point, which is inside the radius of a core point, but itself has not enough data points to be a core point. If a data point is neither a core nor an edge point, it is defined as noise (Figure 18) (Ester et al., 1996).

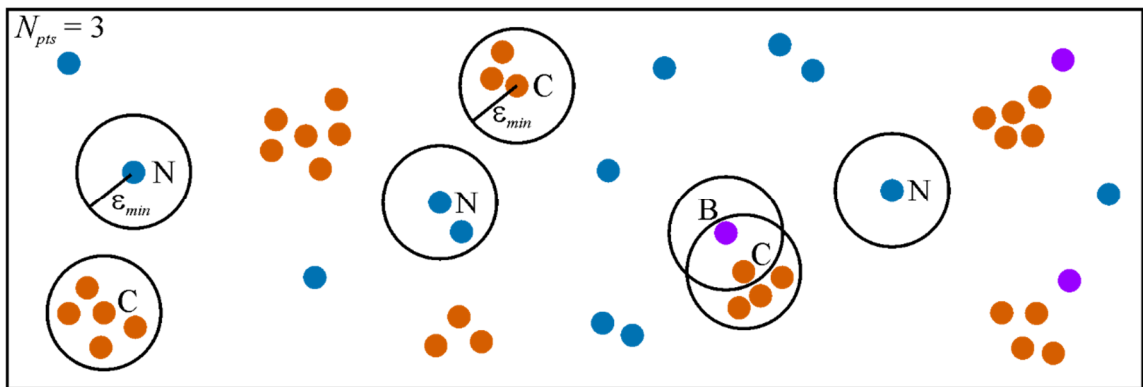


Figure 18: Principle of the DBSCAN algorithm. Example of a DBSCAN algorithm with radius ϵ_{min} and a minimum number of data points $N_{pts} = 3$. Core, border and noise points are represented as C (orange), B (purple) and N (blue), respectively.

2.9 Quantitative super-resolution fluorescence microscopy

In recent years, strategies using fluorescence microscopy and single-molecule localization microscopy were investigated to determine the quantitative number of biomolecules in cells. The first method is intensity-based counting (IBC) (Gross and Webb, 1986). The intensity of the fluorescence of a labeled biological target is measured and compared to the intensity of a known standard. This method is dependent on a robust measurement of the reference sample. Furthermore, a homogenous illumination field is necessary. A difficulty is that fluorophores often change their brightness in different nano-environments, limiting this method to a smaller number of oligomers (Magde et al., 2002). However, IBC was used to obtain quantitative results for e.g. the DNA replication machinery in *Escherichia coli* (Reyes-Lamothe et al., 2010). A second quantitative approach is based on the analysis of photobleaching

steps (Ulbrich and Isacoff, 2007). The difficulty with this strategy consists in the identification of photobleaching steps for higher N due to unknown detection efficiencies. Furthermore, the probability that two fluorophores bleach at the same time increases with larger number of fluorophores.

In order to obtain quantitative data on dense proteins in cells, different methods based on single-molecule localization microscopy were developed. One approach is based on counting blinking events (one blink describes the number of reappearances of a fluorophore transiting from a metastable dark state into to the fluorescent state) of fluorescent proteins for PALM (Fricke et al., 2014). This technique enables to determine protein copy numbers at high sample densities. However, two major challenges need to be addressed. First, fluorescent proteins as well as organic fluorophores typically generate multiple emission events from a single fluorophore. Simply counting the number of emission events leads to an over-estimation of underlying fluorophores. A second challenge is a potential underestimation of the size of the oligomer due to e.g. incomplete protein maturation, misfolding, protonation states or premature photobleaching (Durisic et al., 2014). Multiple groups attempted to solve these challenges. One approach is based on the study of photoswitching kinetics (Fricke et al., 2015). After activation, a fluorophore switches either reversibly to a non-fluorescent dark state or irreversibly to a photobleached state. In addition, it was discovered that the number of blinking events of fluorescent proteins follow a geometric distribution (Lee et al., 2012). In 2016, Hummer *et al.* evolved the theoretical model for a kinetic model with multiple dark states (Hummer et al., 2016) (Equation 11).

$$p_m(n) = \sum_{k=0}^{\min(m,n)} \binom{m}{k} \binom{n}{k} q^{m-k} (1-q)^k p^{k+1} (1-p)^{n-k} \quad (11)$$

$p_m(n)$ describes the blinking probability, n the number of blinking events, $m + 1$ the number of fluorophores, p the probability that a certain fluorophore bleaches after it was in the fluorescent state and q the fraction of undetected fluorophores. This leads to the functions for monomers ($m = 0$), dimers ($m = 1$) and trimers ($m = 2$) (Equation 12, 13, 14).

$$p_0(n) = p(1-p)^n \quad (12)$$

$$p_1(n) = p(1-p)^{n-1} [np(1-q) + q(1-p)] \quad (13)$$

$$p_2(n) = p(1-p)^{n-2} \frac{[n^2 p^2 (1-q)^2 + 2q^2 (1-p)^2 + np(1-q)(4q - p(1+3q))]}{2} \quad (14)$$

Before application, the parameters p and q must be determined. The monomeric fit function $p_0(n)$ is only dependent of the parameter p . The parameter p is determined by imaging and analyzing a known monomer sample, e.g. monomeric mEos2 proteins, on a glass surface. With the knowledge of the parameter p , the parameter q can be obtained by the analysis of a known dimeric sample.

One important aspect is the selection of super-resolved localization clusters. Clusters which show low brightness, too close proximity to other clusters or low circularity in shape, are rejected from analysis (Figure 19) (Krüger et al., 2017a).

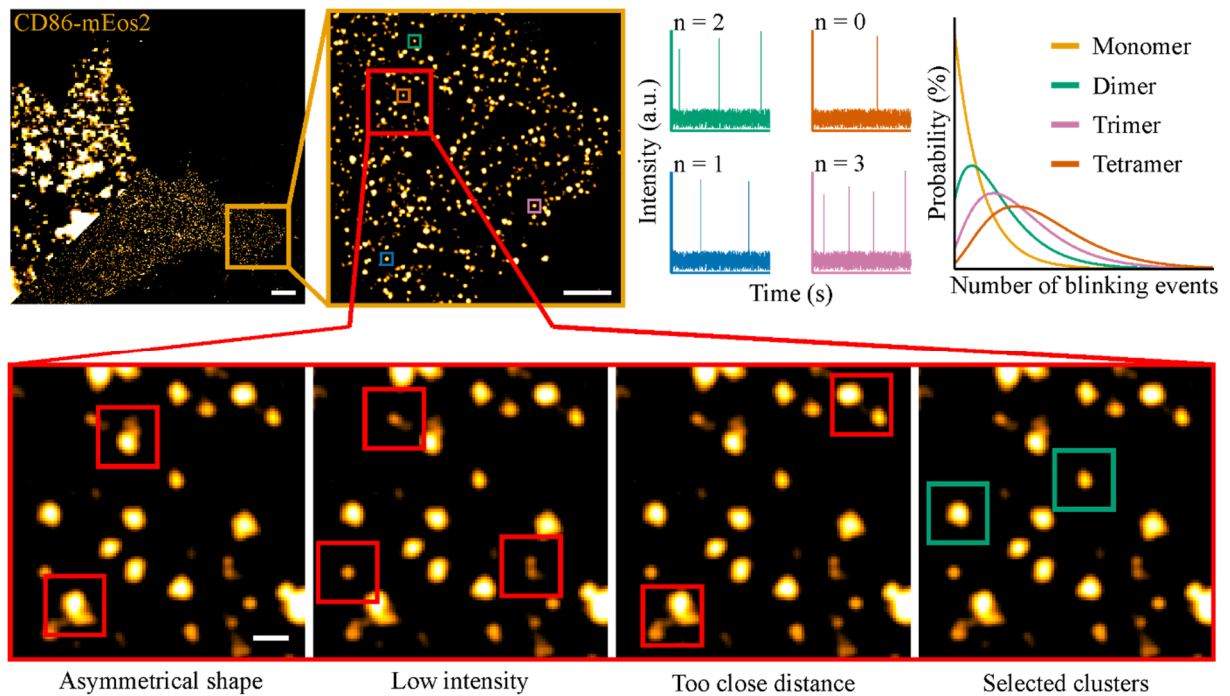


Figure 19: Selection of super-resolved localization clusters for quantitative PALM. *Appropriate clusters must have a round shape, exhibit a minimum intensity and are not allowed to be too close to other clusters. (Scale bars, $2\mu\text{m}$ top left panel, $1\mu\text{m}$ second panel top, 100 nm bottom panel)*

A second quantitative strategy is based on analyzing binding kinetics with DNA-PAINT, called quantitative PAINT (qPAINT) (Jungmann et al., 2016). qPAINT analyzes the frequency of the binding events of the imager strands to the docking strands and compares them with a known standard, allowing the calculation of the oligomeric state of the sample (Jungmann et al., 2016).

MATERIAL AND METHODS

In the following chapter, all material and methods that were used in this thesis are listed and described.

3.1 Cell lines and plasmids

Immortalized TNFR1/2-/- knock-out mouse embryonic fibroblasts (MEFs), the reconstituted stable transfected variant with TNFR1 expressed with mEos2 and two variants of K32A and N66F mutated TNFR1 were provided by Dr. Sjoerd J. L. van Wijk (Frankfurt, Germany). Cells were maintained in Roswell Park Memorial Institute (RPMI) 1640 medium (ThermoFisher Scientific, Germany) with 1 % GlutaMAX (ThermoFisher Scientific, Germany), 10 % fetal bovine serum (FBS) (Capricorn Scientific, Germany), 100 units per ml penicillin (ThermoFisher Scientific, Germany), 100 µg/ml streptomycin (ThermoFisher Scientific, Germany) and 100 µg/ml gentamicin (ThermoFisher Scientific, Germany) at 37 °C with 5 % CO₂.

Plasmids encoding human CD86 and CTLA-4 (both C-terminally fused to mEos2) were created by Joel Beauodin (Heidelberg, Frankfurt). The corresponding cDNA was obtained by Eurofins. mEos2 was fused by the linker sequence encoding GGGGGPVPQWEGFAALLATPVGGAV to the C-terminus of CD86 and CTLA-4 and implemented into the pIRES-puro2 vector. Furthermore, the last 23 amino acids of the CD86-mEos2 and CTLA-4-mEos2 constructs were removed by polymerase chain reaction (PCR) to prevent protein internalization.

3.2 Labeling of TNF α

Recombinant human TNF α was fused to a SNAP-tag (SNAP-F-TNC-TNF α), produced in HEK293 cells and provided by Dr. Juliane Medler and Prof. Dr. Harald Wajant (Würzburg, Germany). Alexa Fluor 647-BG (NEB, Germany) was diluted in dimethyl sulfoxide (DMSO) (Merck, Germany) to a final concentration of 100 µM. 10 µl of a 150 µg/ml SNAP-F-TNC-TNF α solution were incubated with 1 µl of a 1 mM dithiothreitol (DTT) (Merck, Germany) solution for 30 minutes at room temperature. Then 0.8 µl of a 100 µM Alexa Fluor 647-BG stock was added to the solution and incubated for 30 minutes at 37 °C.

3.3 Glass coating and flexiperm constitution

Glass slides (ThermoFisher Scientific, Germany) were washed with isopropanol (VWR, Germany) for 15 minutes in an ultrasonic bath (Elma, Germany), followed by three washing steps with water, and drying with N₂. Slides were cleaned in a plasma cleaner with N₂ (Diener Electronic, Germany) for 15 minutes and coated with 0.8 mg/ml poly(L-lysine)-poly(ethylene glycol) (PLL (Merck, Germany) - PEG (Rapp Polymere, Germany)-RGD (provided by the group of Prof. Dr. Robert Tampé, Frankfurt, Germany) for 90 minutes. Subsequently, slides were washed once with water and dried with N₂. 8-well silicon flexiperm chambers (Greiner, Germany) were mounted on the coated glass slides.

3.4 Sample preparation for quantitative PALM of TNFR1

$1.5 \cdot 10^4$ reconstituted TNFR1/2-/- + TNFR1-mEos2 MEFs (or its variants K32A or N66F) were seeded into the 8-well flexiperm in serum starve medium (RPMI 1640, 1 % GlutaMAX, 100 units per ml penicillin, 100 µg/ml streptomycin and 100 µg/ml gentamicin). For TNFα treatment, 300 µl of 100 ng/ml TNFα-SNAP-A647 were added to the cells and incubated for 30 minutes. For the zafirlukast treatment, cells were incubated for 30 minutes with 100 µM zafirlukast (provided by Dr. Sjoerd J. L. van Wijk, Frankfurt Germany) in serum starve medium with 1 % DMSO to avoid precipitation. For zafirlukast and TNFα treatment, cells were first treated with zafirlukast as described above. Then 1 µl of the TNFα-SNAP-A647 construct was added to a final concentration of 100 ng/ml that incubated for another 30 minutes. For apoptosis induction, cells were first incubated for 30 minutes with 10 µM BV6. Then 1 µl of TNFα-SNAP-A647 was added to a final concentration of 100 ng/ml and incubated for 30 minutes. Necroptosis induction was performed by incubating cells for 30 minutes with 10 µM BV6 and 20 µM zVAD-fmk followed by adding 1 µl of TNFα-SNAP-A647 to a final concentration of 100 ng/ml, which incubated for 30 more minutes. Incubation was conducted at either 4 °C or 37 °C. Finally, cells were washed three times with 0.4 M sucrose (Merck, Germany) in sterile filtered phosphate-buffered saline (PBS) (Gibco (LOT: 1979058), Germany) and fixed (chapter 3.5). Cells were imaged in sterile filtered PBS. Sterile filtration mentioned in this thesis was performed with Filtropur S 0.2 µm pore size filters (Sarstedt, Germany).

3.5 Cell fixation

Chemical fixation of cells was performed in 4 % methanol-free formaldehyde (FA) (ThermoFisher Scientific, Germany), 0.2 % glutaraldehyde (GA) (Merck, Germany) and 400 mM sucrose in sterile filtered PBS for 15 minutes at room temperature. Afterwards, cells were washed three times with sterile filtered PBS.

3.6 Western blot

After washing twice with ice-cold PBS, cells were lysed in 30 mM tris(hydroxymethyl)aminomethane (Tris)-HCl (pH 7.4), 150 mM NaCl, 1 % v/v Triton X-100 and 10 % (v/v) glycerol lysis buffer in combination with complete protease inhibitors (Roche, Germany). Acquired lysates were incubated on ice for 20 minutes. Cell lysates were centrifuged at 13.000 r.p.m. at 4 °C for 20 minutes and boiled in 2 · Laemmli sample buffer with 4 % (w/v) SDS, 20 % (v/v) glycerol, 120 mM Tris-HCl pH 6.8 and 0.02 % bromophenolblue. The solution was resolved using sodium dodecyl sulfate-polyacrylamide gel electrophoresis (SDS-PAGE) and immunoblotted. A chemiluminescence assay with anti-mouse IgG or goat anti-Rabbit IgG labeled with horseradish peroxidase (HRP) (Santa Cruz, USA) was used. Western blot experiments were performed by Dr. Sjoerd J. L. van Wijk (Frankfurt, Germany).

3.7 NF- κ B activation

To investigate NF- κ B activation, $7.5 \cdot 10^5$ cells were seeded in six well plates (Greiner, Germany) for 24 h in RPMI 1640 containing FBS and antibiotics. Afterwards, cells were serum starved in RPMI 1640 devoid of FBS for three hours and incubated with 100 ng/ml TNF α for the indicated time points. The protocol was performed at an incubation temperature of 37 °C. After ligand stimulation, cells were washed and used for further experiments. NF- κ B activation experiments were performed by Dr. Sjoerd J. L. van Wijk (Frankfurt, Germany).

3.8 Immunofluorescence

After the induction of NF- κ B, cells were fixed at room temperature with 4 % paraformaldehyde (Santa Cruz, Germany) in PBS for 20 minutes and washed three times with PBS. Cells were permeabilized with PBS and 0.2 % Triton-X 100 for five minutes at room temperature. After three washing steps with PBS, cells were blocked with 5 % bovine serum albumin (BSA, Roth, Germany) in PBS overnight at 4 °C. Cells were incubated with anti-p65 antibody, which was diluted for four hours at room temperature in 5 % BSA in PBS. Afterwards, cells were washed three times with 0.1 % Tween-20 in PBS and incubated with a corresponding secondary antibody labeled with Alexa Fluor 647 in 5 % BSA/PBS. Then, cells were washed again three times with 5 % BSA/PBS. Nuclei were stained using 4',6-diamidino-2-phenylindole (DAPI) (Molecular Probes, Germany). Fluorescence images were acquired using a Leica SP8 confocal laser-scanning microscope (Leica, Germany). Immunofluorescence experiments were performed by Dr. Sjoerd J. L. van Wijk (Frankfurt, Germany).

3.9 Induction of cell death

Cell lines indicated at the corresponding conditions were seeded with a density of $0.6 \cdot 10^4$ cells per well in sterile 96-well plates (Greiner, Germany) in RPMI 1640 with FBS for 24 hours. For induction of apoptosis, cells were treated with 10 μ M BV6 alone or in combination with 20 μ M zVAD-fmk for necroptosis induction for one hour at 37 °C. Afterwards cells were stimulated with 10 ng/ml TNF α for

24 hours at 37 °C. The fraction of cell death was determined by fluorescence-based quantification of propidium iodide (PI) uptake using Hoechst 33342 and PI double staining (Sigma, Germany). Cell death determination was performed by Dr. Sjoerd J. L. van Wijk (Frankfurt, Germany).

3.10 Fluorescence-activated cell sorting

For the investigation of the expression levels of TNFR1 in the indicated cell lines, $5 \cdot 10^5$ MEFs were washed two times with PBS before the incubation with α TNFR1-Phycoerythrin (PE) (#FAB225P; R&D, Minneapolis, USA) and corresponding mIgG1-PE isotope control (#ICoo2P; R&D, Minneapolis, USA) for 30 minutes at 4 °C. Afterwards, cells were washed twice with PBS to remove free antibodies. Fluorescence-activated cell sorting (FACS) analysis was performed following standard procedures with FACS-Calibur (BD Bioscience, Heidelberg, Germany). FACS experiments were performed by Dr. Juliane Medler (Würzburg, Germany).

3.11 Luciferase assay

To investigate the binding affinity huTNF-F-TNC-gaussia princeps luciferase (GpL) to TNFR1, $1.4 \cdot 10^5$ of the indicated cell lines were measured with increasing concentrations of the TNF-GpL-fusion protein by cellular binding studies. Numbers for unspecific binding were obtained by blocking with 20 μ g/ml recombinant human TNF α for HeLa cells and TNFR1-deficient MEF-transfectants for MEF cells. After an incubation time of 90 minutes at 37 °C, cells were washed three times with ice cold PBS to remove free TNF-GpL-fusion protein. Next, cells were resuspended in 50 μ l RPMI 1640 with 0.5 % FCS and transposed into 96-well plates. In combination with the gaussia luciferase kit (New England Biolabs GmbH, Germany) and the LUmo Luminometer (Anthos Labtec Instruments, Austria) GpL-activity was determined. Numbers for specific binding were obtained by subtracting the unspecific binding from total binding. To obtain the cellular binding affinity of the SNAP-F-TNC-TNF α to TNFR1 homologous competitive experiments were performed. Therefore, several aliquots of $4 \cdot 10^5$ HeLa cells were incubated at 37 °C with a constant concentration of 2.5 ng/ml huTNF-F-TNC-GpL and the indicated increasing concentrations of SNAP-F-TNC-TNF α . 90 minutes after incubation, cells were washed three times with ice cold PBS and measured as described above. These experiments were performed by Dr. Juliane Medler (Würzburg, Germany). Resulting binding curves were analyzed using the Hill function (Equation 15).

$$f(x) = Int(0) + (Int(sat) - Int(0)) \frac{c^n}{(K_D^n + c^n)} \quad (15)$$

$Int(0)$ and $Int(sat)$ describe the lowest and largest intensity value, c the concentration of the indicated TNF α , n is the number of cooperative sites and K_D the dissociation constant.

To obtain the binding sites of the huTNF-F-TNF-GpL per cell (N_{BS}) and thus the mean number of TNFR1 per indicated cell line, the luciferase activity of a known abundance of huTNF-F-TNC-GpL was

analyzed to obtain the luciferase activity per GpL-domain ($A_{GPL-domain}$). The maximal specific binding value (B_{max}) of the respective binding study was determined using GraphPad Prism 5 (one specific binding fit). In combination with the number of cells (CN), the number of TNFR1 per cell was calculated (Equation 16).

$$N_{BS} = \frac{(B_{max} \cdot A_{GPL-domain})}{CN} \quad (16)$$

Dr. Juliane Medler (Würzburg, Germany) performed experiments for the determination of the mean number of TNFR1 per cell.

3.12 Determination of the number of TNFR1 per cell by light microscopy

The size of the surfaces of the cells were obtained from the brightfield images by Fiji. As in the brightfield images only the bottom side of the cell was illustrated, the surface of the cell was approximated to be twice the size of the bottom side. The number of TNFR1 clusters per μm^2 obtained by DBSCAN analysis in combination with the determined surface of the cell was used to calculate the number of TNFR1 clusters per cell.

3.13 Transfection

$20 \cdot 10^4$ MEF^{-/-} cells were seeded into a six-well chamber (Greiner, Germany) in 3 ml RPMI 1640 medium with 1 % GlutaMAX, 10 % fetal bovine serum (FBS), 100 units per ml penicillin, 100 $\mu\text{g}/\text{ml}$ streptomycin and 100 $\mu\text{g}/\text{ml}$ gentamicin and incubated for 24 hours at 37 °C with 5 % CO₂. After incubation, the transfection was initiated. 260 μl Optimem (ThermoFisher Scientific, Germany) and 15.6 μl Lipofectamine 3000 Reagent (ThermoFisher Scientific, Germany) were added and vortexed. 250 μl Optimem, 5 μg of either the CD86- or CTLA4- tagged with mEos2 DNA and 10 μl P3000 (ThermoFisher Scientific, Germany), were mixed by pipetting. 250 μl of the Lipofectamine 3000 mixture were added to the P3000 mixture, which was incubated at room temperature for 12 minutes. 250 μl of this solution was pipetted into each chamber and incubated for 24 hours. After incubation, cells were scraped and seeded in the self-built eight-well flexiperm mounted on a cleaned and PLL-PEG-RGD coated glass slide (chapter 3.3). Cells were fixed as described in chapter 3.5.

3.14 Quantification of pfEMP1

Fresh HbAA and HbAS erythrocytes were cultured in RPMI 1640 medium with 5 % GlutaMAX and 5 % human serum. The *Plasmodium falciparum* strain FCR3 and the mutant G-6 were maintained like described in Trager and Jensen *et al.* (Trager and Jensen, 1976). Cells were cultured at a hematocrit of 4 %, parasitemia of less than 5 % at 37 °C at 5 % O₂, 3 % CO₂ and 96 % humidity. For the G-6 mutant, two mEos2 protein copies were tagged to the VAR2CSA protein of the *Plasmodium falciparum* strain FCR3 using homologous recombination with CRISPR/Cas9-mediated genome editing (Deveau *et al.*, 2010; Ishino *et al.*, 1987).

8-well LabTeks were coated with 0.1 mg/ml concanavalin A for 60 minutes, washed with water and PBS. Purified infected erythrocytes were seeded for 10 minutes, washed with PBS and fixed with 4 % paraformaldehyde (PFA) in PBS. Fixation buffer was removed and chambers were washed with PBS. Quantitative PALM experiments were performed in sterile filtered PBS. Cell culture and sample preparation was performed by Dr. Cecilia Sanchez (Heidelberg, Germany).

3.15 Establishment of molecular quantification with *d*STORM

A DNA double strand with a length of 21 bp labeled with biotin (3') and Alexa Fluor 647 (5') was obtained from GATTAquant (Braunschweig, Germany). Furthermore, a two-point trimeric Alexa Fluor 647 DNA origami system was purchased from GATTAquant (Gatta-STORM Nanoruler). Three Alexa Fluor 647 labeled staple strands (5', through a TTT linker) were placed on two ends of a DNA origami system with a distance of 120 nm (Figure 20). The fluorophores on each end have a distance between four to eight nanometers among each other.

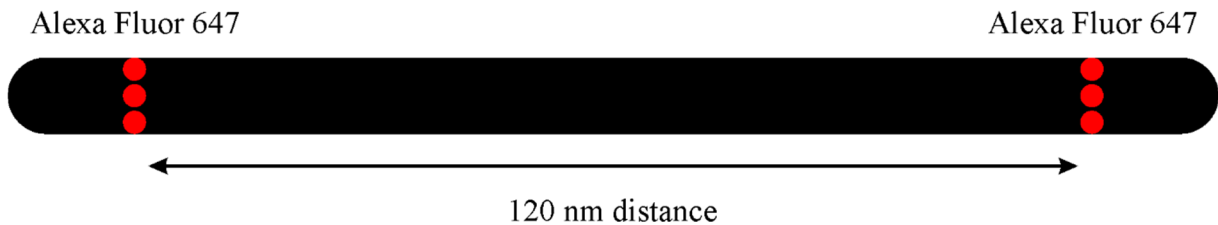


Figure 20: Scheme of the GATTAquant DNA origami Gatta-STORM Nanoruler. *Three Alexa Fluor 647 labeled staple strands were placed on two ends of a DNA origami Gatta-STORM nanoruler with a distance of 120 nm.*

3.16 Sample preparation for quantitative *d*STORM with Alexa Fluor 647

Glass slides and flexiperm assembly was performed as described in chapter 3.3. Instead of the PLL-PEG-RGD incubation, 200 μ l of 0.05 mg/ml bovine serum albumin- (BSA) biotin (Merck, Germany) in PBS (sterile filtered) with 5 % BSA (Merck, Germany) was added to the chambers. After one hour of incubation, chambers were washed three times with sterile filtered PBS, followed by incubation with 0.05 mg/ml streptavidin (Merck, Germany) in sterile filtered PBS for 30 minutes. Either 200 pM of the biotinylated DNA strand labeled with Alexa Fluor 647 or the two-point Alexa Fluor 647 DNA origami system were incubated for five minutes in the presence of 10 mM $MgCl_2$ (Merck, Germany). After washing three times with sterile filtered PBS with 10 mM $MgCl_2$, an imaging buffer containing 60 mM Tris (pH = 8) (Merck, Germany), 10 mM $MgCl_2$ (Merck, Germany), 100 mM MEA (Merck, Germany), 10 % w/v glucose (Merck, Germany), 50 units/ml glucose oxidase (Merck, Germany) and 5000 units/ml catalase (Merck, Germany) was added for *d*STORM measurements.

3.17 SMLM microscope

SMLM experiments were performed on a home-built setup (Figure 21). The platform consists of five laser lines including 641 nm (iBEAM smart (Toptica, Germany) or LBX-638-180 (Oxxius, France)),

MATERIAL AND METHODS

568 nm (Sapphire 568 LP, Coherent, Germany), 532 nm (DPPS-532-NL300, Eksma Optics) and 488 nm (Sapphire LP, Coherent). Laser lines are aligned through dichroic mirrors Laser-MUX 561-594R, LaserMUX 514-543R, LaserMUX 473-491R, 1064R and LaserMUX 427-25 (AHF, Germany). An acousto-optic tunable filter (AOTF) (AAOptics, USA) is used for filtering and intensity adjustment. The fifth laser, a 405 nm laser line (CUBE 405-100C (Coherent, Germany) or LBX-405-50-CSB-PP (Oxxius, France)), passes an ND filter (Thorlabs, Germany) and is aligned to the same optical axes as the laser lines described above. All laser lines are expanded and focused to the back-focal plane of a 100 × oil immersion objective (PLAPO 100 × TIRFM, NA ≥ 1.45 (Olympus, Germany)) by a telescope with a suitable lens-system ($f' = -20$ mm, $\varnothing = 22.4$ mm, and $f' = -250$ mm, $\varnothing = 50.8$ mm (Qioptiq, Germany)). An adjustable mirror in front of the microscope guides light into the objective for TIRF, HILO or wide-field mode. The microscope is equipped with a nosepiece, which minimizes x, y and z drift of the sample. Fluorescence light emitted from the sample passes a dichroic mirror (HC Quad 410/504/582/669 (AHF, Germany)), is directed into an optosplit (Optosplit II (Cairn Research, United Kingdom)), split by its wavelength by dichroic mirrors (650 DCXR or 560 DCXR (AHF, Germany)) and filtered by adequate filters (BrightLine HC 590/20 or ET 700/75 (AHF, Germany)). An EMCCD camera (iXon3, or iXon Ultra (X-10971) (Andor, Ireland)) collects the fluorescence signal.

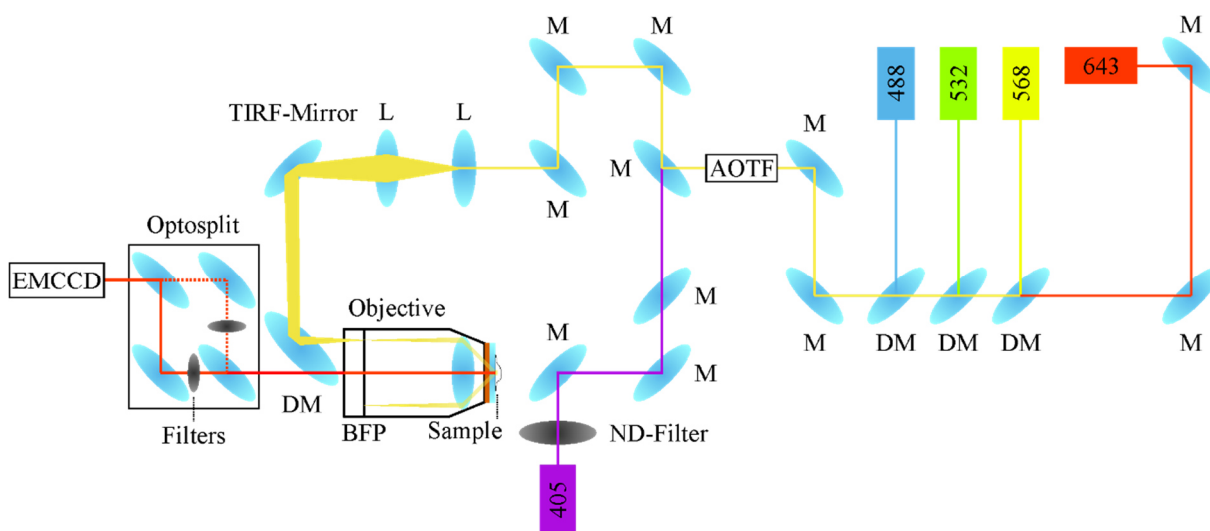


Figure 21: Scheme of the SMLM microscope. Laser lines (643, 568, 532, 488 nm) are aligned and directed to an AOTF by mirrors (M) and dichroic mirrors (DM). A 405 nm laser is directed through a ND-filter and is aligned with the other laser lines behind the AOTF. All laser lines are expanded by a telescope and focused to the back focal plane (BFP) of an objective. A mirror enables to switch between wide-field and TIRF illumination of a sample. Fluorescence emitted by the sample is collected by the same objective, passes a dichroic mirror, directed through an optosplit with appropriate filters and detected by an EMCCD camera.

3.18 SMLM imaging

All SMLM measurements were performed in TIRF mode. PALM imaging of TNFR1 and pfEMP1 was conducted in sterile filtered PBS. For the quantification of TNFR1, samples were excited with 0.21 kW/cm² of 568 nm laser light after photoconverting with increasing UV intensity over time (0 – 8.0 mW/cm²). TNF α labeled with Alexa Fluor 647 was excited with 4.6 W/cm². For the quantification of pfEMP1 an excitation intensity of 0.26 kW/cm² of the 568 nm laser in combination with 0-8.0 mW/cm² UV light intensity were used. SMLM videos between 10000 to 20000 frames using an electron multiplying gain of 200, a pre-amplifier gain of 1 and an integration time of 100 ms were recorded.

In *d*STORM experiments, Alexa Fluor 647 was excited with 643 nm laser light (1 kW/cm²) and reactivated with UV light (0-0.06 W/cm²). Samples were imaged in an imaging buffer as described in chapter 3.16. The EMCCD collected signal with an integration time of 30 ms, a preamplifier gain of 1 and an electron multiplying gain of 200. SMLM videos between 40000 and 100000 frames using an integration time of 30 ms, a preamplifier gain of 1 and an electron multiplying gain of 200 until no more fluorescent events were detected were recorded.

3.19 Quantitative SMLM data analysis

For the analysis of TNFR1 and pfEMP1, rapidSTORM (Wolter et al., 2010), an open source software, was used to determine the positions of single fluorophores and to generate super-resolved images, which were post-processed with the LocAlization Microscopy Analyzer (LAMA) (Malkusch and Heilemann, 2016). For rapidSTORM processing, a pixel size of 157 nm, a PSF FWHM of 360 nm and an intensity threshold of 63 photons was used. Blinking events were localized with a localization precision of < 30 nm (determined by nearest neighbor (NeNA) and Mortensen (Endesfelder et al., 2014; Mortensen et al., 2010)). Using the Kalman filtering tool of rapidSTORM, localizations that occurred in consecutive frames were combined into a single localization. The combined localization list generated by rapidSTORM was used to reconstruct the super-resolved image with LAMA where each localization is represented as one gray value. For the analysis of the oligomeric state of TNFR1 and pfEMP1, clusters were chosen as described in chapter 2.9, where the final blinking events were obtained from the image generated by LAMA. For TNFR1 at least 500 protein clusters from at least ten cells from three independent experiments were analyzed for each condition. For the quantification of VAR2CSA, in total 771 clusters from 130 cells were analyzed from three independent experiments for the HbAA condition, whereas in total 638 fluorescence clusters from 76 cells were analyzed from two independent conditions for the HbAS condition. To obtain the p and q values, MEF^{-/-} cells transfected with CD86 or CTLA-4 with mEos2 were imaged and analyzed. The frequency of blinking events was counted and fitted with equation 11 using a Python script, provided by Dr. Sebastian Malkusch (Frankfurt, Germany), or with the origin software (OriginLab, USA). The bayesian information criterion (BIC) and the log likelihood was calculated using a second Python script, provided by Dr. Sebastian Malkusch (Frankfurt, Germany).

MATERIAL AND METHODS

SMLM videos recorded with Alexa Fluor 647, were analyzed with rapidSTORM and LAMA as described above, with the difference that a threshold of 278 photons and a localization precision of < 14 nm (determined by NeNA (Endesfelder et al., 2014) and Mortensen (Mortensen et al., 2010)) was applied. For the monomeric and the trimeric sample, at least 500 clusters from three independent experiments were analyzed.

Cluster analysis was performed with the DBSCAN algorithm implemented in LAMA. For PALM measurements cluster densities were determined with a radius of $\varepsilon = 30$ nm and a minimum localization value of $N_{pts} = 2$ (average blinking of mEos2 is about 2.3) (determined in chapter 4.1.2).

RESULTS AND DISCUSSION

In this thesis, three projects are presented. First, the oligomeric state of TNFR1 was determined in cells using super-resolution imaging. Second, a method for molecular quantification with organic fluorophores was developed. Third, the oligomeric state of the protein VAR2CSA, which is found on the plasma membrane of erythrocytes infected with *Plasmodium falciparum*, was determined.

4.1 Quantifying the oligomeric state of TNFR1 using PALM

The knowledge of the spatial arrangement and the oligomeric state of TNFR1 is essential for investigations concerning treatment of multiple diseases, as clustering of TNFR1 promotes downstream signaling leading to the activation of NF- κ B (Wajant and Scheurich, 2011) or cell death (Dempsey et al., 2003; Vanamee and Faustman, 2018). Overall, the oligomeric state of TNFR1 in ligand-free and ligand-bound states is under discussion as the ligand-free condition was reported to be monomeric and dimeric (Boschert et al., 2010; Naismith et al., 1995) or monomeric and trimeric (Chan, 2000; Chan, 2007). Thus, in the following chapter a stable reconstituted TNFR1/2^{-/-} + TNFR1-mEos2 MEF cell line and the quantification of TNFR1 in the absence and presence of its ligand TNF α is described. Furthermore, the oligomeric state of TNFR1 containing the point mutations K32A and N66F is shown to investigate the influence of the CRD1 and CRD2 in the oligomerization process. In addition, the oligomeric state of TNFR1 after treatment with zafirlukast and the induction of apoptosis and necroptosis is illustrated to show whether an inhibition or a modification in the signaling cascade changes the oligomeric state. Finally, the comparison of the oligomeric state of TNFR1 in relation to the temperature treatment with 4 °C and 37 °C is discussed.

4.1.1 Reconstitution of TNFR1/2^{-/-} + TNFR1-mEos2 mouse embryo fibroblast

For the quantification of TNFR1 with quantitative photoactivated localization microscopy (chapter 2.9), a stable TNFR1/2^{-/-} double knock out MEF cell line was generated expressing TNFR1 tagged with the photoactivatable fluorescent protein mEos2. Full length human TNFR1 was stably lentivirally transduced into the MEF^{-/-} cell line, where mEos2 was fused to the C-terminus of TNFR1 (TNFR1/2^{-/-} + TNFR1-mEos2). Since TNFR2 is known to bind TNF α and to modulate TNFR1, TNFR2 was also knocked out (Boschert et al., 2010; Santee and Owen-Schaub, 1996). The absence of TNFR2 thus ensures that the unmodulated oligomeric state of TNFR1 is determined. The generation of the stable TNFR1/2^{-/-} + TNFR1-mEos2 MEF cell line was performed and provided by Dr. Sjoerd J. L. van Wijk (Frankfurt, Germany).

RESULTS AND DISCUSSION

Western blot experiments revealed the stable expression of TNFR1-mEos2. Some unspecific background bands were shown, which is addressed by the manufacturer who stated that the TNFR1 rabbit antibody might recognize a 30 kDa splice isoform of TNFR1 in some cell lines (Figure 22A). Upon stimulation with TNF α , the activation of the NF- κ B signaling cascade was detected via the phosphorylation of nuclear factor of kappa light polypeptide gene enhancer in B-cells inhibitor alpha (I κ B α), revealing comparable levels of I κ B α phosphorylation observed in wild-type (wt) MEFs (Figure 22B). Additionally, the NF- κ B signaling of TNFR1/2-/- MEF and TNFR1/2-/- transduced with mEos2 was measured yielding no detectable phospho-I κ B α signal. The functional NF- κ B signaling cascade was confirmed by immunofluorescence of p65/RelA in the reconstituted TNFR1/2-/- + TNFR1-mEos2- and wt MEFs with p65 entering the nucleus (Figure 22C). The NF- κ B activation level induced by TNF α in the reconstituted TNFR1/2-/- + TNFR1-mEos2 MEF cells was comparable to the wt MEF cells. Thus, the genetic change of the MEF cell line was not interfering with the signaling cascade of TNFR1 despite fusing the C-terminal located death domain to mEos2. Furthermore, the increased expression level of TNFR1 compared to HeLa cells had no effect on autoactivation in the absence of TNF α (Figure 22B, t = 0). Thus, a stable cell line expressing TNFR1-mEos2 at near-endogenous level was generated, showing successful activation of NF- κ B after stimulation with TNF α . In addition to the short-term NF- κ B signaling response, experiments were performed to investigate whether long-term signaling cascades such as apoptosis and necroptosis can still be induced. For this purpose, the reconstituted TNFR1/2-/- + TNFR1-mEos2 MEFs were stimulated with TNF α and BV6 for apoptosis induction (El-Mesery et al., 2016) and TNF α , BV6 and zVAD-fmk for necroptosis induction (van Noorden, 2001) and the proportion of PI-positive cells were determined (Figure 22D). Consistent to the wt MEFs, characterizing the long-term signaling cascade apoptosis and necroptosis revealed a fully functional cell death signaling cascade. As expected, the negative controls TNFR1/2-/- -, TNFR1/2-/- empty vector (ev)- and the TNFR1/2-/- + mEos2- MEFs showed no proportion of PI positive cells (Figure 22D). The difference between the wt- and the reconstituted TNFR1/2-/- + TNFR1-mEos2 MEFs with respect to apoptosis and necroptosis detection levels might be explained by the absence of TNFR2, which potentially effects the cell death signaling cascade (Boschert et al., 2010). Notwithstanding, a successful reconstitution of TNFR1/2-/- + TNFR1-mEos2 MEFs was confirmed.

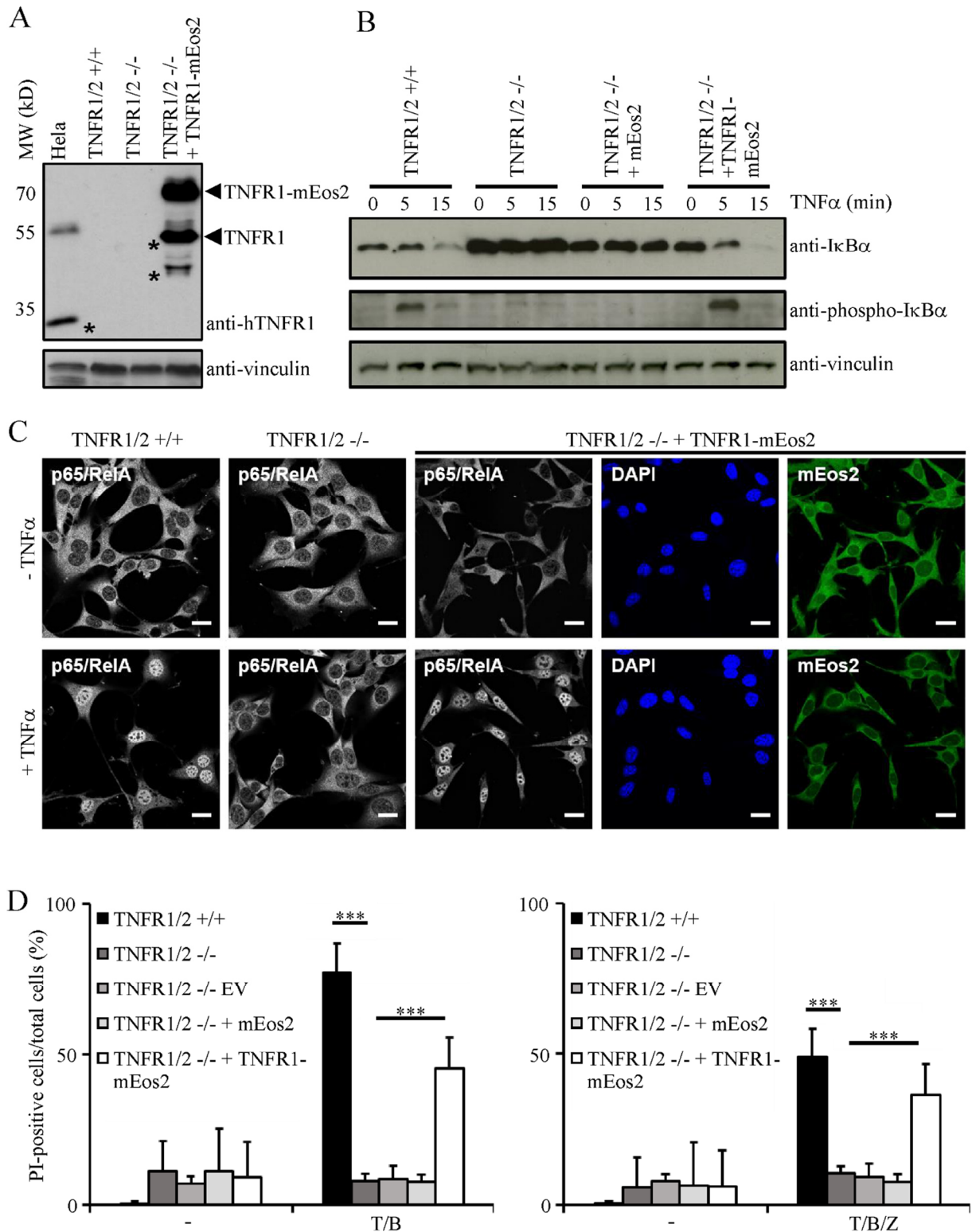


Figure 22: Reconstitution of TNFR1/2-/- + TNFR1-mEos2 MEFs. (A) Western blot shows the expression level of TNFR1 in reconstituted TNFR1/2-/- + TNFR1-mEos2-, TNFR1/2 +/+ and TNFR1/2 -/- MEFs compared to HeLa cells (* non-specific bands). (B) Phosphorylation and I κ B α level in indicated cell lines is shown by western blot analysis. Anti-vinculin presents the loading control. (C) Immunofluorescence reveals nuclear translocation of p65/RelA in the indicated cells after the treatment of TNF α . DAPI was used for DNA staining. The images on the right show the fluorescence signal of

mEos2 fused to *TNFR1* (scale bars, 10 μm). (D) Illustration of the fraction of PI-positive cells compared to total cell numbers under conditions inducing apoptosis (left) and necroptosis (right) of indicated cell lines, *** $p < 0.001$ ($T = \text{TNF}\alpha$, $B = \text{BV6}$, $Z = \text{zVAD-fmk}$). Experiments presented in this figure were performed by Dr. Sjoerd J. L. van Wijk (Frankfurt, Germany).

4.1.2 Investigating the blinking properties of mEos2 in MEF cells

Quantitative PALM requires the determination of characteristic p and q values in the respective cells to correct for over- and undercounting (Hummer et al., 2016). The monomeric standard CD86 fused to mEos2 was transfected into MEF cells and revealed a p value of 0.282, implying that about 30 % of the mEos2 proteins bleach after they were in the fluorescent state (Figure 23A). This is consistent with previous studies, where for mEos2 p values of 0.289 in HeLa cells (Hummer et al., 2016) and 0.320 in HEK 293 cells (Krüger et al., 2017b) were determined. This indicates that the chromophore of mEos2 is protected by its β -barrel structure, leading to similar blinking properties of mEos2.

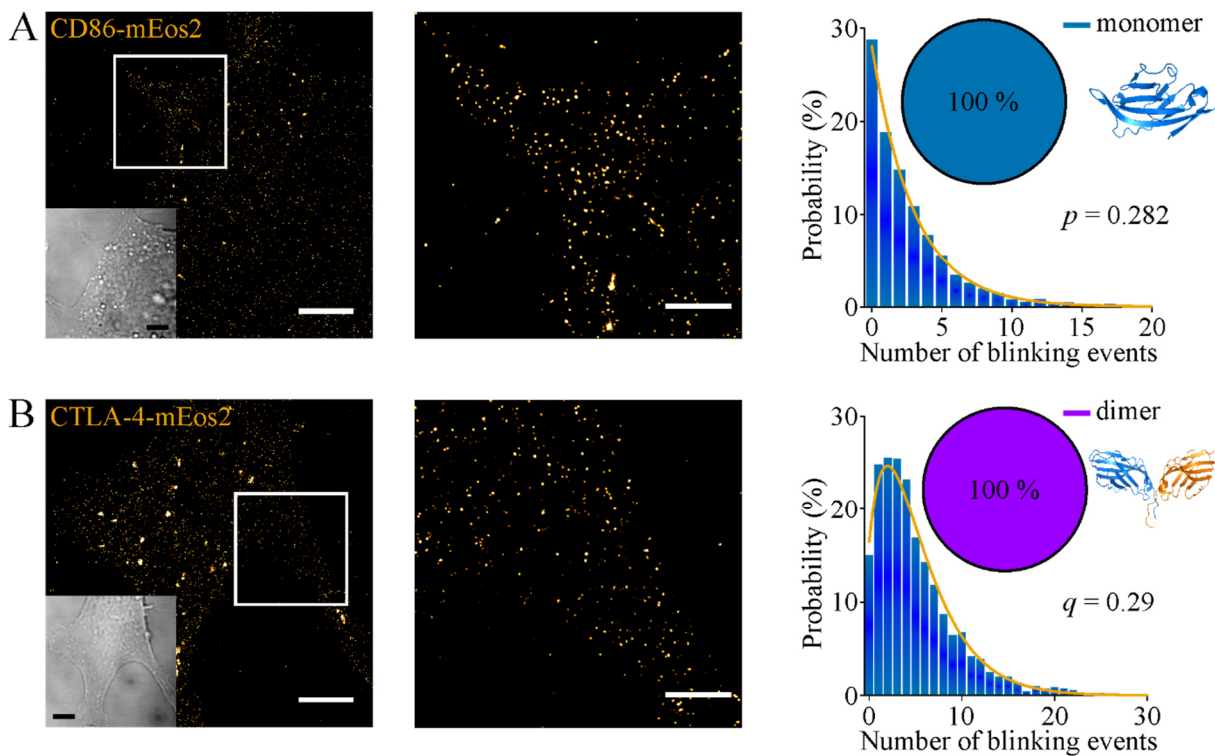


Figure 23: Cellular calibration standards for qPALM. (A) PALM and brightfield image of a MEF cell expressing CD86-mEos2 (left panel) with magnified region (middle panel). Right panel shows the blinking distribution with fit (equation 12, yellow curve). (B) PALM image of a MEF cell expressing CTLA-4 expressed with mEos2. Right panel shows the blinking distribution with fit (equation 13, yellow curve). Both experiments contain the data of ten cells from three independent experiments. (Scale bars, 5 μm PALM and brightfield images (left panels), 1 μm PALM images (middle panels)) (PDB 1NCN, 3OSK).

The parameter q was determined by transfection of the dimeric standard CTLA-4 fused to mEos2. Analysis revealed a q value of 0.29, demonstrating that about 30 % of all mEos2 proteins remain undetected (Figure 23B). This is also in agreement with the values of 0.295 in HeLa cells (Hummer et al., 2016) and 0.29 in HEK 293 cells (Krüger et al., 2017b). These values were used for further quantitative PALM experiments in MEF cells.

4.1.3 qPALM analysis of TNFR1 in TNF α -untreated cells

In order to determine the oligomeric state of TNF α -untreated TNFR1, qPALM experiments with serum starved TNFR1/2-/- + TNFR1-mEos2 MEFs were performed. Clearly separated, super-resolved TNFR1-mEos2 clusters were visualized and selected to obtain the number of blinking event distribution. The Bayesian information criterion (BIC) und log likelihood values were calculated for all possible fitting models, including monomeric, dimeric and trimeric distributions (resulting in seven different models: monomer, dimer, trimer, monomer/dimer, monomer/trimer, dimer/trimer, monomer/dimer/trimer). Results were sorted by their BIC values (Supplementary Table 1) and compared with the log likelihood values. According to Hummer *et al.* in 2016, an increase of the log likelihood value by $\frac{\ln(x)}{2}$ (x = data points) must be given to allow a model with more free fit parameters (Hummer et al., 2016). Considering BIC and log likelihood values for TNF α -untreated cells, a distribution of 66 ± 4 % monomers and 34 ± 4 % dimers was predicted to be the model with the largest probability describing the number of blinking event distribution (Figure 24, Supplementary Table 1, Supplementary Table 23).

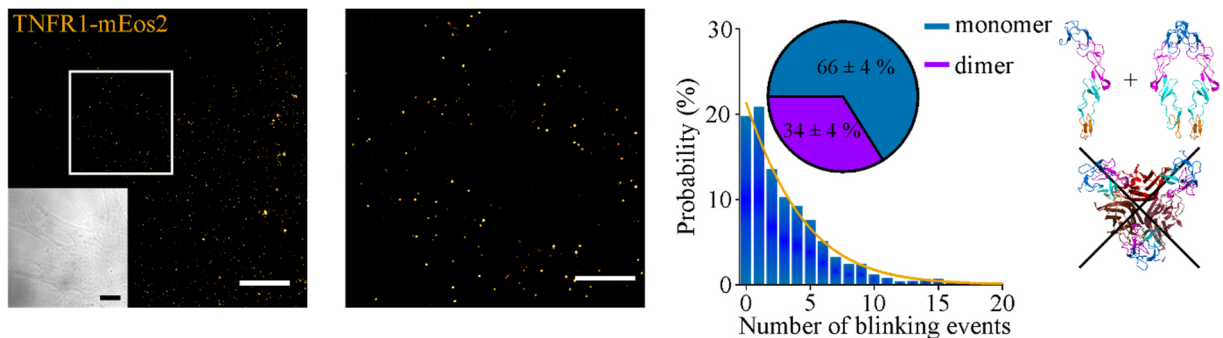


Figure 24: The oligomeric state of TNF α -untreated TNFR1-mEos2 at 4 °C. PALM image of a representative MEF cell expressing TNFR1-mEos2 (left panel) with a zoomed region (middle panel) without the incubation of TNF α . Analysis reveals an oligomeric state of 66 ± 4 % monomers, 34 ± 4 % dimers and no fraction of trimers (equation 11, yellow curve, right panel). Experiments contain the data of ten cells from three independent experiments. (Scale bars, 5 μ m PALM and brightfield image (left panel), 1 μ m PALM image (middle panel)) (PDB 1NCF, 1TNF).

4.1.4 Analyzing TNF α -treated TNFR1 in cells with qPALM

To analyze the oligomeric state of TNF α -treated TNFR1, first the ligand SNAP-Flag-TNC-TNF α was examined for its binding affinity. Therefore, this construct was characterized by luciferase assay to have a binding constant of 6 ± 3 ng/ml for HeLa cells (Figure 25A), which is in a comparable range to fully functional and established huTNF-F-TNC-GpL showing an affinity of 12 ± 5 ng/ml (Figure 25B).

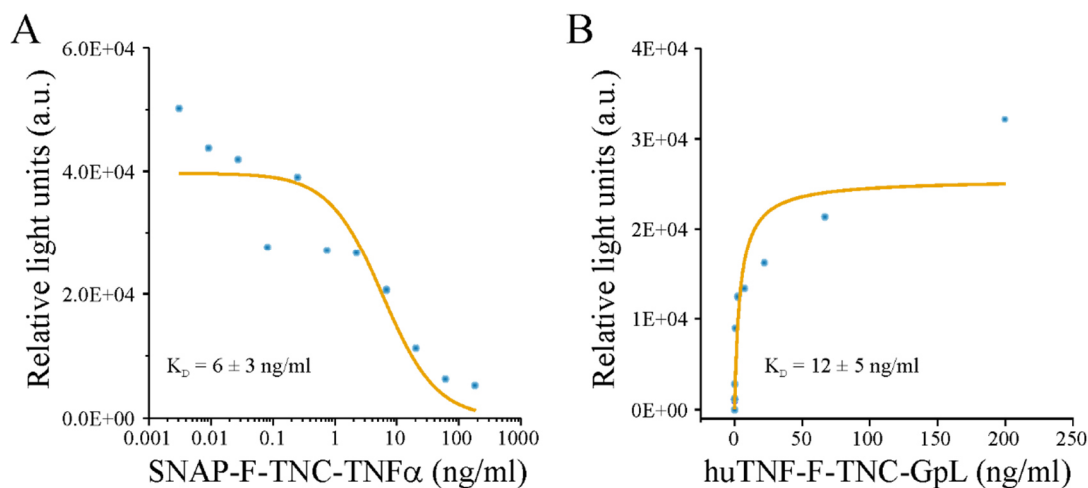


Figure 25: Determination of K_D -values of SNAP-F-TNC-TNF α and huTNF-F-TNC-GpL. (A) Competitive binding curve by titrating SNAP-Flag-TNC-TNF α versus a fixed concentration of huTNF-F-TNC-GpL (2.5 ng/ml) in HeLa cells, revealing a K_D value of 6 ± 3 ng/ml. (B) Binding assay shows a K_D value of 12 ± 5 ng/ml for huTNF-F-TNC-GpL. Yellow curves illustrate the respective fits (functions see chapter 3.11). Experiments presented in this figure were performed by Dr. Juliane Medler (Würzburg, Germany).

The SNAP-Flag-TNC-TNF α was labeled with Alexa Fluor 647 (TNF α -SNAP-A647) (chapter 3.2) and 100 ng/ml were added for 30 minutes to the TNFR1/2-/- +TNFR1-mEos2 MEFs at 4 °C to prevent internalization (Tomoda et al., 1989). Alexa Fluor 647 and mEos2 were imaged consecutively and illustrated (Figure 26). TNFR1-mEos2 cluster showing colocalization with TNF α -SNAP-A647 (ligand-bound) were selected to obtain the number of blinking event distribution (Figure 26, yellow circles). For analysis, BIC and log likelihood analysis were performed with models comprising monomers until nonamers (leading to 511 different models: nine models for single components, 36 for two components, 84 for three components, 126 for four components, 126 for five components, 83 for six components, 35 for seven components, nine for eight components and one for nine components). The model with the largest probability was determined to be a three-state model comprising 13 ± 2 % monomers, 64 ± 2 % trimers and 24 ± 3 % nonamers (Figure 26, Supplementary Table 2, Supplementary Table 23).

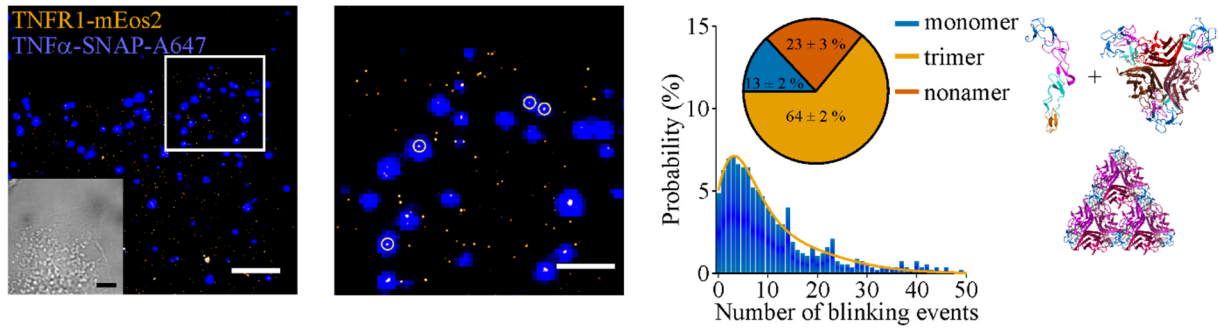


Figure 26: The oligomeric state of TNF α -treated TNFR1-mEos2 at 4 °C. PALM image of a representative MEF cell expressing TNFR1-mEos2 (left panel) with a zoomed region (middle panel) after incubation with TNF α -SNAP-A647. Analysis reveals an oligomeric state of $13 \pm 2\%$ monomers, $64 \pm 2\%$ trimers, and $23 \pm 3\%$ nonamers (equation 11, yellow curve). Experiments contain the data of 14 cells from three independent experiments. (Scale bars, $5 \mu\text{m}$ PALM and brightfield image (left panel), $1 \mu\text{m}$ PALM image (middle panel)) (PDB 1NCF, 1TNF).

Analyzing BIC and log likelihood values for TNFR1 clusters that showed no colocalization to TNF α -SNAP-A647, only $41 \pm 4\%$ monomers and $59 \pm 4\%$ dimers were observed (Figure 27, Supplementary Table 3, Supplementary Table 23).

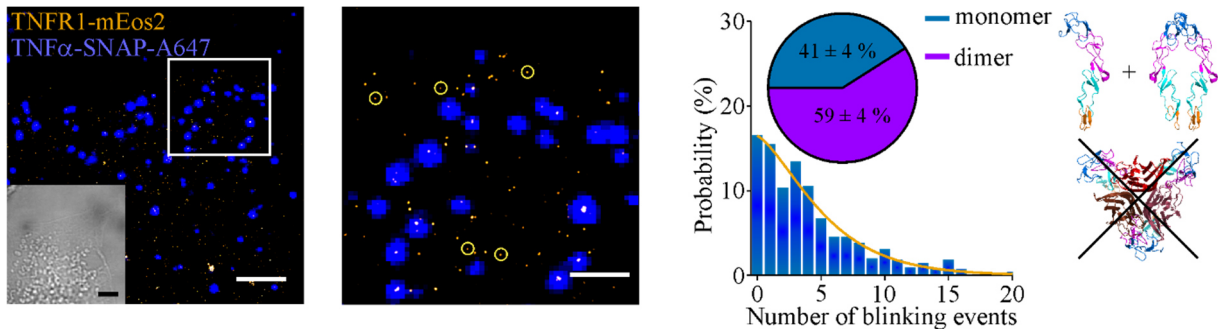


Figure 27: The oligomeric state of TNF α -treated but ligand-free TNFR1-mEos2 at 4 °C. PALM image of a representative MEF cell expressing TNFR1-mEos2 (left panel) with a zoomed region (middle panel) after incubation with TNF α -SNAP-A647. Analysis of TNFR1-mEos2 cluster that show no colocalization to TNF α -SNAP-A647 reveals an oligomeric state of $41 \pm 4\%$ monomers and $59 \pm 4\%$ nonamers (equation 11, yellow curve). Experiments contain the data of 14 cells from three independent experiments (Scale bars, $5 \mu\text{m}$ PALM and brightfield image (left panel), $1 \mu\text{m}$ PALM image (middle panel)) (PDB 1NCF, 1TNF).

4.1.5 qPALM of TNFR1 carrying mutations in the PLAD or ligand binding domain

In order to reveal the function of the PLAD in TNFR1 dimerization in the TNF α -untreated state and the nonameric composition in the TNF α -treated state, a point mutation was generated in the CRD1 (K32A). Consistent with the experiments described above, the oligomeric states of TNFR1(K32A)-mEos2 from serum-starved TNF α -untreated and for 30 minutes at 4 °C with TNF α -SNAP-A647 stimulated cells

RESULTS AND DISCUSSION

were quantified (Figure 28A,B). In both conditions, analysis including BIC and log likelihood values predicted 100 % monomers of TNFR1 on the plasma membrane (Figure 28, Supplementary Table 4, Supplementary Table 5, Supplementary Table 23). Furthermore, due to a lack of colocalization no specific binding of TNF α to TNFR1 was observed.

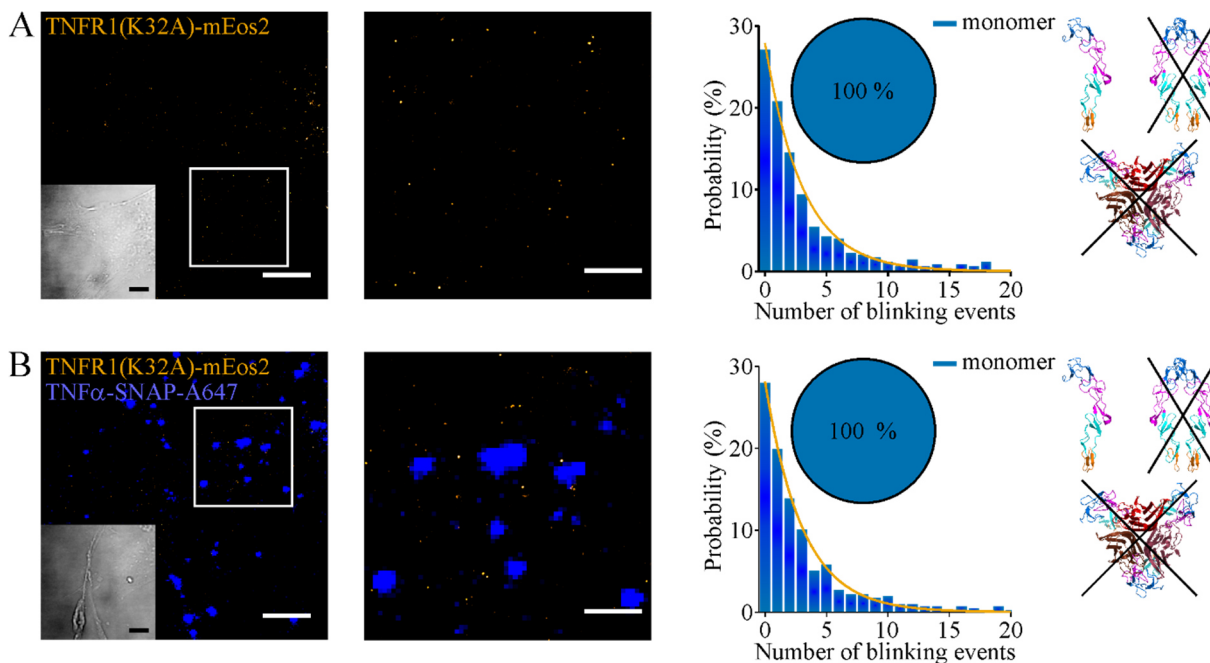


Figure 28: The oligomeric state of TNFR1(K32A)-mEos2 at 4 °C. (A) PALM and brightfield image of one representative TNFR1(K32A)-mEos2 MEF cell (left panel) and zoomed region (middle panel). Quantitative analysis reveals a distribution of 100 % monomers (equation 11, yellow curve). Experiments contain the data of ten cells from three independent experiments (B) PALM and brightfield image of one TNF α -treated TNFR1(K32A)-mEos2 MEF cell (left panel) and zoomed region (middle panel). Quantitative analysis shows 100 % monomers (equation 11, yellow curve). Experiments contain the data of ten cells from three independent experiments (Scale bars, 5 μ m PALM and brightfield images (left panels), 1 μ m PALM images (middle panels)) (PDB INCF, 1TNF).

A second mutation in the ligand-binding domain CRD2 (N66F) was characterized without and after the incubation of 100 ng/ml TNF α for 30 minutes at 4 °C. The models with the largest probability (identified by BIC and log likelihood analysis as described before) revealed a distribution of 54 ± 3 % monomeric and 46 ± 3 % dimeric fraction of TNF α -untreated TNFR1(N66F)-mEos2 (Figure 29A, Supplementary Table 6, Supplementary Table 23) and a distribution of 56 ± 3 % monomeric and 44 ± 3 % dimeric fraction of TNF α -treated TNFR1(N66F)-mEos2 (Figure 29B, Supplementary Table 7, Supplementary Table 23). Again, there was no evidence of effective binding of TNF α to TNFR1.

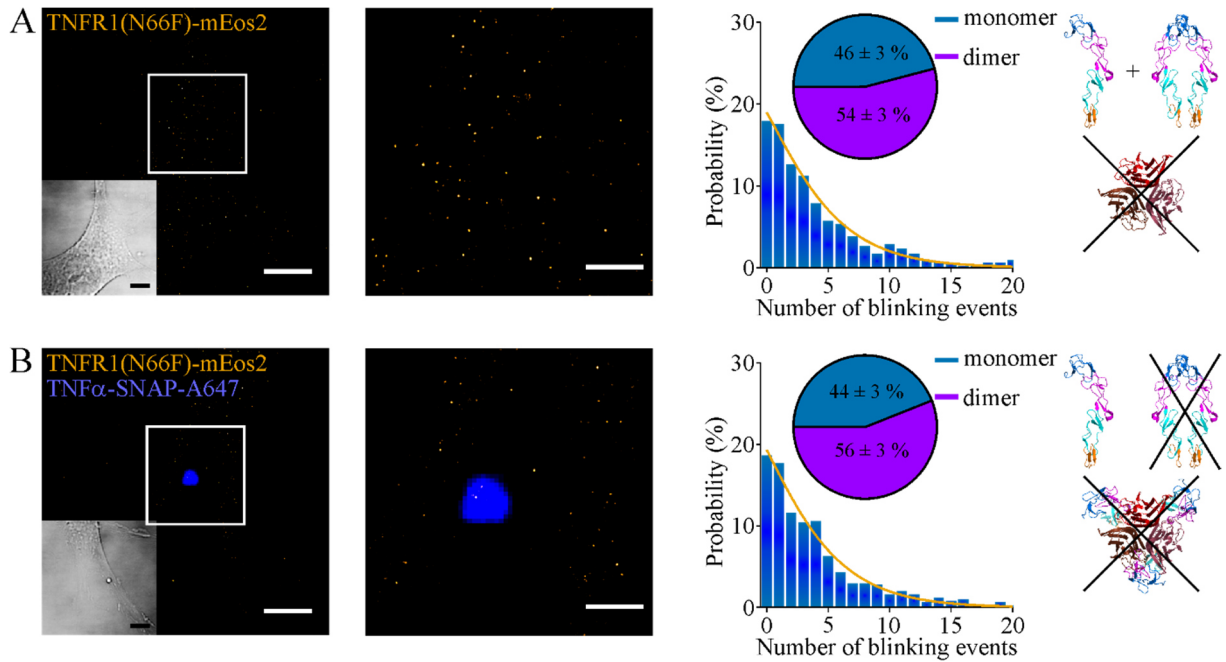


Figure 29: The oligomeric state of TNFR1(N66F)-mEos2 at 4 °C. (A) PALM and brightfield image of one representative TNFR1(N66F)-mEos2 MEF cell (left panel) and zoomed region (middle panel). Quantitative analysis reveals a distribution of $46 \pm 3\%$ monomers and $54 \pm 3\%$ dimers (equation 11, yellow curve). Experiments contain the data of ten cells from three independent experiments (B) PALM and brightfield image of one TNF α -treated TNFR1(N66F)-mEos2 MEF cell (left panel) and zoomed region (middle panel). Quantitative analysis shows a distribution of $44 \pm 3\%$ monomers and $56 \pm 3\%$ dimers (equation 11, yellow curve). Experiments contain the data of ten cells from three independent experiments (Scale bars, 5 μm PALM and brightfield images (left panels), 1 μm PALM images (middle panels)) (PDB 1NCF, 1TNF).

In order to validate these results, fluorescence-activated cell sorting (FACS) was conducted (Figure 30).

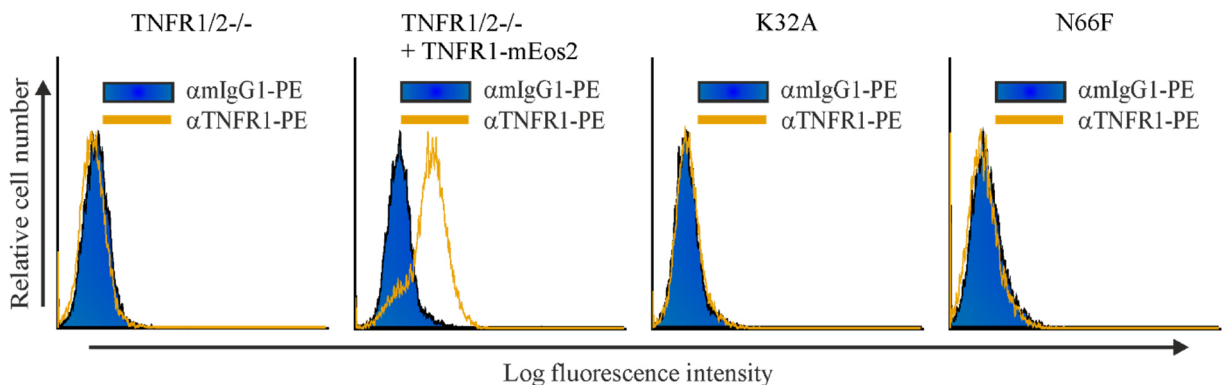


Figure 30: FACS analysis of TNFR1/2^{-/-}, TNFR1/2^{-/-} + TNFR1-mEos2^{-/-}, TNFR1(K32A)-mEos2^{-/-} and TNFR1(N66F)-mEos2 MEF cells. FACS analysis with $\alpha\text{TNFR1-PE}$ antibody binding to TNFR1 (orange curve) and $\alpha\text{IgG1-PE}$ antibody as negative control (blue data) of indicated MEFs. Experiments presented in this figure were performed by Dr. Juliane Medler (Würzburg, Germany).

Experiments revealed only a small increase in the fluorescence for the mutant K32A compared to the TNFR1/2-/- cell line and to the negative control with α mIgG1-PE, but also almost no increase at all in comparison to the TNFR1/2-/- + TNFR1-mEos2 cell line, indicating that the detection of TNFR1 on the plasma membrane was poor or even non-existent. A further decrease of the fluorescence signal was observed for the mutant N66F, suggesting that this mutant was not fully expressed on the plasma membrane.

4.1.6 The influence of zafirlukast on the stoichiometry of TNFR1

Having a quantitative model on the molecular organization of TNFR1 allows studies of pharmacological reagents. Given that TNFR1 is frequently hyperactivated and/or overexpressed in neoplastic diseases such as cancer (Liu and Tang, 2014), disrupting TNFR1 oligomerization could provide novel and targeted treatment strategies. One possibility to inhibit TNFR1 is through the treatment with the drug zafirlukast (Figure 2), which is known to inhibit TNFR1 by binding the PLAD (Lo et al., 2017). TNFR1/2-/- + TNFR1-mEos2 MEFs were treated with zafirlukast for 30 minutes at 4 °C and analyzed (Figure 31). Zafirlukast-treated TNFR1/2-/- + TNFR1-mEos2 MEFs revealed a fraction of 90 ± 3 % monomers and 10 ± 3 % dimers representing a shift to the monomeric fraction compared to the TNF α -untreated condition of TNFR1-mEos2 in its native environment (Figure 24, Supplementary Table 8, Supplementary Table 23).

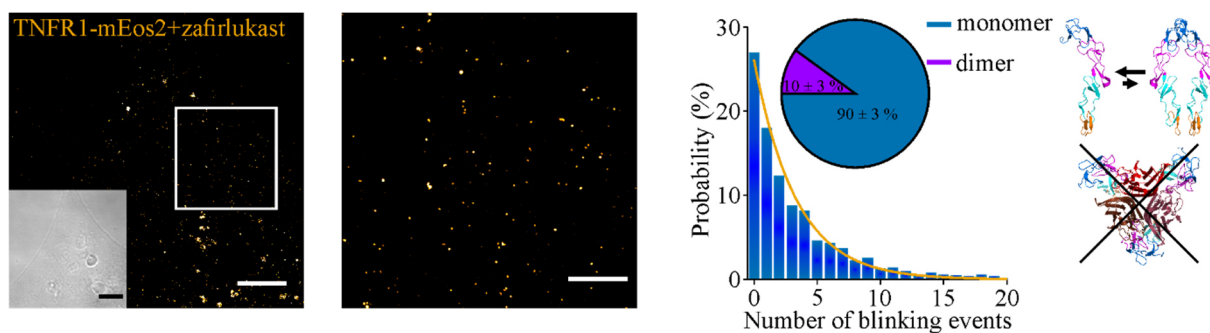


Figure 31: The oligomeric state of TNFR1-mEos2 after zafirlukast treatment at 4 °C. PALM and brightfield image of one representative TNFR1/2-/- + TNFR1-mEos2 MEF cell (left panel) and zoomed region (middle panel) after zafirlukast treatment. Quantitative analysis reveals a distribution of 90 ± 3 % monomers and 10 ± 3 % dimers (equation 11, yellow curve). Experiments contain the data of ten cells from three independent experiments (Scale bars, 5 μ m PALM and brightfield image (left panels), 1 μ m PALM image (middle panel)) (PDB 1NCF, 1TNF).

The analysis regarding the treatment with zafirlukast and TNF α showed with 91 ± 3 % monomers and 9 ± 3 % dimers a comparable distribution as without TNF α incubation (Figure 32, Supplementary Table 9, Supplementary Table 23). Furthermore, due to a lack of colocalization no specific binding of TNF α to TNFR1 was observed.

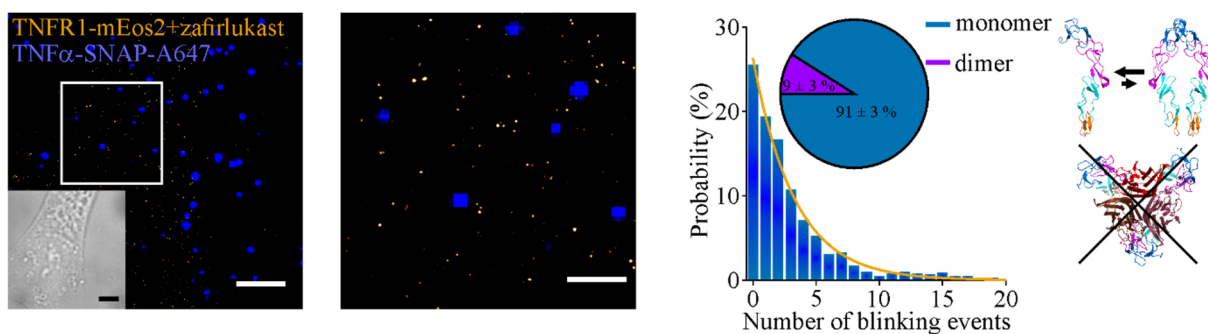


Figure 32: The oligomeric state of TNFR1-mEos2 after treatment with zafirlukast and TNF α at 4 °C. PALM and brightfield image of one representative TNFR1/2-/- + TNFR1-mEos2 MEF cell (left panel) and zoomed region (middle panel) after zafirlukast and TNF α treatment. Quantitative analysis reveals a distribution of 91 ± 3 % monomers and 9 ± 3 % dimers (equation 11, yellow curve). Experiments contain the data of ten cells from three independent experiments (Scale bars, 5 μ m PALM and brightfield image (left panels), 1 μ m PALM image (middle panel)) (PDB 1NCF, 1TNF).

4.1.7 The influence of chemical-induced apoptosis on the stoichiometry of TNFR1

The treatment of TNFR1 with small molecules like zafirlukast is one option to inhibit TNFR1 and thus to treat diseases like asthma (Adkins and Brogden, 1998) or dermatitis (Carucci et al., 1998). Another promising approach to combat e.g. neoplastic tissue includes the induction of apoptosis or necroptosis (Martínez-Reza et al., 2017). This could not only inhibit cell division in cancer cells, but also ensure a coordinated degradation of malignant tissue while avoiding the release of inflammatory and cytotoxic signals (Martínez-Reza et al., 2017). Thus, the oligomeric state of TNFR1 during induced apoptosis using 100 ng/ml TNF α and 10 μ M BV6 incubation at 4 °C for 30 minutes was investigated (Figure 33A, B). The most probable model for the data of the oligomeric state of TNFR1 was determined by analysis of BIC and log likelihood values (Supplementary Table 10). Analysis revealed a distribution of 10 ± 3 % monomers, 70 ± 3 % trimers and 20 ± 2 % nonamers (Figure 33A, Supplementary Table 23). The ligand-free fraction revealed a distribution of 71 ± 3 % monomers and 29 ± 3 % dimers (Figure 33B, Supplementary Table 11, Supplementary Table 23).

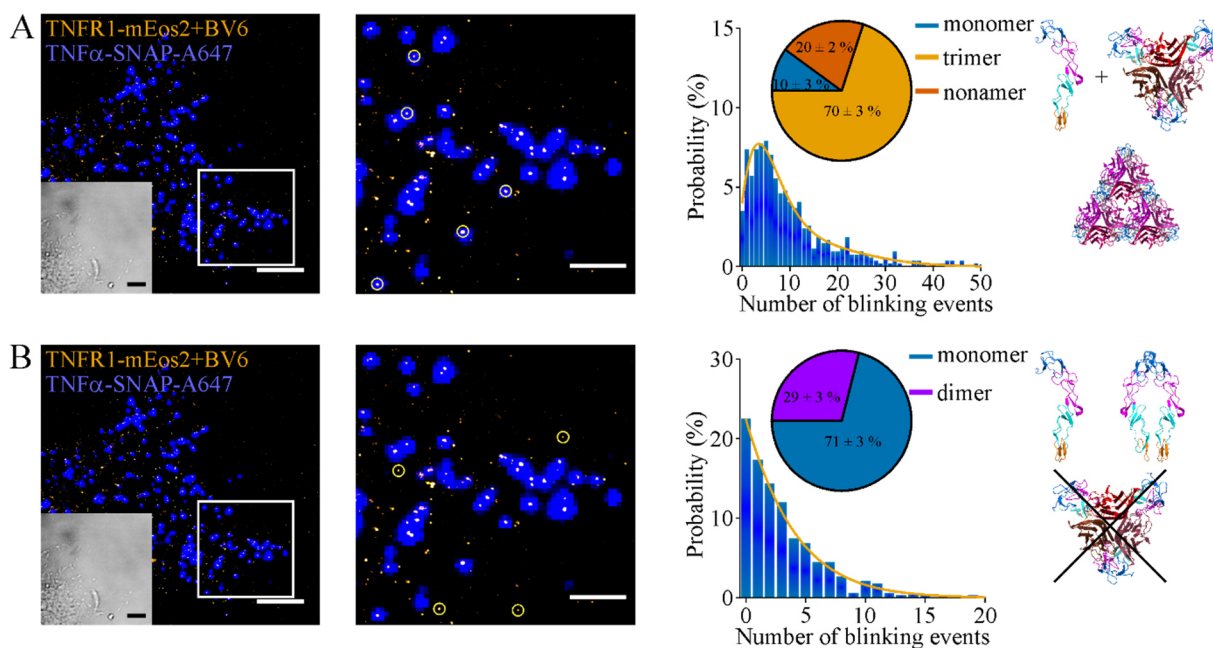


Figure 33: The oligomeric state of TNFR1-mEos2 after apoptosis induction with TNF α and BV6 at 4 °C. (A) PALM and brightfield image of one representative TNFR1/2-/- + TNFR1-mEos2 MEF cell (left panel) and zoomed region (middle panel) after apoptosis induction. Quantitative analysis of ligand-bound TNFR1 reveals a distribution of 10 ± 3 % monomers, 70 ± 3 % trimers and 20 ± 2 % nonamers (equation 11, yellow curve). Experiments contain the data of 13 cells from three independent experiments (B) PALM and brightfield image of one TNFR1/2-/- + TNFR1-mEos2 MEF cell (left panel) and zoomed region (middle panel) after apoptosis induction. Quantitative analysis of ligand-free TNFR1 reveals a distribution of 71 ± 3 % monomers and 29 ± 3 % dimers (equation 11, yellow curve). Experiments contain the data of 13 cells from three independent experiments (Scale bars, 5 μ m PALM and brightfield images (left panels), 1 μ m PALM images (middle panels)) (PDB INCF, 1TNF).

4.1.8 The influence of chemical-induced necroptosis on the stoichiometry of TNFR1

The treatment of diseases by inducing apoptosis in malignant cells is only one promising approach (Martínez-Reza et al., 2017). Numerous diseases, especially neoplastic tissue, are able to develop immunity against apoptosis over time (Arvanitis et al., 2013; Liu, 2010). Therefore, a second variant of programmed cell death called necroptosis was applied as another promising approach for cell death-mediated treatment of tumorigenic tissue. In support of this strategy, recent work highlighted necroptosis as an effective method to treat cancer tissue with high resistance to induced apoptosis (Hannes et al., 2016). Thus, the oligomeric state of TNFR1 during induced necroptosis using 100 ng/ml TNF α , 10 μ M BV6 and 20 μ M zVAD-fmk incubation at 4 °C for 30 minutes was investigated (Figure 34A, B). The most probable model for the oligomeric state of TNFR1 was determined by analysis of BIC and log likelihood values (Supplementary Table 12). Analysis showed a distribution of 15 ± 3 % monomers, 67 ± 3 % trimers and 18 ± 2 % nonamers (Figure 34A, Supplementary Table 23). The ligand-free

fraction revealed a distribution of $72 \pm 3\%$ monomers and $28 \pm 3\%$ dimers (Figure 34B, Supplementary Table 13, Supplementary Table 23).

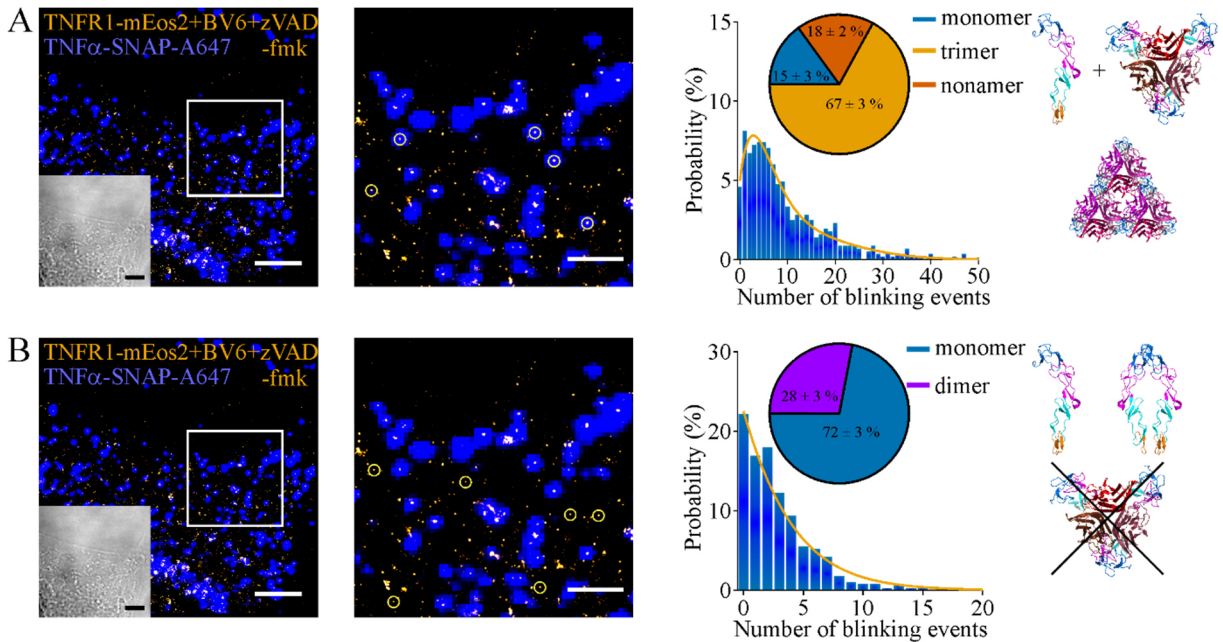


Figure 34: The oligomeric state of TNFR1-mEos2 after necroptosis induction with TNF α , BV6 and zVAD-fmk at 4 $^{\circ}$ C. (A) PALM and brightfield image of one representative TNFR1/2-/- + TNFR1-mEos2 MEF cell (left panel) and zoomed region (middle panel) after necroptosis induction. Quantitative analysis of ligand-bound TNFR1 reveals a distribution of $15 \pm 3\%$ monomers, $67 \pm 3\%$ trimers and $18 \pm 2\%$ nonamers (equation 11, yellow curve). Experiments contain the data of eleven cells from three independent experiments (B) PALM and brightfield image of one TNFR1/2-/- + TNFR1-mEos2 MEF cell (left panel) and zoomed region (middle panel) after necroptosis induction. Quantitative analysis of ligand-free TNFR1 reveals a distribution of $71 \pm 3\%$ monomers and $29 \pm 3\%$ dimers (equation 11, yellow curve). Experiments contain the data of eleven cells from three independent experiments (Scale bars, 5 μ m PALM and brightfield images (left panels), 1 μ m PALM images (middle panels)) (PDB 1NCF, 1TNF).

4.1.9 Discussing the oligomeric state of TNFR1

Quantitative model of TNF α -untreated TNFR1

In literature, western blot (Boschert et al., 2010), crystallographic (Naismith et al., 1995) and FRET (Morton et al., 2019) experiments revealed TNF α -untreated TNFR1 to exist as monomer and dimer. In contrast, in the work of Chan *et al.* in 2000 western blot experiments showed that TNF α -untreated TNFR1 assembles to monomers and trimers (Chan, 2000). The only difference, compared to the study of Boschert *et al.* in 2010, is the usage of 3,3'-dithiobis[sulfosuccinimidylpropionate] (DTSSP, Chan et al., 2000) as crosslinker compared to Bis(sulfosuccinimidyl)suberate (BS³, Boschert et al., 2010). In contrast to BS³, the crosslinking reagent DTSSP contains a disulfide bridge. These results prompted a

general discussion whether TNFR1 is present as monomer and dimer or monomer and trimer on the plasma membrane (Mukai et al., 2010; Wajant, 2015). The results obtained in this thesis with quantitative PALM demonstrated the presence of TNFR1 as monomer and dimer on the plasma membrane of an intact cell. These observations support the low-affinity (mM range) binding model of two TNFR1 by their PLAD, which exists in an equilibrium with monomeric TNFR1 proposed by several studies (Cao et al., 2011; Wajant, 2015). It is supposed that these pre-ligand dimeric arrangements of TNFR1 exist to generate high-affinity binding sites for efficient ligand binding (Naismith et al., 1995; Wajant, 2015).

Quantitative model of TNF α -treated TNFR1

The stoichiometry for TNF α -bound TNFR1 was determined to be a three-state model comprising 13 ± 2 % monomers, 64 ± 2 % trimers and 24 ± 3 % nonamers and offered no evidence for a dimeric fraction of TNFR1 in the ligand-bound state. Therefore, either only the monomeric fraction of ligand-free TNFR1 was bound to TNF α , or the bond between two TNFR1 by their PLAD was disrupted upon binding to TNF α . The latter would be consistent with observations that TNFR1 undergoes a conformational change after TNF α binding (Lewis et al., 2012; Lo et al., 2019), thus disrupting the PLAD-PLAD interaction of the ligand-bound TNFR1 and the ligand-free TNFR1. However, this would imply a specific time point where only two receptors should be bound to one trimeric TNF α . This was not considered in the model with the largest probability, suggesting that the dominant fraction of TNFR1 trimers assembles rather fast. The dominant trimeric fraction is in agreement with the work of Banner *et al.* in 1993, observing the three to three TNFR1-TNF α state, identified by crystallographic experiments (Banner et al., 1993). In 2014, Fricke *et al.* also showed via PALM, that TNFR1 oligomers assemble to a dominant fraction of trimers. Furthermore, they could reveal that oligomers that are larger than trimers exist on the plasma membrane (Fricke et al., 2014). This was the first indication that TNFR1₃-TNF α ₃ arrangements generate larger oligomers through further PLAD-PLAD interactions. These results prompted discussion, as Wajant *et al.* proposed hexameric and nonameric arrangements to exist on the plasma membrane (Wajant, 2015). In 2012, Lewis *et al.* and in 2018, Vanamee *et al.* discussed even a model, where TNFR1 assembles to entire networks, which would lead to TNFR1 oligomers far larger than nonamers (Lewis et al., 2012; Vanamee and Faustman, 2018). At a first view, these models would contradict the argument that the interaction of two PLADs is disrupted by ligand binding. However, two TNFR1, both bound to TNF α , potentially interact with each other again. In this thesis, results obtained by qPALM, support the models proposed by Fricke *et al.* and Wajant *et al.*, where larger oligomers than trimers were detected. The model with nonamers exhibits the largest probability (Figure 35).

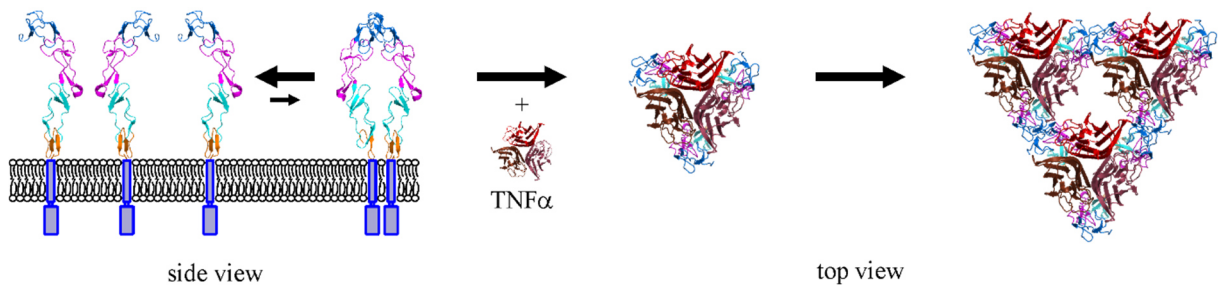


Figure 35: Molecular model for TNFR1 oligomerization. *TNF α -untreated TNFR1 exists in an equilibrium of monomers and dimers. After ligand stimulation, TNFR1 assembles to a trimeric intermediate state followed by a stable triangle shaped nonameric state.*

It must be noted that the monomer-trimer-nonamer arrangement of TNFR1 bound to TNF α model proposed in this thesis represents solely the model with the largest probability. It cannot be excluded that there is a certain time point where only two TNFR1 are bound to one TNF α -trimer, which would result in a dimeric fraction. Furthermore, a hexameric arrangement is also a possible intermediate state, by the binding of two TNFR1₃-TNFR1₃ complexes through PLAD-PLAD interactions. Of note, the model with monomer-dimer-trimer-nonamer and the model with monomer-trimer-hexamer-nonamer were the fifth and sixth best models (from in total 511 models) describing the blinking event distribution (Supplementary Table 2). In this case, the fifth best model (including the dimeric fraction) showed distributions of $9 \pm 2\%$ monomers, $14 \pm 2\%$ dimers, $54 \pm 3\%$ trimers and $23 \pm 2\%$ nonamers, indicating that a dimeric fraction is also present (Figure 36). The sixth best model (including the hexameric fraction) revealed distributions of $14 \pm 2\%$ monomers, $64 \pm 3\%$ trimers, $0 \pm 3\%$ hexamers and $22 \pm 2\%$ nonamers, concluding that the presence of a hexameric fraction exhibits a low probability. Consequently, only three TNFR1₃-TNF α ₃ can assemble to a nonameric composition of TNFR1-TNF α (Figure 36). Possibly, the interaction between two PLADs of two TNFR1₃-TNF α ₃ units is too low to generate a stable structure. Eventually, the formation of a triangular configuration is more stable and necessary for clustering through the interaction of three PLAD-PLAD linkages, where per TNFR1₃-TNF α ₃ unit only one free PLAD is present. The next possible larger oligomeric state, where only one PLAD of every TNFR1₃-TNF α ₃ is free, would be an 18mer. Oligomer units of such magnitudes were discussed to be present in the works from Lewis *et al.* and Vanamee *et al.* (Lewis *et al.*, 2012; Vanamee and Faustman, 2018). However, in this thesis oligomers larger than nonamers were not detected by qPALM.

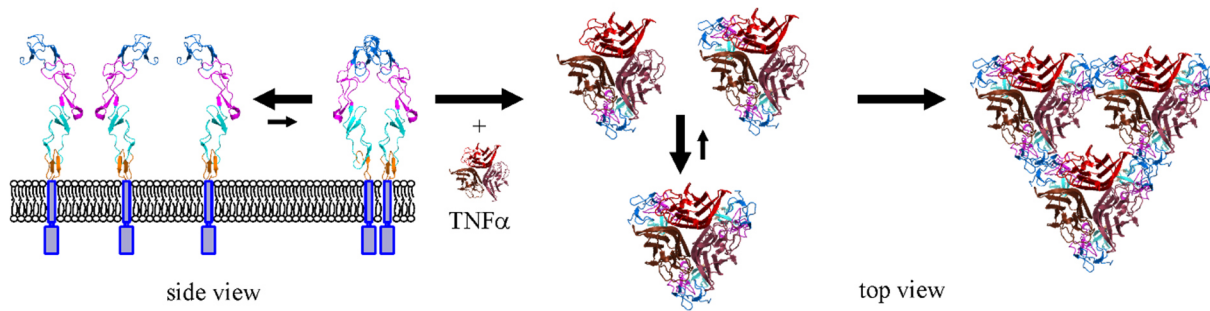


Figure 36: Alternative model for TNFR1 oligomerization. *TNFR1 exists in an equilibrium of monomers and dimers. After ligand stimulation, TNFR1 assembles to a monomeric and dimeric pre-intermediate state resulting in a first stable trimeric intermediate state. Afterwards TNFR1 trimers assemble by further PLAD-PLAD interactions to a nonameric arrangement.*

Considering the quantitative analysis of TNFR1, which is not bound to TNF α (Figure 24), a clear shift towards the dimeric fraction was revealed. Self-organization into a larger percentage of dimers may cause this shift, leading to a larger affinity for ligand binding and thus to more efficient signaling. However, it is also possible that some TNFR1 are bound to TNF α , which were not labeled with Alexa Fluor 647. It is reported that SNAP-tag labelling possesses an efficiency of about 60 % (Virant et al., 2018). Considering that each TNF α trimer contains three SNAP-tags, this results into a probability of about 94 % that one TNF α trimer exhibits at least one Alexa Fluor 647 fluorophore. The remaining 6 % may be responsible for an artificial shift to the dimeric fraction, since an apparently ligand-free TNFR1 cluster was selected, which actually was bound to TNF α . Beyond the evaluation of the oligomeric state, analysis revealed that only 20 ± 9 % of the TNFR1 clusters colocalize with labeled TNF α despite of a TNF α concentrations of 100 ng/ml, which corresponds to the saturated region of the TNFR1-SNAP-Flag-TNC-TNF α binding curve (Supplementary Figure 1, blue curve, Figure 25A). This observation was unexpected, since all receptors located on the plasma membrane should be bound to TNF α . Quantification of the receptor numbers per cell, which were bound to TNF α , suggested 3140 ± 750 TNFR1 per cell. This was in agreement with the number of 2700 ± 2520 TNFR1 per cell determined by luciferase assay analysis, indicating that indeed every receptor on the plasma membrane was bound by TNF α . The remaining fraction of TNFR1 that were analyzed are presumably located in the golgi, i.e. the intracellular environment of the cell (Gaeta et al., 2000; Storey et al., 2002). Since TIRF illumination penetrates the cell up to 200 nm (Axelrod et al., 1984), TNFR1, located near the plasma, is also detected. Unfortunately, it is not possible to distinguish between these two populations with PALM in combination with TIRF microscopy.

Mutations in the PLAD and CRD2 affect clustering of TNFR1

Quantitative results of the K32A mutated TNFR1 MEFs (100 % monomers with and without TNF α treatment) support the model shown in Figure 35 and Figure 36, in which dimeric and potentially

nonameric fractions of TNFR1 are generated by low-affinity PLAD-PLAD interactions. TNF α -treated MEFs showed no specific binding of TNF α -SNAP-A647 to TNFR1, which is in agreement with the work of Chan *et al.* in 2000, where it was shown that K32A mutated TNFR1 lost the ability to bind TNF α (Chan, 2000). Furthermore, western blot analysis revealed that TNF α is unable to induce a NF- κ B response (Supplementary Figure 2B). These results indicate that the ligand-bound trimeric and potentially nonameric arrangements of TNFR1 are the signaling active species. However, luciferase assays detected a small fraction of specific binding of huTNF-F-TNC-GpL to TNFR1(K32A)-mEos2. A K_D value of 91 ± 33 ng/ml was determined, which is significantly lower compared to the K_D value of 16 ± 3 ng/ml for the TNFR1/2-/- +TNFR1-mEos2 MEFs (Supplementary Figure 1, pink curve). Furthermore, PALM experiments revealed that only a small fraction of TNFR1(K32A)-mEos2 MEF cells exhibit an appropriate number of TNFR1 on the plasma membrane for further analysis. This observation is also consistent with the result of FACS analysis, where only a small increase of the fluorescence signal was detected. The insertion of the K32A mutation might influence the protein stability, localization or inter-organelle transport, which was already reported for TNF Receptor Associated Periodic Syndrome (TRAPS), where the unfolded protein response (UPR) increased for TNFR1 mutations (Jarosz-Griffiths *et al.*, 2019).

Quantitative PALM experiments of the N66F mutant revealed that TNFR1 is still in equilibrium with monomers and dimers, but is no longer capable to bind TNF α . This result is in agreement with the work of Chan *et al.* in 2000, who showed that N66F mutated TNFR1 is unable to bind TNF α (Chan, 2000). In addition, luciferase binding experiments revealed also no binding of TNF α to TNFR1 (Supplementary Figure 1). Furthermore, western blot analysis demonstrated clear expression of TNFR1(N66F)-mEos2 but also no activation of NF- κ B after TNF α stimulation. In addition, PALM experiments showed that only a small fraction of TNFR1(N66F)-mEos2 MEF cells exhibit an appropriate number of TNFR1 on the plasma membrane for further analysis. This was confirmed by FACS analysis, where no expression of TNFR1(N66F)-mEos2 (Figure 30) was detected, indicating that either the FACS analysis was not sensitive enough to detect this low level of positive TNFR1(N66F)-mEos2 MEFs or TNFR1(N66F)-mEos2 was not successfully transported and anchored into the plasma membrane. Thus, all TNFR1(N66F)-mEos2 clusters detected by PALM might be located in the intracellular region near the plasma membrane. Consequently, these experiments cannot conclude whether TNF α did not bind to TNFR1(N66F)-mEos2 because the mutation prohibited binding or because the TNFR1(N66F)-mEos2 was not located at the plasma membrane.

Zafirlukast affects clustering of TNFR1

Quantitative results for zafirlukast-treated TNFR1 (90 ± 3 % monomers and 10 ± 3 % dimers without TNF α incubation and 91 ± 3 % monomers and 9 ± 3 % dimers with TNF α incubation) are in agreement with the data investigated by Lo *et al.* in 2017 (Lo *et al.*, 2017), showing that zafirlukast inhibits NF- κ B

and I κ B α degradation in a dose dependent manner. In 2019, Lo *et al.* demonstrated with FRET experiments that zafirlukast disrupts the PLAD-PLAD interactions, disturbing the formation of pre-ligand dimers and thus the ability to effectively bind TNF α (Lo et al., 2019). In this thesis, this deficiency to bind TNF α was also verified by PALM experiments. However, in the work of Lo *et al.* in 2017, a small percentage of TNFR1 bound to TNF α remained. Furthermore, it was demonstrated that overall the NF- κ B signal decreases about 50 % and the I κ B α degradation of about 80 % although the same concentration of TNF α (100 ng/ml) and a saturated concentration of zafirlukast (100 μ M) was used (Lo et al., 2017). Thus, it was expected that at least a small percentage of TNF α would bind TNFR1. Moreover, although cells were treated with a saturated concentration of zafirlukast PALM experiments revealed a fraction of approximately 10 % dimers. Consequently, zafirlukast does not split all TNFR1 dimers into a monomeric fraction. However, this is in agreement with the study from Lo *et al.* in 2017 and 2019, where also a small fraction of dimers was detected (Lo et al., 2017; Lo et al., 2019).

TNFR1 clustering is not influenced by apoptosis induction

Quantitative results for TNFR1 after apoptosis induction were highly comparable to the results obtained in cells that were only treated with TNF α (Figure 26 and 27). Thus, the inhibition of cIAP1/2 by BV6 and the resulting instability of complex I does not affect the oligomeric state of TNFR1 on the plasma membrane, although complex I and TNFR1 are directly associated. This implies that there is no change in the oligomeric state, whether NF- κ B or apoptosis is activated in the cell by TNFR1.

TNFR1 clustering is not influenced by necroptosis induction

Quantitative results for TNFR1 after necroptosis induction were highly comparable to the results obtained in cells that were only treated with TNF α (Figure 26 and 27) and those, which were induced with apoptosis (Figure 33). Thus, the oligomeric state of TNFR1 did not change significantly whether NF- κ B, apoptosis or necroptosis was activated in the cell. This result was expected after the experiments where TNFR1 was quantified after apoptosis induction, since at necroptosis, the same inhibition of complex I occurs compared to apoptosis. Additionally, only complex II is destabilized by zVAD-fmk. Since complex II is intracellularly decoupled from complex I and TNFR1, these quantitative data are in agreement with expectations.

4.1.10 Comparison of the oligomeric state of TNFR1 of 4 °C and 37 °C incubated MEFs

All experiments and results that were presented were performed at an incubation temperature of 4 °C to minimize internalization effects. This ensures that the oligomeric state of TNFR1 on the plasma membrane is determined just before the onset of endocytosis (Tomoda et al., 1989). Within the context of this study, the experiments described in this chapter were also performed at an incubation temperature of 37 °C. Since TNF α and all drugs used in this thesis were incubated for at least 30 minutes, active

endocytosis was in process before samples were fixed and imaged (Rappoport and Simon, 2003). This permits a characterization of the oligomeric state of TNFR1 during vigorous endocytosis. BIC, log likelihood values and the results of the oligomeric states of TNFR1 for all conditions presented in chapter 4.1 (TNF α -treated ligand-bound and free, TNF α -treated TNFR1(K32A)-mEos2, TNF α -treated TNFR1(N66F)-mEos2, TNF α -treated TNFR1-mEos2 with zafirlukast, TNF α -treated ligand-bound and free TNFR1 after apoptosis induction and TNF α -treated ligand-bound and free TNFR1 after necroptosis induction) are shown for 37 °C in Supplementary Table 14-22 and Supplementary Figure 3-7. The results of the oligomeric states of TNFR1 of all the conditions (at 4 °C and 37 °C) are summarized in Figure 37 and Supplementary Table 23.

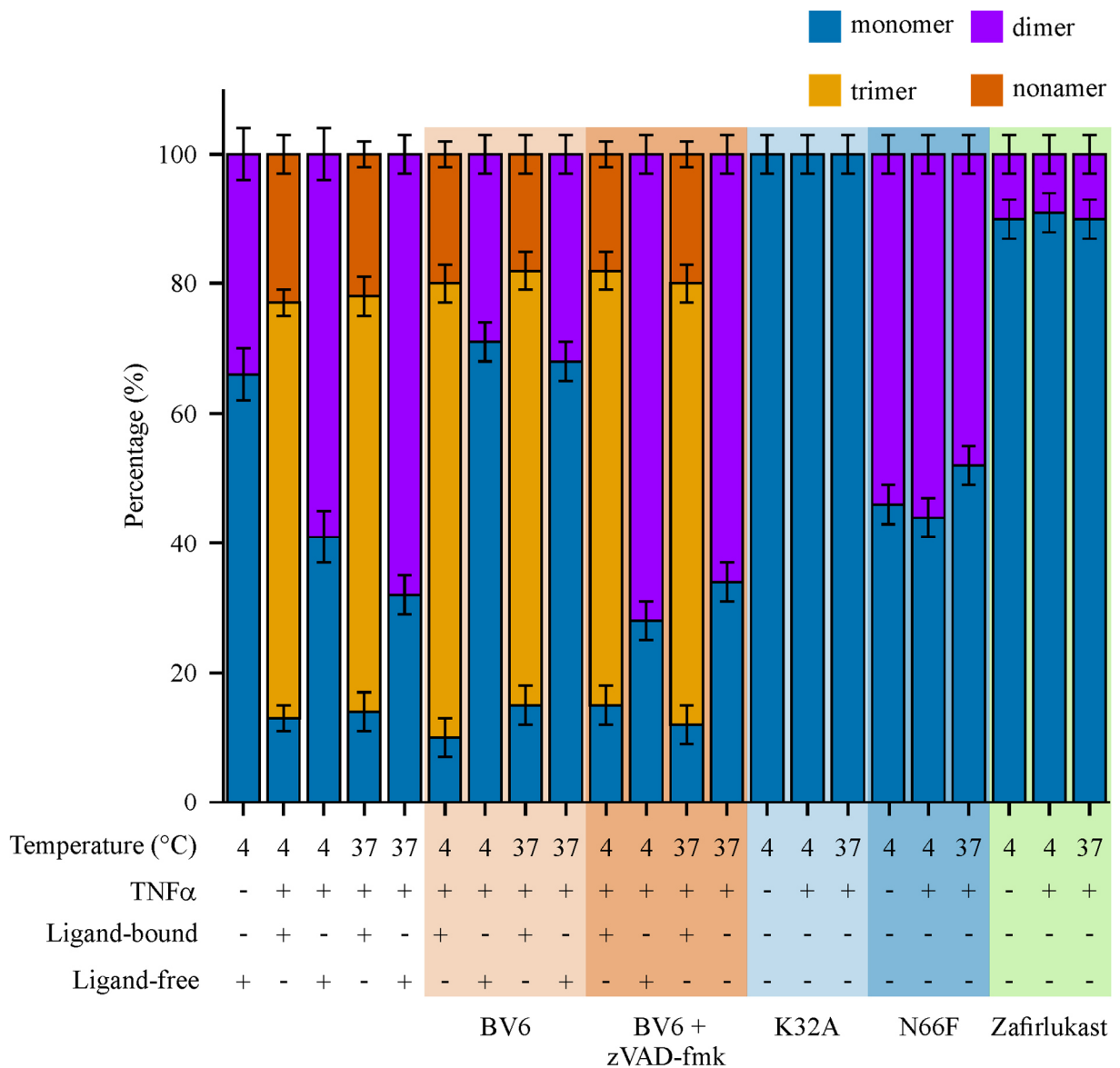


Figure 37: Comparison of the oligomeric states of TNFR1 under different conditions. Illustrated is the oligomeric state of TNFR1 (monomer blue, dimer purple, trimer orange, nonamer red) of all conditions investigated in this thesis.

Strikingly, only little deviation was found between the oligomeric states observed at 4 °C and 37 °C. This implies that the internalized TNFR1-TNF α complexes are either located close to the plasma membrane, or after 30 minutes an equilibrium of the TNFR1 monomer-trimer-nonamer composition is established. This equilibrium seems to be achieved with about 20 % monomers, 60 % trimers and 20 % nonamers. For all conditions wherein TNFR1 was mutated or inhibited by zafirlukast, the trimeric and nonameric fractions disappeared, demonstrating that a working PLAD and ligand binding domain is necessary for efficient ligand binding and the oligomerization of TNFR1 (Chan, 2000; Lo et al., 2017).

4.1.11 TNFR1 cluster analysis by DBSCAN

Next to the quantification of TNFR1 by quantitative PALM, DBSCAN was used to obtain cluster diameters, to identify if there is a change in cluster size for all analyzed conditions. A radius of 30 nm (two \sim times NeNA) (chapter 3.19) was selected, revealing a sufficient large radius to detect single TNFR1 clusters but also to avoid artificial TNFR1 cluster resulting from either splitting one TNFR1 cluster into two artificial clusters, due to a too small radius, or combining two to one cluster due to a too large radius. A value of two was chosen as the minimum number of localizations. A representative PALM and DBSCAN image illustrating selected TNFR1-mEos2 clusters and the cluster diameter distribution of TNF α -untreated TNFR1-mEos2 at 4 °C is shown (Figure 38).

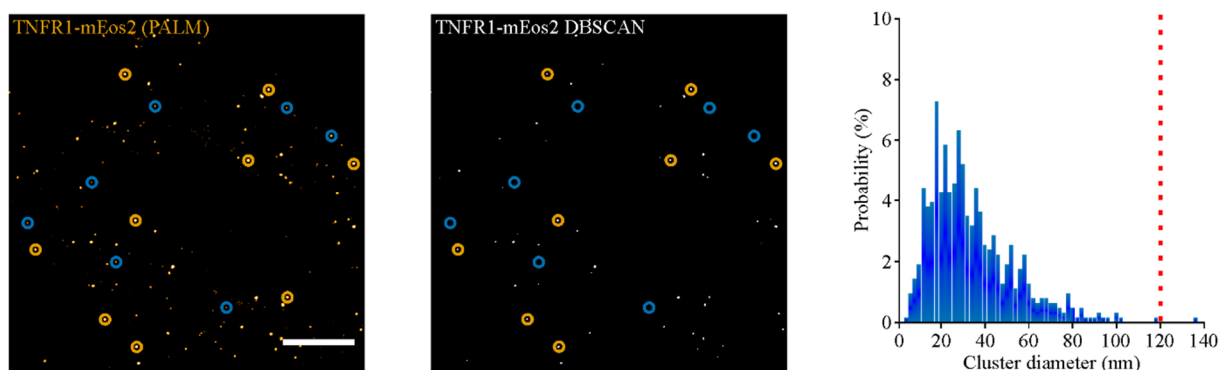


Figure 38: DBSCAN analysis and cluster size extraction. *The zoomed region from Figure 24 as representative PALM image (left) and the corresponding obtained DBSCAN image (right). Orange circles represent TNFR1-mEos2 cluster, which had the minimum number of localizations (two) in its distinct radius (30 nm \sim about two times NeNA). Blue circles show TNFR1-mEos2 cluster, which had less localizations in the given radius (scale bars 1 μ m). Right distribution shows the representative cluster diameters of TNF α -untreated TNFR1-mEos2 at 4 °C (binning of two). A threshold of 120 nm was chosen as maximum cluster diameter.*

The threshold of a maximum cluster diameter of 120 nm was chosen for further comparison of all conditions analyzed in this thesis, similar to the maximum cluster diameter chosen for quantitative PALM (Krüger et al., 2017a; Krüger et al., 2017b). Thus, for all conditions the cluster radius for all selected TNFR1-mEos2 clusters were extracted (at 4 °C and 37 °C) and summarized in Figure 39 and Supplementary Table 24.

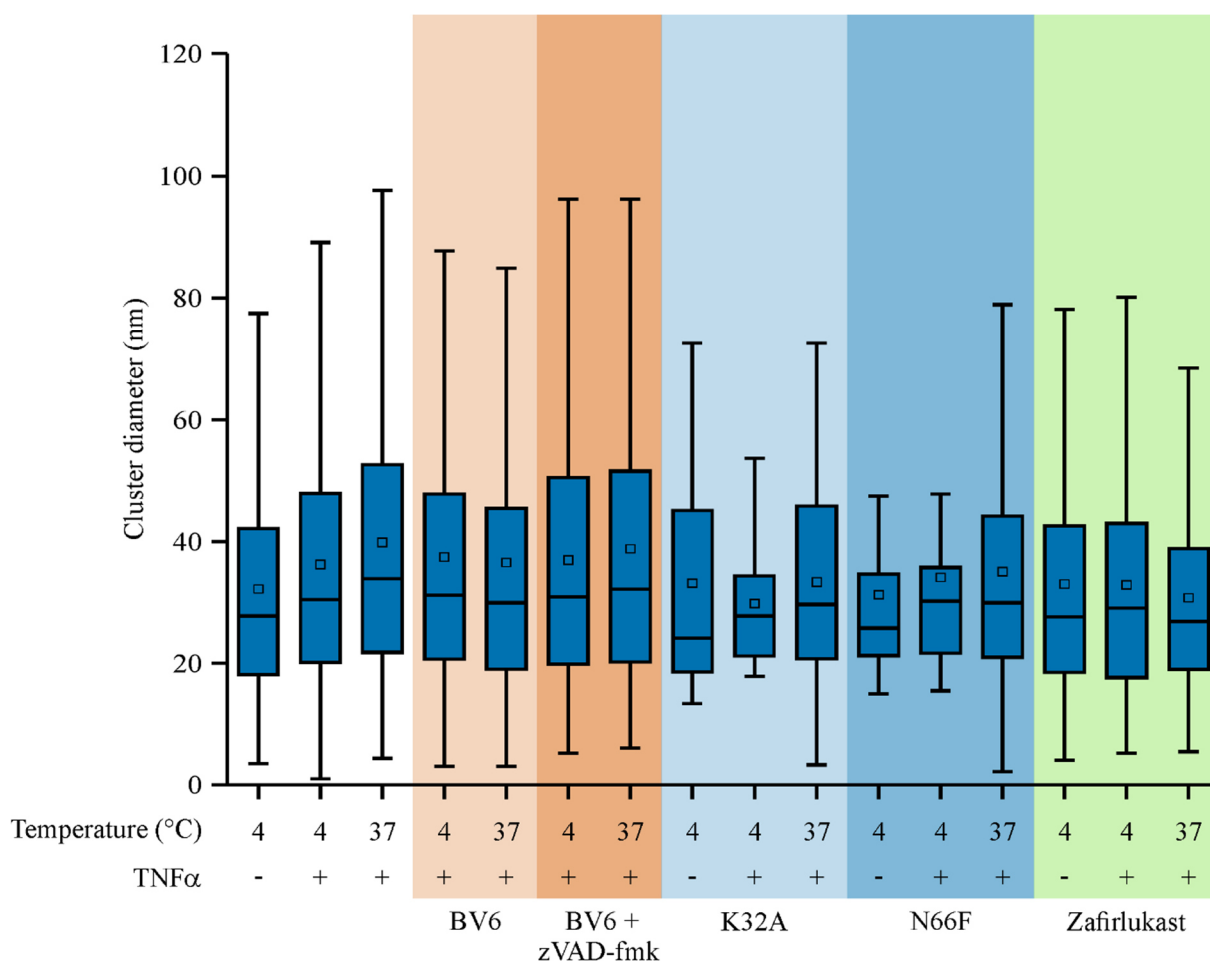


Figure 39: Comparison of the TNFR1-mEos2 cluster diameter. Illustrated are the mean cluster diameters of TNFR1-mEos2 (box plots) of all conditions investigated in this thesis. The blue box shows the data, which are in the interquartile range between 25 % and 75 %. The square in the middle of the box plot gives the mean value, the horizontal line in the middle of the box plot the median. The range indicated by the lines over and under the box show data, which is in the interquartile range of 5 % and 95 %.

DBSCAN analysis revealed TNFR1 cluster mean diameters in the range of 30 nm and 40 nm, where surprisingly two populations were observed (Supplementary Table 24). The first population consists of all conditions where TNF α did not bind to TNFR1. These mean diameters range from 30 nm until 35 nm. For the conditions where TNF α was bound to TNFR1, cluster diameters between 36 nm and 40 nm were revealed, indicating a clustering effect of TNFR1 after ligand binding. Overall, this increase was not suspected, as the TNFR1 cluster diameter determined by DBSCAN analysis is largely dependent of the NeNA values, which are between 15.4 nm and 16.2 nm for all conditions in the same order (Supplementary Table 25). However, Mann-Whitney-U-tests showed that apart for a few exceptions, no significant difference was revealed between the cluster sizes of ligand-bound compared to ligand-free TNFR1 conditions (Supplementary Figure 8). This does not mean that DBSCAN excludes clustering of TNFR1, but only that DBSCAN in combination with PALM is not sensitive enough to discriminate

RESULTS AND DISCUSSION

between the different oligomers of TNFR1. However, the numbers revealed for cluster diameters and NeNA values are in the range of several other publications (Endesfelder et al., 2014; Malkusch and Heilemann, 2016; Oppelt et al., 2018; Sanchez et al., 2019), demonstrating that PALM experiments were performed with sufficient quality.

In addition to the TNFR1-mEos2 diameters, the TNFR1-mEos2 clusters per μm^2 of all conditions investigated in this thesis were determined by DBSCAN analysis and illustrated (Figure 40, Supplementary Table 24).

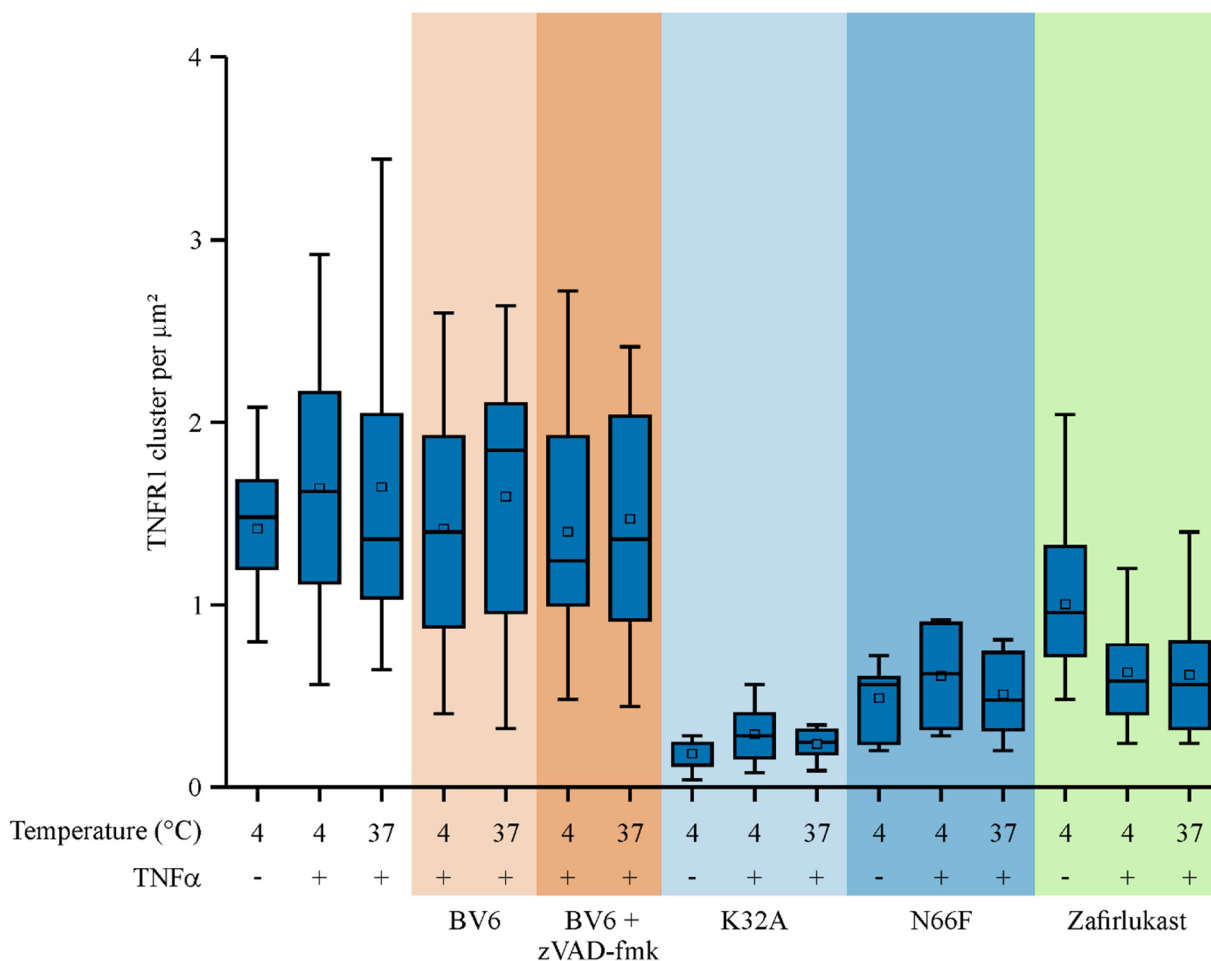


Figure 40: Comparison of the number of TNFR1-mEos2 clusters per μm^2 . Illustrated is the number of TNFR1-mEos2 clusters per μm^2 (box plots) of all conditions investigated in this thesis. The blue box shows the data, which are in the interquartile range between 25 % and 75 %. The square in the middle of the box plot gives the mean value, the horizontal line in the middle of the box plot the median. The range indicated by the lines over and under the box show data, which is in the interquartile range of 5 % and 95 %.

The conditions for TNF α -untreated and TNF α -treated TNFR1 and for apoptosis and necroptosis show comparable values of about 1.5 TNFR1-mEos2 clusters per μm^2 , revealing almost no change in the expression level. This was also confirmed by Mann-Whitney-U-tests demonstrating no significant

differences (Supplementary Figure 8). Thus, the density level of TNFR1-mEos2 seems to be constant in all of the conditions where TNFR1 was not directly affected by mutations and drugs. Once TNFR1 was mutated (K32A or N66F) a significant drop in the expression level is visible, which could be caused due to disturbance of protein stability, localization or inter-organelle transport. The decrease in the expression level was also revealed for all conditions, which were treated with zafirlukast. Thus, the inhibition by zafirlukast seems to downregulate the complex density of TNFR1. This turns zafirlukast to a promising drug as many diseases are connected with the overregulation of the expression level of TNFR1 (Cubillas et al., 2010; Puimège et al., 2014).

4.2 Molecular quantification with Alexa Fluor 647

In this chapter, the results to establish molecular quantification by analyzing photoswitching properties of the fluorophore Alexa Fluor 647 are presented.

4.2.1 Photoswitching properties of Alexa Fluor 647

Quantitative PALM (Fricke et al., 2015; Hummer et al., 2016) is an appropriate method to determine the number of proteins within unresolved protein clusters. The fluorescent protein mEos2 is suitable for quantitative single-molecule localization microscopy due to its superior brightness and its possibility for genetic and thus stoichiometric coupling to target proteins. In contrast to fluorescent proteins, organic fluorophores are brighter, which leads to a better localization-accuracy and thus a better resolution. SNAP-, CLIP- or HALO- tags provide the opportunity to label target proteins stoichiometrically with organic fluorophores (Gautier et al., 2008; Keppler et al., 2003). Thus, organic fluorophores should also be suitable to extract quantitative data from *d*STORM experiments.

In order to perform quantitative studies with organic fluorophores, the mathematical approach valid for photoconvertible fluorescent proteins was adapted for organic fluorophores, since the blinking model for organic fluorophores (e.g. Alexa Fluor 647) follow the principles of Figure 41. In this process, organic fluorophores switch after excitation between metastable dark states and a fluorescent state until the fluorophore is bleached.

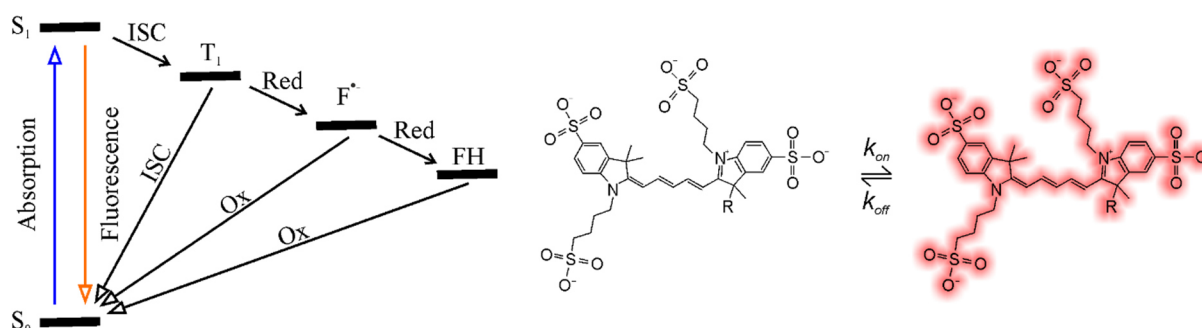


Figure 41: Photoswitching scheme of Alexa Fluor 647. *Alexa Fluor 647 switches reversibly between metastable dark states (T_1 , F^- , FH) and a fluorescent state until the fluorophore bleaches (for details see chapter 2.4). Left photoswitching scheme is adapted from van de Linde et al., 2011b, © 2011, with permission from Nature Publishing group.*

As it is important to detect each fluorescent event of each fluorophore, the video of a quantitative SMLM experiment must be started just before launching the excitation lasers. This is possible for photoconvertible fluorescent proteins, as the intensity of the UV laser can be carefully increased with time, resulting in individually detected fluorescence signals. Starting first the video and second the lasers at samples with organic fluorophores, leads to an initial burst of fluorescence in the first frame, resulting to an overlap of many detected PSFs, where the individual fluorescence signals cannot be distinguished. Thus, the analysis needs to start from the first frame after this emission burst. Since the first fluorescent

event must be subtracted, equation 17 (model for organic fluorophores) follows from equation 11 (model for fluorescent proteins).

$$p_m(n) = \sum_{k=0}^m \binom{m}{k} \frac{(-q)^{m-k}(1-q)^k}{1-[-q+(1-q)p_0]^m} \sum_{l=0}^{\min(k,n)} \binom{k}{l} \binom{n-l+k-1}{k-1} p_0^{k-l} (p-p_0)^l (1-p)^{n-j} - \frac{[-q+(1-q)p_0]^m}{1-[-q+(1-q)p_0]^m} \delta_{n,0} \quad (17)$$

$p_m(n)$ describes the blinking probability, n the number of blinking events, $m + 1$ the number of fluorophores, p the probability that a certain fluorophore bleaches after it was in the fluorescent state and q the fraction of undetected fluorophores. For $n = 0$ the $\delta_{n,0} = 0$, the last term turning zero.

4.2.2 Quantitative dSTORM imaging

For the experimental execution, Alexa Fluor 647 was selected due to its superior photoswitching property and its excellent brightness. A known monomeric Alexa Fluor 647 surface sample was prepared, where double-stranded DNA (21 bp labeled with biotin (3') and Alexa Fluor 647 (5') obtained from GATTAquant) was immobilized on a glass surface coated with BSA-biotin and streptavidin. For the determination of the blinking parameter p , dSTORM experiments were performed under three different UV light intensity reactivation conditions (no UV light; 0.01 kW/cm²; 0.01-0.06 kW/cm² (stepwise increasing activation)) (Figure 42). Number of blinking event cycles were extracted and histograms were analyzed with the adapted function for organic fluorophores. p values of 0.116 ± 0.005 for no UV irradiation, 0.056 ± 0.002 for constant UV irradiation and a comparable p value of 0.054 ± 0.002 for the stepwise UV irradiation were determined (Figure 42).

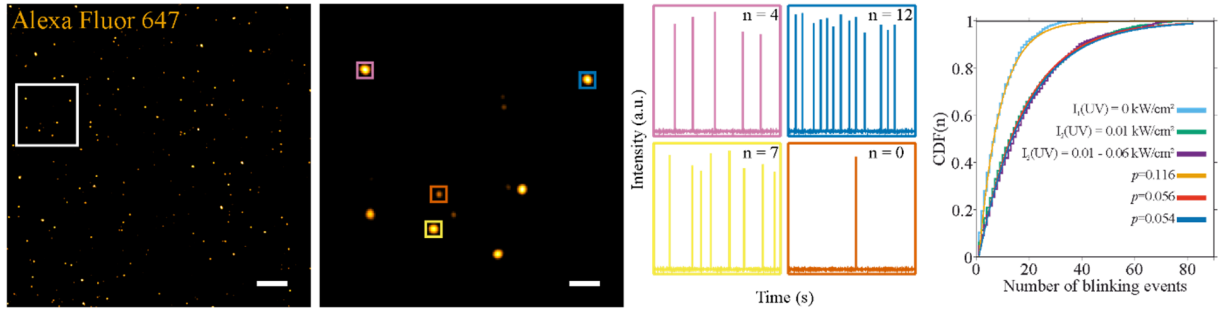


Figure 42: Single-molecule blinking analysis of Alexa Fluor 647. SMLM and zoomed image of representative Alexa Fluor 647 dyes immobilized on a glass surface with exemplary intensity traces. Cumulative illustration of the number of blinking event distribution of Alexa Fluor 647 with no UV (light blue), constant UV (green) and increasing UV (purple) irradiation conditions and corresponding fits (yellow for no UV, red for constant UV and blue for increasing UV irradiation conditions). (Scale bars, 1 μm dSTORM image (left panel), 200 nm dSTORM image (middle panel)). Analysis shown in the right panel was performed by Prof. Dr. Gerhard Hummer (Frankfurt, Germany). Right panel is adapted from Karathanasis et al., 2017; © 2017 Wiley-VCH Verlag GmbH & Co. KGaA, Weinheim, with permission from John Wiley and Sons.

RESULTS AND DISCUSSION

In order to verify whether quantification with Alexa Fluor 647 is also possible for higher oligomers, a DNA origami structure was designed as a calibration standard, comprising three Alexa Fluor 647 staple strands at each end with a distance of 120 nm (commercially obtained by GATTAquant). The single fluorophores of one of these spots exhibit distances between 4 nm and 8 nm. Thus, the two ends of one DNA origami construct can be resolved by *d*STORM, resulting in super-resolved double spots. This construct has two advantages. The first advantage is that double spots with the respective distance were searched and evaluated in super-resolved images, leading to a reduction of the analysis of non-specific background. The second advantage lies in the procedure of DNA hybridization. This ensures that exactly three Alexa Fluor 647 dyes are located at two defined sites.

In the process of imaging and analysis, 358 DNA origami double spots with stepwise increasing UV light intensities were measured and evaluated (Figure 43A). The expected monomer until decamer blinking event curves are plotted with a p value of 0.056 and compared to the blinking event distribution from the trimeric sample (Figure 43B). Analysis revealed that the blinking distribution of the trimeric sample fits well to the predicted trimeric curve. However, for higher number of blinking events the curve shows significant deviations. In contrast to fluorescent proteins, organic fluorophores are in direct contact with the environment and the blinking property of Alexa Fluor 647 is sensitive to it. Eventually, these deviations are due to interactions of Alexa Fluor 647 to the nano-environment to the DNA origami system. To control this assumption, the number of blinking event distribution of the trimeric sample was analyzed with two different p values ($p_1 = p_2 = 0.072$; $p_3 = 0.028$) (Figure 43B) yielding good overlap between data and expected theory.

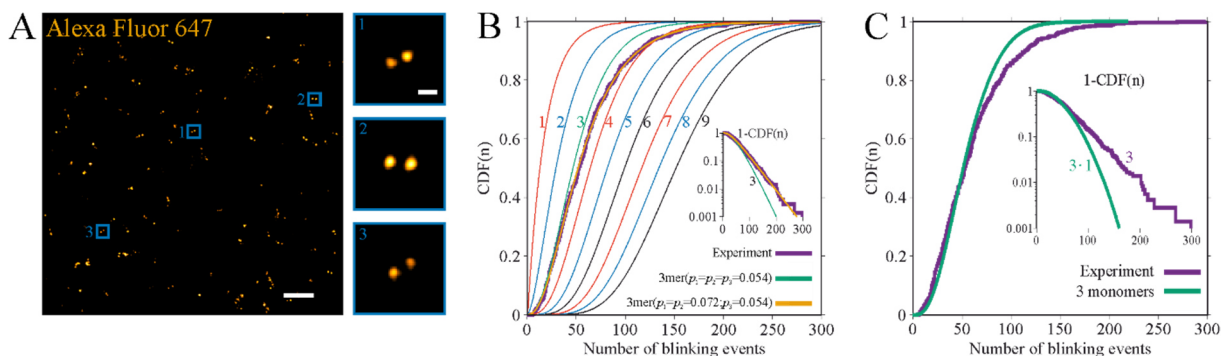


Figure 43: Single-molecule blinking analysis of three Alexa Fluor 647 fluorophores. SMLM image and zoomed regions of two times three Alexa Fluor 647 dyes on two corners of a DNA origami construct. (Scale bars, 1 μm left image, 100 nm zoomed regions) (B+C) Cumulative illustration of the number of blinking event distribution of the trimeric sample (purple line) and ideal curves for monomer until nonamer shown in indicated colors. The ideal trimeric curve does not fit to the experimental trimeric curve. A trimeric fit function with two different p values ($p_1 = 0.072$ and $p_2 = 0.054$) is the most accurate way to describe the experimental data. Analysis shown in B and C was performed by Prof. Dr. Gerhard Hummer (Frankfurt, Germany). B and C is adapted from Karathanasis et al., 2017; © 2017 Wiley-VCH Verlag GmbH & Co. KGaA, Weinheim with permission from John Wiley and Sons.

This indicates that the local environment of Alexa Fluor 647 affects blinking properties.

Overall, different models were fit to the trimeric blinking event distribution (Table 2). Log likelihood analysis revealed that the best model describing the number of blinking event distribution is the model with $p_1 = p_2 = 0.072$ and $p_3 = 0.028$. Interestingly, the data was only fit with a q value of zero. Thus, there is no observation of incomplete labeling. Furthermore, an artificial trimer was generated from the data of the monomeric Alexa Fluor 647 sample to verify whether the nano-environment influences blinking distribution of Alexa Fluor 647 (Figure 43C). Therefore, the data of three monomers were grouped into one ideal trimer. This ideal trimer shows again a significantly difference at higher number of blinking events, again signifying a change in the blinking property.

Table 2: Results of different maximum likelihood fits of trimeric Alexa Fluor 647. Listed are the models, the fit parameter p_1 - p_3 , q and the corresponding log likelihood values L . Model 1: Three fluorophores with variable $p_1 = p_2$, p_3 and q ; Model 2: Two fluorophores with variable p_1 , p_2 and q ; Model 3-7: Three fluorophores with variable $p_1=p_2=p_3$ and q . Analysis of the results presented in this table was performed by Prof. Dr. Gerhard Hummer (Frankfurt, Germany). Table is adapted from Karathanasis *et al.*, 2017; © 2017 Wiley-VCH Verlag GmbH & Co. KGaA, Weinheim with permission from John Wiley and Sons.

MODEL	p_1	p_2	p_3	q	L
1	0.072	0.072	0.028	0	-3522.5
2	0.032	0.032	-	0	-3536.1
3	0.032	-	-	0	-3536.3
4	0.046	-	-	0.035	-3528.2
5	0.052	-	-	0.175	-3533.4
6	0.055	-	-	0.285	-3535.9
7	0.059	-	-	0.375	-3537.1

4.2.3 Future directions for molecular quantification with organic fluorophores

In this thesis, Alexa Fluor 647 was applied as organic fluorophore to operate as alternative quantitative approach to the work of Fricke *et al.* (Fricke *et al.*, 2015). First, it was shown that Alexa Fluor 647 shows more blinking events with higher UV-intensity, as the p values decrease. These observations are consistent with previous studies showing an increasing number of blinking events of Alexa Fluor 647 fluorophores due to the increasing transition from the non-fluorescent dark-state to the fluorescent state by UV light (Dempsey *et al.*, 2011; Xu *et al.*, 2012). However, applying the p value determined for the monomeric sample, it was not possible to analyze the trimeric sample, since the higher number of blinking events matched the model of the theoretical tetrameric curve. The change in the nano-environment could trigger a modification in the photophysical properties of Alexa Fluor 647. These

observation are in agreement with multiple studies showing changes of the quantum yield of Alexa Fluor 647 at different environments (Cox et al., 2004; Szabó et al., 2018). Thus, well-planned experiments where the nano-environment of the organic fluorophores is not changed are necessary for quantitative studies. The application of a protein-tag such as the SNAP-tag could have considerable potential. The organic fluorophore would be coupled to the SNAP-tag via its nucleobase Cystein145. This would place the dye in the center of the SNAP-tag, which is reminiscent of the construct of fluorescent proteins, where the chromophore is protected by its characteristic β -barrel structure. This might lead to more homogenous blinking properties and thus enabling a robust application for quantification with organic fluorophores. In addition, SNAP fusions were successfully used to label biological samples for single-molecule imaging (Barlag et al., 2016; Klein et al., 2011; Sakin et al., 2016; Sungkaworn et al., 2017).

4.3 Quantitative PALM analysis of pfEMP1 in erythrocytes

In the following chapter, the arrangement of the pfEMP1 variant VAR2CSA is analyzed with quantitative PALM and DBSCAN. Furthermore, a spatial model is generated and discussed with different models from literature.

4.3.1 Super-resolution imaging of VAR2CSA in erythrocytes

pfEMP1 is crucial in the pathophysiology of tropical malaria (Leech et al., 1984). VAR2CSA is one variant of pfEMP1, which is expressed in erythrocytes of the placenta after the infection with the parasite *Plasmodium falciparum* (Salanti et al., 2003) in defined areas called knobs (Sharma, 1997). It is known that patients with sickle cell anemia (possessing HbAS erythrocytes) are immune in contrast to humans with normal healthy erythrocytes (HbAA) (Allison, 1964; Willcox et al., 1983) (Figure 7). In order to determine the spatial arrangement of VAR2CSA to comprehend the reasons for the immunity of sickle cell anemia patients to malaria, HbAA and HbAS erythrocytes were infected with the G-6 mutant of the FCR3 parasite, where VAR2CSA is fused with two copies of mEos2. Infected HbAA and HbAS erythrocytes were imaged using PALM in TIRF mode to visualize only the cell surface. Multiple super-resolved fluorescent clusters were revealed on the plasma membrane of G-6 infected HbAA and HbAS erythrocytes, whereas no fluorescent signal was visible on erythrocytes infected with the FCR3 wt (Figure 44A, B, C). Thus, both HbAA and HbAS erythrocytes were successfully infected with the G-6 mutant and VAR2CSA was expressed with mEos2 on the plasma membrane. Furthermore, low background signal was visible, enabling quantitative analysis of VAR2CSA.

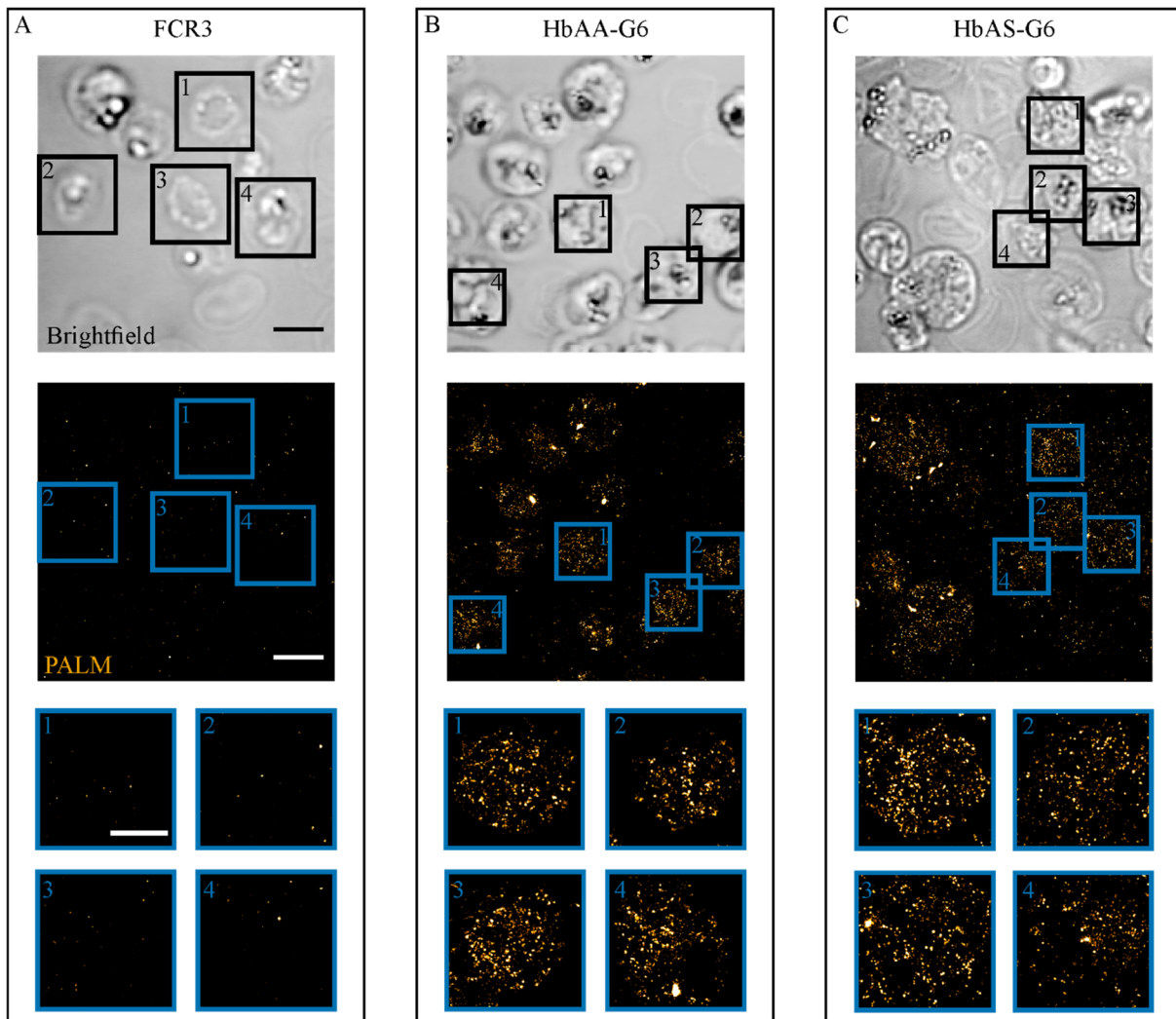


Figure 44: Brightfield and PALM images from FCR3, HbAA-G-6 and HbAS-G-6 probes. Erythrocytes infected with FCR3 (A) (left panel) and G-6-mutants (for HbAA erythrocytes (middle panel) (B) and HbAS erythrocytes (right panel) (C)) are illustrated. From top to bottom first a brightfield- second a PALM- and third magnified images of representative cells are shown. (Scale bars, brightfield and PALM 5 μm , magnified regions 3 μm).

To analyze possible differences in the VAR2CSA arrangement of HbAA and HbAS erythrocytes, DBSCAN analysis was performed. VAR2CSA clusters exhibited an average diameter of 54 ± 27 nm and 64 ± 31 nm in HbAA and HbAS infected erythrocytes (Figure 45), revealing larger VAR2CSA clusters in HbAS compared to HbAA erythrocytes. Significant differences between the cluster size distributions were confirmed by the Mann-Whitney-U-test with a value of $p < 0.001$ (Figure 45).

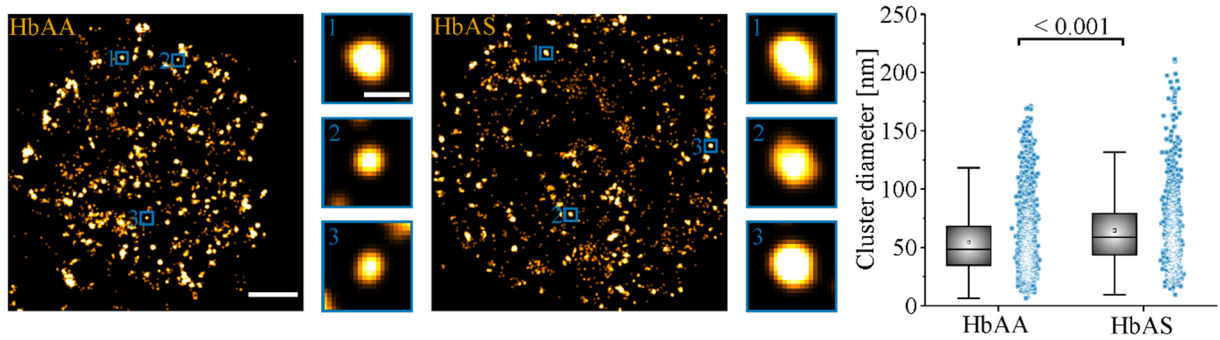


Figure 45: VAR2CSA cluster diameter in HbAA and HbAS erythrocytes. One HbAA and HbAS erythrocyte, each with three zoomed VAR2CSA-mEos2 clusters are shown. In addition, all determined cluster sizes for HbAA and HbAS erythrocytes are illustrated as box- and dot diagrams. (Scale bars, PALM images $1\mu\text{m}$, magnified regions 100 nm). Right panel is adapted from Sanchez *et al.*, 2019.

Apart from the cluster size, the mean numbers of VAR2CSA proteins per knob were determined by analyzing the average number of detection events, corrected for over- and undercounting. To correct for overcounting, localizations of the PALM experiments, which were detected in consecutive frames were grouped to one localization and an average of 2.5 fluorescent events for mEos2 was utilized. This value was determined in the work by Fricke *et al.* in 2015 (Fricke *et al.*, 2015) by analyzing a monomeric mEos2 single-molecule surface and monomeric CD86 transfected with mEos2 in HeLa cells. Furthermore, this value was confirmed by Krüger *et al.* in 2017 (Krüger *et al.*, 2017b), analyzing CD86 transfected with mEos2 in HEK 293 cells and in this thesis where CD86-mEos2 was transfected in MEF cells (chapter 4.1.2). Since same buffer and imaging conditions were used in all of these experiments, it is assumed that the blinking property of mEos2 did not change significantly. To correct for undercounting, calculation was performed with a detection efficiency of 70 %, which is in the range of multiple studies (Hummer *et al.*, 2016 (70.5 %); Krüger *et al.*, 2017b (71 %)) and chapter 4.1.2 with 71 %. Considering corrections for over- and undercounting, HbAA erythrocytes revealed 3.3 ± 1.7 VAR2CSA molecules per knob (771 fluorescence clusters, 130 erythrocytes, three independent experiments). HbAS erythrocytes exhibit 4.3 ± 2.5 VAR2CSA molecules per knob (638 fluorescence clusters, 76 erythrocytes, two independent experiments) (Figure 46A). Thus, HbAS erythrocytes not only possess larger VAR2CSA clusters, but also have in average more VAR2CSA proteins per knob.

After analyzing the VAR2CSA numbers per knob, the spatial configuration of VAR2CSA over the plasma membrane was determined. Thus, the number of VAR2CSA clusters per μm^2 were investigated by DBSCAN analysis. For HbAA erythrocytes, 2.9 ± 1.2 clusters per μm^2 were obtained. In HbAS erythrocytes, 1.6 ± 0.7 VAR2CSA clusters per μm^2 were revealed (Figure 46). Statistical analysis using the Mann-Whitney-U-test indicated that both the distributions of cluster diameters and cluster densities are significantly different ($p < 0.001$, Figure 46A, B).

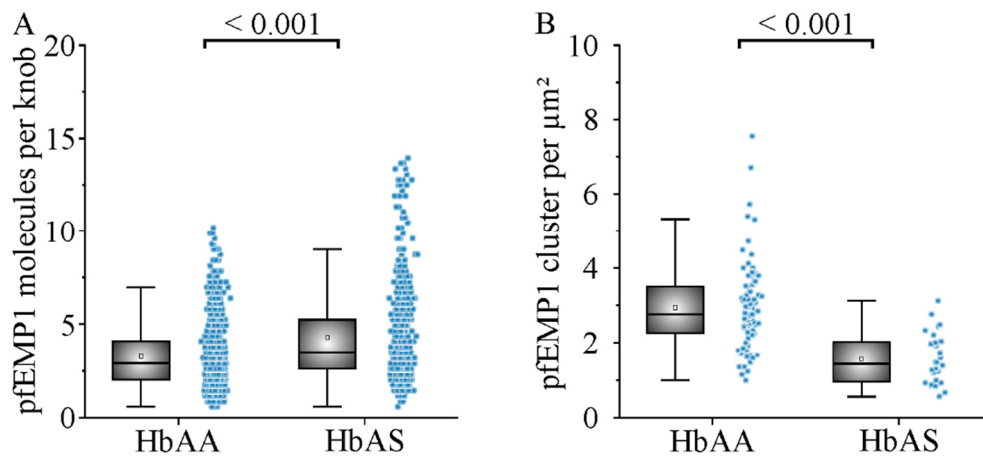


Figure 46: VAR2CSA molecules per knob and pfEMP1 clusters per μm^2 . (A) VAR2CSA molecules per knob are illustrated as box and dot diagram for HbAA and HbAS erythrocytes. (B) The number of VAR2CSA cluster per μm^2 in HbAA and HbAS erythrocytes as box and dot diagram are shown. (***) $p < 0.001$, high significant different). Figure is adapted from Sanchez *et al.*, 2019.

4.3.2 A spatial model of VAR2CSA in HbAA and HbAS erythrocytes

Considering the VAR2CSA diameters determined by DBSCAN analysis (54 ± 27 nm for HbAA and 64 ± 31 nm for HbAS erythrocytes), it can be concluded that the VAR2CSA proteins are centrally located on the knob, as these numbers are smaller than knob diameters determined by cryo-tomograms and scanning electron microscopy (80-90 nm for HbAA and 200 nm for HbAS erythrocytes) (Cyrklaff *et al.*, 2016) (Figure 47, left pattern). Since the localization precision of 13.1 nm (determined by NeNA) is well enough to resolve structures within 80-200 nm, there is no reason to assume that VAR2CSA proteins are located in the peripheral region, as fluorescence cluster would look like a ring form (Figure 47, middle pattern). If VAR2CSA were arranged all over the entire knob structure, fluorescence cluster would exhibit a larger diameter than the diameter of knobs determined by cryo-tomograms and scanning electron microscopy, due to the worse resolution (Figure 47, right pattern).

In the work from Joergensen *et al.* from 2010, it is described that VAR2CSA arranges to a globular conformation in spite of a linear “beads-on-a-string” arrangement (Joergensen *et al.*, 2010). With this assumption and their results that one VAR2CSA protein has a surface size of 110 nm^2 and knobs a surface size of 13000 nm^2 , maximally 110 VAR2CSA molecules could be packed on one knob (Joergensen *et al.*, 2010). As PALM images and DBSCAN analysis indicated that the VAR2CSA cluster diameter is smaller than the diameter of knobs, the number of VAR2CSA molecules per knob is likely less. The numbers determined in this study (3.3 ± 1.7 in HbAA and 4.3 ± 2.5 in HbAS erythrocytes) are in a comparable range as reported by Xu *et al.* in 2013, reporting numbers of six to eight VAR2CSA molecules per knob, determined by microfluidic flow-based adhesion experiments (Xu *et al.*, 2013). VAR2CSA numbers determined by PALM and the usage of the Mann-Whitney-U-test revealed that in average there are less VAR2CSA molecules per knob in HbAA than in HbAS erythrocytes. Since VAR2CSA is the pathogenic factor in malaria, as it clusters with proteins such as the intercellular

adhesion molecule 1 (ICAM-1), CD36, endothelial protein C receptor (EPCR) and CR1 with uninfected erythrocytes (Smith, 2014; Wahlgren et al., 2017), this larger number of VAR2CSA proteins in HbAS erythrocytes seems at the first view unexpected. More VAR2CSA do not cause life-threatening complications, as HbAS erythrocytes show immunity. However, DBSCAN analysis revealed that there are overall more knobs expressing VAR2CSA in HbAA (2.9 ± 1.2 per μm^2) compared to HbAS (1.6 ± 0.7 per μm^2) erythrocytes. Thus, HbAS erythrocytes either contain fewer knobs or do not express VAR2CSA in all knobs. Fairhurst *et al.* showed in 2012 that knobs of HbAS are larger compared to knobs of HbAA erythrocytes (Fairhurst et al., 2012). Therefore, it is indicated that less VAR2CSA clusters are observed in HbAS erythrocytes, as there are fewer knobs. Potentially, this is the disease-inducing factor, as a minimum number of knobs must be expressed with VAR2CSA to cluster with other uninfected erythrocytes.

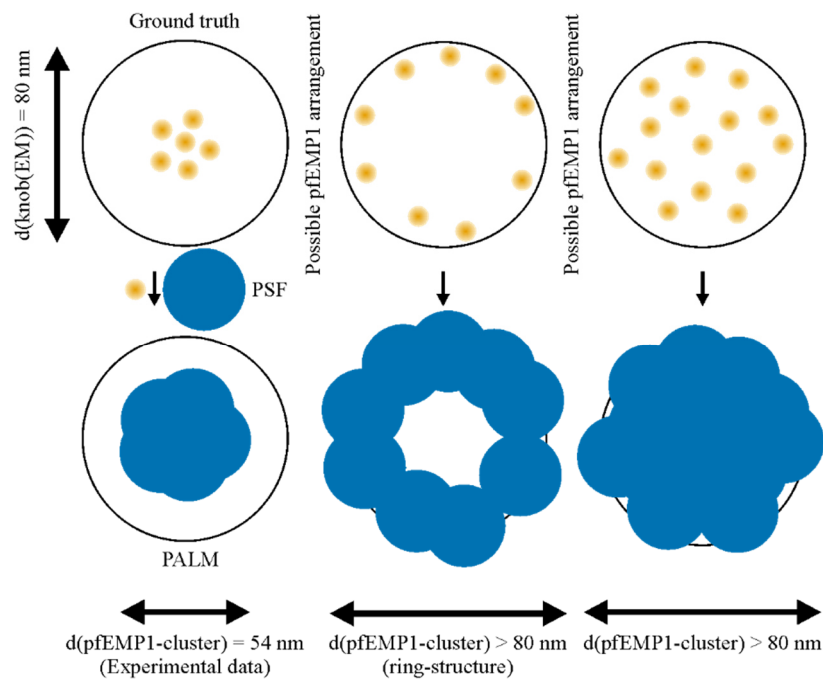


Figure 47: Possible VAR2CSA arrangement scheme. Possible models of the pfEMP1 arrangement on knobs of HbAA erythrocytes and corresponding schemes how the particular PALM image would look like. Experimental data suggests that the left scheme is present in HbAA and HbAS erythrocytes. Figure is adapted from Sanchez *et al.*, 2019.

CONCLUSION AND OUTLOOK

Multiple quantitative approaches in combination with fluorescence microscopy are available to determine numbers of biomolecules in cells. Intensity-based counting or photobleaching analysis were one of the first methods, which are limited in application due to the diffraction-limited resolution of fluorescence microscopy. Methods such as quantitative PAINT or PALM can extract quantitative data within super-resolved images. However, the resolution is sufficient to visualize single protein complexes but not single proteins within these complexes. At this point, gimmicks have to be applied, where quantitative data is extracted from binding frequencies (qPAINT) or blinking kinetics (qPALM). In the context of this study, quantitative models of TNFR1 and VAR2CSA were obtained using qPALM. Furthermore, the application of quantitative *d*STORM was established with Alexa Fluor 647.

5.1 A quantitative model for TNFR1

To create a quantitative model of TNFR1, a stable cell line was generated where TNFR1 was expressed with the fluorescent protein mEos2 on near-endogenous level. These reconstituted cells were successfully verified concerning function of short-term (NF- κ B) and long-term (apoptosis and necroptosis) signaling cascades. These cells provided the basis for visualization and quantification of TNFR1 on the plasma membrane by qPALM. Analysis revealed that TNF α -untreated TNFR1 exists in a mixture of monomers and dimers. In previous studies, these results were also revealed by western blot and crystallographic experiments. TNF α -treated TNFR1 arranges into a dominant fraction of trimers and some larger oligomers with only a small fraction of monomers. Analysis revealed that the largest probability concerning the fraction of “larger oligomers” is the arrangement of nonamers. Models from other studies assume also a dimeric and hexameric arrangement of TNF α -treated TNFR1. However, qPALM analysis revealed a dimeric fraction of TNF α -treated TNFR1, but indicated a low probability of hexameric oligomers. Possibly, the interaction between two PLADs of two TNFR1₃-TNF α ₃ units is too weak to arrange into a stable structure. Eventually, the formation of a triangular structure by the interaction of three PLAD-PLAD linkages, where per TNFR1₃-TNF α ₃ unit only one free PLAD is present, is more stable and necessary for clustering.

The quantification of the TNFR1 K32A mutant demonstrated that a functional PLAD is necessary for the successful arrangement of the TNF α -untreated dimers and ligand binding. Furthermore, the analysis of the TNFR1 N66F mutant revealed that a functional CRD2 domain is also required for efficient ligand

binding. This is in agreement with another study showing the same results by western blot and immunoprecipitation experiments.

Next, the oligomeric state of TNFR1 after the treatment with the drug zafirlukast was investigated. Quantitative analysis showed a shift to the monomeric fraction and the loss of the ability for effective ligand binding due to the inhibition of the PLAD by zafirlukast, which prevents the formation of TNFR1 dimers. Furthermore, western blot experiments revealed the inhibition of the NF- κ B signaling cascade. This makes zafirlukast a promising drug for treating and inhibiting TNFR1 in diseases. Another pioneering possibility to treat diseases caused by TNFR1 malfunction is the induction of cell death to ensure a coordinated degradation of malignant tissue while avoiding the release of inflammatory and cytotoxic signals. Thus, the oligomeric state of TNFR1 was investigated after apoptosis and necroptosis induction. However, no difference was found in the oligomeric state of TNFR1 compared to cells where the NF- κ B signaling cascade was active. This leads to the conclusion that the differences in the biological systems concerning NF- κ B or cell death cascades occur in the signaling cascade, but not in the oligomeric state of TNFR1 on the plasma membrane.

According to the results of this thesis, the oligomeric state of TNFR1 can be divided into signaling active and signaling inactive species. If TNFR1 binds TNF α and transmits a signal into the cell, the majority of the receptors arrange to trimers and partially to nonamers. Signaling inactive TNFR1 was accomplished by the inhibition of extracellular parts of TNFR1, resulting in the abolishment of binding TNF α (Figure 48).

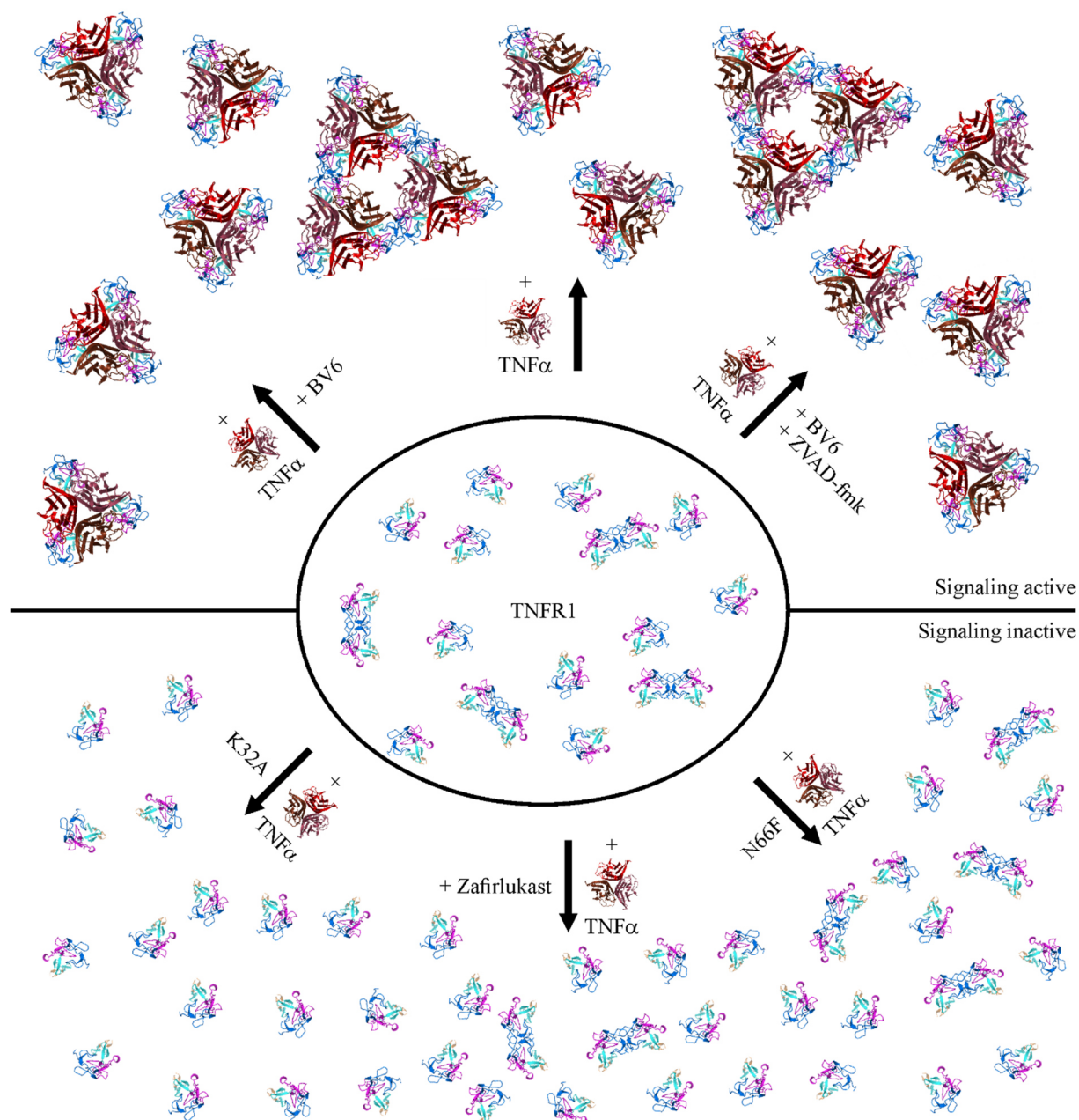


Figure 48: Summary of the oligomeric states of TNFR1. *TNF α -treated TNFR1 showed a dominant fraction of trimers and nonamers, which are the signaling active species. The formation of these species is independent of which signaling cascade is activated. Apoptosis can be induced by BV6 and the addition of BV6 and ZVAD-fmk leads to necroptosis. TNFR1 mutants (K32A, N66F) or TNFR1 inhibited by zafirlukast revealed only monomers or mixtures of monomers and dimers as signaling inactive species.*

After generating a quantitative model of TNFR1, the question arises, what comes next? The quantification of the ligand TNF α is obvious to refine the quantitative model between TNFR1 and TNF α on the plasma membrane. For this experiment, the method of choice would be qPAINT. A SNAP-tag coupled to one TNF α trimer would allow stoichiometric labeling of the ligand. A single-stranded DNA

coupled to a BG should bind to this construct, enabling the visualization and quantification of TNF α bound to TNFR1. In order to obtain a more comprehensive overview of the function of TNFR1, the quantification of some downstream signaling proteins would be of great interest. The quantification of the proteins TRADD, TRAF2, RIP1, and cIAP1/2 would reveal the entire composition of complex I and its relationship to TNFR1, giving more knowledge about the signaling system TNFR1 and thus more potential targets to manipulate the signaling cascade of TNFR1. Quantification of the proteins present in complex II would be of similar importance. However, these protein complexes are located in the intracellular environment, which complicates the quantification using super-resolution microscopy.

5.2 A quantitative model of VAR2CSA

The oligomeric state of the protein VAR2CSA was investigated on the plasma membrane of normal human erythrocytes (HbAA) and erythrocytes from humans with sickle cell anemia (HbAS), after the infection of the parasite *Plasmodium falciparum*, with qPALM. *Plasmodium falciparum* is known to cause tropical malaria in humans by the infection of human erythrocytes where the membrane protein family pfEMP1 is expressed. pFEMP1 expression causes distinct cytoadhering phenotypes leading to the segregation of the erythrocytes in the vascular system. This disturbs an adequate blood flow, which cause life-threatening complications. VAR2CSA is one of the members of the pFEMP1 protein family, which is relevant in tropical malaria from pregnant women and their unborn children. It is known that VAR2CSA mediates cytoadhesion of infected erythrocytes with CSA, which covers the intervillous space of pregnant women. This impairs placenta functions and is life-threatening for pregnant women and their infants. The protein family pFEMP1 (including VAR2CSA) is known to be expressed in certain areas of the erythrocyte plasma membrane called knobs. The spatial arrangement of these knobs and the number of VAR2CSA proteins per knob are from great interest as erythrocytes from patients with sickle cell anemia are immune against malaria. Thus, HbAA and HbAS erythrocytes were infected with a G-6 mutant of FCR3 parasites resulting in the expression of VAR2CSA fused to mEos2. VAR2CSA was visualized for the first time on the single-molecule level on the plasma membrane of intact erythrocytes. Analysis revealed a larger cluster size and more VAR2CSA proteins per knob in HbAS compared to HbAA erythrocytes. However, more VAR2CSA clusters per μm^2 were found in HbAA than in HbAS erythrocytes. Due to the resolution achieved in the PALM experiments and the knowledge that knobs have a diameter of about 90 nm in HbAA and 200 nm in HbAS erythrocytes, it is indicated that the VAR2CSA proteins are located in the center of knobs. Furthermore, a larger number of VAR2CSA proteins per knob do not seem to be the promoting effect for segregation of erythrocytes in the vascular system, since HbAS erythrocytes show immunity against malaria. However, there are more knobs expressed with VAR2CSA in HbAA than in HbAS erythrocytes. Potentially this circumstance is of great importance, as a certain minimum number of knobs need to be expressed with VAR2CSA to have critical effects on the vascular system.

What would be the next step to gain a better overview in malaria disease? In the case of the VAR2CSA system, the quantification of other proteins that are embedded in the area of knobs and potentially interact with VAR2CSA would provide valuable insights. The quantification of proteins such as the knob-associated histidine-rich protein (KAHRP) or ankyrin would be suitable as they were associated with knob activity during malaria infections. Research on a medical aspect would also be of great interest. Medications could be tested to verify changes in the VAR2CSA arrangement in the knobs.

5.3 Quantification with organic fluorophores

Finally, a methodical task was addressed in this thesis. The quantitative qPALM approach was established for the organic fluorophore Alexa Fluor 647. Therefore, single Alexa Fluor 647 dyes linked to DNA and a DNA origami system with two times three Alexa Fluor 647 dyes with a distance of about 120 nm were immobilized on a glass surface and *d*STORM experiments were performed. Prior robust analysis, it was discovered that the theoretical model to analyze the number of blinking events for fluorescent proteins cannot be adopted for organic fluorophores. The first frame where the sample is excited results in a burst of fluorescence of all organic fluorophores, making it impossible to detect the signals of all fluorophores separately. This aspect was included in the theoretical model and monomeric and trimeric Alexa Fluor 647 data were analyzed. Results revealed that the blinking distribution of the three Alexa Fluor 647 fluorophores could not be analyzed with the parameters obtained from the monomer sample. Assuming that one of the three fluorophores differed in its blinking properties, the data was analyzed properly. These differences in the blinking properties were attributed to different nano-environments of the fluorophores. However, this is generally a disadvantage for potential future applications of blinking based quantitative investigations with organic fluorophores. The blinking properties seem to be much more unpredictable compared to fluorescent proteins where the chromophore is protected by its characteristic β -barrel structure. However, how can this approach be used efficiently for future quantification? A solution to minimize the fluctuations of the blinking properties of Alexa Fluor 647 would be the usage of protein tags. In the case of the SNAP-tag, the organic fluorophore would be attached by BG to a specific amino acid of the target protein and thus separated from the surrounding environment by the vicinity of the protein. As a result, the fluorophore would be constantly exposed to the same environment and the blinking properties should not change drastically, thus allowing robust quantitative application with organic fluorophores.

REFERENCES

- Abbe E. Beiträge zur Theorie des Mikroskops und der mikroskopischen Wahrnehmung. *Archiv für Mikroskopische Anatomie*, 9 (1): 413–418, 1873.
- Adam V, Lelimosin M, Boehme S, Desfonds G, Nienhaus K, Field MJ, Wiedenmann J, McSweeney S, Nienhaus GU, and Bourgeois D. Structural characterization of IrisFP, an optical highlighter undergoing multiple photo-induced transformations. *Proceedings of the National Academy of Sciences of the United States of America*, 105 (47): 18343–18348, 2008.
- Adkins JC and Brogden RN. Zafirlukast. A review of its pharmacology and therapeutic potential in the management of asthma. *Drugs*, 55 (1): 121–144, 1998.
- Agbanoma G, Li C, Ennis D, Palfreeman AC, Williams LM, and Brennan FM. Production of TNF- α in macrophages activated by T cells, compared with lipopolysaccharide, uses distinct IL-10-dependent regulatory mechanism. *Journal of immunology (Baltimore, Md. 1950)*, 188 (3): 1307–1317, 2012.
- Aggarwal BB. Signalling pathways of the TNF superfamily: A double-edged sword. *Nature reviews. Immunology*, 3 (9): 745–756, 2003.
- Aggarwal BB, Gupta SC, and Kim JH. Historical perspectives on tumor necrosis factor and its superfamily: 25 years later, a golden journey. *Blood*, 119 (3): 651–665, 2012.
- Airy GB. On the Diffraction of an Object-glass with Circular Aperture. *Transactions of the Cambridge Philosophical Society* (5): 283–291, 1835.
- Aitken CE, Marshall RA, and Puglisi JD. An oxygen scavenging system for improvement of dye stability in single-molecule fluorescence experiments. *Biophysical Journal*, 94 (5): 1826–1835, 2008.
- Akash MSH, Rehman K, and Liaqat A. Tumor Necrosis Factor-Alpha: Role in Development of Insulin Resistance and Pathogenesis of Type 2 Diabetes Mellitus. *Journal of cellular biochemistry*, 119 (1): 105–110, 2018.
- Alberts B, Johnson A, Lewis J, Raff M, Roberts K, and Walter P. *Molecular biology of the cell*. New York, NY: Garland Science Taylor & Francis Group, 2002.
- Allison AC. Polymorphism and natural selection in human populations. *Cold Spring Harbor symposia on quantitative biology*, 29: 137–149, 1964.
- Andersen P, Nielsen MA, Resende M, Rask TS, Dahlbäck M, Theander T, Lund O, and Salanti A. Structural insight into epitopes in the pregnancy-associated malaria protein VAR2CSA. *PLoS pathogens*, 4 (2): e42, 2008.
- Ando R, Mizuno H, and Miyawaki A. Regulated fast nucleocytoplasmic shuttling observed by reversible protein highlighting. *Science (New York, N.Y.)*, 306 (5700): 1370–1373, 2004.

REFERENCES

- Andresen M, Stiel AC, Trowitzsch S, Weber G, Eggeling C, Wahl MC, Hell SW, and Jakobs S. Structural basis for reversible photoswitching in Dronpa. *Proceedings of the National Academy of Sciences*, 104 (32): 13005–13009, 2007.
- Aoki V, Sousa Jr JX, Fukumori LMI, Périgo AM, Freitas EL, and Oliveira ZNP. Imunofluorescência direta e indireta. *Anais Brasileiros de Dermatologia*, 85 (4): 490–500, 2010.
- Ardley HC and Robinson PA. E3 ubiquitin ligases. *Essays in biochemistry*, 41: 15–30, 2005.
- Arvanitis M, Li D-D, Lee K, and Mylonakis E. Apoptosis in *C. elegans*: Lessons for cancer and immunity. *Frontiers in cellular and infection microbiology*, 3: 67, 2013.
- Au P-YB and Yeh W-C. Physiological roles and mechanisms of signaling by TRAF2 and TRAF5. *Advances in experimental medicine and biology*, 597: 32–47, 2007.
- Axelrod D, Burghardt TP, and Thompson NL. Total internal reflection fluorescence. *Annual review of biophysics and bioengineering*, 13: 247–268, 1984.
- Ayres Pereira M, Mandel Clausen T, Pehrson C, Mao Y, Resende M, Daugaard M, Riis Kristensen A, Spliid C, Mathiesen L, E Knudsen L, Damm P, G Theander T, R Hansson S, A Nielsen M, and Salanti A. Placental Sequestration of Plasmodium falciparum Malaria Parasites Is Mediated by the Interaction Between VAR2CSA and Chondroitin Sulfate A on Syndecan-1. *PLoS pathogens*, 12 (8): e1005831, 2016.
- Azevedo VF, Silva MBG, Marinello DK, Santos FDD, and Silva GBG. Leukopenia and thrombocytopenia induced by etanercept: Two case reports and literature review. *Revista brasileira de reumatologia*, 52 (1): 110–112, 2012.
- Bai L, Smith DC, and Wang S. Small-molecule SMAC mimetics as new cancer therapeutics. *Pharmacology & therapeutics*, 144 (1): 82–95, 2014.
- Baker SM, Buckheit RW, and Falk MM. Green-to-red photoconvertible fluorescent proteins: Tracking cell and protein dynamics on standard wide-field mercury arc-based microscopes. *BMC cell biology*, 11: 15, 2010.
- Banner DW, D'Arcy A, Janes W, Gentz R, Schoenfeld HJ, Broger C, Loetscher H, and Lesslauer W. Crystal structure of the soluble human 55 kd TNF receptor-human TNF beta complex: Implications for TNF receptor activation. *Cell*, 73 (3): 431–445, 1993.
- Barlag B, Beutel O, Janning D, Czarniak F, Richter CP, Kommnick C, Göser V, Kurre R, Fabiani F, Erhardt M, Piehler J, and Hensel M. Single molecule super-resolution imaging of proteins in living *Salmonella enterica* using self-labelling enzymes. *Scientific reports*, 6: 31601, 2016.
- Barnwell JW, Asch AS, Nachman RL, Yamaya M, Aikawa M, and Ingravallo P. A human 88-kD membrane glycoprotein (CD36) functions in vitro as a receptor for a cytoadherence ligand on Plasmodium falciparum-infected erythrocytes. *The Journal of clinical investigation*, 84 (3): 765–772, 1989.
- Baudin A, Ozier-Kalogeropoulos O, Denouel A, Lacroute F, and Cullin C. A simple and efficient method for direct gene deletion in *Saccharomyces cerevisiae*. *Nucleic acids research*, 21 (14): 3329–3330, 1993.

- Beer. Bestimmung der Absorption des rothen Lichts in farbigen Flüssigkeiten. *Annalen der Physik und Chemie*, 162 (5): 78–88, 1852.
- Berger R, Jennewein C, Marschall V, Karl S, Cristofanon S, Wagner L, Vellanki SH, Hehlhans S, Rödel F, Debatin K-M, Ludolph AC, and Fulda S. NF- κ B is required for Smac mimetic-mediated sensitization of glioblastoma cells for γ -irradiation-induced apoptosis. *Molecular cancer therapeutics*, 10 (10): 1867–1875, 2011.
- Bernardino L, Agasse F, Silva B, Ferreira R, Grade S, and Malva JO. Tumor necrosis factor-alpha modulates survival, proliferation, and neuronal differentiation in neonatal subventricular zone cell cultures. *Stem cells (Dayton, Ohio)*, 26 (9): 2361–2371, 2008.
- Bertrand MJM, Lippens S, Staes A, Gilbert B, Roelandt R, Medts J de, Gevaert K, Declercq W, and Vandenabeele P. cIAP1/2 are direct E3 ligases conjugating diverse types of ubiquitin chains to receptor interacting proteins kinases 1 to 4 (RIP1-4). *PLoS one*, 6 (9): e22356, 2011.
- Bertrand MJM, Milutinovic S, Dickson KM, Ho WC, Boudreault A, Durkin J, Gillard JW, Jaquith JB, Morris SJ, and Barker PA. cIAP1 and cIAP2 facilitate cancer cell survival by functioning as E3 ligases that promote RIP1 ubiquitination. *Molecular cell*, 30 (6): 689–700, 2008.
- Betzig E, Patterson GH, Sougrat R, Lindwasser OW, Olenych S, Bonifacino JS, Davidson MW, Lippincott-Schwartz J, and Hess HF. Imaging intracellular fluorescent proteins at nanometer resolution. *Science (New York, N.Y.)*, 313 (5793): 1642–1645, 2006.
- Blüml S, Scheinecker C, Smolen JS, and Redlich K. Targeting TNF receptors in rheumatoid arthritis. *International immunology*, 24 (5): 275–281, 2012.
- Boado RJ, Hui EK-W, Lu JZ, Zhou Q-H, and Pardridge WM. Selective targeting of a TNFR decoy receptor pharmaceutical to the primate brain as a receptor-specific IgG fusion protein. *Journal of biotechnology*, 146 (1-2): 84–91, 2010.
- Bodmer J-L, Schneider P, and Tschopp J. The molecular architecture of the TNF superfamily. *Trends in biochemical sciences*, 27 (1): 19–26, 2002.
- Borghi A, Verstrepen L, and Beyaert R. TRAF2 multitasking in TNF receptor-induced signaling to NF- κ B, MAP kinases and cell death. *Biochemical pharmacology*, 116: 1–10, 2016.
- Boschert V, Krippner-Heidenreich A, Branschädel M, Tepperink J, Aird A, and Scheurich P. Single chain TNF derivatives with individually mutated receptor binding sites reveal differential stoichiometry of ligand receptor complex formation for TNFR1 and TNFR2. *Cellular signalling*, 22 (7): 1088–1096, 2010.
- Boussiotis VA, Nadler LM, Strominger JL, and Goldfeld AE. Tumor necrosis factor alpha is an autocrine growth factor for normal human B cells. *Proceedings of the National Academy of Sciences*, 91 (15): 7007–7011, 1994.
- Bradham CA, Plümpe J, Manns MP, Brenner DA, and Trautwein C. Mechanisms of hepatic toxicity. I. TNF-induced liver injury. *The American journal of physiology*, 275 (3 Pt 1): G387-92, 1998.
- Bridgham JT and Johnson AL. Characterization of chicken TNFR superfamily decoy receptors, DcR3 and osteoprotegerin. *Biochemical and biophysical research communications*, 307 (4): 956–961, 2003.

REFERENCES

- Brunasso AMG and Massone C. Thrombocytopenia associated with the use of anti-tumor necrosis factor-alpha agents for psoriasis. *Journal of the American Academy of Dermatology*, 60 (5): 781–785, 2009.
- Cabral JS. *Stem cell manufacturing*, 2016.
- Cai W, Kerner ZJ, Hong H, and Sun J. Targeted Cancer Therapy with Tumor Necrosis Factor-Alpha. *Biochemistry insights*, 2008: 15–21, 2008.
- Cao J, Meng F, Gao X, Dong H, and Yao W. Expression and purification of a natural N-terminal pre-ligand assembly domain of tumor necrosis factor receptor 1 (TNFR1 PLAD) and preliminary activity determination. *The protein journal*, 30 (4): 281–289, 2011.
- Carrington PE, Sandu C, Wei Y, Hill JM, Morisawa G, Huang T, Gavathiotis E, Wei Y, and Werner MH. The structure of FADD and its mode of interaction with procaspase-8. *Molecular cell*, 22 (5): 599–610, 2006.
- Carucci JA, Washenik K, Weinstein A, Shupack J, and Cohen DE. The leukotriene antagonist zafirlukast as a therapeutic agent for atopic dermatitis. *Archives of dermatology*, 134 (7): 785–786, 1998.
- Chan FK-M. A Domain in TNF Receptors That Mediates Ligand-Independent Receptor Assembly and Signaling. *Science*, 288 (5475): 2351–2354, 2000.
- Chan FK-M. Three is better than one: Pre-ligand receptor assembly in the regulation of TNF receptor signaling. *Cytokine*, 37 (2): 101–107, 2007.
- Chen G and Goeddel DV. TNF-R1 signaling: A beautiful pathway. *Science (New York, N.Y.)*, 296 (5573): 1634–1635, 2002.
- Chen J, Zhang L, and Kim S. Quantification and detection of DcR3, a decoy receptor in TNFR family. *Journal of immunological methods*, 285 (1): 63–70, 2004.
- Chen M, Holland MJ, Mir MR, Wong MG, Kelley BP, Grim KD, Bhuchar SS, and Hsu S. Frequency of thrombocytopenia in psoriasis patients treated with tumor necrosis factor-a inhibitors. *Journal of drugs in dermatology JDD*, 10 (3): 280–284, 2011.
- Chen ZJ. Ubiquitination in signaling to and activation of IKK. *Immunological reviews*, 246 (1): 95–106, 2012.
- Chêne A, Gangnard S, Dechavanne C, Dechavanne S, Srivastava A, Tétard M, Hundt S, Leroy O, Havelange N, Viebig NK, and Gamain B. Down-selection of the VAR2CSA DBL1-2 expressed in *E. coli* as a lead antigen for placental malaria vaccine development. *NPJ vaccines*, 3: 28, 2018.
- Cho YS, Challa S, Moquin D, Genga R, Ray TD, Guildford M, and Chan FK-M. Phosphorylation-driven assembly of the RIP1-RIP3 complex regulates programmed necrosis and virus-induced inflammation. *Cell*, 137 (6): 1112–1123, 2009.
- Cholera R, Brittain NJ, Gillrie MR, Lopera-Mesa TM, Diakitè SAS, Arie T, Krause MA, Guindo A, Tubman A, Fujioka H, Diallo DA, Doumbo OK, Ho M, Wellems TE, and Fairhurst RM. Impaired cytoadherence of Plasmodium falciparum-infected erythrocytes containing sickle hemoglobin. *Proceedings of the National Academy of Sciences of the United States of America*, 105 (3): 991–996, 2008.

- Chotivanich K, Udomsangpetch R, McGready R, Proux S, Newton P, Pukrittayakamee S, Looareesuwan S, and White NJ. Central role of the spleen in malaria parasite clearance. *The Journal of infectious diseases*, 185 (10): 1538–1541, 2002.
- Churchman LS, Flyvbjerg H, and Spudich JA. A non-Gaussian distribution quantifies distances measured with fluorescence localization techniques. *Biophysical Journal*, 90 (2): 668–671, 2006.
- Clausen TM, Christoffersen S, Dahlbäck M, Langkilde AE, Jensen KE, Resende M, Agerbæk MØ, Andersen D, Berisha B, Ditlev SB, Pinto VV, Nielsen MA, Theander TG, Larsen S, and Salanti A. Structural and functional insight into how the Plasmodium falciparum VAR2CSA protein mediates binding to chondroitin sulfate A in placental malaria. *The Journal of biological chemistry*, 287 (28): 23332–23345, 2012.
- Conway SP, Etherington C, Peckham DG, and Whitehead A. A pilot study of zafirlukast as an anti-inflammatory agent in the treatment of adults with cystic fibrosis. *Journal of Cystic Fibrosis*, 2 (1): 25–28, 2003.
- Coons AH, Creech HJ, and Jones RN. Immunological Properties of an Antibody Containing a Fluorescent Group. *Experimental Biology and Medicine*, 47 (2): 200–202, 1941.
- Coons AH, Creech HJ, Jones RNr, and Berliner E. The demonstration of pneumococcal antigen in tissues by the use of fluorescent antibody. *Jour Immunol*, 45 (3): 159–170, 1942.
- Coulter A and Harris R. Simplified preparation of rabbit Fab fragments. *Journal of immunological methods*, 59 (2): 199–203, 1983.
- Cox WG, Beaudet MP, Agnew JY, and Ruth JL. Possible sources of dye-related signal correlation bias in two-color DNA microarray assays. *Analytical biochemistry*, 331 (2): 243–254, 2004.
- Croft M, Benedict CA, and Ware CF. Clinical targeting of the TNF and TNFR superfamilies. *Nature reviews. Drug discovery*, 12 (2): 147–168, 2013.
- Cubillas R, Kintner K, Phillips F, Karandikar NJ, Thiele DL, and Brown GR. Tumor necrosis factor receptor 1 expression is upregulated in dendritic cells in patients with chronic HCV who respond to therapy. *Hepatitis research and treatment*, 2010: 429243, 2010.
- Cyrklaff M, Srismith S, Nyboer B, Burda K, Hoffmann A, Lasitschka F, Adjalley S, Bisseye C, Simpore J, Mueller A-K, Sanchez CP, Frischknecht F, and Lanzer M. Oxidative insult can induce malaria-protective trait of sickle and fetal erythrocytes. *Nature communications*, 7: 13401, 2016.
- Day RN and Davidson MW. The fluorescent protein palette: Tools for cellular imaging. *Chemical Society reviews*, 38 (10): 2887–2921, 2009.
- Dempsey GT, Bates M, Kowtoniuk WE, Liu DR, Tsien RY, and Zhuang X. Photoswitching mechanism of cyanine dyes. *Journal of the American Chemical Society*, 131 (51): 18192–18193, 2009.
- Dempsey GT, Vaughan JC, Chen KH, Bates M, and Zhuang X. Evaluation of fluorophores for optimal performance in localization-based super-resolution imaging. *Nature methods*, 8 (12): 1027–1036, 2011.
- Dempsey PW, Doyle SE, He JQ, and Cheng G. The signaling adaptors and pathways activated by TNF superfamily. *Cytokine & growth factor reviews*, 14 (3-4): 193–209, 2003.

REFERENCES

- Deng G-M. Tumor necrosis factor receptor pre-ligand assembly domain is an important therapeutic target in inflammatory arthritis. *BioDrugs clinical immunotherapeutics, biopharmaceuticals and gene therapy*, 21 (1): 23–29, 2007.
- Deveau H, Garneau JE, and Moineau S. CRISPR/Cas system and its role in phage-bacteria interactions. *Annual review of microbiology*, 64: 475–493, 2010.
- Dhuriya YK and Sharma D. Necroptosis: A regulated inflammatory mode of cell death. *Journal of neuroinflammation*, 15 (1): 199, 2018.
- Dietz MS, Fricke F, Krüger CL, Niemann HH, and Heilemann M. Receptor-Ligand Interactions: Binding Affinities Studied by Single-Molecule and Super-Resolution Microscopy on Intact Cells. *ChemPhysChem*, 15 (4): 671–676, 2014.
- Dostert C, Grusdat M, Letellier E, and Brenner D. The TNF Family of Ligands and Receptors: Communication Modules in the Immune System and Beyond. *Physiological reviews*, 99 (1): 115–160, 2019.
- Durisic N, Laparra-Cuervo L, Sandoval-Álvarez A, Borbely JS, and Lakadamyali M. Single-molecule evaluation of fluorescent protein photoactivation efficiency using an in vivo nanotemplate. *Nature methods*, 11 (2): 156–162, 2014.
- Dyba M and Hell SW. Focal spots of size $\lambda/23$ open up far-field fluorescence microscopy at 33 nm axial resolution. *Physical review letters*, 88 (16): 163901, 2002.
- Ea C-K, Deng L, Xia Z-P, Pineda G, and Chen ZJ. Activation of IKK by TNF α requires site-specific ubiquitination of RIP1 and polyubiquitin binding by NEMO. *Molecular cell*, 22 (2): 245–257, 2006.
- Eckelman BP and Salvesen GS. The human anti-apoptotic proteins cIAP1 and cIAP2 bind but do not inhibit caspases. *Journal of Biological Chemistry*, 281 (6): 3254–3260, 2006.
- Edelman GM. Antibody structure and molecular immunology. *Annals of the New York Academy of Sciences*, 190: 5–25, 1971.
- El-Mesery M, Shaker ME, and Elgaml A. The SMAC mimetic BV6 induces cell death and sensitizes different cell lines to TNF- α and TRAIL-induced apoptosis. *Experimental biology and medicine (Maywood, N.J.)*, 241 (18): 2015–2022, 2016.
- Elmore S. Apoptosis: A review of programmed cell death. *Toxicologic pathology*, 35 (4): 495–516, 2007.
- Endesfelder U, Malkusch S, Fricke F, and Heilemann M. A simple method to estimate the average localization precision of a single-molecule localization microscopy experiment. *Histochemistry and cell biology*, 141 (6): 629–638, 2014.
- Engelborghs Y and Visser AJWG (Eds). *Fluorescence Spectroscopy and Microscopy: Methods and Protocols*. Totowa, NJ: Humana Press, 2014.
- Ermolaeva MA, Michallet M-C, Papadopoulou N, Utermöhlen O, Kranidioti K, Kollias G, Tschopp J, and Pasparakis M. Function of TRADD in tumor necrosis factor receptor 1 signaling and in TRIF-dependent inflammatory responses. *Nature immunology*, 9 (9): 1037–1046, 2008.

- Ester M, Kriegel H-P, Sander J, and Xu X. A Density-Based Algorithm for Discovering Clusters in Large Spatial Databases with Noise, 1996.
- Etemadi N, Chopin M, Anderton H, Tanzer MC, Rickard JA, Abeysekera W, Hall C, Spall SK, Wang B, Xiong Y, Hla T, Pitson SM, Bonder CS, Wong WW-L, Ernst M, Smyth GK, Vaux DL, Nutt SL, Nachbur U, and Silke J. TRAF2 regulates TNF and NF- κ B signalling to suppress apoptosis and skin inflammation independently of Sphingosine kinase 1. *eLife*, 4, 2015.
- Fairhurst RM, Bess CD, and Krause MA. Abnormal PfEMP1/knob display on Plasmodium falciparum-infected erythrocytes containing hemoglobin variants: Fresh insights into malaria pathogenesis and protection. *Microbes and infection*, 14 (10): 851–862, 2012.
- Favre N, Da Laperousaz C, Ryffel B, Weiss NA, Imhof BA, Rudin W, Lucas R, and Piguet PF. Role of ICAM-1 (CD54) in the development of murine cerebral malaria. *Microbes and infection*, 1 (12): 961–968, 1999.
- Felgner PL, Gadek TR, Holm M, Roman R, Chan HW, Wenz M, Northrop JP, Ringold GM, and Danielsen M. Lipofection: A highly efficient, lipid-mediated DNA-transfection procedure. *Proceedings of the National Academy of Sciences*, 84 (21): 7413–7417, 1987.
- Ferraro P, Wax A, and Zalevsky Z (Eds). *Coherent Light Microscopy: Imaging and Quantitative Phase Analysis*. Berlin, Heidelberg: Springer-Verlag Berlin Heidelberg, 2011.
- Fischer K, Tognarelli S, Roesler S, Boedicker C, Schubert R, Steinle A, Klingebiel T, Bader P, Fulda S, and Ullrich E. The Smac Mimetic BV6 Improves NK Cell-Mediated Killing of Rhabdomyosarcoma Cells by Simultaneously Targeting Tumor and Effector Cells. *Frontiers in immunology*, 8: 202, 2017.
- Fischer R, Kontermann R, and Maier O. Targeting sTNF/TNFR1 Signaling as a New Therapeutic Strategy. *Antibodies*, 4 (1): 48–70, 2015.
- Fish KN. Total internal reflection fluorescence (TIRF) microscopy. *Current protocols in cytometry*, Chapter 12: Unit12.18, 2009.
- Fölling J, Bossi M, Bock H, Medda R, Wurm CA, Hein B, Jakobs S, Eggeling C, and Hell SW. Fluorescence nanoscopy by ground-state depletion and single-molecule return. *Nature methods*, 5 (11): 943–945, 2008.
- Fricke F, Beaudouin J, Eils R, and Heilemann M. One, two or three? Probing the stoichiometry of membrane proteins by single-molecule localization microscopy. *Scientific reports*, 5: 14072, 2015.
- Fricke F, Malkusch S, Wangorsch G, Greiner JF, Kaltschmidt B, Kaltschmidt C, Widera D, Dandekar T, and Heilemann M. Quantitative single-molecule localization microscopy combined with rule-based modeling reveals ligand-induced TNF-R1 reorganization toward higher-order oligomers. *Histochemistry and cell biology*, 142 (1): 91–101, 2014.
- Fried M and Duffy PE. Designing a VAR2CSA-based vaccine to prevent placental malaria. *Vaccine*, 33 (52): 7483–7488, 2015.
- Gaeta ML, Johnson DR, Kluger MS, and Pober JS. The Death Domain of Tumor Necrosis Factor Receptor 1 Is Necessary but Not Sufficient for Golgi Retention of the Receptor and Mediates Receptor Desensitization. *Laboratory Investigation*, 80 (8): 1185–1194, 2000.

REFERENCES

- Galluzzi L, Kepp O, and Kroemer G. MLKL regulates necrotic plasma membrane permeabilization. *Cell research*, 24 (2): 139–140, 2014.
- Gautier A, Juillerat A, Heinis C, Corrêa IR, Kindermann M, Beaufils F, and Johnsson K. An engineered protein tag for multiprotein labeling in living cells. *Chemistry & Biology*, 15 (2): 128–136, 2008.
- Gbédandé K, Fievet N, Viwami F, Ezinmegnon S, Issifou S, Chippaux J-P, Dossou Y, Moutairou K, Massougboji A, Ndam N, Jongh WA de, Søgaaard TMM, Salanti A, Nielsen MA, Esen M, Mordmüller B, Deloron P, and Luty AJF. Clinical development of a VAR2CSA-based placental malaria vaccine PAMVAC: Quantifying vaccine antigen-specific memory B & T cell activity in Beninese primigravidae. *Vaccine*, 35 (27): 3474–3481, 2017.
- Geddes CD and Lakowicz JR. *Reviews in Fluorescence 2007*. 1st ed. New York, NY: Springer-Verlag New York, 2009.
- Gibson PR. Increased gut permeability in Crohn's disease: Is TNF the link? *Gut*, 53 (12): 1724–1725, 2004.
- Grell M, Wajant H, Zimmermann G, and Scheurich P. The type 1 receptor (CD120a) is the high-affinity receptor for soluble tumor necrosis factor. *Proceedings of the National Academy of Sciences*, 95 (2): 570–575, 1998.
- Gross D and Webb WW. Molecular counting of low-density lipoprotein particles as individuals and small clusters on cell surfaces. *Biophysical Journal*, 49 (4): 901–911, 1986.
- Grotjohann T, Testa I, Reuss M, Brakemann T, Eggeling C, Hell SW, and Jakobs S. rsEGFP2 enables fast RESOLFT nanoscopy of living cells. *eLife*, 1: e00248, 2012.
- Gustafsson MGL. Surpassing the lateral resolution limit by a factor of two using structured illumination microscopy. SHORT COMMUNICATION. *Journal of Microscopy*, 198 (2): 82–87, 2000.
- Haas TL, Emmerich CH, Gerlach B, Schmukle AC, Cordier SM, Rieser E, Feltham R, Vince J, Warnken U, Wenger T, Koschny R, Komander D, Silke J, and Walczak H. Recruitment of the linear ubiquitin chain assembly complex stabilizes the TNF-R1 signaling complex and is required for TNF-mediated gene induction. *Molecular cell*, 36 (5): 831–844, 2009.
- Hamers-Casterman C, Atarhouch T, Muyldermans S, Robinson G, Hamers C, Songa EB, Bendahman N, and Hamers R. Naturally occurring antibodies devoid of light chains. *Nature*, 363 (6428): 446–448, 1993.
- Hannes S, Abhari BA, and Fulda S. Smac mimetic triggers necroptosis in pancreatic carcinoma cells when caspase activation is blocked. *Cancer letters*, 380 (1): 31–38, 2016.
- Hare NC, Hunt DPJ, Venugopal K, Ho G-T, Beez T, Lees CW, Gibson R, Weller B, and Satsangi J. Multiple sclerosis in the context of TNF blockade and inflammatory bowel disease. *QJM monthly journal of the Association of Physicians*, 107 (1): 51–55, 2014.
- Hartley WG. *The light microscope: Its use and development*. Oxford: Senecio Publ. Co, 1993.
- Hayden MS and Ghosh S. Shared principles in NF-kappaB signaling. *Cell*, 132 (3): 344–362, 2008.
- He B, Lu N, and Zhou Z. Cellular and nuclear degradation during apoptosis. *Current opinion in cell biology*, 21 (6): 900–912, 2009.

- Heilemann M, Margeat E, Kasper R, Sauer M, and Tinnefeld P. Carbocyanine dyes as efficient reversible single-molecule optical switch. *Journal of the American Chemical Society*, 127 (11): 3801–3806, 2005.
- Heilemann M, van de Linde S, Schüttpelz M, Kasper R, Seefeldt B, Mukherjee A, Tinnefeld P, and Sauer M. Subdiffraction-resolution fluorescence imaging with conventional fluorescent probes. *Angewandte Chemie (International ed. in English)*, 47 (33): 6172–6176, 2008.
- Heim R, Prasher DC, and Tsien RY. Wavelength mutations and posttranslational autoxidation of green fluorescent protein. *Proceedings of the National Academy of Sciences*, 91 (26): 12501–12504, 1994.
- Hell SW and Wichmann J. Breaking the diffraction resolution limit by stimulated emission: Stimulated-emission-depletion fluorescence microscopy. *Optics Letters*, 19 (11): 780, 1994.
- Henderson JN, Ai H-W, Campbell RE, and Remington SJ. Structural basis for reversible photobleaching of a green fluorescent protein homologue. *Proceedings of the National Academy of Sciences*, 104 (16): 6672–6677, 2007.
- Herschel J. F. W. IV. Ἀμόρφωτα, no. I.— on a case of superficial colour presented by a homogeneous liquid internally colourless. *Philosophical Transactions of the Royal Society of London*, 135: 143–145, 1845.
- Hess ST, Girirajan TPK, and Mason MD. Ultra-high resolution imaging by fluorescence photoactivation localization microscopy. *Biophysical Journal*, 91 (11): 4258–4272, 2006.
- Hof M, Hutterer R, and Fidler V. *Fluorescence Spectroscopy in Biology: Advanced Methods and their Applications to Membranes, Proteins, DNA, and Cells*. 1st ed. s.l.: Springer-Verlag, 2005.
- Hoi H, Shaner NC, Davidson MW, Cairo CW, Wang J, and Campbell RE. A monomeric photoconvertible fluorescent protein for imaging of dynamic protein localization. *Journal of molecular biology*, 401 (5): 776–791, 2010.
- Hooke R and Allestry J. *Micrographia, or, Some physiological descriptions of minute bodies made by magnifying glasses: With observations and inquiries thereupon*. London: Printed for James Allestry, printer to the Royal Society, and to be sold at his shop, at the Rose and Crown in Duck-Lane, 1667.
- Horrocks P, Pinches RA, Chakravorty SJ, Papakrivos J, Christodoulou Z, Kyes SA, Urban BC, Ferguson DJP, and Newbold CI. PfEMP1 expression is reduced on the surface of knobless Plasmodium falciparum infected erythrocytes. *Journal of cell science*, 118 (Pt 11): 2507–2518, 2005.
- Hsu H, Huang J, Shu HB, Baichwal V, and Goeddel DV. TNF-dependent recruitment of the protein kinase RIP to the TNF receptor-1 signaling complex. *Immunity*, 4 (4): 387–396, 1996.
- Hummer G, Fricke F, and Heilemann M. Model-independent counting of molecules in single-molecule localization microscopy. *Molecular biology of the cell*, 27 (22): 3637–3644, 2016.
- Ishino Y, Shinagawa H, Makino K, Amemura M, and Nakata A. Nucleotide sequence of the iap gene, responsible for alkaline phosphatase isozyme conversion in Escherichia coli, and identification of the gene product. *Journal of bacteriology*, 169 (12): 5429–5433, 1987.
- Israël A. The IKK complex, a central regulator of NF-kappaB activation. *Cold Spring Harbor perspectives in biology*, 2 (3): a000158, 2010.

REFERENCES

- Janke C, Magiera MM, Rathfelder N, Taxis C, Reber S, Maekawa H, Moreno-Borchart A, Doenges G, Schwob E, Schiebel E, and Knop M. A versatile toolbox for PCR-based tagging of yeast genes: New fluorescent proteins, more markers and promoter substitution cassettes. *Yeast (Chichester, England)*, 21 (11): 947–962, 2004.
- Jarosz-Griffiths HH, Holbrook J, Lara-Reyna S, and McDermott MF. TNF receptor signalling in autoinflammatory diseases. *International immunology*, 2019.
- Jiang Y, Woronicz JD, Liu W, and Goeddel DV. Prevention of constitutive TNF receptor 1 signaling by silencer of death domains. *Science (New York, N.Y.)*, 283 (5401): 543–546, 1999.
- Joergensen LM, Salanti A, Dobrilovic T, Barfod L, Hassenkam T, Theander TG, Hviid L, and Arnot DE. The kinetics of antibody binding to Plasmodium falciparum VAR2CSA PfEMP1 antigen and modelling of PfEMP1 antigen packing on the membrane knobs. *Malaria journal*, 9: 100, 2010.
- Jungmann R, Avendaño MS, Dai M, Woehrstein JB, Agasti SS, Feiger Z, Rodal A, and Yin P. Quantitative super-resolution imaging with qPAINT. *Nature methods*, 13 (5): 439–442, 2016.
- Kaiser GC and Polk DB. Tumor necrosis factor alpha regulates proliferation in a mouse intestinal cell line. *Gastroenterology*, 112 (4): 1231–1240, 1997.
- Karathanasis C, Fricke F, Hummer G, and Heilemann M. Molecule Counts in Localization Microscopy with Organic Fluorophores. *Chemphyschem a European journal of chemical physics and physical chemistry*, 18 (8): 942–948, 2017.
- Karp G. *Molekulare Zellbiologie: Mit 36 Tabellen*. 1st ed., 2005.
- Kasha M. Characterization of electronic transitions in complex molecules. *Discussions of the Faraday Society*, 9: 14, 1950.
- Keppler A, Gendreizig S, Gronemeyer T, Pick H, Vogel H, and Johnsson K. A general method for the covalent labeling of fusion proteins with small molecules in vivo. *Nature biotechnology*, 21 (1): 86–89, 2003.
- Kerr JF, Wyllie AH, and Currie AR. Apoptosis: A basic biological phenomenon with wide-ranging implications in tissue kinetics. *British journal of cancer*, 26 (4): 239–257, 1972.
- Kerr JFR. History of the events leading to the formulation of the apoptosis concept. *Toxicology*, 181–182: 471–474, 2002.
- Kettelhut IC, Fiers W, and Goldberg AL. The toxic effects of tumor necrosis factor in vivo and their prevention by cyclooxygenase inhibitors. *Proceedings of the National Academy of Sciences*, 84 (12): 4273–4277, 1987.
- Kim TK and Eberwine JH. Mammalian cell transfection: The present and the future. *Analytical and bioanalytical chemistry*, 397 (8): 3173–3178, 2010.
- Kim WJ, Mohan RR, and Wilson SE. Caspase inhibitor z-VAD-FMK inhibits keratocyte apoptosis, but promotes keratocyte necrosis, after corneal epithelial scrape. *Experimental eye research*, 71 (3): 225–232, 2000.
- Klein T, Löschberger A, Proppert S, Wolter S, van de Linde S, and Sauer M. Live-cell dSTORM with SNAP-tag fusion proteins. *Nature methods*, 8 (1): 7–9, 2011.

- Kominami K, Nakabayashi J, Nagai T, Tsujimura Y, Chiba K, Kimura H, Miyawaki A, Sawasaki T, Yokota H, Manabe N, and Sakamaki K. The molecular mechanism of apoptosis upon caspase-8 activation: Quantitative experimental validation of a mathematical model. *Biochimica et biophysica acta*, 1823 (10): 1825–1840, 2012.
- Konev SV. *Fluorescence and Phosphorescence of Proteins and Nucleic Acids*. Boston, MA: Springer US, 1967.
- Krafft GA, Sutton WR, and Cummings RT. Photoactivable fluorophores. 3. Synthesis and photoactivation of fluorogenic difunctionalized fluoresceins. *Journal of the American Chemical Society*, 110 (1): 301–303, 1988.
- Kriegler M, Perez C, DeFay K, Albert I, and Lu SD. A novel form of TNF/cachectin is a cell surface cytotoxic transmembrane protein: Ramifications for the complex physiology of TNF. *Cell*, 53 (1): 45–53, 1988.
- Krüger C, Fricke F, Karathanasis C, Dietz MS, Malkusch S, Hummer G, and Heilemann M. Molecular counting of membrane receptor subunits with single-molecule localization microscopy. In Enderlein J, Gregor I, Gryczynski ZK, Erdmann R, and Koberling F (Eds): SPIE, 2017a: 100710K.
- Krüger CL, Zeuner M-T, Cottrell GS, Widera D, and Heilemann M. Quantitative single-molecule imaging of TLR4 reveals ligand-specific receptor dimerization. *Science signaling*, 10 (503), 2017b.
- Krysko DV, Garg AD, Kaczmarek A, Krysko O, Agostinis P, and Vandenabeele P. Immunogenic cell death and DAMPs in cancer therapy. *Nature reviews. Cancer*, 12 (12): 860–875, 2012.
- Kumari S, Redouane Y, Lopez-Mosqueda J, Shiraishi R, Romanowska M, Lutzmayer S, Kuiper J, Martinez C, Dikic I, Pasparakis M, and Ikeda F. Sharpin prevents skin inflammation by inhibiting TNFR1-induced keratinocyte apoptosis. *eLife*, 3, 2014.
- Labbé K, McIntire CR, Doiron K, Leblanc PM, and Saleh M. Cellular inhibitors of apoptosis proteins cIAP1 and cIAP2 are required for efficient caspase-1 activation by the inflammasome. *Immunity*, 35 (6): 897–907, 2011.
- Lakowicz JR (Ed). *Topics in Fluorescence Spectroscopy: Principles*. Boston, MA: Kluwer Academic Publishers, 2002.
- Lakowicz JR. *Principles of Fluorescence Spectroscopy*. Boston, MA: Springer US, 2006.
- Lambert JH. *I. H. Lambert... Photometria sive de mensura et gradibus luminis, colorum et umbrae: sumptibus viduae Eberhardi Klett*, 1760.
- Lamoyi E and Nisonoff A. Preparation of F(ab')₂ fragments from mouse IgG of various subclasses. *Journal of immunological methods*, 56 (2): 235–243, 1983.
- Lang I, Füllsack S, Wyzgol A, Fick A, Trebing J, Arana JAC, Schäfer V, Weisenberger D, and Wajant H. Binding Studies of TNF Receptor Superfamily (TNFRSF) Receptors on Intact Cells. *The Journal of biological chemistry*, 291 (10): 5022–5037, 2016.
- Lavis LD. Teaching Old Dyes New Tricks: Biological Probes Built from Fluoresceins and Rhodamines. *Annual review of biochemistry*, 86: 825–843, 2017.
- Lawlor D. *Introduction to light microscopy: Tips and tricks for beginners*. [Place of publication not identified]: Springer Nature, 2019.

REFERENCES

- Lee JF, Stovall GM, and Ellington AD. Aptamer therapeutics advance. *Current opinion in chemical biology*, 10 (3): 282–289, 2006.
- Lee S-H, Shin JY, Lee A, and Bustamante C. Counting single photoactivatable fluorescent molecules by photoactivated localization microscopy (PALM). *Proceedings of the National Academy of Sciences of the United States of America*, 109 (43): 17436–17441, 2012.
- Leech JH, Barnwell JW, Miller LH, and Howard RJ. Identification of a strain-specific malarial antigen exposed on the surface of Plasmodium falciparum-infected erythrocytes. *The Journal of experimental medicine*, 159 (6): 1567–1575, 1984.
- Lelimosin M, Adam V, Nienhaus GU, Bourgeois D, and Field MJ. Photoconversion of the fluorescent protein EosFP: A hybrid potential simulation study reveals intersystem crossings. *Journal of the American Chemical Society*, 131 (46): 16814–16823, 2009.
- Lewis AK, Valley CC, and Sachs JN. TNFR1 signaling is associated with backbone conformational changes of receptor dimers consistent with overactivation in the R92Q TRAPS mutant. *Biochemistry*, 51 (33): 6545–6555, 2012.
- Lewis Carl SA, Gillete-Ferguson I, and Ferguson DG. An indirect immunofluorescence procedure for staining the same cryosection with two mouse monoclonal primary antibodies. *Journal of Histochemistry & Cytochemistry*, 41 (8): 1273–1278, 1993.
- Li J, McQuade T, Siemer AB, Napetschnig J, Moriwaki K, Hsiao Y-S, Damko E, Moquin D, Walz T, McDermott A, Chan FK-M, and Wu H. The RIP1/RIP3 necrosome forms a functional amyloid signaling complex required for programmed necrosis. *Cell*, 150 (2): 339–350, 2012.
- Li J, Yin Q, and Wu H. Structural basis of signal transduction in the TNF receptor superfamily. *Advances in immunology*, 119: 135–153, 2013.
- Li W. Eat-me signals: Keys to molecular phagocyte biology and "appetite" control. *Journal of cellular physiology*, 227 (4): 1291–1297, 2012.
- Lippincott-Schwartz J and Patterson GH. Photoactivatable fluorescent proteins for diffraction-limited and super-resolution imaging. *Trends in cell biology*, 19 (11): 555–565, 2009.
- Lippincott-Schwartz J and Patterson GH. Fluorescent Proteins for Photoactivation Experiments. In Sullivan KF (Ed), *Fluorescent proteins*. 2nd ed. Amsterdam: Academic Press, 2008: 45–61.
- Liu C and Tang J. Expression levels of tumor necrosis factor- α and the corresponding receptors are correlated with trauma severity. *Oncology letters*, 8 (6): 2747–2751, 2014.
- Liu K. Role of apoptosis resistance in immune evasion and metastasis of colorectal cancer. *World journal of gastrointestinal oncology*, 2 (11): 399–406, 2010.
- Lo CH, Schaaf TM, Grant BD, Lim CK-W, Bawaskar P, Aldrich CC, Thomas DD, and Sachs JN. Noncompetitive inhibitors of TNFR1 probe conformational activation states. *Science signaling*, 12 (592), 2019.
- Lo CH, Vunnam N, Lewis AK, Chiu T-L, Brummel BE, Schaaf TM, Grant BD, Bawaskar P, Thomas DD, and Sachs JN. An Innovative High-Throughput Screening Approach for Discovery of Small Molecules That Inhibit TNF Receptors. *SLAS discovery advancing life sciences R & D*, 22 (8): 950–961, 2017.

- Lo Y-C, Lin S-C, Rospigliosi CC, Conze DB, Wu C-J, Ashwell JD, Eliezer D, and Wu H. Structural basis for recognition of diubiquitins by NEMO. *Molecular cell*, 33 (5): 602–615, 2009.
- Lodish H and Matsudaira P. *Molecular cell biology*. 4th ed. New York, NY: Freeman, 2000.
- Lopez Arbeloa F, Lopez Arbeloa T, Tapia Estevez MJ, and Lopez Arbeloa I. Photophysics of rhodamines: Molecular structure and solvent effects. *The Journal of Physical Chemistry*, 95 (6): 2203–2208, 1991.
- Los GV, Encell LP, McDougall MG, Hartzell DD, Karassina N, Zimprich C, Wood MG, Learish R, Ohana RF, Urh M, Simpson D, Mendez J, Zimmerman K, Otto P, Vidugiris G, Zhu J, Darzins A, Klaubert DH, Bulleit RF, and Wood KV. HaloTag: A novel protein labeling technology for cell imaging and protein analysis. *ACS chemical biology*, 3 (6): 373–382, 2008.
- Lukyanov KA, Chudakov DM, Lukyanov S, and Verkhusha VV. Innovation: Photoactivatable fluorescent proteins. *Nature reviews. Molecular cell biology*, 6 (11): 885–891, 2005.
- Luo J-L, Kamata H, and Karin M. IKK/NF-kappaB signaling: Balancing life and death--a new approach to cancer therapy. *The Journal of clinical investigation*, 115 (10): 2625–2632, 2005.
- Mabika M and Laburn H. The role of tumour necrosis factor-alpha (TNF-alpha) in fever and the acute phase reaction in rabbits. *Pflugers Archiv European journal of physiology*, 438 (2): 218–223, 1999.
- MacEwan DJ. TNF ligands and receptors--a matter of life and death. *British journal of pharmacology*, 135 (4): 855–875, 2002.
- Magde D, Wong R, and Seybold PG. Fluorescence Quantum Yields and Their Relation to Lifetimes of Rhodamine 6G and Fluorescein in Nine Solvents: Improved Absolute Standards for Quantum Yields¶. *Photochemistry and Photobiology*, 75 (4): 327–334, 2002.
- Mahoney DJ, Cheung HH, Mrad RL, Plenchette S, Simard C, Enwere E, Arora V, Mak TW, Lacasse EC, Waring J, and Korneluk RG. Both cIAP1 and cIAP2 regulate TNFalpha-mediated NF-kappaB activation. *Proceedings of the National Academy of Sciences of the United States of America*, 105 (33): 11778–11783, 2008.
- Malkusch S and Heilemann M. Extracting quantitative information from single-molecule super-resolution imaging data with LAMA - LocAlization Microscopy Analyzer. *Scientific reports*, 6: 34486, 2016.
- Marsters SA, Frutkin AD, Simpson NJ, Fendly BM, and Ashkenazi A. Identification of cysteine-rich domains of the type 1 tumor necrosis factor receptor involved in ligand binding. *Journal of Biological Chemistry*, 267 (9): 5747–5750, 1992.
- Martínez-Reza I, Díaz L, and García-Becerra R. Preclinical and clinical aspects of TNF- α and its receptors TNFR1 and TNFR2 in breast cancer. *Journal of biomedical science*, 24 (1): 90, 2017.
- Mathur J, Radhamony R, Sinclair AM, Donoso A, Dunn N, Roach E, Radford D, Mohaghegh PSM, Logan DC, Kokolic K, and Mathur N. mEosFP-based green-to-red photoconvertible subcellular probes for plants. *Plant physiology*, 154 (4): 1573–1587, 2010.
- McEvoy AL, Hoi H, Bates M, Platonova E, Cranfill PJ, Baird MA, Davidson MW, Ewers H, Liphardt J, and Campbell RE. mMaple: A photoconvertible fluorescent protein for use in multiple imaging modalities. *PloS one*, 7 (12): e51314, 2012.

REFERENCES

- McKinney SA, Murphy CS, Hazelwood KL, Davidson MW, and Looger LL. A bright and photostable photoconvertible fluorescent protein. *Nature methods*, 6 (2): 131–133, 2009.
- McNamara DE, Quarato G, Guy CS, Green DR, and Moldoveanu T. Characterization of MLKL-mediated Plasma Membrane Rupture in Necroptosis. *Journal of visualized experiments JoVE* (138), 2018.
- McQuade T, Cho Y, and Chan FK-M. Positive and negative phosphorylation regulates RIP1- and RIP3-induced programmed necrosis. *The Biochemical journal*, 456 (3): 409–415, 2013.
- Micheau O. Cellular FLICE-inhibitory protein: An attractive therapeutic target? *Expert opinion on therapeutic targets*, 7 (4): 559–573, 2003.
- Micheau O and Tschopp J. Induction of TNF receptor I-mediated apoptosis via two sequential signaling complexes. *Cell*, 114 (2): 181–190, 2003.
- Minsky M. Memoir on inventing the confocal scanning microscope. *Scanning*, 10 (4): 128–138, 1988.
- Mirza S, Hossain M, Mathews C, Martinez P, Pino P, Gay JL, Rentfro A, McCormick JB, and Fisher-Hoch SP. Type 2-diabetes is associated with elevated levels of TNF-alpha, IL-6 and adiponectin and low levels of leptin in a population of Mexican Americans: A cross-sectional study. *Cytokine*, 57 (1): 136–142, 2012.
- Mitchison TJ. Polewards microtubule flux in the mitotic spindle: Evidence from photoactivation of fluorescence. *The Journal of cell biology*, 109 (2): 637–652, 1989.
- Mizuno H, Mal TK, Tong KI, Ando R, Furuta T, Ikura M, and Miyawaki A. Photo-induced peptide cleavage in the green-to-red conversion of a fluorescent protein. *Molecular cell*, 12 (4): 1051–1058, 2003.
- Moller DE. Potential role of TNF-alpha in the pathogenesis of insulin resistance and type 2 diabetes. *Trends in endocrinology and metabolism: TEM*, 11 (6): 212–217, 2000.
- Monick MM and Hunninghake GW. Activation of second messenger pathways in alveolar macrophages by endotoxin. *The European respiratory journal*, 20 (1): 210–222, 2002.
- Morise H, Shimomura O, Johnson FH, and Winant J. Intermolecular energy transfer in the bioluminescent system of *Aequorea*. *Biochemistry*, 13 (12): 2656–2662, 1974.
- Mortensen KI, Churchman LS, Spudich JA, and Flyvbjerg H. Optimized localization analysis for single-molecule tracking and super-resolution microscopy. *Nature methods*, 7 (5): 377–381, 2010.
- Morton PE, Perrin C, Levitt J, Matthews DR, Marsh RJ, Pike R, McMillan D, Maloney A, Poland S, Ameer-Beg S, and Parsons M. TNFR1 membrane reorganization promotes distinct modes of TNF α signaling. *Science signaling*, 12 (592), 2019.
- Mukai Y, Nakamura T, Yoshikawa M, Yoshioka Y, Tsunoda S-i, Nakagawa S, Yamagata Y, and Tsutsumi Y. Solution of the structure of the TNF-TNFR2 complex. *Science signaling*, 3 (148): ra83, 2010.
- Nagata S, Nagase H, Kawane K, Mukae N, and Fukuyama H. Degradation of chromosomal DNA during apoptosis. *Cell death and differentiation*, 10 (1): 108–116, 2003.

- Naismith JH, Devine TQ, Brandhuber BJ, and Sprang SR. Crystallographic Evidence for Dimerization of Unliganded Tumor Necrosis Factor Receptor. *Journal of Biological Chemistry*, 270 (22): 13303–13307, 1995.
- Naismith JH, Devine TQ, Kohno T, and Sprang SR. Structures of the extracellular domain of the type I tumor necrosis factor receptor. *Structure (London, England 1993)*, 4 (11): 1251–1262, 1996.
- Nienhaus K, Nienhaus GU, Wiedenmann J, and Nar H. Structural basis for photo-induced protein cleavage and green-to-red conversion of fluorescent protein EosFP. *Proceedings of the National Academy of Sciences*, 102 (26): 9156–9159, 2005.
- Nisonoff A, Wissler FC, Lipman LN, and Woernley DL. Separation of univalent fragments from the bivalent rabbit antibody molecule by reduction of disulfide bonds. *Archives of Biochemistry and Biophysics*, 89 (2): 230–244, 1960.
- Nocht B and Mayer M. *Die Malaria: Eine Einführung in Ihre Klinik, Parasitologie und Bekämpfung*. Berlin, Heidelberg, s.l.: Springer Berlin Heidelberg, 1936.
- Nyquist H. Certain Topics in Telegraph Transmission Theory. *Transactions of the American Institute of Electrical Engineers*, 47 (2): 617–644, 1928.
- O'Donnell MA and Ting AT. RIP1 comes back to life as a cell death regulator in TNFR1 signaling. *The FEBS journal*, 278 (6): 877–887, 2011.
- Old L. Tumor necrosis factor (TNF). *Science*, 230 (4726): 630–632, 1985.
- Oppelt A, Kaschek D, Huppelschoten S, Sison-Young R, Zhang F, Buck-Wiese M, Herrmann F, Malkusch S, Krüger CL, Meub M, Merkt B, Zimmermann L, Schofield A, Jones RP, Malik H, Schilling M, Heilemann M, van de Water B, Goldring CE, Park BK, Timmer J, and Klingmüller U. Model-based identification of TNF α -induced IKK β -mediated and I κ B α -mediated regulation of NF κ B signal transduction as a tool to quantify the impact of drug-induced liver injury compounds. *NPJ systems biology and applications*, 4: 23, 2018.
- Ormö M, Cubitt AB, Kallio K, Gross LA, Tsien RY, and Remington SJ. Crystal structure of the Aequorea victoria green fluorescent protein. *Science (New York, N.Y.)*, 273 (5280): 1392–1395, 1996.
- Overington JP, Al-Lazikani B, and Hopkins AL. How many drug targets are there? *Nature reviews. Drug discovery*, 5 (12): 993–996, 2006.
- Parameswaran N and Patial S. Tumor necrosis factor- α signaling in macrophages. *Critical reviews in eukaryotic gene expression*, 20 (2): 87–103, 2010.
- Pasparakis M and Vandenabeele P. Necroptosis and its role in inflammation. *Nature*, 517 (7534): 311–320, 2015.
- Pathare SK, Heycock C, and Hamilton J. TNF α blocker-induced thrombocytopenia. *Rheumatology (Oxford, England)*, 45 (10): 1313–1314, 2006.
- Patterson GH and Lippincott-Schwartz J. A photoactivatable GFP for selective photolabeling of proteins and cells. *Science (New York, N.Y.)*, 297 (5588): 1873–1877, 2002.
- Pawley JB. *Handbook of Biological Confocal Microscopy*. Boston, MA: Springer US, 1995.

REFERENCES

- Pegoretti V, Baron W, Laman JD, and Eisel ULM. Selective Modulation of TNF-TNFRs Signaling: Insights for Multiple Sclerosis Treatment. *Frontiers in immunology*, 9: 925, 2018.
- Pero ME, Zullo G, Esposito L, Iannuzzi A, Lombardi P, Canditiis C de, Neglia G, and Gasparini B. Inhibition of apoptosis by caspase inhibitor Z-VAD-FMK improves cryotolerance of in vitro derived bovine embryos. *Theriogenology*, 108: 127–135, 2018.
- Peters R and Trendelenburg M. *Nucleocytoplasmic Transport*. Berlin, Heidelberg: Springer Berlin Heidelberg, 1986.
- Plattner H and Hentschel J. *Zellbiologie: 23 Tabellen*. 2nd ed., 2002.
- Pobezinskaya YL and Liu Z. The role of TRADD in death receptor signaling. *Cell cycle (Georgetown, Tex.)*, 11 (5): 871–876, 2012.
- Potter H. Transfection by electroporation. *Current protocols in molecular biology*, Chapter 9: Unit 9.3, 2003.
- Potter H and Heller R. Transfection by Electroporation. *Current protocols in immunology*, 117: 10.15.1-10.15.9, 2017.
- Prasher DC, Eckenrode VK, Ward WW, Prendergast FG, and Cormier MJ. Primary structure of the *Aequorea victoria* green-fluorescent protein. *Gene*, 111 (2): 229–233, 1992.
- Proudfoot A, Bayliffe A, O’Kane CM, Wright T, Serone A, Bareille PJ, Brown V, Hamid UI, Chen Y, Wilson R, Cordy J, Morley P, Wildt R de, Elborn S, Hind M, Chilvers ER, Griffiths M, Summers C, and McAuley DF. Novel anti-tumour necrosis factor receptor-1 (TNFR1) domain antibody prevents pulmonary inflammation in experimental acute lung injury. *Thorax*, 73 (8): 723–730, 2018.
- Puimège L, Libert C, and van Hauwermeiren F. Regulation and dysregulation of tumor necrosis factor receptor-1. *Cytokine & growth factor reviews*, 25 (3): 285–300, 2014.
- Puliyappadamba VT, Hatanpaa KJ, Chakraborty S, and Habib AA. The role of NF- κ B in the pathogenesis of glioma. *Molecular & cellular oncology*, 1 (3): e963478, 2014.
- Quadt KA, Barfod L, Andersen D, Bruun J, Gyan B, Hassenkam T, Ofori MF, and Hviid L. The density of knobs on *Plasmodium falciparum*-infected erythrocytes depends on developmental age and varies among isolates. *PloS one*, 7 (9): e45658, 2012.
- Rahighi S, Ikeda F, Kawasaki M, Akutsu M, Suzuki N, Kato R, Kensche T, Uejima T, Bloor S, Komander D, Randow F, Wakatsuki S, and Dikic I. Specific recognition of linear ubiquitin chains by NEMO is important for NF- κ B activation. *Cell*, 136 (6): 1098–1109, 2009.
- Rahman MM and McFadden G. Modulation of tumor necrosis factor by microbial pathogens. *PLoS pathogens*, 2 (2): e4, 2006.
- Rappoport JZ and Simon SM. Real-time analysis of clathrin-mediated endocytosis during cell migration. *Journal of cell science*, 116 (Pt 5): 847–855, 2003.
- Rath PC and Aggarwal BB. TNF-induced signaling in apoptosis. *Journal of clinical immunology*, 19 (6): 350–364, 1999.
- Ravichandran KS. Find-me and eat-me signals in apoptotic cell clearance: Progress and conundrums. *The Journal of experimental medicine*, 207 (9): 1807–1817, 2010.

- Rayleigh. On the Theory of Optical Images, with special reference to the Microscope. *Journal of the Royal Microscopical Society*, 23 (4): 474–482, 1903.
- Rayleigh. XV. On the theory of optical images, with special reference to the microscope. *The London, Edinburgh, and Dublin Philosophical Magazine and Journal of Science*, 42 (255): 167–195, 2009.
- Remington SJ. Green fluorescent protein: A perspective. *Protein science a publication of the Protein Society*, 20 (9): 1509–1519, 2011.
- Resch-Genger U, Grabolle M, Cavaliere-Jaricot S, Nitschke R, and Nann T. Quantum dots versus organic dyes as fluorescent labels. *Nature methods*, 5 (9): 763–775, 2008.
- Reyes-Lamothe R, Sherratt DJ, and Leake MC. Stoichiometry and architecture of active DNA replication machinery in *Escherichia coli*. *Science (New York, N.Y.)*, 328 (5977): 498–501, 2010.
- Riches DW, Chan ED, and Winston BW. TNF-alpha-induced regulation and signalling in macrophages. *Immunobiology*, 195 (4-5): 477–490, 1996.
- Rickard JA, Anderton H, Etemadi N, Nachbur U, Darding M, Peltzer N, Lalaoui N, Lawlor KE, Vanyai H, Hall C, Bankovacki A, Gangoda L, Wong WW-L, Corbin J, Huang C, Mocarski ES, Murphy JM, Alexander WS, Voss AK, Vaux DL, Kaiser WJ, Walczak H, and Silke J. TNFR1-dependent cell death drives inflammation in Sharpin-deficient mice. *eLife*, 3, 2014.
- Rodrigues MF, Alves CCS, Figueiredo BBM, Rezende AB, Wohlres-Viana S, Silva VLd, Machado MA, and Teixeira HC. Tumour necrosis factor receptors and apoptosis of alveolar macrophages during early infection with attenuated and virulent *Mycobacterium bovis*. *Immunology*, 139 (4): 503–512, 2013.
- Rothbauer U, Zolghadr K, Muyldermans S, Schepers A, Cardoso MC, and Leonhardt H. A versatile nanotrap for biochemical and functional studies with fluorescent fusion proteins. *Molecular & cellular proteomics MCP*, 7 (2): 282–289, 2008.
- Rowe JA, Moulds JM, Newbold CI, and Miller LH. *P. falciparum* rosetting mediated by a parasite-variant erythrocyte membrane protein and complement-receptor 1. *Nature*, 388 (6639): 292–295, 1997.
- Rozen T and Swidan SZ. Elevation of CSF tumor necrosis factor alpha levels in new daily persistent headache and treatment refractory chronic migraine. *Headache*, 47 (7): 1050–1055, 2007.
- Rust MJ, Bates M, and Zhuang X. Sub-diffraction-limit imaging by stochastic optical reconstruction microscopy (STORM). *Nature methods*, 3 (10): 793–795, 2006.
- Sakin V, Paci G, Lemke EA, and Müller B. Labeling of virus components for advanced, quantitative imaging analyses. *FEBS letters*, 590 (13): 1896–1914, 2016.
- Salanti A, Dahlbäck M, Turner L, Nielsen MA, Barfod L, Magistrado P, Jensen ATR, Lavstsen T, Ofori MF, Marsh K, Hviid L, and Theander TG. Evidence for the involvement of VAR2CSA in pregnancy-associated malaria. *The Journal of experimental medicine*, 200 (9): 1197–1203, 2004.
- Salanti A, Staalsoe T, Lavstsen T, Jensen ATR, Sowa MPK, Arnot DE, Hviid L, and Theander TG. Selective upregulation of a single distinctly structured var gene in chondroitin sulphate A-adhering *Plasmodium falciparum* involved in pregnancy-associated malaria. *Molecular microbiology*, 49 (1): 179–191, 2003.

REFERENCES

- Sanchez CP, Karathanasis C, Sanchez R, Cyrklaff M, Jäger J, Buchholz B, Schwarz US, Heilemann M, and Lanzer M. Single-molecule imaging and quantification of the immune-variant adhesin VAR2CSA on knobs of *Plasmodium falciparum*-infected erythrocytes. *Communications biology*, 2: 172, 2019.
- Santee SM and Owen-Schaub LB. Human tumor necrosis factor receptor p75/80 (CD120b) gene structure and promoter characterization. *Journal of Biological Chemistry*, 271 (35): 21151–21159, 1996.
- Sauer M, Hofkens J, and Enderlein J. *Handbook of fluorescence spectroscopy and imaging: From single molecules to ensembles*. Weinheim: Wiley-VCH, 2011.
- Saxena S, Pant AB, Khanna VK, Singh K, Shukla RK, Meyer CH, and Singh VK. Tumor necrosis factor- α -mediated severity of idiopathic retinal periphlebitis in young adults (Eales' disease): Implication for anti-TNF- α therapy. *Journal of ocular biology, diseases, and informatics*, 3 (1): 35–38, 2010.
- Scheidereit C. IkappaB kinase complexes: Gateways to NF-kappaB activation and transcription. *Oncogene*, 25 (51): 6685–6705, 2006.
- Schermelleh L, Carlton PM, Haase S, Shao L, Winoto L, Kner P, Burke B, Cardoso MC, Agard DA, Gustafsson MGL, Leonhardt H, and Sedat JW. Subdiffraction multicolor imaging of the nuclear periphery with 3D structured illumination microscopy. *Science (New York, N.Y.)*, 320 (5881): 1332–1336, 2008.
- Schmidt N, Haydn T, Schneider I, Busch H, Boerries M, and Fulda S. Smac mimetic induces an early wave of gene expression via NF- κ B and AP-1 and a second wave via TNFR1 signaling. *Cancer letters*, 421: 170–185, 2018.
- Schmitz I, Kirchhoff S, and Krammer PH. Regulation of death receptor-mediated apoptosis pathways. *The international journal of biochemistry & cell biology*, 32 (11-12): 1123–1136, 2000.
- Schürks M, Rist PM, Zee RY, Chasman DI, and Kurth T. Tumour necrosis factor gene polymorphisms and migraine: A systematic review and meta-analysis. *Cephalalgia an international journal of headache*, 31 (13): 1381–1404, 2011.
- Schwabe RF and Brenner DA. Mechanisms of Liver Injury. I. TNF-alpha-induced liver injury: Role of IKK, JNK, and ROS pathways. *American journal of physiology. Gastrointestinal and liver physiology*, 290 (4): G583-9, 2006.
- Segawa K and Nagata S. An Apoptotic 'Eat Me' Signal: Phosphatidylserine Exposure. *Trends in cell biology*, 25 (11): 639–650, 2015.
- Shaner NC, Campbell RE, Steinbach PA, Giepmans BNG, Palmer AE, and Tsien RY. Improved monomeric red, orange and yellow fluorescent proteins derived from *Discosoma* sp. red fluorescent protein. *Nature biotechnology*, 22 (12): 1567–1572, 2004.
- Shanker N and Bane SL. Basic Aspects of Absorption and Fluorescence Spectroscopy and Resonance Energy Transfer Methods. In Detrich HW and Correia JJ (Eds), *Biophysical tools for biologists: Volume 1: In vitro techniques*. Amsterdam, s.l.: Elsevier, 2008: 213–242.
- Sharma YD. Knob proteins in falciparum malaria. *The Indian journal of medical research*, 106: 53–62, 1997.

- Sharonov A and Hochstrasser RM. Wide-field subdiffraction imaging by accumulated binding of diffusing probes. *Proceedings of the National Academy of Sciences*, 103 (50): 18911–18916, 2006.
- Shcherbakova DM and Verkhusha VV. Chromophore chemistry of fluorescent proteins controlled by light. *Current opinion in chemical biology*, 20: 60–68, 2014.
- Shivanandan A, Deschout H, Scarselli M, and Radenovic A. Challenges in quantitative single molecule localization microscopy. *FEBS letters*, 588 (19): 3595–3602, 2014.
- Simeonova PP, Gallucci RM, Hulderman T, Wilson R, Kommineni C, Rao M, and Luster MI. The role of tumor necrosis factor-alpha in liver toxicity, inflammation, and fibrosis induced by carbon tetrachloride. *Toxicology and applied pharmacology*, 177 (2): 112–120, 2001.
- Small A and Stahlheber S. Fluorophore localization algorithms for super-resolution microscopy. *Nature methods*, 11 (3): 267–279, 2014.
- Smith JD. The role of PfEMP1 adhesion domain classification in Plasmodium falciparum pathogenesis research. *Molecular and biochemical parasitology*, 195 (2): 82–87, 2014.
- Smith JD, Subramanian G, Gamain B, Baruch DI, and Miller LH. Classification of adhesive domains in the Plasmodium falciparum erythrocyte membrane protein 1 family. *Molecular and biochemical parasitology*, 110 (2): 293–310, 2000.
- Steffler A, Hopkins SJ, Rothwell NJ, and Luheshi GN. The role of TNF-alpha in fever: Opposing actions of human and murine TNF-alpha and interactions with IL-beta in the rat. *British journal of pharmacology*, 118 (8): 1919–1924, 1996.
- Stennett EMS, Ciuba MA, and Levitus M. Photophysical processes in single molecule organic fluorescent probes. *Chemical Society reviews*, 43 (4): 1057–1075, 2014.
- Stokes GG. Ueber die Veränderung der Brechbarkeit des Lichts. *Annalen der Physik und Chemie*, 163 (11): 480–490, 1852.
- Storey H, Stewart A, Vandenabeele P, and Luzio JP. The p55 tumour necrosis factor receptor TNFR1 contains a trans-Golgi network localization signal in the C-terminal region of its cytoplasmic tail. *The Biochemical journal*, 366 (Pt 1): 15–22, 2002.
- Subach FV, Patterson GH, Manley S, Gillette JM, Lippincott-Schwartz J, and Verkhusha VV. Photoactivatable mCherry for high-resolution two-color fluorescence microscopy. *Nature methods*, 6 (2): 153–159, 2009.
- Sun L, Wang H, Wang Z, He S, Chen S, Liao D, Wang L, Yan J, Liu W, Lei X, and Wang X. Mixed lineage kinase domain-like protein mediates necrosis signaling downstream of RIP3 kinase. *Cell*, 148 (1-2): 213–227, 2012.
- Sun S-C. Non-canonical NF-κB signaling pathway. *Cell research*, 21 (1): 71–85, 2011.
- Sun X, Yin J, Starovasnik MA, Fairbrother WJ, and Dixit VM. Identification of a novel homotypic interaction motif required for the phosphorylation of receptor-interacting protein (RIP) by RIP3. *Journal of Biological Chemistry*, 277 (11): 9505–9511, 2002.
- Sundgren-Andersson AK, Ostlund P, and Bartfai T. IL-6 is essential in TNF-alpha-induced fever. *The American journal of physiology*, 275 (6 Pt 2): R2028-34, 1998.

REFERENCES

- Sungkaworn T, Jobin M-L, Burnecki K, Weron A, Lohse MJ, and Calebiro D. Single-molecule imaging reveals receptor-G protein interactions at cell surface hot spots. *Nature*, 550 (7677): 543–547, 2017.
- Swaroop JJ, Rajarajeswari D, and Naidu JN. Association of TNF- α with insulin resistance in type 2 diabetes mellitus. *The Indian journal of medical research*, 135: 127–130, 2012.
- Szabó Á, Szendi-Szatómári T, Ujlaky-Nagy L, Rádi I, Vereb G, Szöllősi J, and Nagy P. The Effect of Fluorophore Conjugation on Antibody Affinity and the Photophysical Properties of Dyes. *Biophysical Journal*, 114 (3): 688–700, 2018.
- Takada H, Chen N-J, Mirtsos C, Suzuki S, Suzuki N, Wakeham A, Mak TW, and Yeh W-C. Role of SODD in regulation of tumor necrosis factor responses. *Molecular and cellular biology*, 23 (11): 4026–4033, 2003.
- Tan S, Tan HT, and Chung MCM. Membrane proteins and membrane proteomics. *Proteomics*, 8 (19): 3924–3932, 2008.
- Tang P, Hung M-C, and Klostergaard J. Human pro-tumor necrosis factor is a homotrimer. *Biochemistry*, 35 (25): 8216–8225, 1996.
- Tarantino N, Tinevez J-Y, Crowell EF, Boisson B, Henriques R, Mhlanga M, Agou F, Israël A, and Laplantine E. TNF and IL-1 exhibit distinct ubiquitin requirements for inducing NEMO-IKK supramolecular structures. *The Journal of cell biology*, 204 (2): 231–245, 2014.
- Tarrats N, Moles A, Morales A, García-Ruiz C, Fernández-Checa JC, and Marí M. Critical role of tumor necrosis factor receptor 1, but not 2, in hepatic stellate cell proliferation, extracellular matrix remodeling, and liver fibrogenesis. *Hepatology (Baltimore, Md.)*, 54 (1): 319–327, 2011.
- Taylor DL and Waggoner AS (Eds). *Applications of fluorescence in the biomedical sciences: Proceedings of a Meeting*. New York: Liss, 1986.
- Tchoghandjian A, Jennewein C, Eckhardt I, Rajalingam K, and Fulda S. Identification of non-canonical NF- κ B signaling as a critical mediator of Smac mimetic-stimulated migration and invasion of glioblastoma cells. *Cell death & disease*, 4: e564, 2013.
- Thompson RE, Larson DR, and Webb WW. Precise Nanometer Localization Analysis for Individual Fluorescent Probes. *Biophysical Journal*, 82 (5): 2775–2783, 2002.
- Thornberry NA. Caspases: Key mediators of apoptosis. *Chemistry & Biology*, 5 (5): R97-R103, 1998.
- Ting AT and Bertrand MJM. More to Life than NF- κ B in TNFR1 Signaling. *Trends in immunology*, 37 (8): 535–545, 2016.
- Titelbaum DS, Degenhardt A, and Kinkel RP. Anti-tumor necrosis factor alpha-associated multiple sclerosis. *AJNR. American journal of neuroradiology*, 26 (6): 1548–1550, 2005.
- Tokunaga M, Imamoto N, and Sakata-Sogawa K. Highly inclined thin illumination enables clear single-molecule imaging in cells. *Nature methods*, 5 (2): 159–161, 2008.
- Tomoda H, Kishimoto Y, and Lee YC. Temperature effect on endocytosis and exocytosis by rabbit alveolar macrophages. *Journal of Biological Chemistry*, 264 (26): 15445–15450, 1989.
- Tracey KJ and Cerami A. Tumor necrosis factor: A pleiotropic cytokine and therapeutic target. *Annual review of medicine*, 45: 491–503, 1994.

- Trager W and Jensen J. Human malaria parasites in continuous culture. *Science*, 193 (4254): 673–675, 1976.
- Tryon RC. *Cluster analysis correlation profile and orthometric (factor) analysis for the isolation of unities in mind and personality*,. Ann Arbor Mich: Edwards Brother Inc. lithoprinters and Publishers, 1939.
- Tsuchiya Y, Nakabayashi O, and Nakano H. FLIP the Switch: Regulation of Apoptosis and Necroptosis by cFLIP. *International journal of molecular sciences*, 16 (12): 30321–30341, 2015.
- Ulbrich MH and Isacoff EY. Subunit counting in membrane-bound proteins. *Nature methods*, 4 (4): 319–321, 2007.
- Ulich TR, del Castillo J, Ni RX, Bikhazi N, and Calvin L. Mechanisms of tumor necrosis factor alpha-induced lymphopenia, neutropenia, and biphasic neutrophilia: A study of lymphocyte recirculation and hematologic interactions of TNF alpha with endogenous mediators of leukocyte trafficking. *Journal of leukocyte biology*, 45 (2): 155–167, 1989.
- Uppoor R and Niebergall PJ. beta-D(+) glucose-glucose oxidase-catalase for use as an antioxidant system. *Pharmaceutical development and technology*, 1 (2): 127–134, 1996.
- van de Linde S, Krstić I, Prisner T, Doose S, Heilemann M, and Sauer M. Photoinduced formation of reversible dye radicals and their impact on super-resolution imaging. *Photochemical & photobiological sciences Official journal of the European Photochemistry Association and the European Society for Photobiology*, 10 (4): 499–506, 2011a.
- van de Linde S, Löscherger A, Klein T, Heidbreder M, Wolter S, Heilemann M, and Sauer M. Direct stochastic optical reconstruction microscopy with standard fluorescent probes. *Nature Protocols*, 6 (7): 991–1009, 2011b.
- van de Linde S and Sauer M. How to switch a fluorophore: From undesired blinking to controlled photoswitching. *Chemical Society reviews*, 43 (4): 1076–1087, 2014.
- van Deventer SJH. Anti-tumour necrosis factor therapy in Crohn's disease: Where are we now? *Gut*, 51 (3): 362–363, 2002.
- van Hauwermeiren F, Vandenbroucke RE, Grine L, Lodens S, van Wonterghem E, Rycke R de, Geest N de, Hassan B, and Libert C. TNFR1-induced lethal inflammation is mediated by goblet and Paneth cell dysfunction. *Mucosal immunology*, 8 (4): 828–840, 2015.
- van Horsen R, Hagen TLM ten, and Eggermont AMM. TNF-alpha in cancer treatment: Molecular insights, antitumor effects, and clinical utility. *The oncologist*, 11 (4): 397–408, 2006.
- van Noorden CJ. The history of Z-VAD-FMK, a tool for understanding the significance of caspase inhibition. *Acta histochemica*, 103 (3): 241–251, 2001.
- van Thor JJ, Gensch T, Hellingwerf KJ, and Johnson LN. Phototransformation of green fluorescent protein with UV and visible light leads to decarboxylation of glutamate 222. *Nature structural biology*, 9 (1): 37–41, 2002.
- Vanamee ÉS and Faustman DL. Structural principles of tumor necrosis factor superfamily signaling. *Science signaling*, 11 (511), 2018.

REFERENCES

- Varfolomeev E, Blankenship JW, Wayson SM, Fedorova AV, Kayagaki N, Garg P, Zobel K, Dynek JN, Elliott LO, Wallweber HJA, Flygare JA, Fairbrother WJ, Deshayes K, Dixit VM, and Vucic D. IAP antagonists induce autoubiquitination of c-IAPs, NF-kappaB activation, and TNFalpha-dependent apoptosis. *Cell*, 131 (4): 669–681, 2007.
- Vénéreau E, Ceriotti C, and Bianchi ME. DAMPs from Cell Death to New Life. *Frontiers in immunology*, 6: 422, 2015.
- Vince JE, Pantaki D, Feltham R, Mace PD, Cordier SM, Schmukle AC, Davidson AJ, Callus BA, Wong WW-L, Gentle IE, Carter H, Lee EF, Walczak H, Day CL, Vaux DL, and Silke J. TRAF2 must bind to cellular inhibitors of apoptosis for tumor necrosis factor (tnf) to efficiently activate nf- κ b and to prevent tnf-induced apoptosis. *The Journal of biological chemistry*, 284 (51): 35906–35915, 2009.
- Vince JE, Wong WW-L, Khan N, Feltham R, Chau D, Ahmed AU, Benetatos CA, Chunduru SK, Condon SM, McKinlay M, Brink R, Leverkus M, Tergaonkar V, Schneider P, Callus BA, Koentgen F, Vaux DL, and Silke J. IAP antagonists target cIAP1 to induce TNFalpha-dependent apoptosis. *Cell*, 131 (4): 682–693, 2007.
- Virant D, Traenkle B, Maier J, Kaiser PD, Bodenhöfer M, Schmees C, Vojnovic I, Pisak-Lukáts B, Endesfelder U, and Rothbauer U. A peptide tag-specific nanobody enables high-quality labeling for dSTORM imaging. *Nature communications*, 9 (1): 930, 2018.
- Waggoner A. Fluorescent labels for proteomics and genomics. *Current opinion in chemical biology*, 10 (1): 62–66, 2006.
- Wahlgren M, Goel S, and Akhouri RR. Variant surface antigens of Plasmodium falciparum and their roles in severe malaria. *Nature reviews. Microbiology*, 15 (8): 479–491, 2017.
- Wajant H. Principles of antibody-mediated TNF receptor activation. *Cell death and differentiation*, 22 (11): 1727–1741, 2015.
- Wajant H and Scheurich P. Tumor necrosis factor receptor-associated factor (TRAF) 2 and its role in TNF signaling. *The international journal of biochemistry & cell biology*, 33 (1): 19–32, 2001.
- Wajant H and Scheurich P. TNFR1-induced activation of the classical NF- κ B pathway. *The FEBS journal*, 278 (6): 862–876, 2011.
- Walczak H. TNF and ubiquitin at the crossroads of gene activation, cell death, inflammation, and cancer. *Immunological reviews*, 244 (1): 9–28, 2011.
- Wallach D, Kovalenko A, and Feldmann M (Eds). *Advances in TNF Family Research: Proceedings of the 12th International TNF Conference, 2009*. 1st ed. New York, NY: Springer Science+Business Media LLC, 2011a.
- Wallach D, Kovalenko A, and Feldmann M (Eds). *Advances in TNF Family Research: Proceedings of the 12th International TNF Conference, 2009*. 1st ed. New York, NY: Springer Science+Business Media LLC, 2011b.
- Wang H, Sun L, Su L, Rizo J, Liu L, Wang L-F, Wang F-S, and Wang X. Mixed lineage kinase domain-like protein MLKL causes necrotic membrane disruption upon phosphorylation by RIP3. *Molecular cell*, 54 (1): 133–146, 2014.

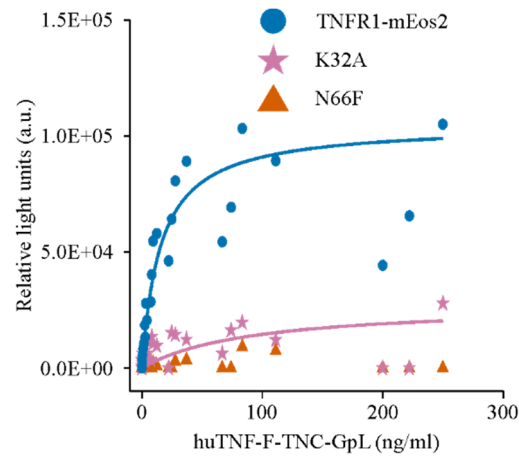
- Wang X, Xiao S, and Xia Y. Tumor Necrosis Factor Receptor Mediates Fibroblast Growth Factor-Inducible 14 Signaling. *Cellular physiology and biochemistry international journal of experimental cellular physiology, biochemistry, and pharmacology*, 43 (2): 579–588, 2017.
- Wang X-H, Hong X, Zhu L, Wang Y-T, Bao J-P, Liu L, Wang F, and Wu X-T. Tumor necrosis factor alpha promotes the proliferation of human nucleus pulposus cells via nuclear factor- κ B, c-Jun N-terminal kinase, and p38 mitogen-activated protein kinase. *Experimental biology and medicine (Maywood, N.J.)*, 240 (4): 411–417, 2015.
- Wang Y-L, Chou F-C, Chen S-J, Lin S-H, Chang D-M, and Sytwu H-K. Targeting pre-ligand assembly domain of TNFR1 ameliorates autoimmune diseases - an unrevealed role in downregulation of Th17 cells. *Journal of autoimmunity*, 37 (3): 160–170, 2011.
- Webb RH. Confocal optical microscopy. *Reports on Progress in Physics*, 59 (3): 427–471, 1996.
- Weinberg JR, Boyle P, Meager A, and Guz A. Lipopolysaccharide, tumor necrosis factor, and interleukin-1 interact to cause hypotension. *The Journal of laboratory and clinical medicine*, 120 (2): 205–211, 1992.
- Weinberg JR, Wright DJ, and Guz A. Interleukin-1 and tumour necrosis factor cause hypotension in the conscious rabbit. *Clinical science (London, England 1979)*, 75 (3): 251–255, 1988.
- Westphal V and Hell SW. Nanoscale resolution in the focal plane of an optical microscope. *Physical review letters*, 94 (14): 143903, 2005.
- Wheatley SP and Wang Y-l. Chapter 18 Indirect Immunofluorescence Microscopy in Cultured Cells. In Wilson L, Matsudaira PT, and Mather JP (Eds), *Animal Cell Culture Methods*. 1st ed. s.l.: Elsevier textbooks, 1998: 313–332.
- White NJ, Pukrittayakamee S, Hien TT, Faiz MA, Mokuolu OA, and Dondorp AM. Malaria. *The Lancet*, 383 (9918): 723–735, 2014.
- Wiedenmann J, Ivanchenko S, Oswald F, Schmitt F, Röcker C, Salih A, Spindler K-D, and Nienhaus GU. EosFP, a fluorescent marker protein with UV-inducible green-to-red fluorescence conversion. *Proceedings of the National Academy of Sciences*, 101 (45): 15905–15910, 2004.
- Willcox M, Björkman A, Brohult J, Pehrson PO, Rombo L, and Bengtsson E. A case-control study in northern Liberia of Plasmodium falciparum malaria in haemoglobin S and beta-thalassaemia traits. *Annals of tropical medicine and parasitology*, 77 (3): 239–246, 1983.
- Winkel C, Neumann S, Surulescu C, and Scheurich P. A minimal mathematical model for the initial molecular interactions of death receptor signalling. *Mathematical biosciences and engineering MBE*, 9 (3): 663–683, 2012.
- Wolfbeis OS (Ed). *Fluorescence Spectroscopy: New Methods and Applications*. Berlin, Heidelberg: Springer, 1993.
- Wolter S, Schüttpelz M, Tscherepanow M, van de Linde S, Heilemann M, and Sauer M. Real-time computation of subdiffraction-resolution fluorescence images. *Journal of microscopy*, 237 (1): 12–22, 2010.
- Wu H, Tschopp J, and Lin S-C. Smac mimetics and TNFalpha: A dangerous liaison? *Cell*, 131 (4): 655–658, 2007.

REFERENCES

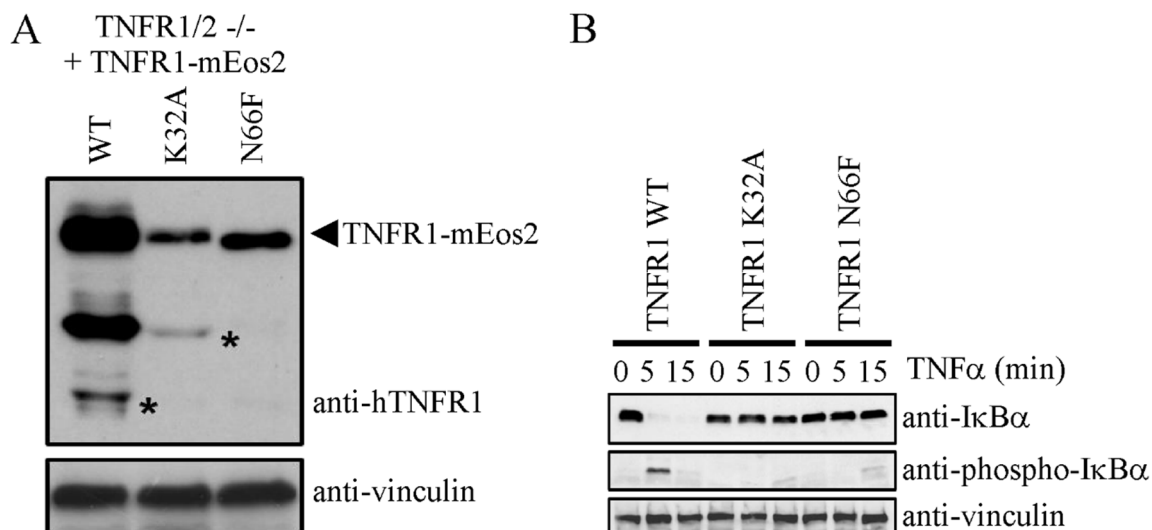
- Wu X-N, Yang Z-H, Wang X-K, Zhang Y, Wan H, Song Y, Chen X, Shao J, and Han J. Distinct roles of RIP1-RIP3 hetero- and RIP3-RIP3 homo-interaction in mediating necroptosis. *Cell death and differentiation*, 21 (11): 1709–1720, 2014.
- Wu Y-T, Tan H-L, Huang Q, Sun X-J, Zhu X, and Shen H-M. zVAD-induced necroptosis in L929 cells depends on autocrine production of TNF α mediated by the PKC-MAPKs-AP-1 pathway. *Cell death and differentiation*, 18 (1): 26–37, 2011.
- Xu K, Babcock HP, and Zhuang X. Dual-objective STORM reveals three-dimensional filament organization in the actin cytoskeleton. *Nature methods*, 9 (2): 185–188, 2012.
- Xu X, Efremov AK, Li A, Lai L, Dao M, Lim CT, and Cao J. Probing the cytoadherence of malaria infected red blood cells under flow. *PloS one*, 8 (5): e64763, 2013.
- Yang H, Ma Y, Chen G, Zhou H, Yamazaki T, Klein C, Pietrocola F, Vacchelli E, Souquere S, Sauvat A, Zitvogel L, Kepp O, and Kroemer G. Contribution of RIP3 and MLKL to immunogenic cell death signaling in cancer chemotherapy. *Oncoimmunology*, 5 (6): e1149673, 2016.
- Yin H and Flynn AD. Drugging Membrane Protein Interactions. *Annual review of biomedical engineering*, 18: 51–76, 2016.
- Zhang J, Campbell RE, Ting AY, and Tsien RY. Creating new fluorescent probes for cell biology. *Nature reviews. Molecular cell biology*, 3 (12): 906–918, 2002.
- Zhang M, Chang H, Zhang Y, Yu J, Wu L, Ji W, Chen J, Liu B, Lu J, Liu Y, Zhang J, Xu P, and Xu T. Rational design of true monomeric and bright photoactivatable fluorescent proteins. *Nature methods*, 9 (7): 727–729, 2012.
- Zhang X, Zhang M, Li D, He W, Peng J, Betzig E, and Xu P. Highly photostable, reversibly photoswitchable fluorescent protein with high contrast ratio for live-cell superresolution microscopy. *Proceedings of the National Academy of Sciences of the United States of America*, 113 (37): 10364–10369, 2016.
- Zhou XX and Lin MZ. Photoswitchable fluorescent proteins: Ten years of colorful chemistry and exciting applications. *Current opinion in chemical biology*, 17 (4): 682–690, 2013.

APPENDIX

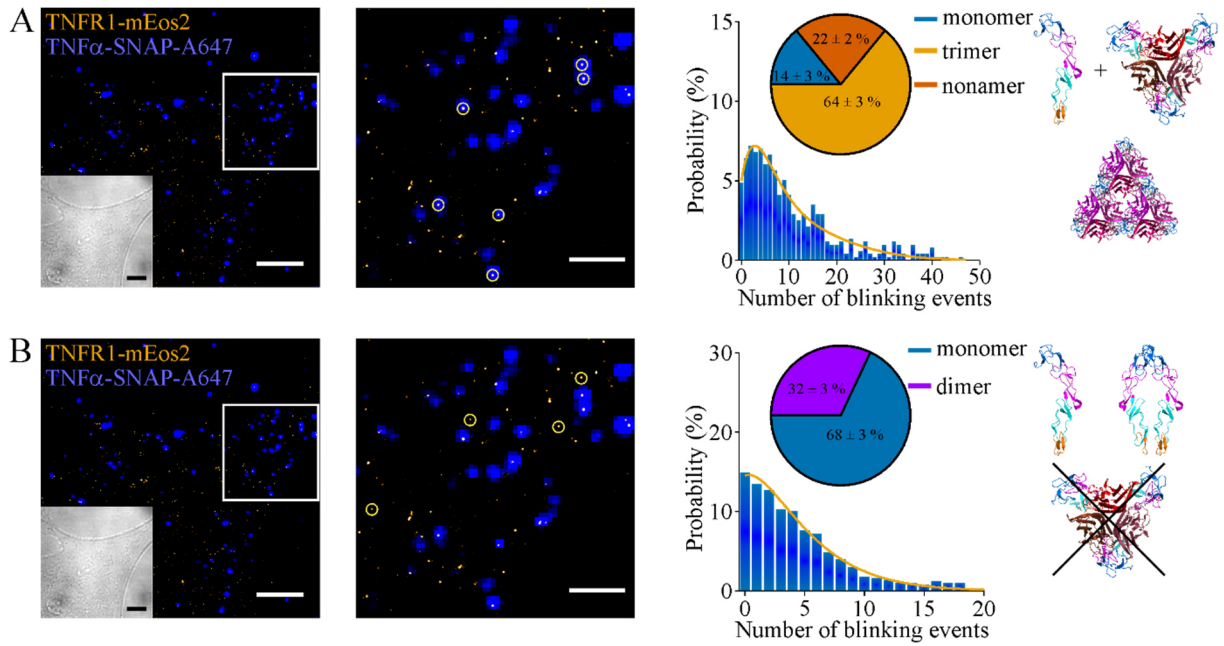
SUPPLEMENTARY FIGURES



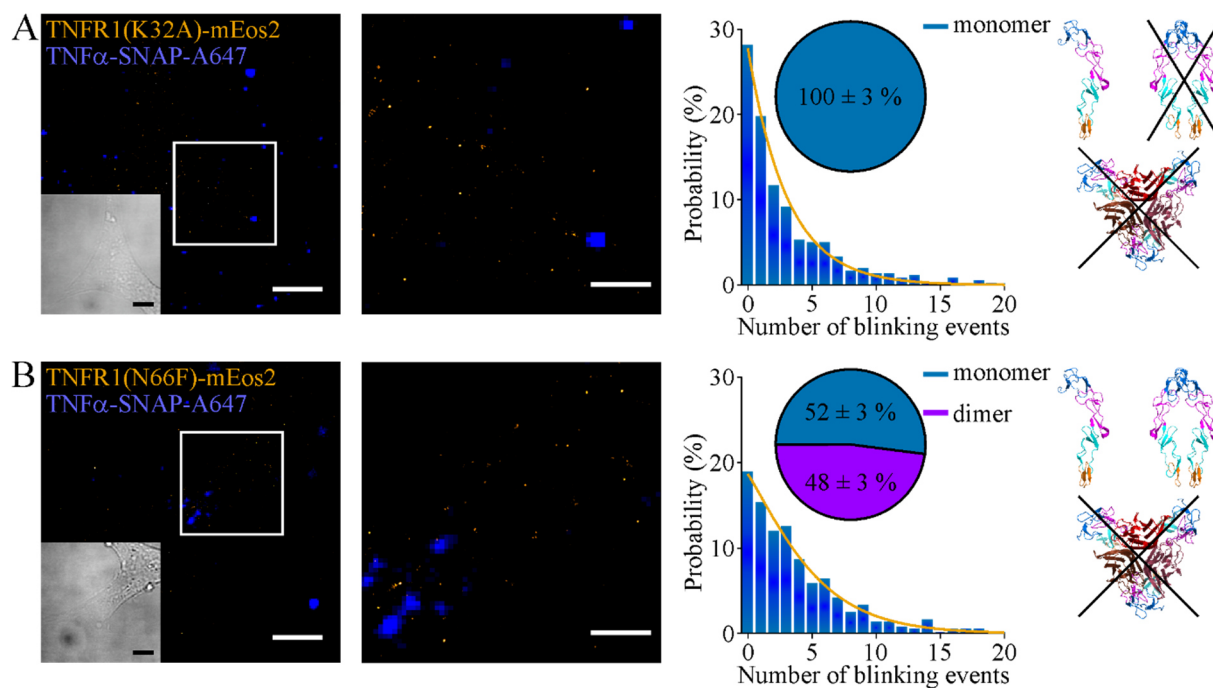
Supplementary Figure 1: TNF α binding assays. Luciferase assay of human TNF α with a GpL domain to TNFR1/2-/- + TNFR1-mEos2, TNFR1(K32A)-mEos2 and TNFR1(N66F)-mEos2 MEFs. Ligand binding was observed for the TNFR1/2-/- + TNFR1-mEos2 ($K_D = 16 \pm 3$ ng/ml) and TNFR1(K32A)-mEos2 ($K_D = 91 \pm 3$ ng/ml) MEFs. No ligand binding was observed for the TNFR1(N66F)-mEos2 MEF cell line. Experiments presented in this figure were performed by Dr. Juliane Medler (Würzburg, Germany).



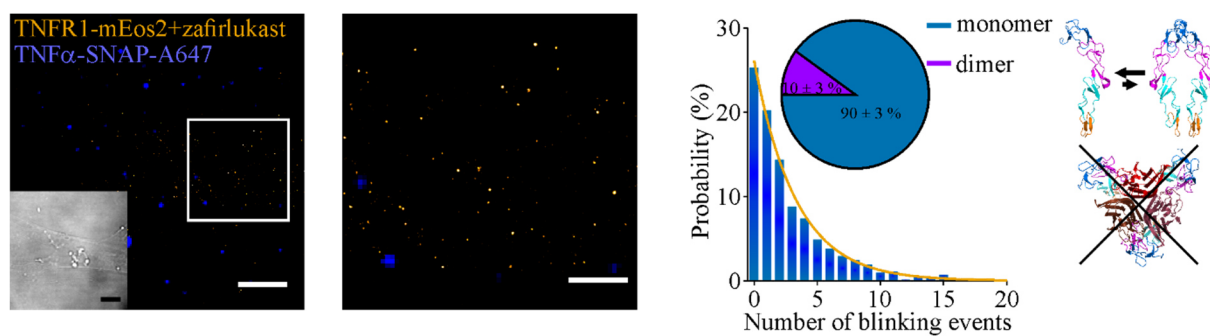
Supplementary Figure 2: Western blot analysis of TNFR1(K32A)-mEos2 and TNFR1(N66F)-mEos2 MEFs. (A) Western blot analysis shows the expression level of TNF α -untreated TNFR1-mEos2 in TNFR1/2^{-/-} + TNFR1-mEos2, TNFR1(K32A)-mEos2 and TNFR1-(N66F)-mEos2 MEFs. (B) Western blot analysis reveals the anti-I κ B α and the anti-phospho-I κ B α level of TNF α -untreated and TNF α -treated TNFR1/2^{-/-} + TNFR1-mEos2, TNFR1(K32A)-mEos2 and TNFR1-(N66F)-mEos2 MEFs after five and 15 minutes incubation time. Experiments presented in this figure were performed by Dr. Sjoerd J. L. van Wijk (Frankfurt, Germany).



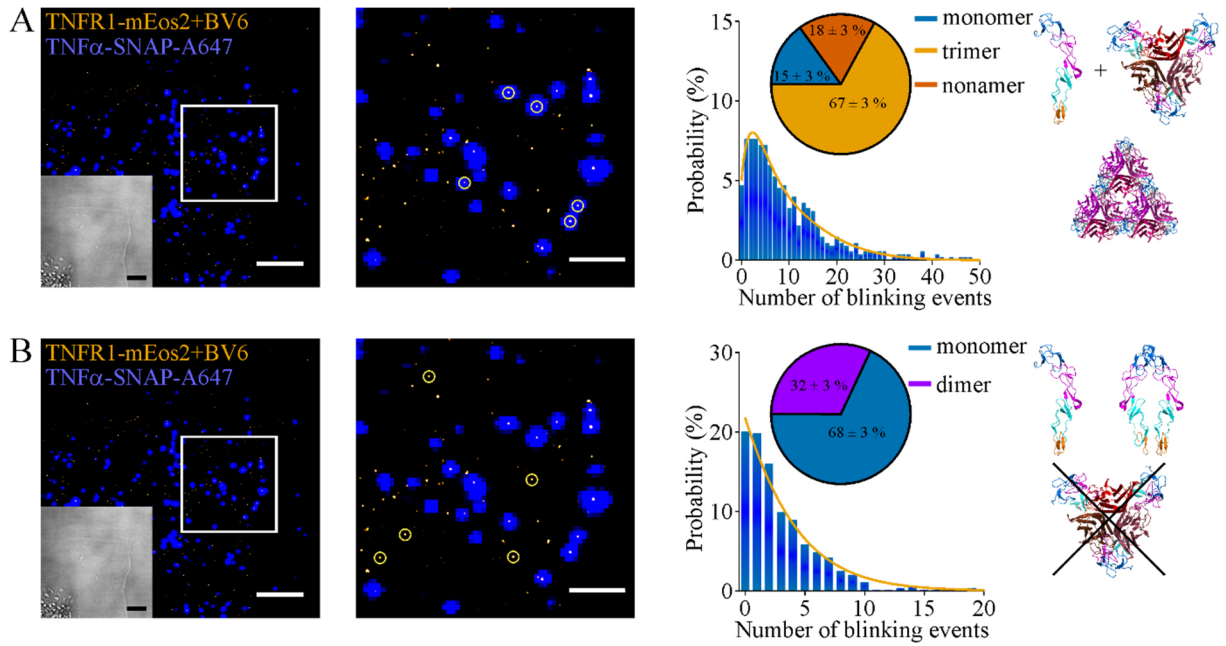
Supplementary Figure 3: The oligomeric state of TNFR1-mEos2 at 37 °C. (A) PALM and brightfield image of one representative *TNFR1/2-/-* + *TNFR1-mEos2* MEF cell (left panel) and zoomed region (middle panel) after *TNF α* treatment. Quantitative analysis of ligand-bound *TNFR1* reveals a distribution of 15 ± 3 % monomers, 67 ± 3 % trimers and 18 ± 2 % nonamers (equation 11, yellow curve). (B) PALM and brightfield image of one *TNFR1/2-/-* + *TNFR1-mEos2* MEF cell (left panel) and zoomed region (middle panel) after *TNF α* treatment. Quantitative analysis of ligand-free *TNFR1* reveals a distribution of 71 ± 3 % monomers and 29 ± 3 % dimers (equation 11, yellow curve). Incubation was performed at 37 °C. (Scale bars, 5 μ m PALM and brightfield images (left panels), 1 μ m PALM images (middle panels)) (PDB 1NCF, 1TNF).



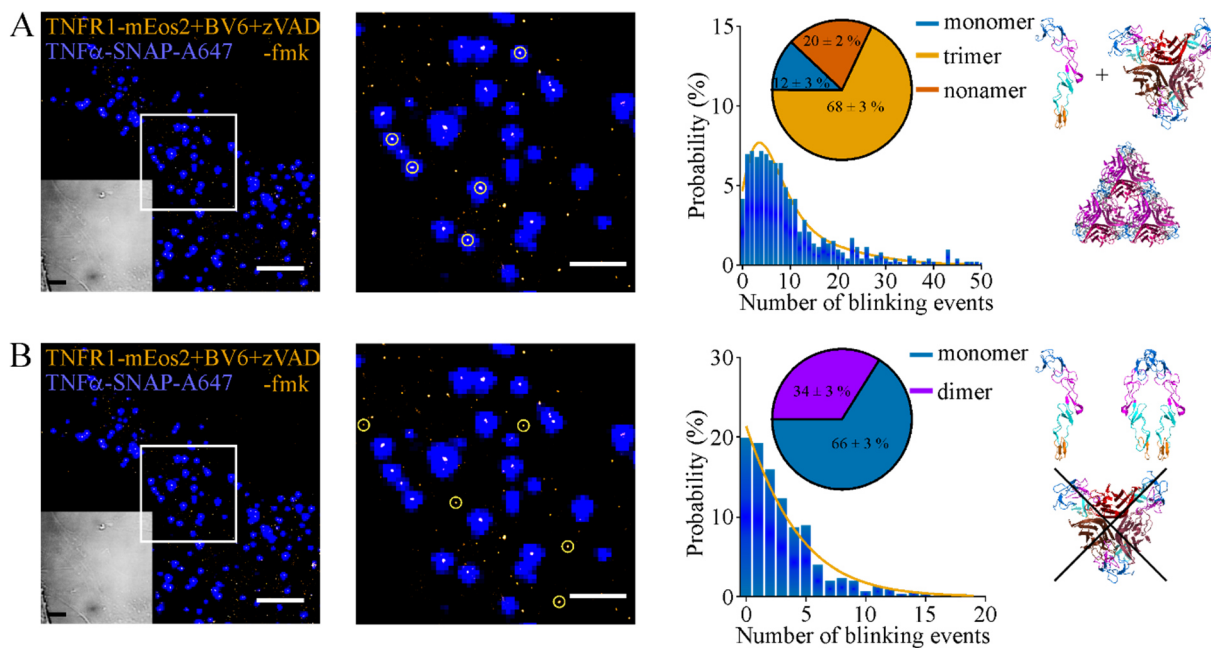
Supplementary Figure 4: The oligomeric state of TNFR1(K32A)-mEos2 at 37 °C. (A) PALM and brightfield image of one representative TNF α -treated TNFR1(K32A)-mEos2 MEF cell (left panel) and zoomed region (middle panel) incubated at 37 °C. Quantitative analysis of ligand-bound TNFR1 reveals a distribution of 100 \pm 3 % monomers (equation 11, yellow curve). (B) PALM and brightfield image of one representative TNF α -treated TNFR1(N66F)-mEos2 MEF cell (left panel) and zoomed region (middle panel) incubated at 37 °C. Quantitative analysis of ligand-bound TNFR1 reveals a distribution of 52 \pm 3 % monomers and 48 \pm 3 % dimers (equation 11, yellow curve). (Scale bars, 5 μ m PALM and brightfield images (left panel), 1 μ m PALM image (middle panel)) (PDB 1NCF, 1TNF).



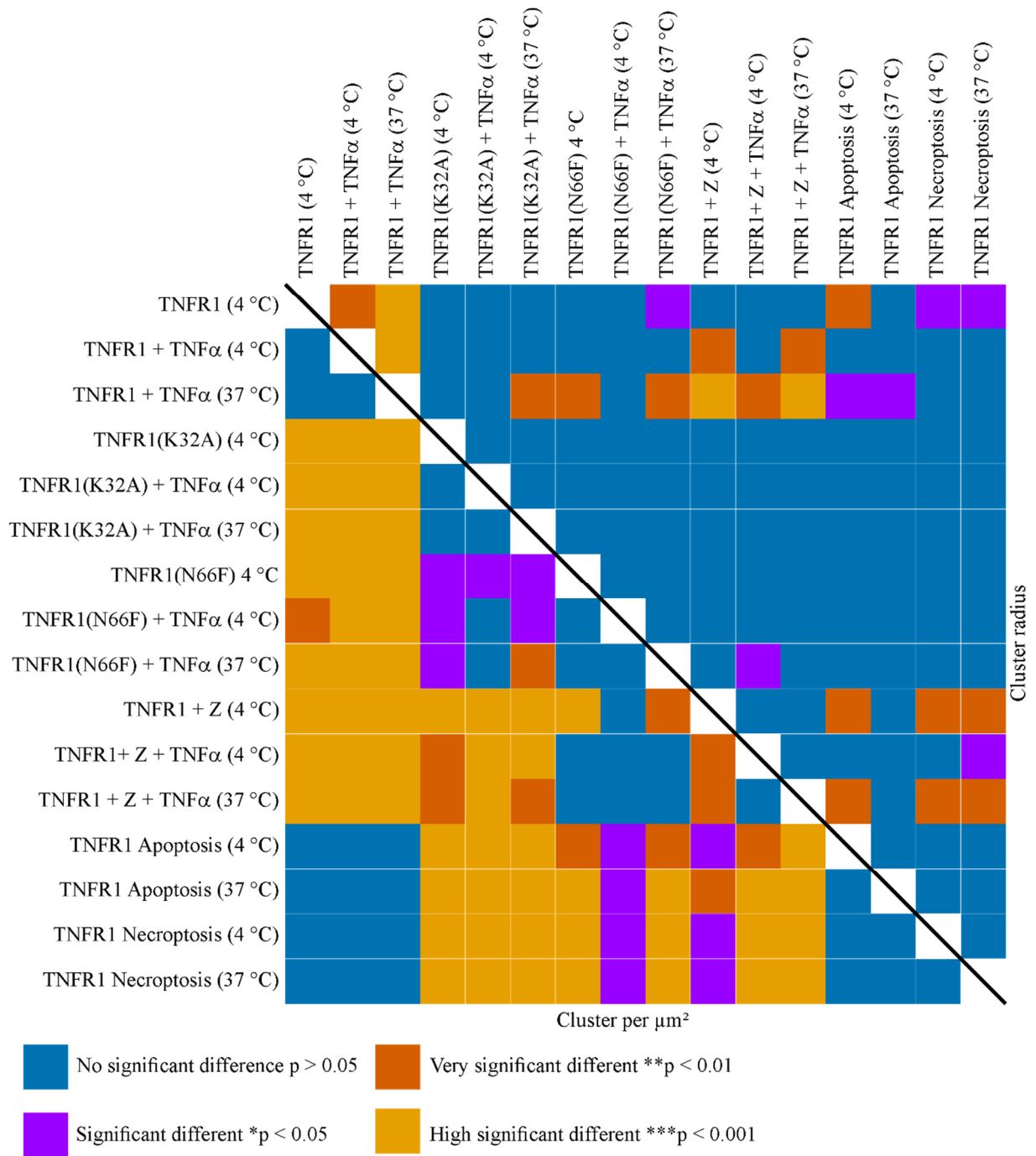
Supplementary Figure 5: The oligomeric state of TNFR1-mEos2 after zafirlukast treatment at 37 °C. PALM and brightfield image of one representative TNFR1/2 $^{-/-}$ + TNFR1-mEos2 MEF cell (left panel) and zoomed region (middle panel) after zafirlukast treatment. Quantitative analysis of ligand-bound TNFR1 reveals a distribution of 90 \pm 3 % monomers and 10 \pm 3 % dimers (equation 11, yellow curve). Incubation was performed at 37 °C. (Scale bars, 5 μ m PALM and brightfield images (left panel), 1 μ m PALM image (middle panel)) (PDB 1NCF, 1TNF).



Supplementary Figure 6: The oligomeric state of TNFR1-mEos2 after apoptosis induction at 37 °C. (A) PALM and brightfield image of one representative *TNFR1*^{2-/-} + *TNFR1*-mEos2 MEF cell (left panel) and zoomed region (middle panel) after apoptosis induction. Quantitative analysis of ligand-bound *TNFR1* reveals a distribution of $15 \pm 3\%$ monomers, $67 \pm 3\%$ trimers and $18 \pm 3\%$ nonamers (equation 11, yellow curve). (B) PALM and brightfield image of one *TNFR1*^{2-/-} + *TNFR1*-mEos2 MEF cell (left panel) and zoomed region (middle panel) after apoptosis induction. Quantitative analysis of ligand-free *TNFR1* reveals a distribution of $68 \pm 3\%$ monomers and $32 \pm 3\%$ dimers (equation 11, yellow curve). Incubation was performed at 37 °C. (Scale bars, 5 μ m PALM and brightfield images (left panels), 1 μ m PALM images (middle panels)) (PDB 1NCF, 1TNF).



Supplementary Figure 7: The oligomeric state of TNFR1-mEos2 after necroptosis induction at 37 °C. (A) PALM and brightfield image of one representative TNFR1/2-/- + TNFR1-mEos2 MEF cell (left panel) and zoomed region (middle panel) after necroptosis induction. Quantitative analysis of ligand-bound TNFR1 reveals a distribution of $12 \pm 3\%$ monomers, $68 \pm 3\%$ trimers and $20 \pm 2\%$ nonamers (equation 11, yellow curve). (B) PALM and brightfield image of one TNFR1/2-/- + TNFR1-mEos2 MEF cell (left panel) and zoomed region (middle panel) after necroptosis induction. Quantitative analysis of ligand-free TNFR1 reveals a distribution of $66 \pm 3\%$ monomers and $34 \pm 3\%$ dimers (equation 11, yellow curve). Incubation was performed at 37 °C. (Scale bars, 5 μm PALM and brightfield images (left panels), 1 μm PALM images (middle panels)) (PDB INCF, 1TNF).



Supplementary Figure 8: Mann-Whitney-U-tests for analyzed DBSCAN data of all TNFR1 conditions. Mann-Whitney-U-tests for all analyzed TNFR1 conditions for the TNFR1 cluster radius (right top) and TNFR1 cluster per μm^2 (left bottom) obtained from DBSCAN analysis. Blue shows no significant difference, green significant difference, red very significant difference and orange high significant difference between the indicated conditions.

SUPPLEMENTARY TABLES

Supplementary Table 1: Statistical analysis of TNF α -untreated TNFR1. *Listed are all possible models (with monomers M, dimers D and trimers T), corresponding Bayesian information criterions and log likelihood values with which the number of blinking event distribution of TNF α -untreated TNFR1 was analyzed.*

MODEL	BIC	LOGL
M + D	4172.267	-2082.735
M + D + T	4179.065	-2082.735
M + T	4179.546	-2086.375
M	4211.71	-2105.855
D	4417.864	-2208.932
D + T	4424.662	-2208.932
T	5256.721	-2628.361

Supplementary Table 2: Statistical analysis of TNF α -treated and ligand-bound TNFR1 data.

Listed are the 20 best models (with monomers M , dimers D and trimers T), corresponding Bayesian information criterions and log likelihood values with which the number of blinking event distribution of TNF α -treated and ligand-bound TNFR1 was analyzed.

MODEL	BIC	LOGL
M + T + 9	3915.026	-1951.157
D + 4 + 9	3916.443	-1951.865
D + T + 9	3916.613	-1951.95
D + 5 + 9	3920.444	-1953.866
M + D + T + 9	3920.733	-1950.833
M + T + 6 + 9	3921.382	-1951.157
M + T + 4 + 9	3921.382	-1951.157
M + T + 8 + 9	3921.382	-1951.157
M + T + 5 + 9	3921.382	-1951.157
M + T + 7 + 9	3921.382	-1951.157
D + T + 4 + 9	3922.494	-1951.713
M + D + 4 + 9	3922.69	-1951.811
D + 4 + 8 + 9	3922.799	-1951.865
D + 4 + 6 + 9	3922.799	-1951.865
D + 4 + 5 + 9	3922.799	-1951.865
D + 4 + 7 + 9	3922.799	-1951.865
D + T + 5 + 9	3922.931	-1951.931
D + T + 6 + 9	3922.969	-1951.95
D + T + 7 + 9	3922.969	-1951.95
D + T + 8 + 9	3922.969	-1951.95

Supplementary Table 3: Statistical analysis of TNF α -treated but ligand-free TNFR1 data. *Listed are all possible models (with monomers M, dimers D and trimers T), corresponding Bayesian information criteria and log likelihood values with which the number of blinking event distribution of TNF α -treated but ligand-free TNFR1 was analyzed.*

MODEL	BIC	LOGL
M + D	2813.249	-1403.469
M + T	2815.627	-1404.658
M + D + T	2817.098	-1402.237
D	2861.19	-1430.595
D + T	2867.502	-1430.595
M	2936.032	-1468.016
T	3217.079	-1608.54

Supplementary Table 4: Statistical analysis of TNF α -untreated TNFR1(K32A)-mEos2. *Listed are all possible models (with monomers M, dimers D and trimers T), corresponding Bayesian information criteria and log likelihood values with which the number of blinking event distribution of TNF α -untreated TNFR1(K32A)-mEos2 was analyzed.*

MODEL	BIC	LOGL
M	1627.29	-810.645
M + T	1627.755	-810.947
M + D + T	1633.615	-810.947
M + D	1638.35	-816.244
D	1795.087	-897.544
D + T	1800.948	-897.544
T	2169.243	-1084.622

Supplementary Table 5: Statistical analysis of TNF α -treated TNFR1(K32A)-mEos2. Listed are all possible models (with monomers *M*, dimers *D* and trimers *T*), corresponding Bayesian information criterions and log likelihood values with which the number of blinking event distribution of TNF α -treated TNFR1(K32A)-mEos2 was analyzed.

MODEL	BIC	LOGL
M	1933.706	-963.353
M + T	1933.782	-963.873
M + D + T	1939.818	-963.873
M + D	1946.302	-970.133
D	2137.571	-1068.785
D + T	2143.606	-1068.785
T	2585.175	-1292.587

Supplementary Table 6: Statistical analysis of TNF α -untreated TNFR1(N66F)-mEos2. Listed are all possible models (with monomers *M*, dimers *D* and trimers *T*), corresponding Bayesian information criterions and log likelihood values with which the number of blinking event distribution of TNF α -untreated TNFR1(N66F)-mEos2 was analyzed.

MODEL	BIC	LOGL
M + D	2718.064	-1355.251
M + T	2718.191	-1355.965
M + D + T	2724.452	-1355.965
D	2805.422	-1402.711
D + T	2811.684	-1402.711
M	2839.921	-1419.96
T	3168.884	-1584.442

Supplementary Table 7: Statistical analysis of TNF α -treated TNFR1(N66F)-mEos2. *Listed are all possible models (with monomers M, dimers D and trimers T), corresponding Bayesian information criteria and log likelihood values with which the number of blinking event distribution of TNF α -treated TNFR1(N66F)-mEos2 was analyzed.*

MODEL	BIC	LOGL
M + D	2631.293	-1314.029
M + T	2634.727	-1314.246
M + D + T	2640.961	-1314.246
D	2725.902	-1362.951
D + T	2732.137	-1362.951
M	2744.844	-1372.422
T	3090.615	-1545.308

Supplementary Table 8: Statistical analysis of TNF α -untreated TNFR1 treated with zafirlukast. *Listed are all possible models (with monomers M, dimers D and trimers T), corresponding Bayesian information criteria and log likelihood values with which the number of blinking event distribution of TNF α -untreated TNFR1 treated with zafirlukast was analyzed.*

MODEL	BIC	LOGL
M + D	7110.646	-3551.664
M + T	7117.964	-3557.258
M + D + T	7149.723	-3571.202
M	7221.536	-3610.768
D	7725.277	-3862.639
D + T	7732.595	-3862.639
T	9217.224	-4608.612

Supplementary Table 9: Statistical analysis of TNF α -treated TNFR1 treated with zafirlukast.

Listed are all possible models (with monomers *M*, dimers *D* and trimers *T*), corresponding Bayesian information criteria and log likelihood values with which the number of blinking event distribution of TNF α -treated TNFR1 treated with zafirlukast was analyzed.

MODEL	BIC	LOGL
M + D	3583.224	-1788.268
M + T	3589.516	-1791.414
M + D + T	3589.913	-1788.268
M	3593.158	-1796.579
D	3955.112	-1977.556
D + T	3961.8	-1977.556
T	4829.831	-2414.915

Supplementary Table 10: Statistical analysis of TNF α -treated TNFR1 induced with apoptosis.

Listed are the 20 best models (with monomers *M*, dimers *D* and trimers *T*), corresponding Bayesian information criterions and log likelihood values with which the number of blinking event distribution of TNF α -treated and ligand-bound TNFR1 induced with apoptosis was analyzed.

MODEL	BIC	LOGL
M + T + 9	3813.054	-1900.254
D + T + 9	3815.101	-1902.23
D + 4 + 9	3815.603	-1902.504
D + T + 8 + 9	3819.351	-1900.23
D + T + 7 + 9	3819.351	-1900.23
D + T + 6 + 9	3819.351	-1900.23
D + T + 4 + 9	3819.351	-1900.23
D + T + 5 + 9	3819.351	-1900.23
M + D + T + 9	3819.351	-1900.23
M + T + 8 + 9	3823.399	-1902.254
M + T + 6 + 9	3823.399	-1902.254
M + T + 4 + 9	3823.399	-1902.254
M + T + 5 + 9	3823.399	-1902.254
M + T + 7 + 9	3823.399	-1902.254
D + 4 + 8 + 9	3823.9	-1902.504
D + 4 + 7 + 9	3823.9	-1902.504
D + 4 + 6 + 9	3823.9	-1902.504
M + D + 4 + 9	3823.9	-1902.504
D + 4 + 5 + 9	3823.9	-1902.504
D + 5 + 9	3825.013	-1906.21

Supplementary Table 11: Statistical analysis of TNF α -treated but ligand-free TNFR1 induced with apoptosis. Listed are all possible models (with monomers *M*, dimers *D* and trimers *T*), corresponding Bayesian information criterions and log likelihood values with which the number of blinking event distribution of TNF α -treated but ligand-free TNFR1 induced with apoptosis was analyzed

MODEL	BIC	LOGL
M + D	1567.981	-781.085
M + T	1567.985	-781.087
M + D + T	1573.113	-780.745
M	1579.699	-789.85
D	1664.735	-832.368
D + T	1670.546	-832.368
T	1980.851	-990.425

Supplementary Table 12: Statistical analysis of TNF α -treated TNFR1 induced with necroptosis.

Listed are the 20 best models (with monomers *M*, dimers *D* and trimers *T*), corresponding Bayesian information criterions and log likelihood values with which the number of blinking event distribution of TNF α -treated and ligand-bound TNFR1 induced with necroptosis was analyzed.

MODEL	BIC	LOGL
M + T + 9	3796.793	-1892.054
D + T + 9	3797.511	-1892.414
D + 5 + 9	3799.08	-1893.198
D + 4 + 9	3799.084	-1893.2
D + T + 4 + 9	3803.042	-1892.008
M + D + T + 9	3803.085	-1892.029
D + 6 + 9	3803.12	-1895.218
D + 4 + 6 + 9	3803.135	-1892.054
M + D + 4 + 9	3803.135	-1892.054
D + 4 + 8 + 9	3803.135	-1892.054
D + 4 + 5 + 9	3803.135	-1892.054
D + 4 + 7 + 9	3803.135	-1892.054
D + T + 5 + 9	3803.323	-1892.148
D + T + 6 + 9	3803.631	-1892.302
D + T + 7 + 9	3803.841	-1892.407
D + T + 7 + 9	3803.854	-1892.414
M + T + 8	3804.247	-1895.781
D + 5 + 7 + 9	3805.422	-1893.198
D + 5 + 8 + 9	3805.422	-1893.198
M + D + 5 + 9	3805.422	-1893.198

Supplementary Table 13: Statistical analysis of TNF α -treated but ligand-free TNFR1 induced with necroptosis. Listed are all possible models (with monomers *M*, dimers *D* and trimers *T*), corresponding Bayesian information criterions and log likelihood values with which the number of blinking event distribution of TNF α -treated but ligand-free TNFR1 induced with necroptosis was analyzed.

MODEL	BIC	LOGL
M + D	1733.043	-863.546
M + T	1734.078	-864.064
M	1734.128	-867.064
M + D + T	1738.889	-863.494
D	1867.563	-933.782
D + T	1873.514	-93.782
T	2262.723	-1131.362

Supplementary Table 14: Statistical analysis of TNF α -treated and ligand-bound TNFR1 incubated at 37 °C. Listed are the 20 best models (with monomers *M*, dimers *D* and trimers *T*), corresponding Bayesian information criterions and log likelihood values with which the number of blinking event distribution of TNF α -treated and ligand-bound TNFR1 incubated at 37 °C.

MODEL	BIC	LOGL
D + T + 9	3471.892	-1729.704
D + 4 + 9	3472.277	-1729.896
D + T + 9	3473.63	-1730.573
D + 5 + 9	3474.705	-1731.11
M + D + T + 9	3477.639	-1729.456
M + T + 6 + 9	3478.134	-1729.704
M + T + 5 + 9	3478.134	-1729.704
M + T + 4 + 9	3478.134	-1729.704
M + T + 8 + 9	3478.134	-1729.704
M + T + 7 + 9	3478.134	-1729.704
M + D + 4 + 9	3478.289	-1729.781
D + T + 4 + 9	3478.518	-1729.896
D + 4 + 7 + 9	3478.519	-1729.896
D + 4 + 6 + 9	3478.519	-1729.896
D + 4 + 8 + 9	3478.519	-1729.896
D + 4 + 5 + 9	3478.519	-1729.896
D + 6 + 8	3479.048	-1733.282
D + T + 5 + 9	3479.228	-1730.251
D + T + 6 + 9	3479.73	-1730.502
D + T + 8	3479.821	-1733.668

Supplementary Table 15: Statistical analysis of TNF α -treated but ligand-free TNFR1 incubated at 37 °C. Listed are all possible models (with monomers *M*, dimers *D* and trimers *T*), corresponding Bayesian information criteria and log likelihood values with which the number of blinking event distribution of TNF α -treated but ligand-free TNFR1 incubated at 37 °C was analyzed.

MODEL	BIC	LOGL
M + D	2600.629	-1297.21
M + T	2601.85	-1297.821
M + D + T	2602.998	-1295.291
D	2622.476	-1311.238
D + T	2628.685	-1311.238
M	2752.885	-1376.442
T	2893.796	-1446.898

Supplementary Table 16: Statistical analysis of TNF α -treated TNFR1(K32A)-mEos2 incubated at 37 °C. Listed are all possible models (with monomers *M*, dimers *D* and trimers *T*), corresponding Bayesian information criteria and log likelihood values with which the number of blinking event distribution of TNF α -treated TNFR1(K32A)-mEos2 incubated at 37 °C was analyzed.

MODEL	BIC	LOGL
M	1694.066	-844.091
M + T	1699.949	-844.091
M + D + T	1707.013	-850.565
M + D	1717.198	-858.599
D	1857.685	-928.843
D + T	1863.568	-928.843
T	2226.581	-1113.29

Supplementary Table 17: Statistical analysis of TNF α -treated TNFR1(N66F)-mEos2 incubated at 37 °C. Listed are all possible models (with monomers *M*, dimers *D* and trimers *T*), corresponding Bayesian information criterions and log likelihood values with which the number of blinking event distribution of TNF α -treated TNFR1(N66F)-mEos2 incubated at 37 °C was analyzed.

MODEL	BIC	LOGL
M + D	1838.854	-911.485
M + T	1844.635	-916.434
M + D + T	1846.225	-920.171
D	1893.137	-946.569
D + T	1899.021	-946.569
M	1910	-955
T	2147.36	-1073.68

Supplementary Table 18: Statistical analysis of TNF α -treated TNFR1 treated with zafirlukast incubated at 37 °C. Listed are all possible models (with monomers *M*, dimers *D* and trimers *T*), corresponding Bayesian information criterions and log likelihood values with which the number of blinking event distribution of TNF α -treated TNFR1 treated with zafirlukast and incubated at 37 °C was analyzed.

MODEL	BIC	LOGL
M + D	4021.7	-2004.835
M + T	4028.464	-2007.468
M + D + T	4040.363	-2016.8
M	4063.548	-2031.774
D	4393.961	-2196.981
D + T	4400.725	-2196.981
T	5289.205	-2644.602

Supplementary Table 19: Statistical analysis of TNF α -treated and ligand-bound TNFR1 after apoptosis induction at 37 °C. Listed are the 20 best models (with monomers *M*, dimers *D* and trimers *T*), corresponding Bayesian information criterions and log likelihood values with which the number of blinking event distribution of TNF α -treated and ligand-bound TNFR1 after apoptosis induction incubated at 37 °C was analyzed.

MODEL	BIC	LOGL
M + T + 9	3794.036	-1890.703
D + T + 9	3795.949	-1891.659
D + 4 + 9	3796.115	-1891.742
D + 5 + 9	3796.485	-1891.927
M + D + 4 + 9	3800.3	-1890.677
D + 4 + 8 + 9	3800.352	-1890.703
D + T + 4 + 9	3800.352	-1890.703
D + 4 + 7 + 9	3800.352	-1890.703
D + 4 + 6 + 9	3800.352	-1890.703
D + 4 + 5 + 9	3800.352	-1890.703
M + D + T + 9	3800.881	-1890.967
D + T + 5 + 9	3801.272	-1891.163
D + 6 + 9	3801.978	-1894.674
D + T + 6 + 9	3802.093	-1891.573
D + T + 8 + 9	3802.264	-1891.659
D + T + 7 + 9	3802.264	-1891.659
M + T + 7 + 9	3802.43	-1891.742
M + T + 5 + 9	3802.43	-1891.742
M + T + 8 + 9	3802.43	-1891.742
M + T + 6 + 9	3802.43	-1891.742

Supplementary Table 20: Statistical analysis of TNF α -treated but ligand-free TNFR1 after apoptosis induction at 37 °C. Listed are all possible models (with monomers *M*, dimers *D* and trimers *T*), corresponding Bayesian information criteria and log likelihood values with which the number of blinking event distribution of TNF α -treated but ligand-free TNFR1-mEos2 after apoptosis induction at 37 °C was analyzed.

MODEL	BIC	LOGL
M + D	1959.943	-976.949
M + T	1961.847	-977.901
M + D + T	1965.903	-976.906
M	1972.765	-986.382
D	2080.272	-1040.136
D + T	2086.317	-1040.136
T	2482.868	-1241.434

Supplementary Table 21: Statistical analysis of TNF α -treated and ligand-bound TNFR1 after necroptosis induction at 37 °C. Listed are the 20 best models (with monomers *M*, dimers *D* and trimers *T*), corresponding Bayesian information criterions and log likelihood values with which the number of blinking event distribution of TNF α -treated and ligand-bound TNFR1 after necroptosis induction incubated at 37 °C was analyzed.

MODEL	BIC	LOGL
M + T + 9	3710.639	-1848.043
D + T + 9	3712.155	-1849.801
D + 4 + 9	3713.255	-1850.351
M + D + T + 9	3714.878	-1848.024
D + T + 5 + 9	3714.915	-1848.043
D + T + 4 + 9	3714.915	-1848.043
D + T + 6 + 9	3714.915	-1848.043
D + T + 8 + 9	3714.915	-1848.043
D + T + 7 + 9	3714.915	-1848.043
M + T + 8 + 9	3718.432	-1849.801
M + T + 5 + 9	3718.432	-1849.801
M + T + 6 + 9	3718.432	-1849.801
M + T + 7 + 9	3718.432	-1849.801
D + T + 6 + 9	3718.432	-1849.801
D + 4 + 6 + 9	3719.532	-1850.351
D + 4 + 8 + 9	3719.532	-1850.351
D + 4 + 7 + 9	3719.532	-1850.351
M + D + 4 + 9	3719.532	-1850.351
D + 4 + 5 + 9	3719.532	-1850.351
D + 5 + 9	3720.446	-1853.946

Supplementary Table 22: Statistical analysis of TNF α -treated but ligand-free TNFR1 after necroptosis induction at 37 °C. Listed are all possible models (with monomers *M*, dimers *D* and trimers *T*), corresponding Bayesian information criterions and log likelihood values with which the number of blinking event distribution of TNF α -treated but ligand-free TNFR1-mEos2 after necroptosis induction at 37 °C was analyzed.

MODEL	BIC	LOGL
M + D	1356.014	-675.153
M	1358.881	-679.441
M + T	1359.773	-677.033
M + D + T	1361.721	-675.153
D	1441.672	-720.836
D + T	1447.379	-720.836
T	1726.159	-863.079

Supplementary Table 23: Comparison of quantitative results of all TNFR1 conditions. *Listed are the particular condition and the distribution of the corresponding oligomeric states (M = monomer, D = dimer, T = trimer).*

CONDITION	OLIGOMERIC STATE
TNFR1(wt)-mEos2 (4 °C)	
- TNF α	66 \pm 4 % (M), 34 \pm 4 % (D)
+ TNF α (only colocalizing with TNFR1)	13 \pm 2 % (M), 64 \pm 2 % (T), 23 \pm 3 % (9mer)
+ TNF α (not colocalizing with TNFR1)	41 \pm 4 % (M), 59 \pm 4 % (D)
TNFR1(wt)-mEos2 (37 °C)	
+ TNF α (only colocalizing with TNFR1)	14 \pm 3 % (M), 64 \pm 3 % (T), 22 \pm 2 % (9mer)
+ TNF α (not colocalizing with TNFR1)	32 \pm 3 % (M), 68 \pm 3 % (D)
TNFR1(K32A)-mEos2 (4 °C)	
- TNF α	100 \pm 3 % (M)
+ TNF α (all TNFR1 clusters analyzed)	100 \pm 3 % (M)
TNFR1(K32A)-mEos2 (37 °C)	
+ TNF α (all TNFR1 clusters analyzed)	100 \pm 3 % (M)
TNFR1(N66F)-mEos2 (4 °C)	
- TNF α	46 \pm 3 % (M), 54 \pm 3 % (D)
+ TNF α (all TNFR1 clusters analyzed)	44 \pm 3 % (M), 56 \pm 3 % (D)
TNFR1(N66F)-mEos2 (37 °C)	
+ TNF α (all TNFR1 clusters analyzed)	52 \pm 3 % (M), 48 \pm 3 % (D)
TNFR1(wt)-mEos2 + zafirlukast (4 °C)	
- TNF α	90 \pm 3 % (M), 10 \pm 3 % (D)
+ TNF α (all TNFR1 clusters analyzed)	91 \pm 3 % (M), 9 \pm 3 % (D)
TNFR1(wt)-mEos2 + zafirlukast (37 °C)	
+ TNF α (all TNFR1 clusters analyzed)	90 \pm 3 % (M), 10 \pm 3 % (D)
TNFR1(wt)-mEos2 + apoptosis induction (4 °C)	
+ TNF α (only colocalizing with TNFR1)	10 \pm 3 % (M), 70 \pm 3 % (T), 20 \pm 2 % (9mer)
+ TNF α (not colocalizing with TNFR1)	71 \pm 3 % (M), 29 \pm 3 % (D)
TNFR1(wt)-mEos2 + apoptosis induction (37 °C)	
+ TNF α (only colocalizing with TNFR1)	15 \pm 3 % (M), 67 \pm 3 % (T), 18 \pm 3 % (9mer)
+ TNF α (not colocalizing with TNFR1)	68 \pm 3 % (M), 32 \pm 3 % (D)

SUPPLEMENTARY TABLES

TNFR1(wt)-mEos2 + necroptosis induction (4 °C)	
+ TNF α (only colocalizing with TNFR1)	15 \pm 3 % (M), 67 \pm 3 % (T), 18 \pm 2 % (9mer)
+ TNF α (not colocalizing with TNFR1)	28 \pm 3 % (M), 72 \pm 3 % (D)
TNFR1(wt)-mEos2 + necroptosis induction (37 °C)	
+ TNF α (only colocalizing with TNFR1)	12 \pm 3 % (M), 68 \pm 3 % (T), 20 \pm 2 % (9mer)
+ TNF α (not colocalizing with TNFR1)	34 \pm 3 % (M), 66 \pm 3 % (D)

Supplementary Table 24: Comparison of mean diameter and clusters per μm^2 of all TNFR1 conditions. Listed are the particular condition, the corresponding mean diameter and the mean number of cluster per μm^2 of TNFR1 determined by PALM.

CONDITION	DIAMETER [nm]	CLUSTERS PER μm^2
TNFR1(wt)-mEos2 (4 °C)		
- TNF α	32 \pm 19	1.4 \pm 0.4
+ TNF α	36 \pm 23	1.6 \pm 0.7
TNFR1(wt)-mEos2 (37 °C)		
+ TNF α	40 \pm 25	1.7 \pm 0.9
TNFR1(K32A)-mEos2 (4 °C)		
- TNF α	33 \pm 20	0.2 \pm 0.1
+ TNF α	30 \pm 11	0.3 \pm 0.2
TNFR1(K32A)-mEos2 (37 °C)		
+ TNF α	33 \pm 17	0.2 \pm 0.1
TNFR1(N66F)-mEos2 (4 °C)		
- TNF α	31 \pm 18	0.5 \pm 0.2
+ TNF α	34 \pm 19	0.6 \pm 0.4
TNFR1(N66F)-mEos2 (37 °C)		
+ TNF α	35 \pm 20	0.5 \pm 0.3
TNFR1(wt)-mEos2 + zafirlukast (4 °C)		
- TNF α	33 \pm 21	1.0 \pm 0.4
+ TNF α	33 \pm 20	0.6 \pm 0.3
TNFR1(wt)-mEos2 + zafirlukast (37 °C)		
+ TNF α	31 \pm 18	0.6 \pm 0.4
TNFR1(wt)-mEos2 + apoptosis induction (4 °C)	38 \pm 24	1.4 \pm 0.7
TNFR1(wt)-mEos2 + apoptosis induction (37 °C)	37 \pm 24	1.6 \pm 0.7
TNFR1(wt)-mEos2 + necroptosis induction (4 °C)	37 \pm 23	1.4 \pm 0.6
TNFR1(wt)-mEos2 + necroptosis induction (37 °C)	39 \pm 25	1.5 \pm 0.7

Supplementary Table 25: Comparison of the NeNA values determined for all investigated TNFR1 conditions. Listed are the particular condition and the corresponding NeNA values for all measured TNFR1 conditions.

CONDITION	NENA VALUES
TNFR1(wt)-mEos2 (4 °C)	
- TNF α	15.7 \pm 1.7
+ TNF α	15.8 \pm 1.5
TNFR1(wt)-mEos2 (37 °C)	
+ TNF α	15.8 \pm 1.9
TNFR1(K32A)-mEos2 (4 °C)	
- TNF α	15.9 \pm 1.8
+ TNF α	16.1 \pm 1.0
TNFR1(K32A)-mEos2 (37 °C)	
+ TNF α	15.9 \pm 2.3
TNFR1(N66F)-mEos2 (4 °C)	
- TNF α	15.4 \pm 1.7
+ TNF α	16.2 \pm 1.7
TNFR1(N66F)-mEos2 (37 °C)	
+ TNF α	15.5 \pm 1.5
TNFR1(wt)-mEos2 + zafirlukast (4 °C)	
- TNF α	16.1 \pm 1.1
+ TNF α	15.8 \pm 1.0
TNFR1(wt)-mEos2 + zafirlukast (37 °C)	
+ TNF α	16.2 \pm 1.1
TNFR1(wt)-mEos2 + apoptosis induction (4 °C)	
+ TNF α	15.8 \pm 1.9
TNFR1(wt)-mEos2 + apoptosis induction (37 °C)	
+ TNF α	15.9 \pm 1.2
TNFR1(wt)-mEos2 + necroptosis induction (4 °C)	
+ TNF α	15.4 \pm 1.3
TNFR1(wt)-mEos2 + necroptosis induction (37 °C)	
+ TNF α	15.7 \pm 1.3

LIST OF ABBREVIATIONS

	2D	2-dimensional
	3D	3-dimensional
A	A	Adenine
	a.u.	arbitrary unit
	A647	Alexa Fluor 647
	AIDS	Acquired immune deficiency syndrome
	AOTF	Acousto-optic tunable filter
	APD	Avalanche photodiode
B	BFP	Back focal plane
	BG	Benzylguanine
	BIC	Bayesian information criterion
	bp	base pair
	BS ³	Bis(sulfosuccinimidyl)suberate
	BSA	Bovine serum albumine
C	C	Cytosine
	CD27, 30, 36, 40, 54, 80, 86	Cluster of differentiation 27, 30, 36, 40, 54, 80, 86
	cDNA	complementary DNA
	cFLIP	FADD-like IL-1 β -converting enzyme (FLICE)-inhibitory protein
	cIAP	cellular inhibitor of apoptosis
	CLSM	Confocal laser-scanning microscopy
	CR1	Complement receptor 1
	CRD	Cysteine-rich domain
	CRISPR	Clustered regularly interspaced short palindromic repeats-associated
	CSA	Chondroitin-4-sulfate
	CTLA-4	Cytotoxic T-lymphocyte-associated protein 4
	CUAAC	Copper(I)-catalyzed azide-alkyne cycloaddition
D	DAMP	Damage-associated molecular patterns
	DAPI	4',6-diamidino-2-phenylindole
	DBL	Duffy binding like

LIST OF ABBREVIATIONS

	DBSCAN	Density-based spatial clustering of applications with noise
	DED	Death effector domain
	DISC	Death inducing signaling complex
	DM	Dichroic mirror
	DMSO	Dimethyl sulfoxide
	DNA	Deoxyribonucleic acid
	<i>d</i> STORM	<i>direct</i> stochastic optical reconstruction microscopy
	DTSSP	3,3'-dithiobis[sulfosuccinimidylpropionate]
	DTT	Dithiothreitol
	DR3	Death receptor 3
E	EM	Electron microscopy
	EMCCD	Electron multiplying charge coupled device
	EPCR	Endothelial protein C receptor
	Epi	Epifluorescence
	EV	Empty vector
F	F ^{•-}	Anionic radical
	FA	Formaldehyde
	FAB	Fragment antigen binding
	FACS	Fluorescence-activated cell sorting
	FADD	Fas associated protein with a death domain
	FASR	FAS-receptor
	FH	Leuco-form
	FBS	Fetal bovine serum
	FLICE	FADD-like IL-1 β -converting enzyme
	fPALM	Fluorescence photoactivated localization microscopy
G	G	Guanine
	GA	Glutaraldehyde
	GFP	Green fluorescent protein
	GpL	Gaussia princeps luciferase
	GSDIM	Ground-state depletion followed by individual molecule return
H	HILO	Highly inclined and laminated optical sheet microscopy

	HOIL	Homo-oxidized ubiquitin ligase 1
	HOIP	HOIL-1 interacting protein
	HOMO	Highest occupied molecular orbital
	HRP	Horseradish peroxidase
I	IBC	Intensity-based counting
	IC	Internal conversion
	ICAM-1	Intercellular adhesion molecule 1
	IgG	Immunoglobulin G
	IKK	I κ B kinase
	IrisFP	Iris fluorescent protein
	ISC	Intersystem crossing
L	LAMA	LocAlization Microscopy Analyzer
	LPS	Lipopolysaccharide
	LUBAC	Linear ubiquitin chain assembly complex
	LUMO	Lowest unoccupied molecular orbital
M	M	Mirror
	MEA	β -mercaptoethylamine
	MEF	Mouse embryonic fibroblast
	mEos2	Monomeric Eos 2
	mEos3.2	Monomeric Eos 3.2
	mEosFP	Monomeric Eos fluorescent protein
	MLKL	Mixed lineage kinase domain like pseudokinase
N	NA	Numerical aperture
	NEMO	NF- κ B essential modulator
	NeNA	Nearest neighbor analysis
	NF- κ B	Nuclear factor kappa-light-chain-enhancer of activated B-cells
	NHS	N-hydroxysuccinimide
	NIK	NF- κ B-inducing kinase
	NOA	NEMO Optineurin Abin
O	O ⁶ -BG	O ⁶ -benzylguanine
	Ox	Oxidation

LIST OF ABBREVIATIONS

P	paFP	Photoactivatable fluorescent proteins
	paGFP	Photoactivatable green fluorescent protein
	PAINT	Points accumulation for imaging in nanoscale topography
	PALM	Photoactivated localization microscopy
	PBS	Phosphate-buffered saline
	PCA	Protocatechuic acid
	PCD	Protocatechuate-3,4-dioxygenase
	PCR	Polymerase chain reaction
	PE	Phycoerythrin
	PEG	Poly(ethylene glycol)
	PFA	Paraformaldehyde
	pfEMP1	<i>Plasmodium falciparum</i> erythrocyte membrane protein 1
	PI	Propidium iodide
	PLAD	Pre-ligand assembly domain
	PLL	Poly(L-lysine)
	PMT	Photomultiplier tube
	PSF	Point spread function
Q	qPAINT	quantitative points accumulation for imaging in nanoscale topography
R	Red	Reduction
	Rhim	RIP homotypic interaction motif
	RIP1, 3	Receptor interacting protein 1, 3
	RNA	Ribonucleic acid
	ROI	Region of interest
	RPMI	Roswell Park Memorial Institute
	rsEGFP2	Reversibly switching enhanced green fluorescent protein 2
S	SIM	Structured illumination microscopy
	SMAC	Second mitochondrial derived activator of caspases
	SMLM	Single-molecule localization microscopy
	SODD	Silencer of death domain
	SPAAC	Second the strain-promoted azide-alkyne cycloaddition

	STED	Stimulated-emission depletion
	STORM	Stochastic optical reconstruction microscopy
T	T	Thymine
	T/B/Z	TNF α /BV6/zVAD-fmk
	tdEos	tandem Eos
	TIM	TRAF interacting motives
	TIRF	Total internal reflection fluorescence
	TLR	Toll-like receptor
	TNF α	Tumor necrosis factor alpha
	TNFR1/2	Tumor necrosis factor receptor 1/2
	TNFSF	Tumor necrosis factor superfamily
	TRADD	TNF receptor-associated death domain
	TRAF	Tumor necrosis factor receptor-associated factor
	TRAILR3/4	Tumor necrosis factor related apoptosis inducing ligand receptor 3/4
	TRAPS	TNF Receptor Associated Periodic Syndrome
U	UBD	Ubiquitin-binding domain
	UBAN	Ubiquitin-binding domain present in A20-binding inhibitor of NF- κ B and NEMO
	UPR	Unfolded protein response
	UV	Ultraviolet
V	VSVG	Vesicular stomatitis virus
W	wf	wild-field
	wt	wild-type

LIST OF FIGURES

Figure 1: Crystal structures of TNFR1 and its ligand TNF α .	3
Figure 2: Chemical structure of zafirlukast.	4
Figure 3: TNFR1 signaling cascade.	6
Figure 4: Chemical structure of the apoptosis inducing BV6.	7
Figure 5: Chemical structure of apoptosis inhibitor zVAD-fmk.	7
Figure 6: Necroptotic signaling cascade after TNFR1 activation.	8
Figure 7: Electron microscopy images of HbAA and HbAS erythrocytes.	9
Figure 8: Jablonski diagram.	12
Figure 9: Scheme of a light microscope.	12
Figure 10: Airy disc and Rayleigh limit.	13
Figure 11: Wide-field, TIRF and HILO illumination schemes.	14
Figure 12: Kinetic schemes of fluorescent proteins.	16
Figure 13: Chemical structures of selected organic fluorophores.	18
Figure 14: Photoswitching scheme of organic fluorophores.	19
Figure 15: SNAP-tag reaction with O ⁶ -benzylguanine.	20
Figure 16: Direct and indirect immunofluorescence.	21
Figure 17: Deterministic and stochastic super-resolution microscopy techniques.	23
Figure 18: Principle of the DBSCAN algorithm.	25
Figure 19: Selection of super-resolved localization clusters for quantitative PALM.	27
Figure 20: Scheme of the GATTAquant DNA origami Gatta-STORM Nanoruler.	33
Figure 21: Scheme of the SMLM microscope.	34
Figure 22: Reconstitution of TNFR1/2-/- + TNFR1-mEos2 MEFs.	39
Figure 23: Cellular calibration standards for qPALM.	40
Figure 24: The oligomeric state of TNF α -untreated TNFR1-mEos2 at 4 °C.	41
Figure 25: Determination of K _D -values of SNAP-F-TNC-TNF α and huTNF-F-TNC-GpL.	42
Figure 26: The oligomeric state of TNF α -treated TNFR1-mEos2 at 4 °C.	43
Figure 27: The oligomeric state of TNF α -treated but ligand-free TNFR1-mEos2 at 4 °C.	43
Figure 28: The oligomeric state of TNFR1(K32A)-mEos2 at 4 °C.	44
Figure 29: The oligomeric state of TNFR1(N66F)-mEos2 at 4 °C.	45
Figure 30: FACS analysis of TNFR1/2-/-, TNFR1/2-/- + TNFR1-mEos2-, TNFR1(K32A)-mEos2- and TNFR1(N66F)-mEos2 MEF cells.	45
Figure 31: The oligomeric state of TNFR1-mEos2 after zafirlukast treatment at 4 °C.	46
Figure 32: The oligomeric state of TNFR1-mEos2 after treatment with zafirlukast and TNF α at 4 °C.	47

Figure 33: The oligomeric state of TNFR1-mEos2 after apoptosis induction with TNF α and BV6 at 4 °C.	48
Figure 34: The oligomeric state of TNFR1-mEos2 after necroptosis induction with TNF α , BV6 and zVAD-fmk at 4 °C.	49
Figure 35: Molecular model for TNFR1 oligomerization.....	51
Figure 36: Alternative model for TNFR1 oligomerization.	52
Figure 37: Comparison of the oligomeric states of TNFR1 under different conditions.....	55
Figure 38: DBSCAN analysis and cluster size extraction.....	56
Figure 39: Comparison of the TNFR1-mEos2 cluster diameter.	57
Figure 40: Comparison of the number of TNFR1-mEos2 clusters per μm^2	58
Figure 41: Photoswitching scheme of Alexa Fluor 647.....	60
Figure 42: Single-molecule blinking analysis of Alexa Fluor 647.....	61
Figure 43: Single-molecule blinking analysis of three Alexa Fluor 647 fluorophores.	62
Figure 44: Brightfield and PALM images from FCR3, HbAA-G-6 and HbAS-G-6 probes.	66
Figure 45: VAR2CSA cluster diameter in HbAA and HbAS erythrocytes.	67
Figure 46: VAR2CSA molecules per knob and pfEMP1 clusters per μm^2	68
Figure 47: Possible VAR2CSA arrangement scheme.....	69
Figure 48: Summary of the oligomeric states of TNFR1.....	72

LIST OF TABLES

Table 1: Tumor necrosis factor superfamily..... 2
Table 2: Results of different maximum likelihood fits of trimeric Alexa Fluor 647..... 63

LIST OF SUPPLEMENTARY FIGURES

Supplementary Figure 1: TNF α binding assays.....	I
Supplementary Figure 2: Western blot analysis of TNFR1(K32A)-mEos2 and TNFR1(N66F)-mEos2 MEFs.....	II
Supplementary Figure 3: The oligomeric state of TNFR1-mEos2 at 37 °C.....	III
Supplementary Figure 4: The oligomeric state of TNFR1(K32A)-mEos2 at 37 °C.....	IV
Supplementary Figure 5: The oligomeric state of TNFR1-mEos2 after zafirlukast treatment at 37 °C.....	IV
Supplementary Figure 6: The oligomeric state of TNFR1-mEos2 after apoptosis induction at 37 °C...V	
Supplementary Figure 7: The oligomeric state of TNFR1-mEos2 after necroptosis induction at 37 °C.....	VI
Supplementary Figure 8: Mann-Whitney-U-tests for analyzed DBSCAN data of all TNFR1 conditions.....	VII

LIST OF SUPPLEMENTARY TABLES

Supplementary Table 1: Statistical analysis of TNF α -untreated TNFR1.	VIII
Supplementary Table 2: Statistical analysis of TNF α -treated and ligand-bound TNFR1 data.	IX
Supplementary Table 3: Statistical analysis of TNF α -treated but ligand-free TNFR1 data.	X
Supplementary Table 4: Statistical analysis of TNF α -untreated TNFR1(K32A)-mEos2.	X
Supplementary Table 5: Statistical analysis of TNF α -treated TNFR1(K32A)-mEos2.	XI
Supplementary Table 6: Statistical analysis of TNF α -untreated TNFR1(N66F)-mEos2.	XI
Supplementary Table 7: Statistical analysis of TNF α -treated TNFR1(N66F)-mEos2.	XII
Supplementary Table 8: Statistical analysis of TNF α -untreated TNFR1 treated with zafirlukast.	XII
Supplementary Table 9: Statistical analysis of TNF α -treated TNFR1 treated with zafirlukast.	XIII
Supplementary Table 10: Statistical analysis of TNF α -treated TNFR1 induced with apoptosis.	XIV
Supplementary Table 11: Statistical analysis of TNF α -treated but ligand-free TNFR1 induced with apoptosis.	XV
Supplementary Table 12: Statistical analysis of TNF α -treated TNFR1 induced with necroptosis.	XVI
Supplementary Table 13: Statistical analysis of TNF α -treated but ligand-free TNFR1 induced with necroptosis.	XVII
Supplementary Table 14: Statistical analysis of TNF α -treated and ligand-bound TNFR1 incubated at 37 °C.	XVIII
Supplementary Table 15: Statistical analysis of TNF α -treated but ligand-free TNFR1 incubated at 37 °C.	XIX
Supplementary Table 16: Statistical analysis of TNF α -treated TNFR1(K32A)-mEos2 incubated at 37 °C.	XIX
Supplementary Table 17: Statistical analysis of TNF α -treated TNFR1(N66F)-mEos2 incubated at 37 °C.	XX
Supplementary Table 18: Statistical analysis of TNF α -treated TNFR1 treated with zafirlukast incubated at 37 °C.	XX
Supplementary Table 19: Statistical analysis of TNF α -treated and ligand-bound TNFR1 after apoptosis induction at 37 °C.	XXI
Supplementary Table 20: Statistical analysis of TNF α -treated but ligand-free TNFR1 after apoptosis induction at 37 °C.	XXII
Supplementary Table 21: Statistical analysis of TNF α -treated and ligand-bound TNFR1 after necroptosis induction at 37 °C.	XXIII
Supplementary Table 22: Statistical analysis of TNF α -treated but ligand-free TNFR1 after necroptosis induction at 37 °C.	XXIV
Supplementary Table 23: Comparison of quantitative results of all TNFR1 conditions.	XXV

Supplementary Table 24: Comparison of mean diameter and clusters per μm^2 of all TNFR1 conditions.
..... XXVII

Supplementary Table 25: Comparison of the NeNA values determined for all investigated TNFR1
conditions. XXVIII

Acknowledgments

First and foremost, I like to express my very special thanks to Prof. Dr. Mike Heilemann for the opportunity to perform my PhD work in his research group. Through your encouragement, support and trust, I had the opportunity to gain a lot of experience in scientific working. Furthermore, I thank you for the opportunity to participate in various conferences.

Furthermore, I would like to thank Prof. Dr. Gerhard Hummer for taking the time and review this thesis. Collaboration with you and your research group over the last few years was at any time very pleasurable and productive.

I am also deeply grateful to Dr. Sjoerd J. L. van Wijk. Collaborating with you was a catalyst for my professional development. Our meetings have always enriched my scientific knowledge.

Great thanks go to the collaboration partners, Prof. Dr. Harald Wajant and Dr. Juliane Medler. Many thanks for all of your efforts to support us in our work. The collaboration was all the time pleasant and inspiring.

Next, I want to thank Prof. Dr. Michael Lanzer and Dr. Cecilia Sanchez. Collaborating with you was very exciting and productive.

Furthermore, I would like to thank Dr. Jakob Bullerjahn for his patiently and valuable support in the field of the theoretical and mathematical analysis.

I want to thank Petra Freund. Many thanks for your patience, as well as your great support in the cell culture. I owe you every great cell in this work. Great thanks to Jochen Feldhaar who was able to solve every technical problem I had. I would also like to thank Renate Gregori, Steffi Wegner, Peter Richter and Sophia Thul for their outstanding support.

Special thanks goes to Dr. Marina Dietz, who had accompanied me since my master thesis. Many thanks for your tremendous patience, as well as your willingness to help me at any time if necessary. Without you, I would never have accomplished the exciting adventure of a PhD student.

Great thanks go also to the whole Heilemann group and everyone who shared the last years with me. Many thanks to Dr. Ulrike Endesfelder for inspiring me so much with super-resolution microscopy. Thanks to Dr. Carmen Krüger, Dr. Anika Raulf and Dr. Franziska Fricke that you included me so nicely in your office crew. Discussion about science and other topics enriched my life. One more “thank you” goes to Dr. Franziska Fricke who instructed me in quantitative SMLM analysis with great dedication. Thank you for your patience and all the advices. Special thanks goes to Dr. Christoph Spahn, who helped me several times with phenomenal advices. Thank you for a great time and all the fun at all the retreats as roommates. However, most of all, I thank you for the cow. Great thanks to Dr. Sebastian Malkusch for his patiently and valuable support for helping with analysis. Next, I want to thank Dr. Hans-Dieter

Barth, Dr. Alexandre Fürstenberg, Kathrin Klehs, Carolin Böger, Nina Deußner-Helfmann, Mathilda Glaesmann, Marie-Lena Harwardt, Tim Baldering and Mark Schröder. Getting to know you and the rest of the Heilemann group was one of the greatest pleasures I enjoyed in the last four years. All the activities we did together like the trip to the Röhn, the triathlon, the annual baking of cookies for Christmas, lasertag, escape rooms and much more were a lot of fun. I could talk to any of you about anything at any time. The working atmosphere created here is remarkable. With you, I found not only colleagues but also true friends.

Special thanks goes to my friends, Oliver, Daniel, Andreas and Naixuan. Relaxing with you on holidays, conversations about life-essential topics or just spending time with you guys is invaluable. You are family to me.

Then I would like to thank all other friends who accompanied and supported me on this way

Finally, my greatest thanks go to my brother, sister, parents, grandparents and Anita. I would never made it here without you.

Curriculum Vitae

Personal Data

—————

Name	Christos Karathanasis
Date of birth	13. November 1989
Place of birth	Frankfurt, Germany

Education & research experience

—————

Since 10/2015	PhD thesis at the Institute of Physical and Theoretical Chemistry Johann Wolfgang Goethe-University, Frankfurt am Main
03/2013 – 02/2015	Master of Science in Biophysics Johann Wolfgang Goethe-University, Frankfurt am Main Master Thesis: „Etablierung von bildbasierter Fluoreszenzkorrelations- spektroskopie zur Untersuchung der Dynamik von Membranproteinen“
10/2009 – 02/2013	Bachelor of Science in Biophysics Johann Wolfgang Goethe-University, Frankfurt am Main Bachelor Thesis: “Charakterisierung der Filtrationseigenschaften von Membranfilter für Proteine”

List of Publications

Karathanasis C., Medler J., Fricke F., Smith S., Malkusch S., Widera D., Fulda S., Wajant H., van Wijk S.J.L., Dikic I., Heilemann M. Single-molecule imaging reveals the oligomeric state of functional TNF-induced plasma membrane TNFR1 clusters in cells. *Science Signaling* (in revision, 2019)

Sanchez C.P., **Karathanasis C.**, Sanchez R., Cyrklaff M., Jäger J., Buchholz B., Schwarz U.S., Heilemann M., Lanzer M. Single-molecule imaging and quantification of the immune-variant adhesion VAR2CSA on knobs of *Plasmodium falciparum*-infected erythrocytes. *Nature Communications Biology* 2, Article number: 172 (2019)

Böger C., Baldering T.N., Krüger C.L., Harwardt M-L., Mertinkus K.R., Schröder M.S., **Karathanasis C.**, Deussner-Helfmann N.S., Barth H-D., Malkusch S., Dietz M.S., Hummer G., Wohland T., Heilemann M. Quantification of membrane receptor complexes with single-molecule localization microscopy. *Proceedings Volume Spie 10884, Single Molecule Spectroscopy and Superresolution Imaging XII* (2019)

Baldering T.N., Dietz M.S., Gatterdam K., **Karathanasis C.**, Wieneke R., Tampé R., Heilemann M. Synthetic and genetic dimers as quantification ruler for single-molecule counting with PALM. *Molecular Biology of the Cell*, Volume 30, Number 12, 1369-1376 (2019)

Harwardt M-L., Young P., Bleymüller W.M., Meyer T., **Karathanasis C.**, Niemann H.H., Heilemann M., Dietz M.S. Membrane dynamics of resting and InIB-bound MET receptor tyrosine kinase studied by single-molecule tracking. *FEBS open bio*, Volume 7, Number 9, 1422-1440 (2017)

Karathanasis C., Fricke F., Hummer G., Heilemann M. Molecule counts in localization microscopy with organic fluorophores. *ChemPhysChem*, Volume 18, Number 8, 942-948 (2017)

Krüger C., Fricke F., **Karathanasis C.**, Dietz M.S., Malkusch S., Hummer G., Heilemann M. Molecular counting of membrane receptor subunits with single-molecule localization microscopy. *Proceedings Volume Spie 100710, Single Molecule Spectroscopy and Superresolution Imaging X* (2017)

Volz Y., Koschut., Matzke A., Dietz M.S., **Karathanasis C.**, Richert L., Wagner M.G., Mely Y., Heilemann M., Niemann H.H., Orian-Rousseau V. Direct binding of hepatocyte growth factor and vascular endothelial growth factor to CD44v6. *Bioscience Reports*, Volume 35, Number 4 (2015)